

## AN ABSTRACT OF THE DISSERTATION OF

Theeranun Siritanon for the degree of Doctor of Philosophy in Chemistry presented on July 8, 2011.

Title: Structure-Property Relationships in Oxides Containing Tellurium

Abstract approved: \_\_\_\_\_  
Munirpallam A. Subramanian

Oxides of post-transition metals often show unique structures and properties due to the presence of lone pair electrons and the diffused *s* orbitals. The present work focuses on synthesis and characterizations of oxides containing Te, a heavy post transition metal.

New series of pyrochlore oxides of the formula  $Cs(M,Te)_2O_6$  ( $M = Al, Ga, Cr, Fe, Co, In, Ho, Lu, Yb, Er, Ge, Rh, Ti, Zn, Ni, \text{ and } Mg$ ) have been prepared. The samples were highly colored (ranging from black to dark green) indicating a possible mixed valency for Te with appreciable charge transfer between them in the octahedral sites. Electronic conductivity was observed in some phases and could be as high as  $2S/cm$  ( $M=Ge$ ). Seebeck coefficients of conducting samples show negative values which suggest that electrons are the major charge carriers. Temperature dependence of conductivity indicates that the samples are semiconductors with, in some cases, degenerate semiconducting behavior. Detailed studies on the conduction mechanism indicate the mixed valency of tellurium which leads to semiconducting behavior and the color of the compounds.

Systematic studies of cesium tellurate with  $\text{CsTe}_2\text{O}_{6-x}$  where  $x = 0, 0.15, 0.25, 1.5$  have been investigated. On heating at slightly above  $600^\circ\text{C}$ ,  $\text{CsTe}_2\text{O}_6$  loses oxygen resulting in cubic structure with disordered  $\text{Te}^{4+}/\text{Te}^{6+}$  and oxygen vacancies. Two novel phases of  $\text{CsTe}_2\text{O}_{6-x}$  were prepared with orthorhombic structure. The first phase with  $x$  value of about 0.2-0.3 crystallizes in *Pnma* symmetry. At higher values of  $x$ , a new compound was discovered with a structure related to  $\text{Rb}_4\text{Te}_8\text{O}_{23}$ . Optical properties of the compounds are consistent with their colors.  $\text{CsTe}_2\text{O}_6$  belongs to class II mixed valency according to Robin and Day classification. However, structures and properties of  $\text{CsTe}_2\text{O}_{6-x}$  phases indicate that they are class I mixed valence compounds. Series of compounds with formula  $\text{CsTe}_{2-x}\text{W}_x\text{O}_6$  with  $x=0.2-0.5$  have been made which can be considered as solid solution of  $\text{CsTe}_2\text{O}_6$  and  $\text{CsTe}_{0.5}\text{W}_{1.5}\text{O}_6$ . Although the two end members adopt rhombohedral and trigonal structure, these solid solution phases crystallize in cubic defect pyrochlore structure with  $\text{W}^{6+}$ ,  $\text{Te}^{6+}$ , and  $\text{Te}^{4+}$  randomly occupying 16c octahedral site. The compounds show no electronic conductivity at room temperature.

Novel cubic pyrochlore with the formula  $(\text{CdBi})(\text{MTe})\text{O}_7$ ,  $\text{M} = \text{Al, Cr, Ga, In, Fe, Mn, and Sc}$  were synthesized by solid state reaction using oxides of the constituent elements. Magnetic properties analyses show paramagnetism in  $\text{M} = \text{Cr and Mn}$  but antiferromagnetism with short-range correlation in  $\text{M} = \text{Fe}$  phase. All compositions are insulating. Dielectric measurements show relatively low dielectric constants which are independent of temperature and frequency.

Metallic  $\text{Tl}_2\text{TeO}_6$  and insulating  $\text{In}_2\text{TeO}_6$  are both known to crystallize in the  $\text{Na}_2\text{SiF}_6$ -type structure. We have now prepared a complete  $\text{Tl}_{2-x}\text{In}_x\text{TeO}_6$  series in a search for a compositionally controlled metal-insulator transition that might be expected if a complete solid solution can be obtained. Unit cell edges and volume vary monotonically with no indication of miscibility gap. The metal-insulator transition occurs at an  $x$  value of about 1.4, which can be rationalized on a percolation model. No superconductivity could be detected down to 5K.

$\text{Rh}_2\text{MO}_6$ ,  $M = \text{Mo}, \text{W}, \text{and Te}$  were synthesized by solid state reaction. Electronic properties as well as thermoelectric properties were investigated and discussed. The compounds crystallize in rutile-related structure and all show relatively high electronic conductivities with  $\text{Rh}_2\text{TeO}_6$  showing the highest electronic conductivity ( $\sim 500$  S/cm at room temperature) despite localized electrons in  $\text{Rh}^{3+}$  and  $\text{Te}^{6+}$ . Measurable magnetic moments also indicate valence degeneracy between Rh and the M cation. The measured Seebeck coefficients are relatively low and positive indicating hole-type conduction.

©Copyright by Theeranun Siritanon  
July 8, 2011  
All Rights Reserved

Structure-Property Relationships in Oxides Containing Tellurium

by

Theeranun Siritanon

A DISSERTATION

submitted to

Oregon State University

in partial fulfillment of  
the requirements for the  
degree of

Doctor of Philosophy

Presented July 8, 2011  
Commencement June 2012

Doctor of Philosophy dissertation of Theeranun Siritanon presented on July 8, 2011.

APPROVED:

---

Major Professor, representing Chemistry

---

Chair of the Department of Chemistry

---

Dean of the Graduate School

I understand that my dissertation will become part of the permanent collection of Oregon State University libraries. My signature below authorizes release of my dissertation to any reader upon request.

---

Theeranun Siritanon, Author

## ACKNOWLEDGEMENTS

I left my country and came to USA with hope and fear; I hoped to gain knowledge and I feared of everything which seemed to be so different from what I have known in the first twenty three years of my life. With all helps and supports from so many people during these 3 years, I am now leaving USA for my home country with knowledge, warmed heart, and opened mind.

I consider myself a very lucky person to have a chance to learn from Dr. Mas Subramanian, my advisor. I appreciate all scientific and academic knowledge I gained from him and I am most grateful for his enthusiasm, patience, kindness, wisdom, and opened mindness. As a scientist, he guided me through all the processes of doing researches and inspired me with his patience and enthusiasm. As a teacher, he taught me how to learn and to live with his wisdom. He supported and helped me through a very difficult time with his kindness. As a human being, he showed me how life works and introduced me to a much wider world. It is his interests in my success that actually made me succeed in my study. I would never have reached this point without him. Thank you.

It is my honor and fortunate to have a chance to interact, discuss, and learn from Dr. Arthur W. Sleight. I appreciate every conversation and communication with him as I always learn something in some ways or another. I am most grateful for his patience when he tries to explain what he knows so well to a student who barely knows anything. It is his knowledge and dedication that greatly improve quality of all the works and inspires me.

I also thank Dr. Michael Lerner, Dr. Janet Tate, Dr. David Roundy, and Dr. William Warnes for serving as my committees. Dr. Tate and Dr. Lerner are also my teacher who taught and introduced me to many useful knowledge. I also appreciate their generosity in sharing resources and facilities. I would like to express my gratitude to Dr. Lev Zakarov for single crystal analyses. I am grateful for all the time and efforts he has put to solve the problems and improve the quality of the answers. Center for Neutron Research at the National Institute of Standards and Technology (NIST) is acknowledged for providing facility for neutron diffraction.

There are a lot of people who have also played significant roles in my success. First I would like to thank all members of Dr. Subramanian's research group; Dr. Hiroshi Mizoguchi, Dr. Jun Li, Dr. Krishnendu Biswas, Dr. Romain Berthelot, Dr. Andrew Smith, James Eilertsen, Sean Muir, Anvin Gatimu, Peng Jiang, Geneva Laurita-Plankis, Rosa Grajczyk, and Whitney Schmidt. They support me in many different ways and make a friendly and nice group. Special thanks for Dr. Mizoguchi, Dr. Biswas, Dr. Smith, James, Sean, and Alvin for teaching all techniques in the lab and for all the helps they have provided for their junior and friend including many helpful discussions. Also special thanks for Dr. Li for teaching me how to do structural refinements.

I acknowledge Chemistry Department for giving me an opportunity and providing facilities and financial supports for me to learn and do research. I also thank all friends and colleagues for making a nice department and thank all department staffs who always answer all questions and provide supports whenever needed.



In general, I want to thank everyone in Corvallis as they all contribute to make a very warm and friendly place. Special thanks for all Thai students who have been helping me with everything and reducing my homesick. I also thank Mary Ann, Taemee, Deanna, and Courtney for great and valuable conversations. Most of my knowledge and understandings on customs, traditions, cultures, and languages come from them. They make my time here more memorable and make Corvallis an even better place to stay.

I am grateful to Thai government and DPST scholarship for giving me opportunities and financial supports. They introduce me to science and provide whatever needed for me to reach my goal as a scientist. All the staffs have been so nice, resourceful, and helpful. Being in a scholarship also allows me to interact with many role models who have inspired me in different ways. I am always grateful to Dr. Thapanee Sarakonsri. As my former advisor, she always supports me both academically and mentally.

Special thanks to Ton, Natthaphon Raengthon, and Niw, Suwit Suthirakun who proofread this thesis. I really appreciate your time and effort.

With love and gratitude, I thank my family; my father, mother, and brother. It is their generosity and supports that allow me to go after my dream. It is their love that encourage me to go through all difficulties. Their laughs and smiles are the most important moral support that helps me to fulfill this study.

## CONTRIBUTION OF AUTHORS

I would like to acknowledge many people who have contributed to this work. I appreciate your helps and supports which have greatly improved quality of this study. Dr. Mas Subramanian and Dr. Arthur Sleight have contributed significantly to every chapter in this thesis.

Chapter 4: Dr. Art Ramirez provided magnetic data for some pyrochlore samples before we obtained our PPMS at OSU. Dr. Jun Li performed structural refinements based on powder diffraction data. Dr. Lev Zakarov collected and analyzed all single crystals in this work. Dr. Jasmine Millican, Dr. Robin Macaluso, and Dr. Judith Stalick are acknowledged for collecting neutron diffraction data at NIST. Geneva Laurita-Plankis has assisted in sample preparations.

Chapter 5: Dr. Jun Li performed structural refinements based on powder diffraction data. Dr. Lev Zakarov collected and analyzed all single crystals in this work, and Dr. Judith Stalick is acknowledged for collecting neutron diffraction data.

Chapter 8: Dr. Krishnendu Biswas performed data collection for thermoelectric properties of the samples and contributed in many useful discussions.

Throughout this work, several funding agencies have contributed financial supports making it possible to synthesize new materials and perform measurements on them.

## TABLE OF CONTENTS

|  | <u>Page</u> |
|--|-------------|
| 1. Introduction.....                                 | 1           |
| 1.1 Oxides .....                                     | 1           |
| 1.2 Electronic Properties and Band Structure .....   | 2           |
| 1.3 Thermoelectric Properties .....                  | 5           |
| 1.4 Dielectric Properties.....                       | 7           |
| 1.5 Magnetic Properties .....                        | 10          |
| 1.6 Mixed Valence Compounds.....                     | 13          |
| 1.7 Structural Refinement .....                      | 15          |
| 1.8 References:.....                                 | 18          |
| 2. Introduction to Tellurium and Its Oxides.....     | 20          |
| 2.1 Tellurium Element .....                          | 20          |
| 2.2 Oxides of Tellurium.....                         | 21          |
| 2.2.1 Binary Oxides .....                            | 21          |
| 2.2.2 Other Tellurium Oxides .....                   | 24          |
| 2.3 Properties .....                                 | 34          |
| 2.4 References.....                                  | 34          |
| 3. Experimental Methods of Analysis.....             | 38          |
| 3.1 X-ray Diffraction .....                          | 38          |
| 3.1.1 Single Crystal X-ray Diffraction.....          | 40          |
| 3.1.2 Powder X-ray Diffraction .....                 | 41          |
| 3.2 Powder Neutron Diffraction .....                 | 43          |
| 3.3 Physical Property Measurement System (PPMS)..... | 44          |
| 3.3.1 DC Electrical Resistivity.....                 | 45          |
| 3.3.2 Magnetometry.....                              | 46          |

## TABLE OF CONTENTS (Continued)

|  | <u>Page</u> |
|--|-------------|
| 3.4 Seebeck Coefficient .....  | 48          |
| 3.5 Thermoelectric Properties .....  | 49          |
| 3.5.1 Seebeck Coefficient and Resistivity at High Temperature, ZEM-3 .....                               | 49          |
| 3.5.2 Thermal Diffusivity Measurements, Netzsch MicroFlash® .....  | 50          |
| 3.5.3 Specific Heat Measurements, DSC .....  | 51          |
| 3.6 Thermogravimetric Analysis; TGA .....  | 52          |
| 3.7 Dielectric Measurement .....   | 52          |
| 3.8 Optical Measurement .....  | 53          |
| 3.9 References .....   | 54          |
| 4. Electronically Conducting Tellurium Oxide Pyrochlores.....  | 56          |
| 4.1 Abstract .....   | 56          |
| 4.2 Introduction.....  | 58          |
| 4.2.1 Crystallography of the Pyrochlores .....   | 58          |
| 4.2.2 Description of Pyrochlore Structure .....  | 60          |
| 4.2.3 Defect Pyrochlores.....  | 65          |
| 4.2.4 Pyrochlore Oxides and Their Applications.....  | 67          |
| 4.2.5 Tellurium Oxide Pyrochlores.....   | 69          |
| 4.3 Electronic Conductivity in Some New Tellurium Oxides with the Pyrochlore Structure                   | 71          |
| 4.3.1 Introduction.....  | 71          |
| 4.3.2 Results and Discussion .....   | 73          |
| 4.3.3 Conclusion .....   | 83          |
| 4.3.4 Experimental .....   | 83          |
| 4.4 Structural Studies and Electrical Properties of Cs/Al/Te/O Phases with the Pyrochlore Structure..... | 85          |
| 4.4.1 Introduction.....  | 85          |
| 4.4.2 Results.....   | 86          |
| 4.4.3 Discussion.....  | 97          |
| 4.4.4 Conclusion .....   | 110         |

## TABLE OF CONTENTS (Continued)

|   | <u>Page</u> |
|---|-------------|
| 4.4.5 Experimental .....  | 111         |
| 4.5 Synthesis and Characterization of Novel $\text{Rb}(\text{M},\text{Te})_2\text{O}_6$ Pyrochlores .....                       | 113         |
| 4.5.1 Introduction .....  | 113         |
| 4.5.2 Results .....   | 113         |
| 4.5.3 Discussion .....  | 114         |
| 4.5.4 Conclusion .....  | 116         |
| 4.5.5 Experimental .....  | 117         |
| 4.6 References .....  | 117         |
| 5. Effects of Oxygen Deficiency and Tungsten Substitution on the Structure and<br>Properties of $\text{CsTe}_2\text{O}_6$ ..... | 121         |
| 5.1 Abstract .....  | 121         |
| 5.2 Introduction .....  | 122         |
| 5.2.1 Cation Ordering in Pyrochlores .....  | 122         |
| 5.2.2 Oxygen Deficiency in Pyrochlores .....  | 124         |
| 5.3 Oxygen Deficient Phases of $\text{CsTe}_2\text{O}_6$ .....  | 125         |
| 5.3.1 Introduction .....  | 125         |
| 5.3.2 Results .....   | 127         |
| 5.3.3 Discussion .....  | 141         |
| 5.3.4 Conclusion .....  | 147         |
| 5.3.5 Experimental .....  | 148         |
| 5.4 W-Substitued $\text{CsTe}_2\text{O}_6$ .....  | 150         |
| 5.4.1 Introduction .....  | 150         |
| 5.4.2 Results and Discussion .....  | 152         |
| 5.4.3 Conclusion .....  | 156         |
| 5.4.4 Experimental .....  | 157         |
| 5.5 References: .....   | 157         |
| 6. New pyrochlore of the type $\text{CdBi}(\text{M},\text{Te})_2\text{O}_7$ .....   | 159         |
| 6.1 Abstract .....  | 159         |

## TABLE OF CONTENTS (Continued)

|  | <u>Page</u> |
|--|-------------|
| 6.2 Introduction.....  | 159         |
| 6.2.1 Quaternary pyrochlores.....  | 159         |
| 6.2.2 Magnetic pyrochlore oxides.....                                      | 160         |
| 6.3 Results and Discussion .....   | 162         |
| 6.3.1 Structure.....   | 162         |
| 6.3.2 Magnetic properties .....  | 165         |
| 6.3.3 Dielectric properties.....   | 168         |
| 6.4 Experimental .....   | 171         |
| 6.5 References.....  | 172         |
| 7. Compositionally Controlled Metal-Insulator Transition in .....          | 173         |
| 7.1 Abstract .....   | 173         |
| 7.2 Introduction.....  | 173         |
| 7.2.1 $M_2TeO_6$ structure .....   | 174         |
| 7.2.2 Metal- Insulator transition in Oxides .....                          | 176         |
| 7.3 Results.....   | 179         |
| 7.4 Discussion .....   | 184         |
| 7.5 Conclusion .....   | 187         |
| 7.6 Experimental .....   | 188         |
| 7.7 References.....  | 188         |
| 8. Thermoelectric Properties of $Rh_2MO_6$ , $M=Mo$ , $Te$ , and $W$ ..... | 191         |
| 8.1 Abstract .....   | 191         |
| 8.2 Introduction.....  | 191         |
| 8.3 Results.....   | 193         |
| 8.4 Discussion .....   | 198         |
| 8.5 Conclusions.....   | 202         |

TABLE OF CONTENTS (Continued)

|   | <u>Page</u> |
|---|-------------|
| 8.6 Experimental .....                      | 203         |
| 8.7 References .....                        | 204         |
| 9. General Conclusions and Future Work..... | 205         |
| Bibliography.....                           | 207         |

## LIST OF FIGURES

| <u>Figure</u>  | <u>Page</u> |
|--|-------------|
| Figure 1.1: Energy band diagram of metals (a) and semiconductors/insulators (b) .....  | 3           |
| Figure 1.2: Temperature dependence of materials is basically used to classify material as a metal, a semiconductor, or a superconductor [after 3].....   | 4           |
| Figure 1.3: Energy band diagram of n-type semiconductor (a) and p-type semiconductor (b).....  | 4           |
| Figure 1.4: Fermi distribution of electrons at hot and cold end of metal [after 9].....  | 6           |
| Figure 1.5: Parallel conducting plates separated by vacuum (a) and dielectric material (b). .....  | 8           |
| Figure 1.6: Profile fit from Reitveld refinement. Observed (points) and calculated (solid line) neutron powder diffraction profiles are shown [19].....  | 17          |
| Figure 2.1: Tellurium structure (a) and appearance (b). .....  | 20          |
| Figure 2.2: TeO <sub>2</sub> structure; α-form (a) and β-form (b). Red and yellow balls represent O and Te, respectively.....  | 21          |
| Figure 2.3: β-TeO <sub>3</sub> structure; polyhedral model (a) and ball and stick model (b) with red and yellow balls represent O and Te, respectively.....  | 22          |
| Figure 2.4: Ball and stick model of Te <sub>2</sub> O <sub>5</sub> structure. Red, yellow, and green balls represent O, Te <sup>6+</sup> and Te <sup>4+</sup> , respectively. ....   | 23          |
| Figure 2.5: Arrangements of anion (red) around Te <sup>4+</sup> (blue) comparing with octahedral coordination (a). The arrangements lead to trigonal pyramid (b), distorted bisphenoid (c), and square pyramid (d) [14]......                                      | 25          |
| Figure 2.6: CaTeO <sub>3</sub> structure (a) and coordination of Te <sup>4+</sup> (b). Yellow, blue, and red balls represent Te, Ca, and O, respectively [after 15]......  | 26          |
| Figure 2.7: Projection of the crystal structure of orthorhombic CuTeO <sub>3</sub> showing the octahedral arrangement along ac plane and along b direction (a). Projection of the ideal cubic perovskite structure showing 180° M-O-M interactions (b) [36]. ..... | 27          |



## LIST OF FIGURES (Continued)

| <u>Figure</u>   | <u>Page</u> |
|---|-------------|
| Figure 2.8: MVTeO <sub>5</sub> structure. Yellow, green, blue, and red ball represent Te, V, M, and O, respectively [after 39].   | 28          |
| Figure 2.9: CaTe <sub>2</sub> O <sub>5</sub> structure showing layers of [Ca] and [Te <sub>2</sub> O <sub>5</sub> ] and the tunnels. Yellow, blue, and red balls represent Te, Ca, and O, respectively.   | 29          |
| Figure 2.10: SeTeO <sub>4</sub> structure (a) where the arrows show direction of dipole moment from Te <sup>4+</sup> and Se <sup>4+</sup> . Coordination around Te <sup>4+</sup> and Se <sup>4+</sup> are shown in (b) [42].  | 30          |
| Figure 2.11: NaBiTeO <sub>5</sub> structure [52] (Na <sup>+</sup> cations are removed for clarity).   | 32          |
| Figure 3.1: Bragg's law for x-ray diffraction.  | 39          |
| Figure 3.2: Schematic diagram of a four-circle diffractometer [2].  | 41          |
| Figure 3.3: Rigaku MiniFlex II diffractometer.  | 42          |
| Figure 3.4: Quantum Design Physical Property Measurement System set up for ACMS measurements.   | 44          |
| Figure 3.5: PPMS resistivity puck with a bar sample connected to position 1 using the four probe contact technique.   | 46          |
| Figure 3.6: Representation of the ACMS coil set and tube assemblage (left), expanded view with labels of the ACMS coil set detection unit (center), and mounted 'as prepared' sample (right). ACMS coil set illustrations taken and modified from Quantum Design application notes [7]. | 47          |
| Figure 3.7: Set up for Seebeck coefficient measurement. Sample pellet is put in between two silver electrodes.  | 48          |
| Figure 3.8: ZEM Thermoanalyzer (a) and sample in the measuring chamber (b).   | 49          |
| Figure 3.9: Instrument design for Netzsch MicroFlash <sup>®</sup> [8].  | 51          |
| Figure 3.10: Dielectric set up with LCR meter (left) and two parallel electrodes (right).   | 53          |

## LIST OF FIGURES (Continued)

| <u>Figure</u>   | <u>Page</u> |
|---|-------------|
| Figure 3.11: Illustration of a fiber optic system used in diffuse reflectance measurements (inset is an illustration of the end of a fiber optic cable). A standard sample of BaSO <sub>4</sub> can be seen, bottom right.....  | 54          |
| Figure 4.1: Pyrochlore mineral [3].....   | 59          |
| Figure 4.2: (a) Pyrochlore structure as derived from a fluorite lattice (anions are removed for clarity). Purple, blue, and orange tetrahedra represent the 8a, 48f, and 8b anion position, respectively. (b) Example of 48f anion shifting toward 8a vacant site to reduce electrostatic repulsion between four B cations..... | 61          |
| Figure 4.3: Change in shape of coordination polyhedral of A and B ions with 48f oxygen parameter x in A <sub>2</sub> B <sub>2</sub> O <sub>6</sub> O' structure. Coordination around B becomes a regular octahedron from x=0.3125 (5/16) and for x=0.375 (3/8) the coordination around A becomes a regular cube. [2,9].....     | 62          |
| Figure 4.4: (a) A <sub>2</sub> O' chain, (b) M <sub>2</sub> O <sub>6</sub> octahedral network, (c) pyrochlore structure ...   | 63          |
| Figure 4.5: The arrangement in B <sub>4/2</sub> O <sub>6</sub> network (a) and A <sub>2</sub> O' network (b) in pyrochlore structure. ....  | 65          |
| Figure 4.6: Crystallographic sites for A cation in AM <sub>2</sub> O <sub>6</sub> defect pyrochlore. Ball and stick model shows the arrangement of A <sub>2</sub> O' chain where the polyhedral represent B <sub>2</sub> O <sub>6</sub> octahedral network.....   | 66          |
| Figure 4.7: Possible substitutions at A and B sites of A <sup>3+</sup> <sub>2</sub> B <sup>4+</sup> <sub>2</sub> O <sub>7</sub> (a) and A <sup>3+</sup> <sub>2</sub> B <sup>4+</sup> <sub>2</sub> O <sub>7</sub> (b). * indicates that only partial substitution is possible [2]. ....  | 68          |
| Figure 4.8: Structure of cubic AM <sub>2</sub> X <sub>6</sub> pyrochlores as a network of corner shared M <sub>2</sub> X <sub>6</sub> octahedra with A <sup>1+</sup> (dark blue) in an interstitial site (8b site). ....  | 73          |
| Figure 4.9: Comparison of observed pattern of CsAl <sub>0.33</sub> Te <sub>1.67</sub> O <sub>6</sub> (a) with simulated patterns when Cs is in 8b site (b) and 16d site (c). ....   | 75          |
| Figure 4.10: Average ionic radius of octahedral cations vs. a lattice parameter for Cs(M,Te)O <sub>6</sub> phases.....  | 76          |
| Figure 4.11: Magnetic property of Cs(M,Te) <sub>2</sub> O <sub>6</sub> , M= Co <sup>3+</sup> and Mn <sup>3+</sup> . ....  | 77          |

LIST OF FIGURES (Continued)

| <u>Figure</u>   | <u>Page</u> |
|---|-------------|
| Figure 4.12: Log of resistivity for Cs(M,Te) <sub>2</sub> O <sub>6</sub> phases plotted vs. temperature. ....   | 78          |
| Figure 4.13: Log of resistivity for Cs(M,Te) <sub>2</sub> O <sub>6</sub> phases plotted vs. 1/T.....  | 79          |
| Figure 4.14: Log of resistivity for Cs(M,Te) <sub>2</sub> O <sub>6</sub> phases plotted vs. 1/T <sup>1/4</sup> .....  | 80          |
| Figure 4.15: Schematic energy diagrams for (a) hypothetical cubic CsTe <sub>2</sub> O <sub>6</sub> that is metallic due to a ¼ filled 5s band, (b) actual rhombohedral CsTe <sub>2</sub> O <sub>6</sub> , and (c) cubic Cs(M,Te) <sub>2</sub> O <sub>6</sub> phases. ....   | 81          |
| Figure 4.16: Single crystals of Cs(M,Te) <sub>2</sub> O <sub>6</sub> defect pyrochlores .....   | 88          |
| Figure 4.17: Observed (open circles) and calculated (solid line) neutron powder diffraction data of CsAl <sub>x</sub> Te <sub>2-x</sub> O <sub>6</sub> showing the major cubic pyrochlore phase (peak positions denoted as vertical bars on the top), together with minor impurity phases. ....   | 92          |
| Figure 4.18: Rietveld refinement of neutron powder diffraction data for CsAl <sub>1/3</sub> Te <sub>5/3</sub> O <sub>6</sub> . Applied neutron wavelength was 1.5401(2) Å (NIST BT-1). The raw data are plotted as open circles with calculated fit on top. The bottom curve shows the difference between the observed and the calculated data. Vertical bars in the first row indicate the reflection positions of cubic CsAl <sub>1/3</sub> Te <sub>5/3</sub> O <sub>6</sub> with cell edge 10.0889(1) Å. Vertical bars in the second row represent the asymmetric strain simulated as a second cubic phase with slightly larger cell edge 10.1140(1) Å. .... | 93          |
| Figure 4.19: Scanning electron microscope images of CsAl <sub>1/3</sub> Te <sub>5/3</sub> O <sub>6</sub> (x = 0.33) powder at different magnifications. ....  | 95          |
| Figure 4.20: Resistivity of CsAl <sub>x</sub> Te <sub>2-x</sub> O <sub>6</sub> neutron samples plotted vs. temperature. The values of x are nominal Al content. Uncertainties are not indicated, but are commensurate with the scatter of the data. ....  | 96          |
| Figure 4.21: Variation of electrical resistivity versus room temperature of CsAl <sub>x</sub> Te <sub>2-x</sub> O <sub>6</sub> neutron samples. Uncertainties are not indicated, but are less than the point size. ....   | 96          |

LIST OF FIGURES (Continued)

| <u>Figure</u>  | <u>Page</u> |
|--|-------------|
| Figure 4.22: (a) Structure of cubic Cs(Al,Te) <sub>2</sub> O <sub>6</sub> pyrochlores as a network of corner shared (Al/Te)O <sub>6</sub> octahedra (blue, 16c sites) with Cs (orange) in 8b interstitial sites. Oxygen atoms (48f) are shown in turquoise color. (b) Although the first Cs–O coordination sphere is a perfect octahedron, the symmetry of the Cs (orange, 8b sites) is actually tetrahedral. Apexes of the tetrahedron around Cs can be viewed as centers of the four colored triangles formed by corner shared (Al/Te)O <sub>6</sub> octahedra. Four neighboring Cs atoms (orange) are also tetrahedrally located around the center Cs. Different colors are used for the same (Al/Te)O <sub>6</sub> octahedra to show the tetrahedral symmetry, and the Al/Te and O atoms are not shown for clarity. .... | 100         |
| Figure 4.23: Neighboring Rb atoms (red) in pyrochlore RbAl <sub>1/3</sub> Te <sub>5/3</sub> O <sub>6</sub> are tetrahedrally arranged (lines drawn between adjacent Rb atoms to guide the eye). The Rb probability density function (PDF) cannot be described as an ellipsoid due to the tetrahedral symmetry. The application of anharmonic refinement of the PDF leads to tetrahedral-shaped probability density isosurfaces (yellow) centered in Rb atoms at 8b sites. The electron density is moving toward the empty 16d sites (blue). The lines joining the 8b sites are 3-fold axes, which extend through the 8b sites. The 32e sites lie on this 3-fold axis. Placing atoms in 32e sites close to the 8b sites approximates an anharmonic motion. ....   | 101         |
| Figure 4.24: Asymmetric peak broadening in CsAl <sub>x</sub> Te <sub>2-x</sub> O <sub>6</sub> neutron powder diffraction patterns showing the impact of internal strain. ....  | 102         |
| Figure 4.25: Variation of cell edge with refined Al content in CsAl <sub>x</sub> Te <sub>2-x</sub> O <sub>6</sub> . Cell edges for ground crystals (from the same batch of the single crystal analyzed) were calculated by LeBail fit of powder XRD data with Si as an internal standard. The refined Al <i>x</i> values for the ground crystals were taken from the corresponding single crystal refinements. The errors in cell edge are smaller than the points (see Table 4.12), and error bars for <i>x</i> represent 1 $\sigma$ . ....   | 103         |

## LIST OF FIGURES (Continued)

| <u>Figure</u>   | <u>Page</u> |
|---|-------------|
| <p>Figure 4.26: Schematic energy level diagrams for rhombohedral CsTe<sub>2</sub>O<sub>6</sub> and cubic CsAl<sub>x</sub>Te<sub>2-x</sub>O<sub>6</sub> phases showing O 2<i>p</i> and Te 5<i>s</i> states only. The filled 5<i>s</i> states for Te<sup>4+</sup> in CsTe<sub>2</sub>O<sub>6</sub> are at lower energy than the empty 5<i>s</i> states due to the longer Te<sup>4+</sup>–O distances relative to the Te<sup>6+</sup>–O distances. In cubic CsAl<sub>x</sub>Te<sub>2-x</sub>O<sub>6</sub> phases the Te<sup>4+</sup> states are pushed up in energy as the lattice compresses the Te<sup>4+</sup>–O distances with increasing <i>x</i>. At <i>x</i> = 0.33 the Te<sup>4+</sup> donor states disappear.....</p> | 106         |
| <p>Figure 4.27: Bond distances (a) and angles (b) vs. cell edge for all the Cs(M,Te)<sub>2</sub>O<sub>6</sub> (M = Te, In, Zn, Mn, Ga, Al and Ge) pyrochlore samples prepared in this and previous work. Black and blue solid lines in (b) indicate the ranges of M–O–M and O–M–O bond angles, respectively, found for all the A(M,M')<sub>2</sub>O<sub>6</sub> (A = K, Rb, Cs, Tl) pyrochlores [2]. Uncertainties are not indicated, but are less than the point size. ....</p>  | 108         |
| <p>Figure 4.28: Bond valence sums of Cs (CN = 18, 6 short bonds and 12 long bonds) for all the Cs(M,Te)<sub>2</sub>O<sub>6</sub> (M = Te, In, Zn, Mn, Ga, Al and Ge) pyrochlore samples prepared in this and previous work. BVS adjusted to the softness of the Cs–O bond (blue) are slightly smaller than BVS not corrected with bond softness (black). ....</p>   | 109         |
| <p>Figure 5.1: Tetrahedral arrangement of BO<sub>6</sub> octahedra in cubic pyrochlore (a), rhombohedral pyrochlore showing 1:3 ordering (b), and tetragonal pyrochlore with 1:1 ordering. Different colors represent different octahedral.....</p>   | 123         |
| <p>Figure 5.2: CsTe<sub>2</sub>O<sub>6</sub> structure showing ordering of Te<sup>4+</sup> (blue) and Te<sup>6+</sup> (brown) and anisotropic thermal ellipsoids of Te and O (turquoise). ....</p>  | 126         |
| <p>Figure 5.3: CsTe<sub>2</sub>O<sub>4.5</sub> structure (a) showing arrangement of Te<sup>4+</sup> polyhedral (yellow polyhedral) with Cs<sup>+</sup> in interstitial sites (pink ball). Tetrahedral arrangement is shown separately for clarification in (b) comparing with that of cubic pyrochlore (c). ....</p>  | 126         |
| <p>Figure 5.4: Thermogravimetric analysis of CsTe<sub>2</sub>O<sub>6</sub>.....</p>   | 127         |
| <p>Figure 5.5: Powder x-ray diffraction pattern of CsTe<sub>2</sub>O<sub>6-x</sub> phases.....</p>  | 129         |

## LIST OF FIGURES (Continued)

| <u>Figure</u>  | <u>Page</u> |
|--|-------------|
| Figure 5.6: LeBail fit of neutron powder diffraction data for orthorhombic CsTe <sub>2</sub> O <sub>5.75</sub> prepared in silica ampoules at 500°C. Peak splitting and broadening in higher angles indicate that the symmetry is not cubic. The inset shows the close up view of the two peaks (cubic hkl values: 115 and 044) showing peak splitting due to orthorhombic symmetry. ....  | 130         |
| Figure 5.7: Electrical conductivity (log scale) vs. 1000/T for CsTe <sub>2</sub> O <sub>6</sub> . ....   | 131         |
| Figure 5.8: A segment of the chain containing the Te <sup>4+</sup> and O vacancies and the important bond distances are marked in Å. The difference in the Te-O distances for the two Te atoms results from a shift of 0.34 Å for Te3 toward the O vacancy (midpoint of chain). The Te3 atoms (dark blue) are assumed to all be Te <sup>4+</sup> , and the Te2 atoms (orange) are a mixture of Te <sup>4+</sup> and Te <sup>6+</sup> .....   | 136         |
| Figure 5.9: Lattice parameters (a) and unit cell volumes (b) of CsTe <sub>2</sub> O <sub>6-x</sub> phases. Standard uncertainties are not indicated, but are less than the point size. ....  | 137         |
| Figure 5.10: Thermogravimetric analysis (TGA) of nominal CsTe <sub>2</sub> O <sub>5.75</sub> phase under O <sub>2</sub> atmosphere showing weight gain corresponding to x=0.25 in CsTe <sub>2</sub> O <sub>6-x</sub> . ....  | 138         |
| Figure 5.11: Observed powder XRD of nominal CsTe <sub>2</sub> O <sub>4.85</sub> (a) compared with simulated pattern which was calculated based on Cs analog of Rb <sub>4</sub> Te <sub>8</sub> O <sub>23</sub> (b).....  | 141         |
| Figure 5.12: The arrangement of M and M' cations in the pyrochlore structure with 1:3 ( top left) and 1:1 ordering (top right). Each of the 6 edges of a tetrahedron define a chain extended through the lattice. In the case of 1:3 ordering, 3 chains become all M cations and 3 chains become alternating M and M' cations. In the case of 1:1 ordering, one chain is all M cations, one is all M' cations, and the other 4 chains are alternating M and M' cations. Bottom left and right show polyhedral arrangement of 1:3 and 1:1, respectively. .... | 142         |
| Figure 5.13: Rb <sub>4</sub> Te <sub>8</sub> O <sub>23</sub> structure. Blue and yellow polyhedra represent polyhedra of Te <sup>4+</sup> and Te <sup>6+</sup> , respectively. Pink balls represent Rb. ....   | 146         |
| Figure 5.14: Optical properties (b) and appearance (a) of CsTe <sub>2</sub> O <sub>6-x</sub> .....   | 147         |

## LIST OF FIGURES (Continued)

| <u>Figure</u>  | <u>Page</u> |
|--|-------------|
| Figure 5.15: Crystal structure of $\text{Cs}_2\text{TeW}_3\text{O}_{12}$ (a) and $\text{Cs}_2\text{Te}_4\text{O}_{12}$ ( $\text{CsTe}_2\text{O}_6$ ). Cs has been removed for clarity..... | 151         |
| Figure 5.16: Powder X-ray patterns of $\text{CsTe}_{2-x}\text{W}_x\text{O}_6$ .....  | 153         |
| Figure 5.17: Plots of cell parameters and cell volumes versus tungsten content, x, in $\text{CsTe}_{2-x}\text{W}_x\text{O}_6$ .....  | 154         |
| Figure 5.18: Color (a) and optical property (b) of $\text{CsTe}_{2-x}\text{W}_x\text{O}_6$ .....   | 155         |
| Figure 6.1: Geometric frustration of antiferromagnetically alignment on a triangle (a) and tetrahedron (b) [13].....   | 161         |
| Figure 6.2: Powder X-ray diffraction pattern of $\text{CdBiMTeO}_7$ .....  | 163         |
| Figure 6.3: 1:1 cation ordering with NaCl-type arrangement in perovskite [14].....   | 164         |
| Figure 6.4: Plots of unit cell parameters and cell volumes versus average ionic radii at B site.....   | 165         |
| Figure 6.5: Temperature dependence of magnetic susceptibility and inverse magnetic susceptibility of $\text{CdBiCrTeO}_7$ .....  | 166         |
| Figure 6.6: Temperature dependence of magnetic susceptibility and inverse magnetic susceptibility of $\text{CdBiMnTeO}_7$ .....  | 167         |
| Figure 6.7: Temperature dependence of magnetic susceptibility and inverse magnetic susceptibility of $\text{CdBiFeTeO}_7$ .....  | 168         |
| Figure 6.8: Temperature dependence of dielectric constants of some representative compounds.....   | 169         |
| Figure 6.9: Temperature dependence of dielectric constant (a) and dielectric loss (b) of some representative compounds.....  | 170         |
| Figure 7.1: $\text{M}_2\text{TeO}_6$ structure (olive octahedra represent $\text{Te}^{6+}$ and the other colors represent $\text{M}^{3+}$ octahedra) .....                                 | 175         |

## LIST OF FIGURES (Continued)

| <u>Figure</u>  | <u>Page</u> |
|--|-------------|
| Figure 7.2: Schematic band diagram for $\text{Sm}_{1-x}\text{Nd}_x\text{NiO}_3$ showing transition from insulator (a) to semimetal state (b) [after 27].....   | 178         |
| Figure 7.3: Percolation model when few sites are occupied (a) and when the cluster is formed through the lattice (b) [29].....   | 179         |
| Figure 7.4: Powder X-ray diffraction of $\text{Tl}_{2-x}\text{In}_x\text{TeO}_6$ solid solutions.....  | 181         |
| Figure 7.5: Lattice parameters (upper) and unit cell volumes (lower) of $\text{Tl}_{2-x}\text{In}_x\text{TeO}_6$ solid solution.....   | 182         |
| Figure 7.6: Room temperature resistivities and Seebeck coefficients of $\text{Tl}_{2-x}\text{In}_x\text{TeO}_6$ .....  | 183         |
| Figure 7.7: Normalized resistivities, $\rho/\rho_{300\text{K}}$ of some representative compositions... 183   | 183         |
| Figure 8.1: Rutile (a) and trirutile (b) structure. Different colors represent different types of cations.....   | 193         |
| Figure 8.2: Powder X-ray diffraction patterns of $\text{Rh}_2\text{MO}_6$ phases.....  | 195         |
| Figure 8.3: XRD patterns for $\text{Rh}_2\text{WO}_6$ with line for calculated patterns and open circles for observed patterns. (a) Calculated pattern for fully ordered $\text{Rh}_2\text{WO}_6$ where the higher angle peak is a superstructure peak. (b) Observed pattern and pattern calculated for $(\text{Rh}_{1.54}\text{W}_{0.46})(\text{W}_{0.54}\text{Rh}_{0.46})\text{O}_6$ (c) Observed pattern of a second sample slightly less ordered and a pattern calculated for $(\text{Rh}_{1.5}\text{W}_{0.5})(\text{W}_{0.5}\text{Rh}_{0.5})\text{O}_6$ ..... | 196         |
| Figure 8.4: Plots of resistivity (a) and Seebeck coefficient (b) of $\text{Rh}_2\text{MO}_6$ vs. temperature.....  | 197         |
| Figure 8.5: Magnetism of $\text{Rh}_2\text{MO}_6$ phases. ....   | 200         |
| Figure 8.6: Thermal conductivity of $\text{Rh}_2\text{MO}_6$ .....   | 201         |
| Figure 8.7: Power Factor (a) and ZT (b) plots for $\text{Rh}_2\text{MO}_6$ phases.....   | 202         |



## LIST OF TABLES

| <u>Table</u>   | <u>Page</u> |
|--|-------------|
| Table 1.1: Different kinds of magnetic behavior and their characteristics. ....  | 12          |
| Table 1.2: Classification of mixed valence compounds [14]. ....  | 14          |
| Table 1.3: Refinable parameters in Rietveld refinement [18]. ....  | 18          |
| Table 4.1: Pyrochlore Structure Data (Origin at B site) [after ref.2]. ....  | 59          |
| Table 4.2: Tellurium oxides with AB <sub>2</sub> O <sub>6</sub> defect pyrochlore structure .....  | 70          |
| Table 4.3: Cs(M,Te) <sub>2</sub> O <sub>6</sub> pyrochlores prepared in this work. ....  | 74          |
| Table 4.4: Curie-Weiss analysis of magnetic susceptibility. ....   | 77          |
| Table 4.5: Reactants used in this work. ....   | 84          |
| Table 4.6: Crystal data and structure refinements of Cs(M,Te) <sub>2</sub> O <sub>6</sub> , M = Ga, In, and Ge. ....   | 87          |
| Table 4.7: Atomic coordinates and displacement factors of Cs(M,Te) <sub>2</sub> O <sub>6</sub> , M = Ga, In, and Ge. ....  | 88          |
| Table 4.8: Crystal data and structure refinements of CsAl <sub>x</sub> Te <sub>2-x</sub> O <sub>6</sub> , x = 0.25, 0.33, and 0.45 .....                                       | 89          |
| Table 4.9: Atomic coordinates and displacement factors of CsAl <sub>x</sub> Te <sub>2-x</sub> O <sub>6</sub> , x = 0.25, 0.33, and 0.45. ....                                  | 90          |
| Table 4.10: Bond lengths and bond angles. ....   | 90          |
| Table 4.11: Calculated percentage of impurity from powder refinement .....   | 93          |
| Table 4.12: Structural refinement results of powder neutron and X-ray ( <i>Italic</i> ) data for CsAl <sub>x</sub> Te <sub>2-x</sub> O <sub>6</sub> . ....                     | 94          |
| Table 4.13: Bond lengths, bond angles and bond valence sums calculated from powder neutron structural refinements of CsAl <sub>x</sub> Te <sub>2-x</sub> O <sub>6</sub> . .... | 95          |
| Table 4.14: Rb(M,Te) <sub>2</sub> O <sub>6</sub> pyrochlores prepared in this work .....   | 114         |

LIST OF TABLES (Continued)

| <u>Table</u>  | <u>Page</u> |
|---|-------------|
| Table 4.15: Crystallographic data of $\text{RbAl}_{0.33}\text{Te}_{1.67}\text{O}_6$ .....                       | 115         |
| Table 4.16: Atomic coordinates and displacement factors of $\text{RbAl}_{0.33}\text{Te}_{1.67}\text{O}_6$ ..... | 116         |
| Table 4.17: Selected bond lengths and angles of $\text{RbAl}_{0.33}\text{Te}_{1.67}\text{O}_6$ .....            | 116         |
| Table 5.1: Crystal data and structure refinements of $\text{CsTe}_2\text{O}_6$ .....                            | 132         |
| Table 5.2: Atomic coordinates and Displacement factor of $\text{CsTe}_2\text{O}_6$ .....                        | 133         |
| Table 5.3: Selected bond lengths and angles of $\text{CsTe}_2\text{O}_6$ .....                                  | 133         |
| Table 5.4: Neutron structural refinement of $\text{CsTe}_2\text{O}_{5.75}$ (prepared at 500 °C) .....           | 135         |
| Table 5.5: Selected interatomic distances (Å) for $\text{CsTe}_2\text{O}_{5.75}$ .....                          | 136         |
| Table 5.6: Neutron structural refinement of $\text{CsTe}_2\text{O}_{5.8}$ (quenched from 610 °C).....           | 138         |
| Table 5.7: Crystallographic data of $\text{CsTe}_2\text{O}_{5.8}$ single crystal .....                          | 140         |
| Table 6.1: Novel pyrochlore oxides of the type $(\text{CdBi})(\text{MTe})\text{O}_7$ made in this study .       | 164         |
| Table 6.2: Magnetic properties of $\text{CdBiMTeO}_7$ , M= Cr, Mn .....   | 166         |
| Table 7.1: Typical metal-insulator transitions in oxides [12] .....   | 177         |
| Table 8.1: Cell parameters of $\text{Rh}_2\text{MO}_6$ .....  | 195         |

This thesis is dedicated to

My parents

For their endless love, support, and encouragement

# Structure-Property Relationships in Oxides Containing Tellurium

## Chapter

### 1. Introduction

#### 1.1 Oxides

Oxides are the major family of solid state materials. Because of their stabilities and various properties, they are used for many useful applications. Each property of oxides usually varies in a wide scale. For example, electronic conductivity in oxides can be as low as  $10^{-14}$  S/cm in  $\text{SiO}_2$  [1] to as high as infinite value in superconductors like  $\text{Bi}_2\text{Sr}_{3-x}\text{Ca}_x\text{Cu}_2\text{O}_{8+y}$  [2]. Magnetic properties in oxides can vary from ferromagnetic to antiferromagnetic, and ferrimagnetic. Although large numbers of solid oxides are amorphous, crystalline materials with systematically long-range ordering of atoms will be the focus of this work.

The variety of oxides arises from the variety of structures, bonding characters, and compositions all of which have strong relationship with physical and electrical properties. These relationships are used, with general knowledge on chemical nature of elements, to design new materials with desired properties for certain applications. The general introduction and principles of some properties will be discussed in the following sections. More detailed and specific introduction can be found in each chapter.

## 1.2 Electronic Properties and Band Structure

The electronic properties of materials are well described by electronic structure. According to the molecular orbital theory of diatomic molecule, atomic orbitals from each atom overlap with each other forming 2 molecular orbitals; bonding and antibonding. Similarly, solid can be viewed as a large molecule containing infinite number of atoms; each atom contributes an atomic orbital to overlap with others resulting in an infinite number of molecular orbitals. The 'band' of energy level is then formed by these molecular orbitals which are closely spaced in energy. Bands are separated by 'band gap', the energy levels where there is no molecular orbital [3]. When the band is not completely filled by electrons, electrons close to the highest occupied orbitals can be easily activated to the next empty levels where they can move freely. As a result, the material is a metallic conductor. However, when the band is completely full, relatively large energy is needed to promote electrons since the next available empty orbital is separated by the band gap. Therefore, the material is not conducting at room temperature. The magnitude of the band gap defines whether the material is a semiconductor or an insulator [3]. The band energy diagrams of metallic, semiconductor, and insulator are shown in Figure 1.1.

Electronic conductivity of materials,  $\sigma$ , depends on number of free electrons ( $n$ ) and their mobility ( $\mu$ ) as shown by equation

$$\sigma = ne\mu$$

where  $e$  is an electron charge [4-5]. In general, when temperature is increased, more free electrons are created resulting in higher  $n$  value but lattice vibration will decrease

their mobility and lower  $\mu$  factor. The first effect is dominant in semiconductors and insulators; therefore, their conductivities increase with temperature. On the other hand; although higher temperature increases  $n$  in metal, it affects more to mobility and conductivity in metal decrease as temperature increases (Fig. 1.2). Materials are superconductor when they have zero resistance at temperature lower than critical value,  $T_c$ .

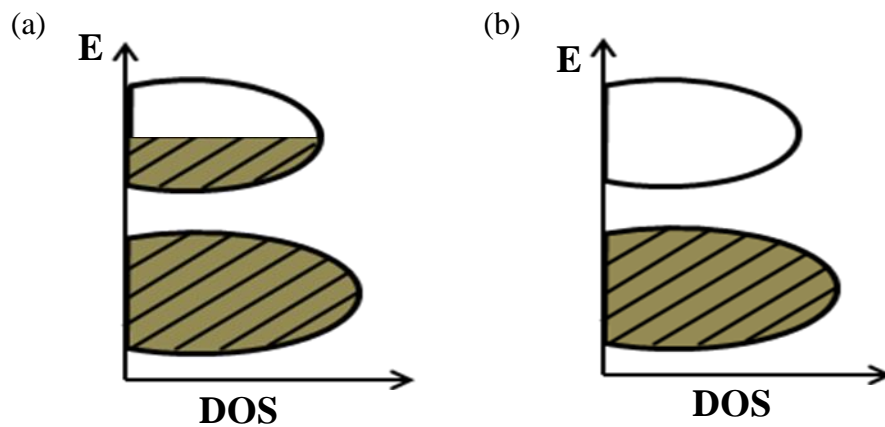


Figure 1.1: Energy band diagram of metals (a) and semiconductors/insulators (b)

Extrinsic semiconductor is prepared by the addition of extra impurity atoms usually with different valency. Atoms with more electrons than the parent atoms will provide extra electrons to the substance. This process introduces 'donor band' to the band structure and the material is called n-type semiconductor. Alternatively, p-type semiconductor is obtained by the addition of atoms with less electrons which will provide extra 'holes' to the materials and introduce 'acceptor band' to the band structure (Fig. 1.3). As a consequence, the major charge carriers in n-type and p-type semiconductors are electrons and holes, respectively.

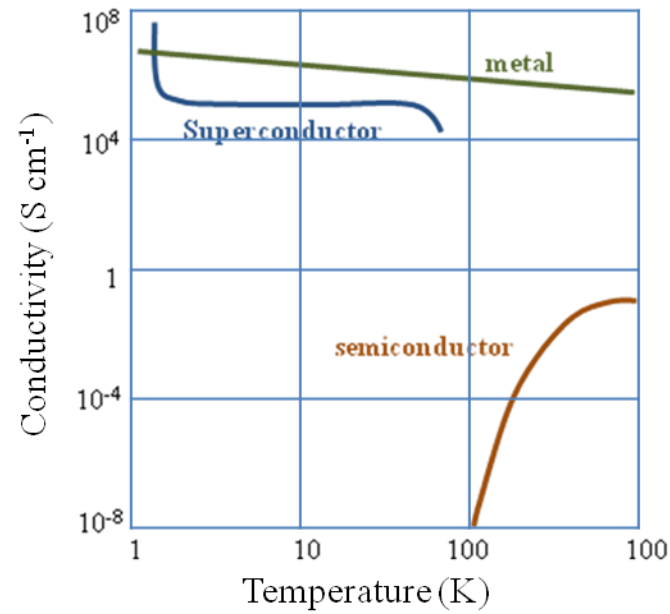


Figure 1.2: Temperature dependence of materials is basically used to classify material as a metal, a semiconductor, or a superconductor [after 3].

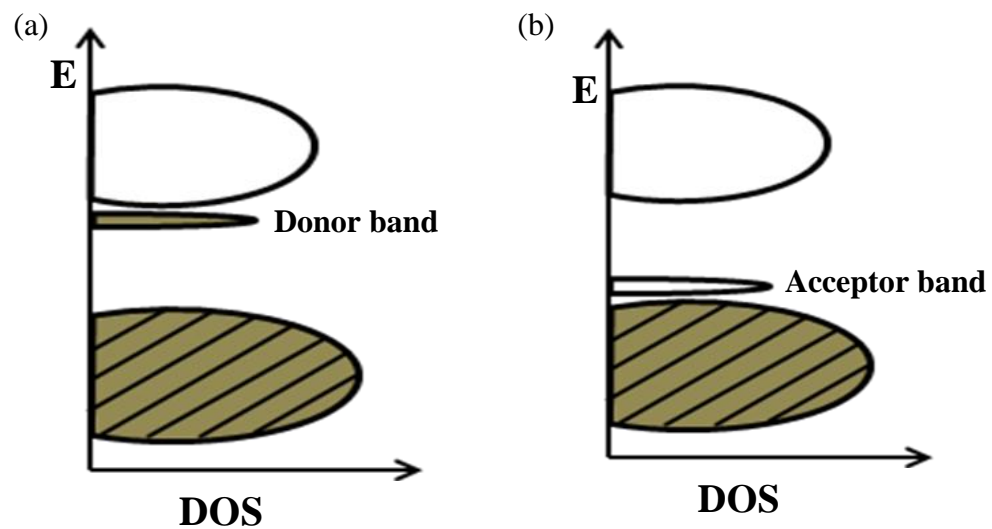


Figure 1.3: Energy band diagram of n-type semiconductor (a) and p-type semiconductor (b).

Temperature dependence in semiconductor usually follows Arrhenius-like behavior in the form:

$$\sigma = \sigma_0 \exp \frac{-E_a}{k_B T}$$

where  $E_a$  is activation energy of conduction,  $k_B$  is Boltzmann constant, and  $\sigma_0$  is constant. However, some exceptions and variations are also found [4-5].

### 1.3 Thermoelectric Properties

Thermoelectric effect is a direct conversion between heat gradient and electricity. Thermoelectric is based on two main effects; Seebeck and Peltier effect.

Seebeck effect was discovered by Seebeck in early 1800's. Consider a simple case of Fermi distribution of metal when the two ends are kept at different temperatures. As shown in Figure 1.4, Fermi distribution of the hot end is 'soft' with more concentration of free electrons above Fermi level. On the other hand, 'sharp' Fermi distribution is found at the cold end. As electrons move from higher to lower energy, they tend to move from hot end to cold end and build up an electric field. A steady state is reached when the built up electric field is equal to electrochemical potentials created by the temperature difference [1,6]. To measure the electric field resulting from Seebeck effect, contacts must be made between two dissimilar materials and Seebeck coefficient,  $S$ , is defined by

$$S = \frac{\Delta V}{\Delta T}$$



when  $\Delta V$  and  $\Delta T$  are voltage difference and temperature difference between the two ends [6-7]. Negative Seebeck coefficient indicates that electrons are the major charge carriers while positive value suggests that holes are dominant [8].

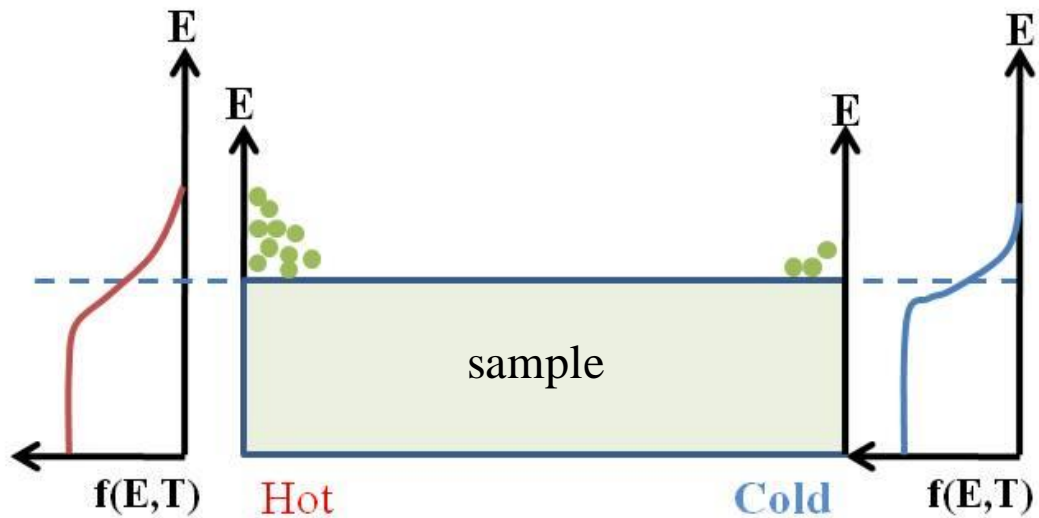


Figure 1.4: Fermi distribution of electrons at hot and cold end of metal [after 9].

Peltier effect was reported shortly after the discovery of Seebeck effect. It was found that electrical current applied at the junction of two dissimilar materials led to the liberation or absorption of heat depending on the current direction. Peltier coefficient,  $\Pi$ , is defined by

$$\Pi = ST$$

where  $S$  and  $T$  are Seebeck coefficient and temperature, respectively. The rate of heat absorption or liberation at the junction,  $Q_P$ , is equal to

$$Q_p = \Pi I = S T I$$

where  $I$  is electric current.

The efficiency of thermoelectric material depends not only on Seebeck coefficient but also on many factors. It is therefore determined by a term called figure of merit,  $ZT$ .

$$ZT = \frac{S^2 \sigma T}{\kappa} = \frac{S^2 T}{\rho \kappa}$$

where,  $S$  is the Seebeck coefficient,  $\sigma$  is the electrical conductivity,  $\rho$  is the electrical resistivity, and  $\kappa$  is the total thermal conductivity ( $\kappa = \kappa_E + \kappa_L$ ;  $\kappa_E$  and  $\kappa_L$  are electronic and lattice contributions, respectively). To obtain high  $ZT$ , the material should have high Seebeck coefficient and electrical conductivity but low thermal conductivity. However, high electrical conductivity is usually accompanied by low Seebeck coefficient and high electronic component of thermal conductivity. Therefore, good thermoelectric materials are usually found in semiconductors as they possess properties of both metals and insulators. For a useful application,  $ZT$  of more than 1 is required [10].

#### **1.4 Dielectric Properties**

Dielectric materials are insulators. They are mainly used for capacitors and insulators. In order to be good dielectric materials, many properties have to be considered especially dielectric constant,  $\kappa$ , and dielectric loss,  $\kappa'$ .

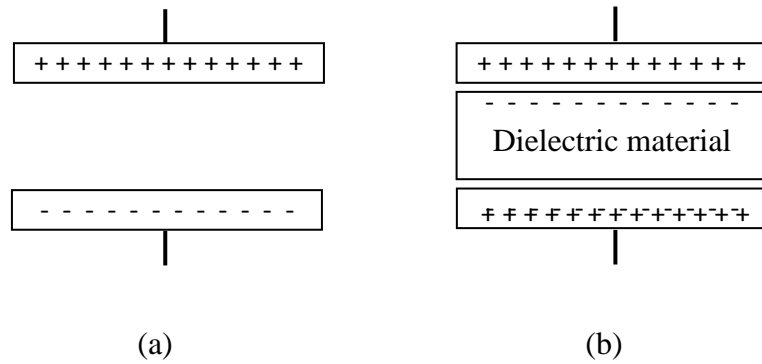


Figure 1.5: Parallel conducting plates separated by vacuum (a) and dielectric material (b).

Consider a pair of conducting plate with area  $A$  parallel to each other separated by distance  $d$  as shown in Figure 1.5(a). When vacuum is placed in between two plates, the capacitance  $C_0$  is

$$C_0 = \frac{\epsilon_0 A}{d}$$

when  $\epsilon_0$  is permittivity of free space ( $8.854 \times 10^{-12} \text{ Fm}^{-1}$ ). When potential difference,  $V$ , is applied, charge  $Q_0 = C_0 V$  is stored on the two plates. If a material is put in between the plates under the same potential difference  $V$ , charge  $Q_1$  is now stored in the material (Fig. 1.5(b)). Since  $V$  is constant,  $C_0$  is increased to  $C_1$  [5]. The relative permittivity ( $\epsilon'$ ) or dielectric constant ( $\kappa$ ) is then defined by

$$\kappa = \frac{C_1}{C_0}$$

Dielectric constant of dry air is about 1 but oxides can have high dielectric constant. For example,  $\text{CaCu}_3\text{Ti}_4\text{O}_{12}$  has dielectric constant in the order of  $10^4$  at 1 kHz [11]. The magnitude of dielectric constant is defined by the degree of polarization or charge displacement that occurs in the material. The polarizability in materials has

four components; electronic polarizability, ionic polarizability, dipolar polarizability, and space charge polarizability [1,5]. Not all materials show all components of polarizability and each component requires different time to respond to the applied electric field. This phenomenon causes some phase delay of the charging current in the alternative field (AC). As a result, the charging current is changed from being  $90^\circ$  in advance as in  $I_c = i\omega CV$  to being only  $90^\circ - \delta$  in advance. When the phase lag occurs, energy is loss in the form of heat, i.e. dielectric losses. In most applications, the good dielectric materials should have high dielectric constant but low dielectric losses.

Dielectric constants of materials are usually obtained from a pellet of polycrystalline sample or sometimes a pellet of multiphase sample. In order to determine accurate dielectric properties in these cases, mixing rules have been applied. In such rules, a mixture of phases is treated as layer materials with layers of two or more phases align either parallel or normal to the conducting plates. For paralleled phases, the equation:

$$\frac{1}{\kappa} = \frac{v_1}{\kappa_1} + \frac{v_2}{\kappa_2}$$

is used to calculate dielectric constant of each phase ( $\kappa_1, \kappa_2$ ) from the observed  $\kappa$  where  $v_1$  and  $v_2$  are volume fractions of each phase. When the layers are normal to the capacitor plates, the relationship becomes

$$\kappa = v_1 \kappa_1 + v_2 \kappa_2$$

The intermediate value between these two extreme cases can be obtained from logarithm mixing rule:

$$\text{Log } \kappa = \sum_i v_i \text{log} \kappa_i$$

Moreover, if a material is considered as a dispersion of phase 1 with  $\kappa_d$  in a matrix of phase 2 with  $\kappa'_m$ , Maxwell relation is used:

$$\kappa = \frac{v_m \kappa_m \left( \frac{2}{3} + \frac{\kappa_d}{3\kappa_m} \right) + v_d \kappa_d}{v_m \left( \frac{2}{3} + \frac{\kappa_d}{3\kappa_m} \right) + v_d}$$

In general, the normal parallel and Maxwell's relation are satisfactory for most purpose especially for porosity correction [1].

### 1.5 Magnetic Properties

When all electrons are paired, materials exhibit diamagnetism. However, some materials show other magnetic behaviors due to the presence of unpaired electrons. Since these unpaired electrons usually locate on metal cations, magnetic behaviors are mainly found in oxides of transition metals or lanthanide with unpaired  $d$  or  $f$  electrons.

When a substance is placed in magnetic field,  $H$ , the magnetic induction,  $B$ , which defines the lines of force in the substance is equal to

$$B = H + 4\pi I$$

where  $I$  is the magnetic moment per volume of the sample. The permeability,  $P$ , and susceptibility,  $\chi$ , are then related by

$$P = \frac{B}{H} = 1 + 4\pi\chi$$

The molar susceptibility,  $\chi_m$ , can be calculated from

$$\chi_m = \frac{\chi F}{d}$$

when  $F$  = formula weight,  $d$  = density of the sample. In general,  $P$ ,  $\chi$ ,  $\chi_m$ , and their temperature dependence are used to categorize magnetic substances as summarized in Table 1.1.

As mentioned earlier, *diamagnetism* is a result of paired electrons which can be observed in all substances. When placed in magnetic field, the materials show repulsive force and hence a small negative magnetization.

On the other hand, different phenomena are observed in materials containing unpaired electrons. In the absence of magnetic field; when unpaired electrons are randomly aligned in the substance without interaction between neighboring moments, the material is classified as *paramagnetic*. In the presence of external magnetic field, the moments tend to line up in the field direction resulting in positive susceptibility. Most of paramagnetic materials follow the simple Curie-Weiss law:

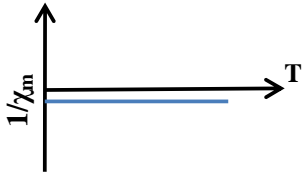
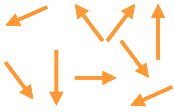
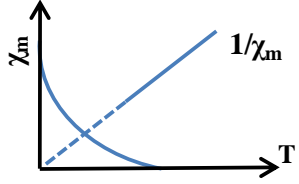
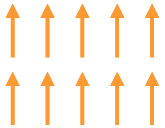
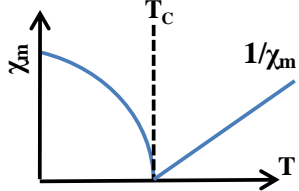
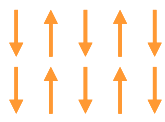
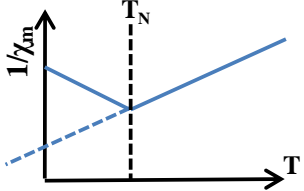
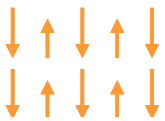
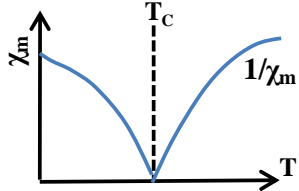
$$\chi_m = \frac{C}{(T + \theta)}$$

where  $C$  is the Curie constant,  $\theta$  is the Weiss constant, and  $T$  is temperature. A plot of  $1/\chi_m$  versus temperature will show straight line. Curie constant and Weiss constant are obtained from slope of the plot and the x-intercept, respectively. Theoretically, the magnitude of the moment using spin-only approximation is defined by

$$\mu = \sqrt{\frac{3kC}{N_A}} = 2.84 \sqrt{C} \mu_B$$

where  $k$  is Boltzmann's constant,  $N_a$  is Avagadro's number, and  $\mu_B$  is Bohr magneton.

Table 1.1: Different kinds of magnetic behavior and their characteristics.

| Classification & orientation of magnetic moments  | Critical temperature                                 | Magnitude of $\chi_m$    | Temperature dependence of $\chi_m$  |
|---|--|--------------------------|---|
| <b>Diamagnetic</b>  | None   | $-10^{-6}$ to $-10^{-5}$ |    |
| <b>Paramagnetic</b><br>        | None   | $10^{-5}$ to $10^{-3}$   |    |
| <b>Ferromagnetic</b><br>     | $T_C$<br>Curie Temp.<br>$X_m = C/(T-\theta)$         | Large below $T_C$        |   |
| <b>Antiferromagnetic</b><br> | $T_N$<br>Neel Temp.<br>$X_m = C/(T\pm\theta)$        | $10^{-5}$ to $10^{-3}$   |  |
| <b>Ferrimagnetic</b><br>     | $T_C$<br>Curie Temp.<br>$X_m \approx C/(T\pm\theta)$ | Large below $T_C$        |  |

*Ferromagnetism* and *antiferromagnetism* occur when unpaired electrons strongly couple with neighboring ions resulting in parallel and antiparallel magnetic moments, respectively. Ferromagnetic and antiferromagnetic materials do not follow the Curie-Weiss law. At temperature lower than critical value called Curie temperature, ferromagnetic material show a very large magnetic moment which rapidly increases as temperature decreases. On the other hand; at temperature lower than critical value called Neel temperature, magnetic moment of antiferromagnetic substance increase with temperature. However, above the critical temperature, both materials behave like paramagnetic materials as shown in Table 1.1.

## 1.6 Mixed Valence Compounds

Mixed valence compounds are the substances in which an element(s) is present in more than one oxidation states [12]. Mixed valence situation can be found only in elements which can possess variable oxidation states. These elements include some members of d-block and f-block elements, lanthanides, actinides, and post-transition elements. Robin and Day classified the mixed valence compounds into 3 classes based on the similarity of the sites containing different valency [13]. Some examples are shown in Table 1.2.

**Class I:** In class I mixed valency, ions with dissimilar oxidation states are in the very different environments. There is no interaction between them; therefore, there is no special properties arising from the mixed valence situation and the compounds possess properties of each individual valency.



Table 1.2: Classification of mixed valence compounds [14].

| Class      | Compound  | Oxidation states  |
|------------|---|---|
| Class I    | KCr <sub>3</sub> O <sub>8</sub><br>GaCl <sub>2</sub>  | Cr(III, VI)<br>Ga(I, III)   |
| Class II   | Eu <sub>3</sub> S <sub>4</sub><br>Fe <sub>4</sub> [Fe(CN) <sub>6</sub> ] <sub>3</sub> .xH <sub>2</sub> O<br>Na <sub>x</sub> WO <sub>3</sub> (x<0.3)<br>[(C <sub>2</sub> H <sub>5</sub> NH <sub>2</sub> ) <sub>4</sub> PtCl](ClO <sub>4</sub> ) <sub>2</sub><br>CsAuCl <sub>3</sub><br>Cs <sub>2</sub> SbCl <sub>6</sub> | Eu(II,III)<br>Fe(II, III)<br>W(V, VI)<br>Pt(II, IV)<br>Au(I,III)<br>Sb(III,V) |
| Class IIIA | Nb <sub>6</sub> Cl <sub>14</sub> .8H <sub>2</sub> O   | Nb(2.33)  |
| Class IIIB | Na <sub>x</sub> WO <sub>3</sub> (0.3<x<0.9)<br>Ag <sub>2</sub> F<br>La <sub>1-x</sub> Sr <sub>x</sub> MnO <sub>3</sub><br>K <sub>2</sub> Pt(CN) <sub>4</sub> Br <sub>0.3</sub> 3H <sub>2</sub> O<br>Hg <sub>2.67</sub> AsF <sub>6</sub>   | W(6-x)<br>Ag(0.5)<br>Mn(3+x)<br>Pt(2.3)<br>Hg(0.37)                           |

**Class II:** Although ions with different oxidation states in class II materials are in distinguishable sites, the difference between them are not as large as in class I materials. Many class II compounds contain ions in distinct crystallographic sites because each oxidation state has specific site preference. For example in Fe<sub>4</sub>[Fe(CN)<sub>6</sub>]<sub>3</sub>.xH<sub>2</sub>O (Prussian blue), Fe<sup>2+</sup> coordinates to CN through carbon end while Fe<sup>3+</sup> prefers nitrogen end of the ligand. However, in many cases the sites are distinguished only by ‘lattice distortion’ or ‘valence trapping’ where one oxidation state has longer bond lengths. As a consequence, ‘activation energy’ is needed for electrons to hop to the neighboring ions. This activation energy is a characteristic of class II mixed valency. Charge transfer in class II compounds usually results in colored materials.

**Class III:** The compounds in class III have ions with different valency in the identical sites where electrons are delocalized between them and the ions have one fractional

oxidation state. There are two sub classes in this class; class IIIA where electrons are delocalized within a cluster and class IIIB where electron delocalization occur through the material resulting in metallic conduction.

A transition from class II to class III is often found. For instance; when  $x$  in  $\text{Na}_x\text{WO}_3$  is small, extra electrons from Na are trapped near  $\text{Na}^+$  in the lattice and the compound is considered class II mixed valency. Increase in Na content can lead to a transition to class III where electrons are delocalized and metallic conduction is achieved [14].

### **1.7 Structural Refinement**

Crystal structure including atomic positions, bond lengths, bond angles, and atomic occupancy has a large effect on properties of materials. Therefore, obtaining correct and accurate information on these parameters is a very important step in solid state chemistry. Two forms of materials are used to obtain this information in general: single crystal and polycrystalline sample. It is easier to obtain crystal information of an unknown structure from single crystal diffraction because the single crystal diffraction data provide three dimensions of crystallographic information while only one dimension of information can be obtained from the powder diffraction [15].

Although direct method, Peterson map, or other specialized methods including Fourier difference maps can be used to locate atoms in the structure, they rarely give very accurate positions. Therefore, the 'refinement' is done to optimize these starting positions. The principle of refinement is to get a good agreement between the observed data and the data calculated from the model. In order to achieve

most accurate structural information, many advanced functions and methods are used. One of the most important methods used to refine diffraction data is the Rietveld method which will be discussed here [16-17].

In the Rietveld method, the least square refinements are performed until the entire observed pattern and the entire calculated pattern fit best. The calculated pattern is obtained from refined models for crystal structure, instrumental factors, and other specimen characteristics [18]. Powder diffraction data used in refinement consists of thousands of observed intensities,  $y_i$ , at each step,  $i$ , with a small increment between steps [18]. The refinement is done to simultaneously fit all thousands of  $y_i$  with the calculated values,  $y_{ei}$ , at each step. Convergence is reached when the  $S_y$  residual is minimized where

$$S_y = \sum_i w_i (y_i - y_{ei})^2$$

$w_i = 1/y_i$ ,  $y_i$  = observed intensity at  $i^{\text{th}}$  step,  $y_{ei}$  = calculated intensity at  $i^{\text{th}}$  step.

The Rietveld method requires a reasonably good model to start with. The model contains many refinable parameters, some of which are shown in Table 1.3. Multiple phase refinement can be achieved quantitatively. Figure 1.6 shows an example of the profile fit from structural refinement. Many programs have been developed to perform such refinement using the Rietveld method. For example, GSAS (Generalized Structure Analysis System) [20] is a software package widely used to perform refinement on both neutron and X-ray diffraction [21-23]. Other similar programs are also available such as RIETAN [23] and Fullprof [25].

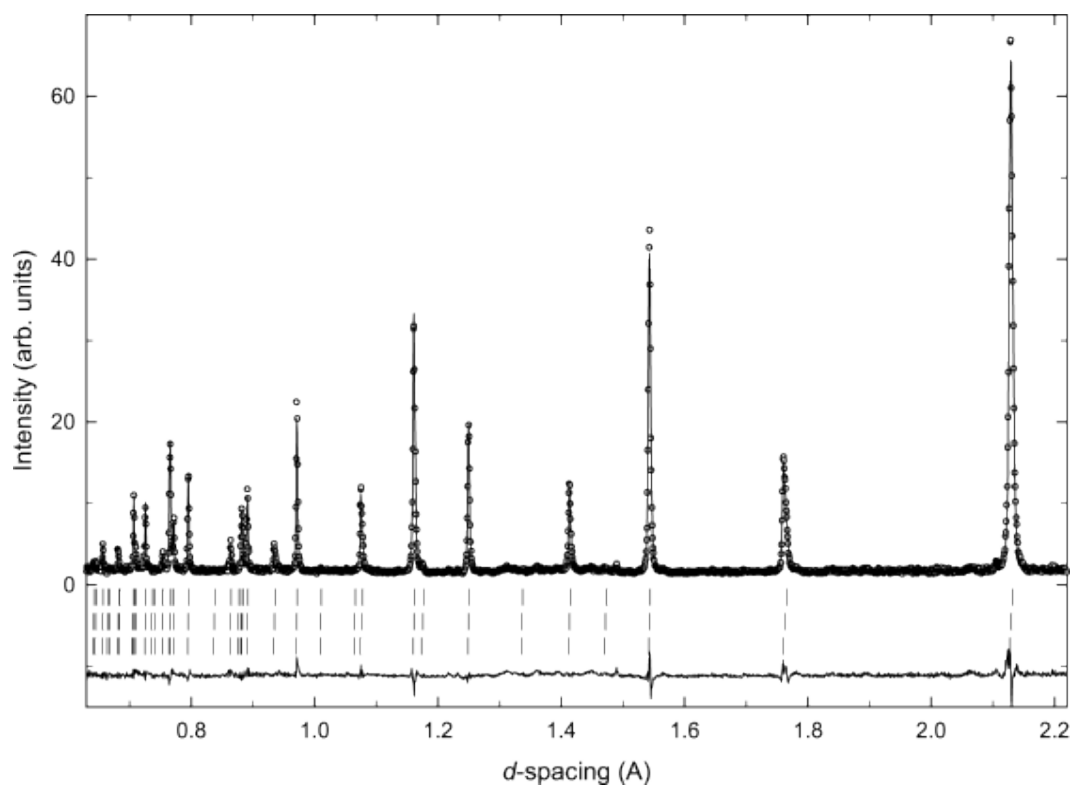


Figure 1.6: Profile fit from Reitveld refinement. Observed (points) and calculated (solid line) neutron powder diffraction profiles are shown [19]

Table 1.3: Refinable parameters in Rietveld refinement [18].

|  |
|--|
| <u>For each phase present</u><br>position coordinates ( $x_j, y_j, z_j$ )<br>Individual thermal parameter<br>site-occupancy<br>Scale factor (quantitative phase possibility)<br>Specimen-profile breadth parameters<br>Lattice parameters<br>Overall temperature factor<br>Preferred orientation<br>Crystallite size and microstrain<br>Extinction |
| <u>Global</u><br>2 $\theta$ -Zero<br>Instrumental profile<br>Background<br>Wavelength<br>Specimen displacement<br>Specimen transparency<br>Absorption  |

### 1.8 References:

1. W. D. Kingery, H. K. Bowen, D. R. Uhlmann, *Introduction to Ceramics*, 2<sup>nd</sup> ed., John Wiley & Sons: New York, (1976).
2. M. A. Subramanian, C. C. Torardi, J. C. Calabrese, J. Gopalakrishnan, K. J. Morrisry, T. R. Askrw, R. B. Flippen, U. Chowdhry, A. W. Sleight, *Science*, **239** (1988), 1015.
3. P. Atkins, T. Overton, J. Rourke, M. Weller, F. Armstrong, *Inorganic Chemistry*, 4<sup>th</sup> ed., Oxford University Press, (2006).
4. A. R. West, *Basic Solid State Chemistry*, John Wiley & Sons: New York, (1988).
5. A. R. West, *Solid State Chemistry and Its Applications*, John Wiley & Sons: New York, (1984).
6. P. A. Cox, *The electronic Structure and Chemistry of Solids*, Oxford University Press, (1987).
7. T. M. Tritt, M. A. Subramanian, *MRS Bull.*, **31** (2006), 188.
8. S. O. Kasap, *Thermoelectric Effects in Metals: Thermocouples*, An e-booklet (1997-2001).

9. H. Föll, "Electronic Materials", Accessed February 2011.  
[http://www.tf.unikiel.de/matwis/amat/elmat\\_en/index.html](http://www.tf.unikiel.de/matwis/amat/elmat_en/index.html)
10. G. D. Mahan, J. O. Sofo, *Proc. Natl. Acad. Sci.*, **19** (1996), 7436.
11. M. A. Subramanian, D. Li, N. Duan, B. A. Reisner, A. W. Sleight, *Solid State Chem.* **151** (2000), 323.
12. D. D. Brown, '*Mixed-Valence Compounds; Theory and Applications in Chemistry, Physics, Geology, and Biology*', Proceedings of the NATO Advanced Study Institute, (1979).
13. M. B. Robin, P. Day, *Adv. Inorg. Chem. Radiochem.*, **10** (1967), 247.
14. P. A. Cox, '*The electronic Structure and Chemistry of Solids*', Oxford University Press, (1987).
15. W. I. F. David, K. Shankland, L. B. McCusker, Ch. Baerlocher, '*Structure Determination from Powder Diffraction Data*', Oxford University Press, (2002).
16. H. M. Rietveld, *Acta Crystallogr.*, **22** (1967), 151
17. H. M. Rietveld, *J. Appl. Crystallogr.*, **2** (1969), 65.
18. R. A. Young, '*The Reitveld Method*', Oxford University Press, (1993).
19. S. Margadonna, T. Muranaka, K. Prassides., I. Maurin, K. Brigatti, R. M. Ibberson, M. Arai, M. Takana, J. Akimitsu, *J. Phys.: Condens. Matter.*, **13** (2001), L795.
20. A.C. Larson and R.B. Von Dreele, '*General Structure Analysis System (GSAS)*', Los Alamos National Laboratory Report LAUR, 2004, 86.
21. A. Gualtieri, P. Norby, J. Hanson, J. Hriljac, *J. Appl. Cryst.* **29** (1996), 707.
22. R. M. Wilson, J. C. Elliott, S. E. P. Dowker, R. I. Smith, *Biomater.*, **25**(2004), 2205.
23. J. Li, A. E. Smith, K.-S. Kwong, C. Powell, A. W. Sleight, M. A. Subramanian, *J. Solid State Chem.*, **183** (2010), 1388.
24. F. Izumi, T. Ikeda, *Mater. Sci. Forum*, **321-324** (2000), 198.
25. J. Rodriguez-Carvajal, *Physica B*, **192** (1993), 55.

## Chapter

### 2. Introduction to Tellurium and Its Oxides

#### 2.1 Tellurium Element

Tellurium, Te, was first isolated from ores in Transylvania in 1782 by F. J. Müller von Reichenstein, an Austrian chemist [1]. It is usually isolated by neutralization of alkaline tellurite with  $\text{H}_2\text{SO}_4$ . Although there are several allotropes of Te, there is only one crystalline form which contains a network of spiral chain as shown in Figure 2.1 with the physical appearance.

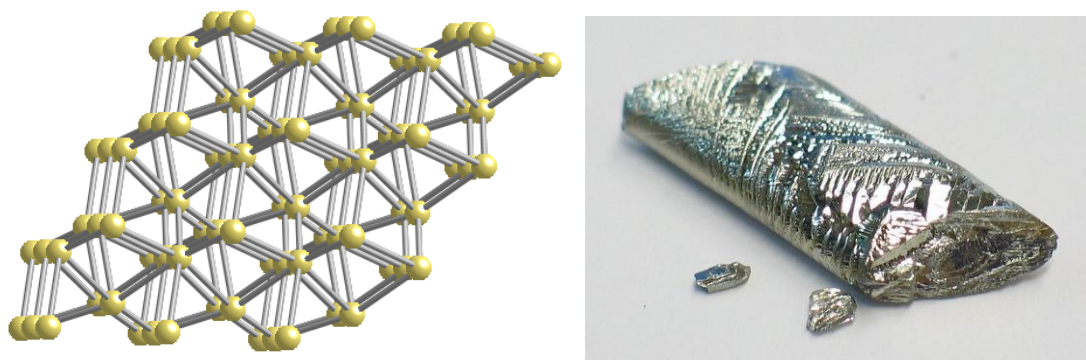


Figure 2.1: Tellurium structure (a) and appearance (b).

Te is in group 16 or VIA in the periodic table with atomic number of 52. Electronic configuration of Te is  $[\text{Kr}] 4d^{10} 5s^2 5p^4$ . It is less reactive than O and S in the same group but can combine with most elements directly. The most stable compounds of Te are telluride ( $\text{Te}^{2-}$ ) of strongly positive elements of group IA, IIA, and lanthanides; and the compounds with electronegative elements like O, F, and Cl [1].

## 2.2 Oxides of Tellurium

### 2.2.1 Binary Oxides

Tellurium monoxide, TeO, transiently exists in flame but cannot be isolated [1]. TeO<sub>2</sub> has two standard modifications at room temperature and ambient pressure; synthetic paratellurite,  $\alpha$ -TeO<sub>2</sub>, and mineral tellurite,  $\beta$ -TeO<sub>2</sub>, as shown in Figure 2.2[2].

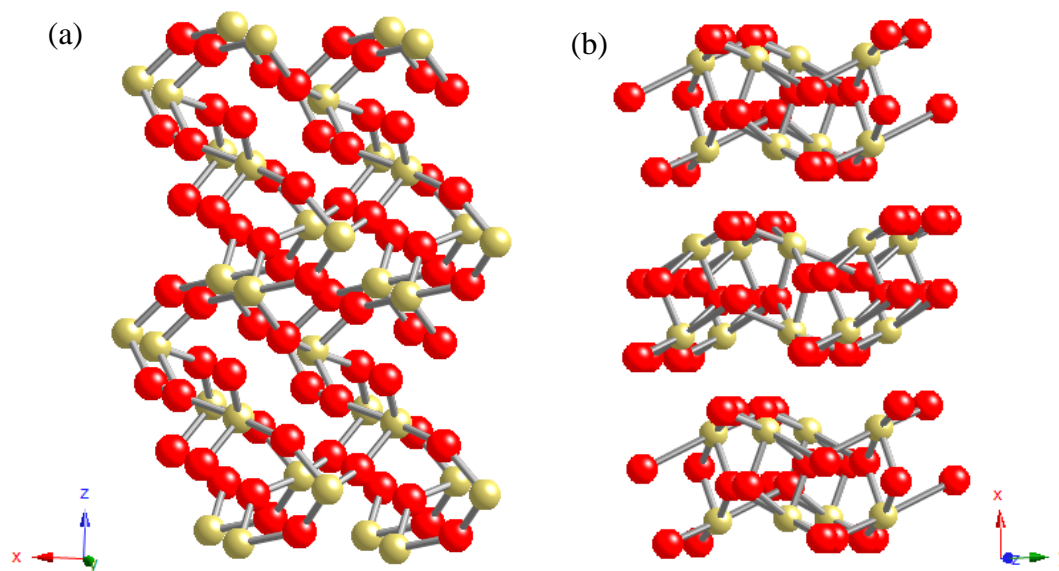


Figure 2.2: TeO<sub>2</sub> structure;  $\alpha$ -form (a) and  $\beta$ -form (b). Red and yellow balls represent O and Te, respectively.

$\alpha$ -TeO<sub>2</sub> forms colorless tetragonal crystal with space group  $P4_32_12$  [3] or  $P4_12_12$  [4]. Each Te atom is coordinated by 4 oxygens forming pseudo-trigonal bipyramidal [TeO<sub>4</sub>] units. These units form a rutile-like 3-dimensional structure as shown in Figure 2.3(a) [1].  $\beta$ -TeO<sub>2</sub> adopts orthorhombic structure, space group  $Pbca$  [5], where the similar [TeO<sub>4</sub>] units share edges to form layers (Fig. 2.3(b)). TeO<sub>2</sub> can



be prepared by many methods such as a reaction of  $O_2$  with elemental Te and a thermal decomposition of hexaoxotelluric acid ( $H_6TeO_6$ ) [1-2]. At high pressure, 3-dimensional  $\gamma$ - $TeO_2$  can be prepared with  $P2_12_12_1$  space group [6].  $TeO_2$  melts at 733 °C to form amorphous phase which consists of  $TeO_4$  pyramidal units [7]. Dioxide of tellurium is virtually insoluble in water but soluble in HCl solution [8].

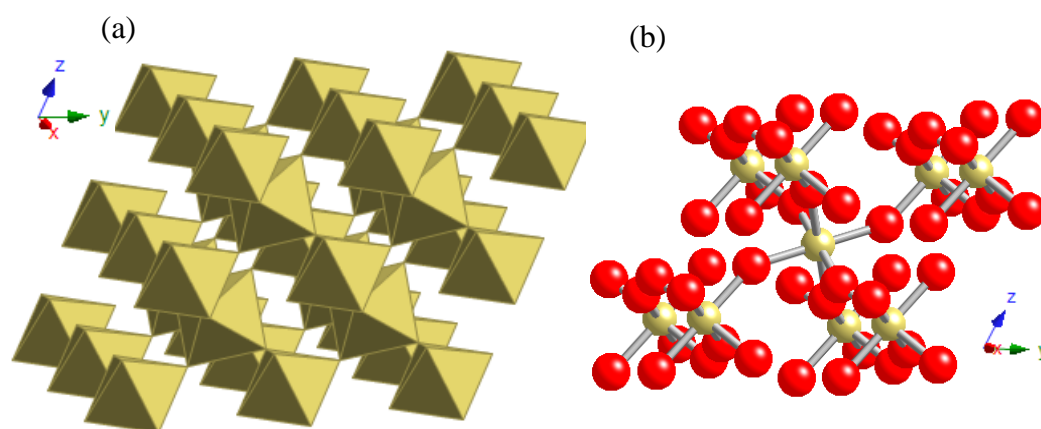


Figure 2.3:  $\beta$ - $TeO_3$  structure; polyhedral model (a) and ball and stick model (b) with red and yellow balls represent O and Te, respectively.

Trioxide of tellurium is known in three modifications:  $\alpha$ ,  $\beta$ , and  $\gamma$  form. Yellow-orange  $\alpha$ - and  $\gamma$ -  $TeO_3$  can be prepared by thermal decomposition of  $Te(OH)_6$ . However, the detailed analysis indicates that both substances contain mixtures of  $Te(VI)$ ,  $Te(IV)$ ,  $O^{2-}$ ,  $OH$ , possible  $H_2O$ ,  $O_2$  and  $O_2$ . Hence they are not pure trioxide [9]. The difference between the two forms is that  $\alpha$ -form is amorphous while the  $\gamma$ -form is crystalline [9]. The real  $TeO_3$  is grey  $\beta$ -form which was prepared by heating  $\alpha$ - $TeO_3$  in the presence of  $H_2SO_4$  and  $O_2$  in a sealed tube [1-2].  $\beta$ -form with  $R\bar{3}c$  space

group, is more stable, less reactive, and insoluble in water, concentrated HCl, or concentrated KOH solution [10]. Figure 2.3 shows  $\beta$ -TeO<sub>3</sub> structure with Te in corner sharing and slightly distorted octahedra.

Te<sub>4</sub>O<sub>9</sub>, space group  $R\bar{3}$ , is obtained by hydrothermal synthesis using Te(OH)<sub>6</sub>, TeO<sub>2</sub>, and H<sub>2</sub>O. The structure contains Te<sup>4+</sup> and Te<sup>6+</sup> in different crystallographic sites with Te<sup>4+</sup>: Te<sup>6+</sup> ratio = 3:1. While Te<sup>6+</sup> forms octahedra with oxygen, Te<sup>4+</sup> is only coordinated by 4 oxygens to form trigonal bipyramidal units with lone-pair electrons in the equatorial position [11].

Polycrystalline sample of Te<sub>2</sub>O<sub>5</sub>, was prepared by thermal decomposition of Te(OH)<sub>6</sub> while the single crystals were grown by hydrothermal synthesis [11-12]. Structural determination on the crystals resulted in  $P2_1$  space group. The coordination of Te<sup>4+</sup> and Te<sup>6+</sup> are similar to those in Te<sub>4</sub>O<sub>9</sub>. 3-dimension network is formed from corner sharing TeO<sub>6</sub> octahedra and TeO<sub>4</sub> chains as shown in Figure 2.4.

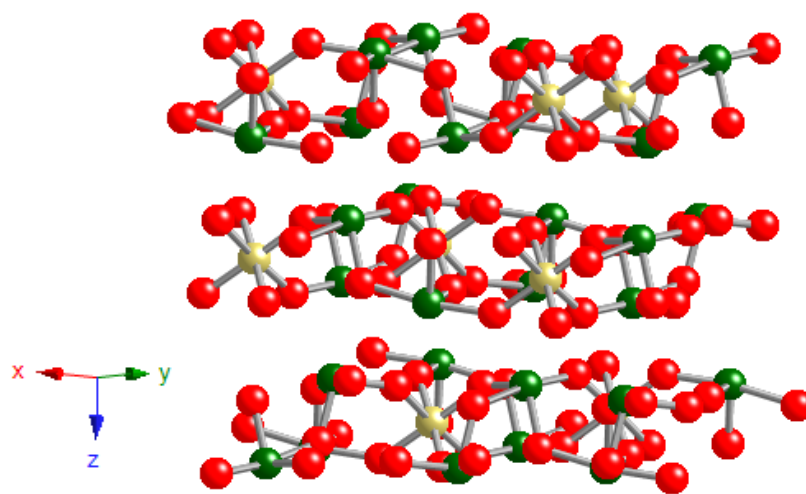


Figure 2.4: Ball and stick model of Te<sub>2</sub>O<sub>5</sub> structure. Red, yellow, and green balls represent O, Te<sup>6+</sup> and Te<sup>4+</sup>, respectively.

## 2.2.2 Other Tellurium Oxides

Many ternary oxides containing tellurium are known and it is impossible to address all of them here. However, some representative compounds will be briefly discussed in the following sections. In general, two oxidation states of tellurium form oxides:  $\text{Te}^{4+}$  and  $\text{Te}^{6+}$ . Although there are some reported on possible  $\text{Te}^{5+}$  containing oxides but only few examples are known.  $\text{Te}^{6+}$  is usually in octahedral 6-fold coordination. On the other hand, distorted polyhedra are usually found for  $\text{Te}^{4+}$  since the structure has to accommodate lone pair electrons.

### 2.2.2.1 Oxides of $\text{Te}^{4+}$

The special feature of compounds containing  $\text{Te}^{4+}$  arises from stereo-active lone pair  $5s^2$  electrons. The most common arrangements around  $\text{Te}^{4+}$  are  $\text{TeO}_3$  trigonal pyramid and  $\text{TeO}_4$  distorted bipyramid. They can be viewed as tetrahedral  $\text{AO}_3\text{E}$ , and bipyramidal  $\text{AO}_4\text{E}$ , respectively when E is lone pair electrons [13].  $\text{TeO}_5$  arrangement is found in some cases and is comparable to  $\text{AO}_5\text{E}$  octahedral. Some other configurations around  $\text{Te}^{4+}$  are also known such as  $\text{A}_2\text{O}_5$ ,  $\text{A}_2\text{O}_6$ , and  $\text{A}_3\text{O}_8$  where some oxygen is shared among  $\text{Te}^{4+}$  [13-14]. Figure 2.5 shows some arrangements of anions around cations with  $s^2$  lone pair electrons comparing to octahedral coordination.

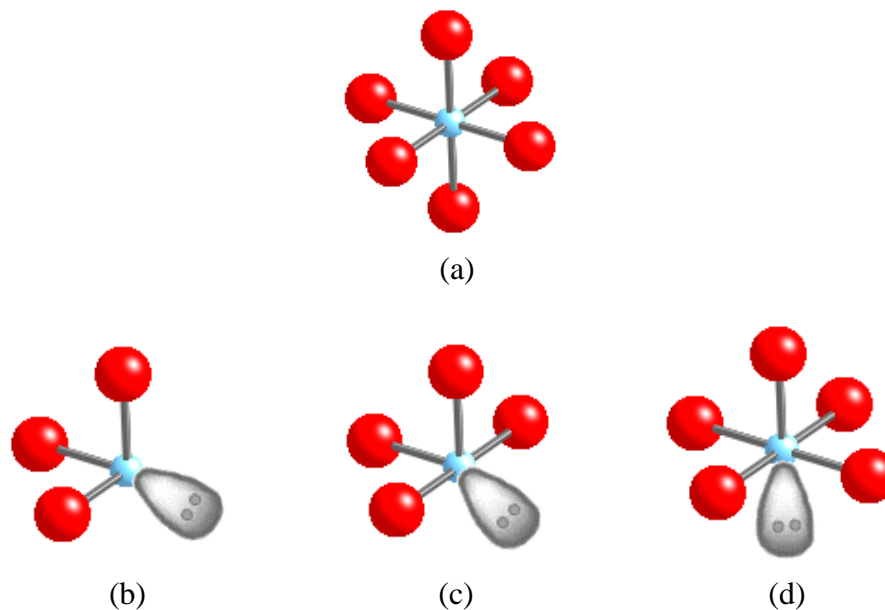


Figure 2.5: Arrangements of anion (red) around  $\text{Te}^{4+}$  (blue) comparing with octahedral coordination (a). The arrangements lead to trigonal pyramid (b), distorted bisphenoid (c), and square pyramid (d) [14].

Trigonal pyramidal  $\text{TeO}_3$  unit is found in many  $\text{ATeO}_3$  tellurites. Detailed structural analysis was done on  $\text{CaTeO}_3$  which indicated four different modifications: tetragonal  $\alpha$ -form, triclinic  $\beta$ -form, triclinic  $\beta'$ -form, and monoclinic  $\gamma$ -form. All modifications have a common feature of isolated and distorted trigonal-pyramidal  $[\text{TeO}_3]^{2-}$  units and  $[\text{CaO}_x]$  polyhedral with  $x=6-8$  [15-16]. The structures consist of channels which provide space for lone pair electrons of  $\text{Te}^{4+}$  as shown in Figure 2.6.

Similarly,  $\text{SrTeO}_3$  consists of 3-dimensional network of trigonal-prismatic  $[\text{TeO}_3]^{2-}$  units linking with  $[\text{SrO}_x]$ ,  $x= 7-8$  units. However, the two units link in a different way leading to different structures.  $\text{SrTeO}_3$  exhibits unique structure which undergoes several phase transitions with temperature [17-23]. Ferroelectric properties

were found in  $\text{CaTeO}_3$  and  $\text{SrTeO}_3$  because of the asymmetric polar direction, high polarizability, and a preference for particular stereochemistry [15].

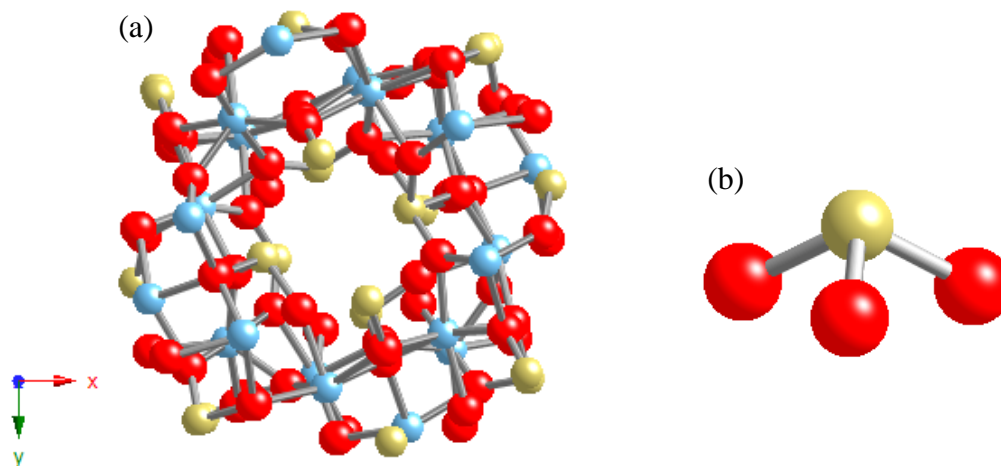


Figure 2.6:  $\text{CaTeO}_3$  structure (a) and coordination of  $\text{Te}^{4+}$  (b). Yellow, blue, and red balls represent Te, Ca, and O, respectively [after 15].

Other  $\text{ATeO}_3$  phases are also known. Structure and electronic properties of orthorhombic  $\text{MgTeO}_3$  was studied by Rai *et al.* [24].  $\text{BaTeO}_3$  crystallizes in monoclinic  $P2_1/m$  space group where Te forms pyramidal  $\text{TeO}_3$  sharing edges and corners with  $\text{BaO}_9$  polyhedra [25].  $\text{ATeO}_3$ , A = Mn, Co, Ni, Cu, Zn, Cd, and Hg were studied in many works.  $\text{MnTeO}_3$  was first prepared by Törmer *et al.* in 1972 from solid state reaction of oxide of manganese and  $\text{TeO}_2$  under inert gas [26].  $\text{CoTeO}_3$  was prepared from reaction between  $\text{Co}^{2+}$  and  $\text{K}_2\text{TeO}_3$  solution [27], hydrothermal synthesis [28] and solid state reaction [29].  $\text{NiTeO}_3$  was prepared from solid state reaction [29]. In 1974, Kohn *et al.* studied detailed structure and magnetic properties of  $\text{MnTeO}_3$ ,  $\text{CoTeO}_3$ , and  $\text{NiTeO}_3$  prepared from high pressure synthesis which

crystallized in *Pnma* space group [13,30]. The basic trigonal pyramidal is also seen in these high-pressure phases. Thermochemistry and phase diagram of these compounds were widely studied [31-35].

$\text{CuTeO}_3$  oxide adopts distorted  $\text{ABO}_3$  perovskite structure where  $\text{Cu}^{2+}$  occupy smaller B site and  $\text{Te}^{4+}$  with lone pair electrons occupy A site.  $\text{CuO}_6$  octahedra share corners to form 3-dimensional network whose cavity is occupied by  $\text{Te}^{4+}$ . The structure differs from ideal perovskite as 3 out of 12 oxygens are closer to  $\text{Te}^{4+}$ . As a consequence, the structure is orthorhombic rather than cubic [36]. Figure 2.7 demonstrates the comparison between  $\text{CuTeO}_3$  distorted perovskite and the ideal perovskite. Studies have been done on the magnetic interaction in this compound [37-38].

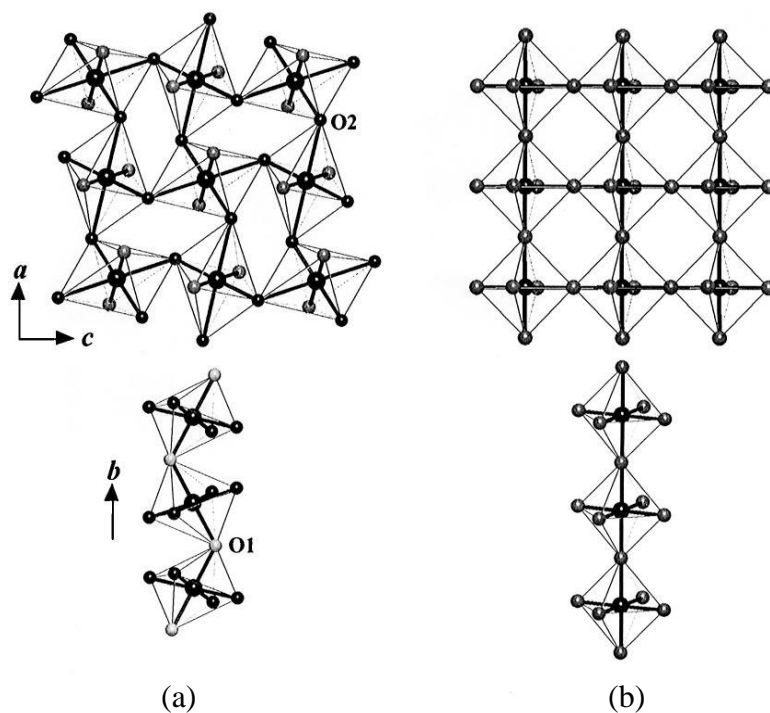


Figure 2.7: Projection of the crystal structure of orthorhombic  $\text{CuTeO}_3$  showing the octahedral arrangement along  $ac$  plane and along  $b$  direction (a). Projection of the ideal cubic perovskite structure showing  $180^\circ$  M-O-M interactions (b) [36].

MVTeO<sub>5</sub> series, M=Na, K, and Ag crystallize in  $P2_1/c$  space group containing TeO<sub>4</sub> as shown in Figure 2.8 [39]. Each Te<sup>4+</sup> is coordinated with 4 oxygen forming polyhedra which share oxygens in Te<sub>2</sub>O<sub>6</sub> group; these Te<sub>2</sub>O<sub>6</sub> groups connect to VO<sub>4</sub> tetrahedra. The metal atom M forms bicapped triangular prisms with 8 oxygens and share faces to form infinite zig-zag string [39].

The similar unit is found in a polymorph of CaTe<sub>2</sub>O<sub>5</sub>. In this case, TeO<sub>4</sub>E distorted bipyramidal units share edges and corners to form Te<sub>2</sub>O<sub>5</sub> layers which are interleaved with Ca layers as shown in Figure 2.9. Oxygen atoms from the layers form tunnels along [010] direction accommodating lone pair electrons of Te<sup>4+</sup> [40-41].

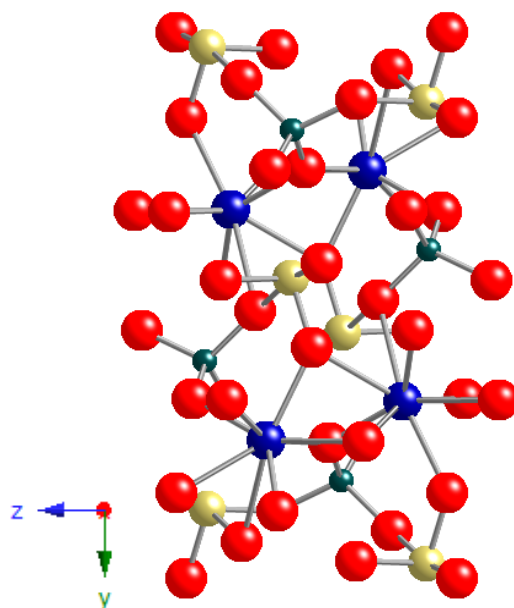


Figure 2.8: MVTeO<sub>5</sub> structure. Yellow, green, blue, and red ball represent Te, V, M, and O, respectively [after 39].

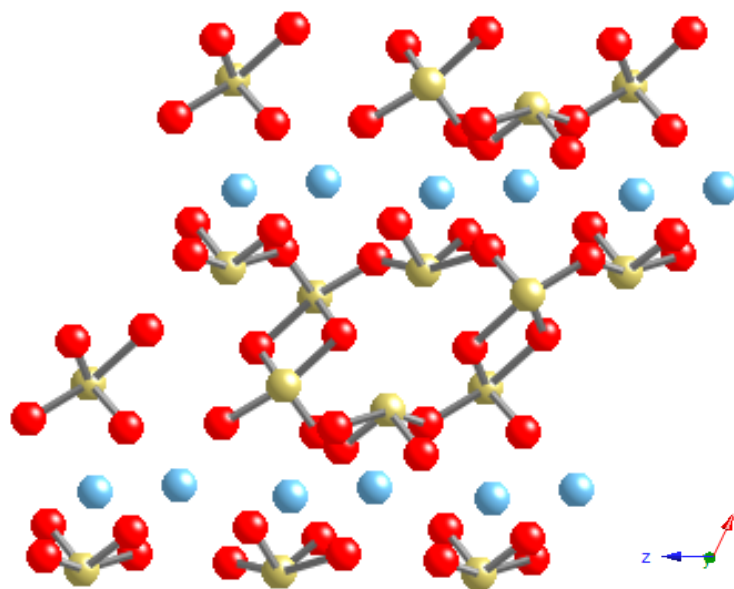


Figure 2.9:  $\text{CaTe}_2\text{O}_5$  structure showing layers of  $[\text{Ca}]$  and  $[\text{Te}_2\text{O}_5]$  and the tunnels. Yellow, blue, and red balls represent Te, Ca, and O, respectively.

Relatively few oxides containing  $\text{TeO}_5$  configuration are known. Most of them coexist with other configurations. An example of  $\text{Te}^{4+}$  in purely  $\text{TeO}_5$  coordination is  $\text{SeTeO}_4$  oxide which crystallizes in  $Ia$  space group. The structure consists of  $\text{TeO}_5$  units connecting with  $\text{SeO}_3$  through  $\text{Se-O-Te}$  and  $\text{Te-O-Te}$  bonds (Fig. 2.10) [42]. Interestingly, the compound only contains cations with non-bonded electrons,  $\text{Te}^{4+}$  and  $\text{Se}^{4+}$ , which affects topology of the structure. As a result,  $\text{SeTeO}_4$  is non-centrosymmetric which could be a promising second-harmonic generating material [39].



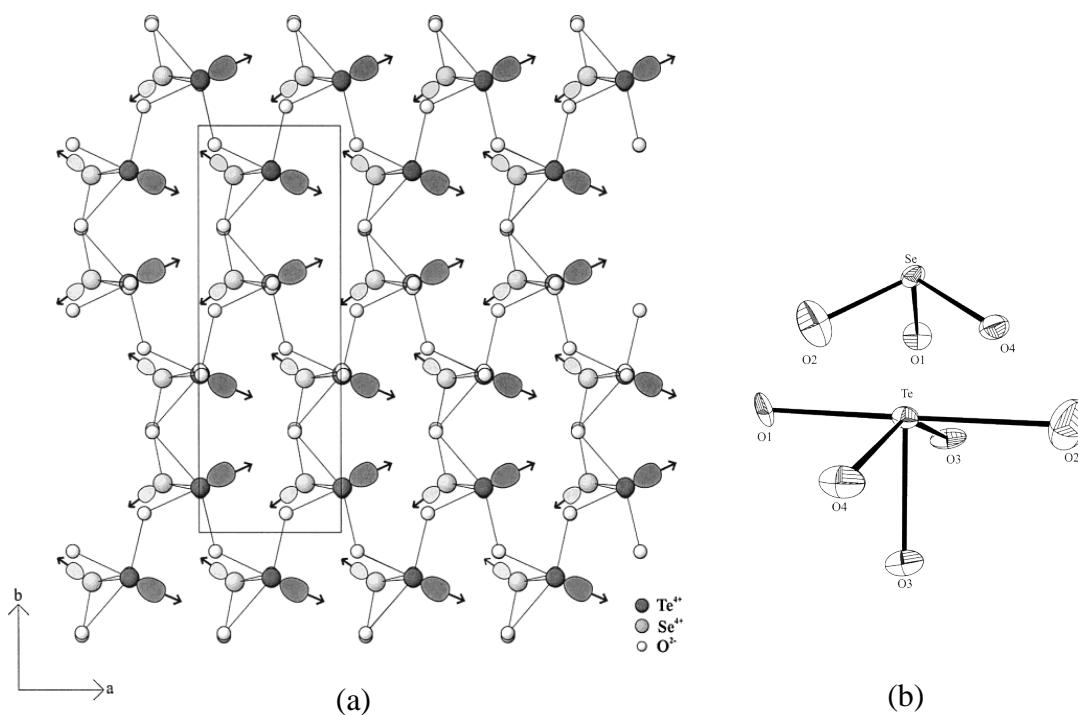


Figure 2.10:  $\text{SeTeO}_4$  structure (a) where the arrows show direction of dipole moment from  $\text{Te}^{4+}$  and  $\text{Se}^{4+}$ . Coordination around  $\text{Te}^{4+}$  and  $\text{Se}^{4+}$  are shown in (b) [42].

Coexistence of different configurations is common for oxides containing  $\text{Te}^{4+}$ . Most of them crystallize in non-centrosymmetric structure. Examples are  $\text{Ca}_4\text{Te}_5\text{O}_{14}$  [43],  $\text{Ga}_2\text{Te}_4\text{O}_{11}$  [44], and  $\text{Tl}_2\text{Te}_3\text{O}_7$  [45]. Nevertheless, it is very rare to have all the three coordinations in the same structure. One example is  $\text{NH}_4\text{ATe}_4\text{O}_9 \cdot 2\text{H}_2\text{O}$ ,  $\text{A}=\text{Rb}$ ,  $\text{Cs}$  prepared from hydrothermal synthesis [46]. The compound consists of  $\text{TeO}_x$ ,  $x=3,4,5$  layers separated by  $\text{NH}_4^+$ ,  $\text{H}_2\text{O}$ ,  $\text{Rb}^+$ , or  $\text{Cs}^+$  resulting in 2-dimensional structure. However, the overall structure is centrosymmetric by having lone-pair electrons point in opposite directions [46].

The very unusual coordination of  $\text{Te}^{4+}$  is octahedral. However, it is found in  $\text{CsTe}_2\text{O}_6$  with defect pyrochlore structure where both Te; 0.5 of  $\text{Te}^{4+}$  and 1.5 of  $\text{Te}^{6+}$ , are in 6-fold coordination [47].  $\text{A}_2\text{Te}_2\text{O}_7$  pyrochlores with  $\text{A} = \text{La}, \text{Nd}, \text{and Pr}$  were also reported to contain  $\text{Te}^{4+}$  in octahedral coordination but the prepared samples were not completely pure in some cases [48-49].

#### 2.2.2.2 Oxides of $\text{Te}^{6+}$

The most common environment for  $\text{Te}^{6+}$  in oxides is 6-fold coordination. However, some examples of  $\text{Te}^{6+}$  in 4-fold tetrahedral environment are known.

Half of Te in  $\text{Rb}_2\text{TeO}_9$  is coordinated by 4 oxygens to form tetrahedral arrangement [50]. In 1999, Weller *et al.* confirmed the existence of  $\text{Te}^{6+}$  in tetrahedra in  $\text{Cs}_2\text{TeO}_9$  by EXAFS (Extended X-ray Absorption Fine Structure), X-ray diffraction and  $^{125}\text{Te}$  MASNMR (Magic-Angle Spinning Nuclear Magnetic Resonance). It was found that the structure contain discrete  $[\text{TeO}_4]^{2-}$  units which is in 8-fold coordination to Cs [51].

Much more oxides containing  $\text{Te}^{6+}$  in octahedral coordination with oxygen are known; although in some cases, the coordination is not perfect octahedral but distorted in some ways. For example,  $\text{NaBiTeO}_5$  crystallizes in  $P2_1/c$  space group where  $\text{Te}^{6+}$  coordination is nearly normal octahedral.  $\text{TeO}_6$  units connect with  $\text{BiO}_4$  units through Bi-O-Te and Te-O-Te bonds as shown in Figure 2.12 [54]. More examples in relatively simple structures include perovskite or pyrochlore and their modifications [53-57].

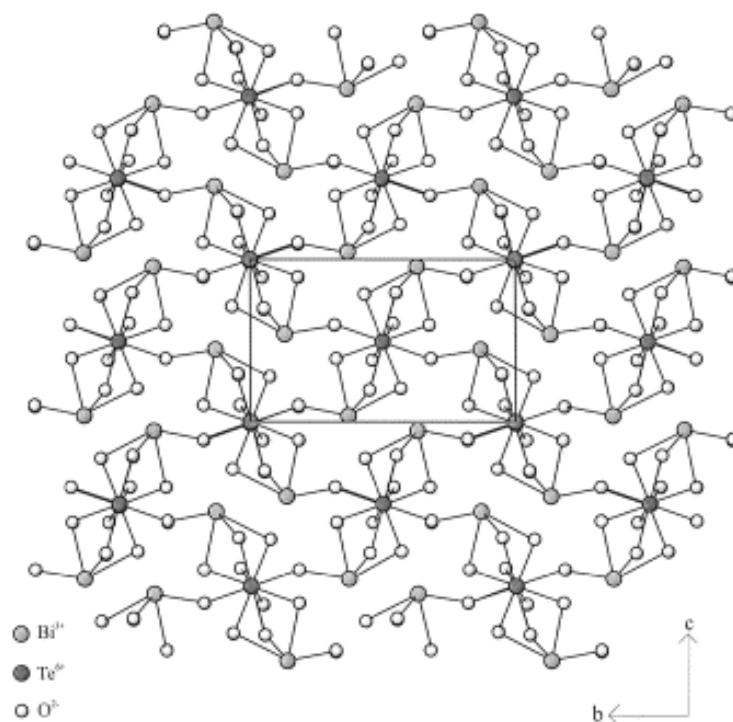


Figure 2.11: NaBiTeO<sub>5</sub> structure [52] (Na<sup>+</sup> cations are removed for clarity).

### 2.2.2.3 Oxides of Te<sup>5+</sup>

Te<sup>5+</sup> in oxides tends to disproportionate to Te<sup>4+</sup> and Te<sup>6+</sup>. Oxides that seem to have Te<sup>5+</sup> always contain Te<sup>4+</sup> and Te<sup>6+</sup> in separate sites. For example, Te<sub>2</sub>O<sub>5</sub> and Ag<sub>2</sub>Te<sub>2</sub>O<sub>6</sub> are actually Te<sup>4+</sup>Te<sup>6+</sup>O<sub>5</sub> and Ag<sub>2</sub>Te<sup>4+</sup>Te<sup>6+</sup>O<sub>6</sub>, respectively.

To the best of knowledge, BaTl<sub>0.5</sub>Te<sub>0.5</sub>O<sub>3</sub> is the only example of possible Te<sup>5+</sup> in oxide. The compound adopts cubic perovskite structure and has relatively high electronic resistivity of about 0.2 Ωcm at room temperature [58]. Although there was no clear evidence confirming the oxidation state of Te, comparison of the cell parameter with other similar compounds strongly suggested the existence of Te<sup>5+</sup> in octahedral coordination [58].

#### 2.2.2.4 Mixed Valence Tellurium Oxides

Coexistence of both  $\text{Te}^{4+}$  and  $\text{Te}^{6+}$  in some oxides results in mixed valence compounds. According to Robin and Day classification [59] as discussed in section 1.6, there are three classes of mixed valence compounds. Oxides of tellurium exist in all classes.

Compounds in class I mixed valency contain  $\text{Te}^{4+}$  and  $\text{Te}^{6+}$  in different coordination. While the most common coordination of  $\text{Te}^{4+}$  are  $[\text{TeO}_3]$  and  $[\text{TeO}_4]$ ,  $\text{Te}^{6+}$  is usually coordinated by 6 oxygens forming octahedral arrangement. Therefore, most of the mixed valence tellurium oxides fall in this class. Since there is no significant interaction between the two oxidation states, the compounds are usually white or pale yellow with no measureable electronic conductivity. Some examples are  $\text{Te}_2\text{O}_5$  ( $\text{Te}^{4+}\text{Te}^{6+}\text{O}_5$ ),  $\text{Ag}_2\text{Te}_2\text{O}_6$  ( $\text{Ag}_2\text{Te}^{4+}\text{Te}^{6+}\text{O}_6$ ), and  $\text{SrTe}_3\text{O}_8$  ( $\text{SrTe}_2^{4+}\text{Te}^{6+}\text{O}_8$ ) [60-62].

$\text{CsTe}_2\text{O}_6$  is the obvious example of tellurium oxides in class II mixed valency. In this compound, both  $\text{Te}^{4+}$  and  $\text{Te}^{6+}$  are in the same coordination of octahedral arrangement but different crystallographic sites. Some interaction between the two tellurium species leads to the intense dark brown color [47].

Metallic conduction has never been observed in mixed valence tellurium oxides. To the best of our knowledge, the most conducting tellurate is  $\text{BaTl}_{0.5}\text{Te}_{0.5}\text{O}_3$  ( $0.2 \Omega\text{cm}$ ) [58]. The only other examples are compounds with formula  $\text{Cs}(\text{M},\text{Te})\text{O}_6$  when  $\text{M}=\text{Al}$ ,  $\text{Ge}$ ,  $\text{In}$ ,  $\text{Tl}$ , and  $\text{Ga}$  prepared in this work [63-64]. However, although  $\text{Te}^{4+}$  and  $\text{Te}^{6+}$  are in the same crystallographic site in both cases, semiconducting

behavior with activation energy of conduction in these compounds suggests that carriers are not completely delocalized and they are still class II mixed valency.

### 2.3 Properties

Stereo-active lone pair electrons on  $\text{Te}^{4+}$  often result in non-centrosymmetric structures which exhibit useful properties.  $\text{SrTeO}_3$  shows ferroelectric properties in temperature range 312-485°C [17] and have been widely studied [65-66]. Dityat'ev *et al.* reported that substitution of Pb and La for Sr extended ferroelectric temperature range of  $\text{SrTeO}_3$  [67].  $\text{Bi}_2\text{TeO}_5$  exhibits valuable pyroelectric and photovoltaic properties [68]. Moreover,  $\text{Bi}_2\text{TeO}_5$  is suitable for second harmonic generation (SHG) which is a nonlinear optical process that transforms the incoming photons into new photons with twice energy [69]. Goodey *et al.* reported  $\text{Te}^{4+}$  containing  $\text{Na}_2\text{TeW}_2\text{O}_9$  phase (*Ia* space group) which also exhibits SHG properties [70].

Some other interesting properties are studied in oxides of tellurium including transparent conductor in  $\text{In}_2\text{TeO}_6$  [71], catalytic properties for allylic oxidation of olefins in  $\text{MTeMoO}_6$  ( $\text{M} = \text{Cd}^{2+}, \text{Co}^{2+}, \text{Mn}^{2+}, \text{Zn}^{2+}, \text{Mg}^{2+}$ ) [72-77], ionic conductivity in  $\text{ATi}_{0.5}\text{Te}_{1.5}\text{O}_6$  ( $\text{A} = \text{K}, \text{Rb}, \text{Cs}, \text{Tl}$ ) [58], and luminescence properties in  $\text{Eu}^{3+}$ -doped  $\text{Y}_2\text{Te}_4\text{O}_{11}$  and  $\text{Y}_2\text{Te}_5\text{O}_{13}$  [78].

### 2.4 References

1. N. N. Greenwood, A. Earnshaw, 'Chemistry of the Elements', Pergamon Press, (1984).
2. J. Loub, *Collect. Czech. Chem. Commun.*, **58** (1993), 1717.
3. I. P. Kondratyuk, L. A. Muradyan, Yu. V. Pisarevskii, B. I. Simonov, *Kristallogr.*, **21** (1987), 609.

4. P. A. Thomas, *J. Phys. C*, **21** (1988), 4611.
5. H. Beyer, *Z. Kristallogr.*, **124** (1967), 228.
6. T. G. Worlton, R. A. Beyerlein, *Phys. Rev. B.*, **12** (1975), 1899.
7. M. Durand, B. Ayrault, Y. Marqueton, E. A. Decamps, *C. R. Acad. Sci.*, **B283** (1976), 377.
8. D. R. Lide, 'Handbook of Chemistry and Physics CRC', 84<sup>th</sup> ed., CRC press, (2003)
9. J. Loub, J. Rosicky, *Z. Anorg. Allg. Chem.*, **365** (1969), 308.
10. J. Loub, *Z. Anorg. Allg. Chem.*, **362** (1968), 98.
11. O. Lindqvist, W. Mark, *Acta Cryst.*, **B31** (1975), 1255.
12. J. Rosicky, J. Loub, J. Pavel, *Z. Anorg. Allg. Chem.*, **334** (1965), 312.
13. K. Kohn, K. Inoue, O. Horie, S.-I. Akimoto, *J. Solid State Chem.*, **18** (1976), 27.
14. I. D. Brown, *J. Solid State Chem.*, **11** (1974), 214.
15. B. Stöger, W. Matthias, E. Zobetz, G. Giester, *Acta Cryst.*, **B65** (2009), 167.
16. R. Rai, S. Sharma, R. N. P. Choudhary, *J. Mater. Sci. Lett.*, **21** (2001), 297.
17. T. Yamada, H. Iwasaki, *Appl. Phys. Lett.*, **21** (1972), 89.
18. O. A. Dityatiev, P. S. Berdonosov, V. A. Dolgikh, D. W. Aldous, P. Lightfoot, *Solid State Sci.*, **8** (2006), 830.
19. V. E. Zavodnik, *Acta Crystallogr. Sect. E: Struct. Rep. Online*, **E63** (2007), i75.
20. V. E. Zavodnil, S. A. Ivanov, A. I. Stash, *Acta Crystallogr. Sect. E: Struct. Rep. Online*, **E64** (2008), i52.
21. V. E. Zavodnil, S. A. Ivanov, A. I. Stash, *Acta Crystallogr. Sect. E: Struct. Rep. Online*, **E63** (2007), i151.
22. V. E. Zavodnil, S. A. Ivanov, A. I. Stash, *Acta Crystallogr. Sect. E: Struct. Rep. Online*, **E63** (2007), i111.
23. V. E. Zavodnil, S. A. Ivanov, A. I. Stash, *Acta Crystallogr. Sect. E: Struct. Rep. Online*, **E63** (2007), i75.
24. R. S. Rai, S. Sharma, R. N. P. Choudhary, *Ferroelectr.*, **275** (2002), 11.
25. F. Folger, *Z. Anorg. Allg. Chem.*, 411 (1975), 111.
26. M. Trömer, D. Schmid, *Z. Anorg. Allg. Chem.*, **387** (1972), 230.
27. G. S. Deshmukh, V. D. Anand, A. K. Vishwanath, *Fresen. Z. Anal. Chem.*, **172** (1960), 260.
28. G. Gattow, O. J. Lieder, *Naturwissenschaften*, **50** (1963), 662.
29. K. K. Samplavskaya, M. Kh. Karapet'yants, *Zh. Neorg. Khim.*, **22** (1977), 2333.
30. K. Kohn, S. Akimoto, Y. Uesu, K. Asai, *J. Phys. Soc. Jpn.*, **37** (1974), 1169.
31. T. S. Lakshmi Narasimhan, M. S. Baba, R. Viswanathan, *J. Phys. Chem. A*, **110** (2006), 13705.
32. G. Gospodinov, L. Atanasova, *J. Therm. Anal. Calorim.*, **83** (2006), 273.
33. T. S. Narasimhan, M. S. Baba, S. Nalini, R. Viswanathan, *Thermochim. Acta*, **410** (2004), 149.
34. C. Malika, O. M. Sreedharan, *Thermochim. Acta*, **190** (1991), 217.
35. D. Kolar, V. Urbanc, L. Golic, V. Ravnik, B. Volavsek, *J. Inorg. Nucl. Chem.*, **33** (1971), 3693.

36. M. A. Subramanian, A. P. Ramirez, W. J. Marshall, *Phys. Rev. Lett.*, **82** (1999), 1558.
37. M. A. Subramanian, A. P. Ramirez, *Mat. Res. Soc. Symp. Proc. (Solid-State Chemistry of Inorganic Materials II)*, **547** (1999), 169.
38. G. Lawes, T. Kimura, C. M. Varma, M. A. Subramanian, N. Rogado, R. J. Cava, A. P. Ramirez, *Prog. Solid State Chem.*, **37** (2009), 40.
39. P. Rozier, L. Vendier, J. Galy, *Acta Cryst.*, **C58** (2002), i111.
40. M. Weil, B. Stöger, *Acta Cryst.*, **C64** (2008), i79.
41. N. Barrier, J. M. Rueff, M. B. Lepetit, J. Contreras-Garcia, S. Malo, B. Raveau, *Solid State Sci.*, **11** (2009), 289.
42. Y. Porter, N. S. P. Bhuvanesh, P. Shiv Halasyamani, *Inorg. Chem.*, **40** (2001), 1172.
43. M. Weil, *Solid State Sci.*, **6** (2004), 29.
44. M. Dutreilh, P. Thomas, J. C. Champarnaud-Mesjard, B. Frit, *Solid State Sci.*, **3** (2001), 423.
45. B. Jeansannetas, P. Thomas, J. C. Champarnaud-Mesjard, B. Frit, *Mat. Res. Bull.*, **32** (1997), 51.
46. J.-H. Kim, P. Shiv Halasyamani, *J. Solid State Chem.*, **181** (2008), 2108.
47. B. O. Loopstra, K. Goubitz, *Acta Cryst. C*, **42** (1986), 520.
48. Ismunandar, I. Haryanto, S. Dewi, *Jurnal Matematika dan Sains*, **8** (2003), 27
49. F. A. Weber, T. Schleid, *Z. Anorg. Allg. Chem.*, **626** (2000), 1285.
50. Th. Wisser, R. Hoppe, *Z. Anorg. Allg. Chem.*, **584** (1990), 105.
51. M. T. Weller, M. J. Pack, N. B. Binsted, S. E. Dann, *J. Alloys Compd.*, **282** (1999), 76.
52. K. Min Ok, P. Shiv, Halasyamani, *Solid State Sci.*, **4** (2002), 793.
53. E. D. Politova, Y. N. Venevtsev, *Mat. Res. Bull.*, **10** (1975), 319.
54. L. Ortega-San Martin, J. P. Chapman, G. Cuello, J. Gonzalez-Calbet, M. I. Arriortua, T. Rojo, *Z. Anorg. Allog. Chem.*, **631** (2005), 2127
55. P. M. Woodward, A. W. Sleight, L.-S. Du, C. P. Grey, *J. Solid State Chem.*, **147** (1999), 99./
56. A. Castro, I. Rasines, X. M. Turrillas, *J. Solid State Chem.*, **80** (1989), 227.
57. Y.-S. Hong, M. Zakhour, M. A. Subramanian, J. Darriet, *J. Mater. Chem.*, **8** (1998), 1889.
58. M. A. Subramanian, R. L. Harlow, A. P. Ramirez, *Inter. J. Inorg. Mater.*, **2** (2000), 131.
59. M. B. Robin, P. Day, *Adv. Inorg. Chem. Radiochem.*, **10** (1967), 247.
60. O. Lindqvist, J. Moret, *Acta Cryst. Sect. B*, **29** (1973), 643.
61. W. Klein, J. Curda, E.-M. Peters, M. Z. Jansen, *Anorg. Allg. Chem.*, **631** (2005), 2893.
62. N. Barrier, S. Malo, O. Hernandez, M. Hervieu, B. Raveau, *J. Solid State Chem.*, **179** (2006), 3484.
63. T. Siritanon, G. Laurita, R. T. Macaluso, J. N. Millican, A.W. Sleight, M.A. Subramanian, *Chem. Mater.*, **21** (2009), 5572.

64. J. Li, T. Siritanon, J. K. Stalick, A. W. Sleight, M. A. Subramanian, *Inorg. Chem.*, in press.
65. T. Yamada, H. Iwasaki. *J. Appl. Phys.* **44** (1973), p. 3934.
66. M. V. Pentegova, Y. Y. Tomashpol'skii, *Neorg. Mater.*, **12** (1976), 362.
67. O. A. Dityat'ev, S. Yu. Stefanovich, V. A. Prituzhalov, V. A. Dolgikh, *Inorg. Matter.*, **40** (2004), 740.
68. S. Yu. Stefanovich, V. A. Zhurov, S. A. Ivanov, L. A. Sadovskaya, K. V. Domoratsky, V. A. Dolgikh, *Ferroelectr.*, **241** (2000), 303.
69. A. Simon, J. Ravez, P. Hagenmuller, B. Frit, *Solid State. Commun.*, **29** (1979), 815.
70. J. Goodey, J. Broussard, P. Shiv, Halasyamani, *Chem. Mater.*, **14** (2002), 3174.
71. R. D. Shannon, J. L. Gillson, R. J. Bouchard, *J. Phys. Chem. Solids.*, **38** (1977), 877.
72. P. Forzatti, G. Tieghi, *J. Solid State Chem.*, **25** (1978), 387.
73. R. Kozlowski, J. Sloczynski, *J. Solid State Chem.*, 18 (1976), 51.
74. P. Forzatti, P. Tittarelli, *J. Solid State Chem.*, **33** (1980), 421.
75. G. Tieghi, P. Forzatti, *J. Appl. Crystallogr.*, **11** (1978), 291.
76. I. L. Botto, E. J. Baran, *Z. Anorg. Allg. Chem.*, **468** (1980), 221.
77. J. Sloczynski, *Z. Anorg. Allg. Chem.*, **438** (1978), 287.
78. P. Höss, A. Osvet, F. Meister, M. Batentschuk, A. Winnacker, T. Schleid, *J. Solid State Chem.*, **181** (2008), 2783.



## Chapter

### 3. Experimental Methods of Analysis

Experimental solid state chemistry is based on only two important processes; sample preparation and sample characterization. Powder diffraction of both X-ray and neutron is the crucial technique to characterize samples and identify phases. On the other hand, various properties of materials could be obtained from various methods using different instruments. The following sections discuss principles and theory of some methods of analysis.

#### 3.1 X-ray Diffraction

There are 2 main techniques of X-ray diffraction in solid state chemistry. Single crystal X-ray diffraction is the main tool for solving crystal structures while powder X-ray diffraction is mainly used for phase identification. Both techniques were used as the main characterization of all samples in this work to identify the compounds and obtain crystallographic information.

There are three main parts in every X-ray diffractometer; X-ray source, sample holder, and detector. The X-ray source usually has 3 components; an electrons source, an accelerating voltage, and a metal target. Electrons beam from the electron source is accelerated by a very high voltage, normally 30,000 to 50,000 volts, and bombarded to the metal target. High energy electron beam ejects electrons from the core  $1s$  level of the metal target. The process leaves vacancies behind and results in atoms in excited state. To go back to the ground state, the outer electrons of the metal target will emit

radiation and fall into these vacancies. The emitted radiation has specific energy and is called characteristic K radiation. Radiation from the source is filtered and only monochromatic radiation with single wavelength is allowed to interact with the sample [1]. X-ray is incident on the sample and scattered. At most conditions, these scattered beams cancel each other. However, at some specific conditions, they reinforce and result in detectable beam. The specific conditions are explained by Bragg's law;

$$n\lambda = 2d\sin\theta$$

where  $n$  is an integer number,  $\lambda$  is wavelength of X-ray,  $d$  is lattice spacing, and  $\theta$  is the angle as shown in Figure 3.1. The diffracted beams are detected by a detector. Using this relationship, lattice spacing of the crystal is obtained by the interaction of X-ray of known wavelength with crystals at various angles.

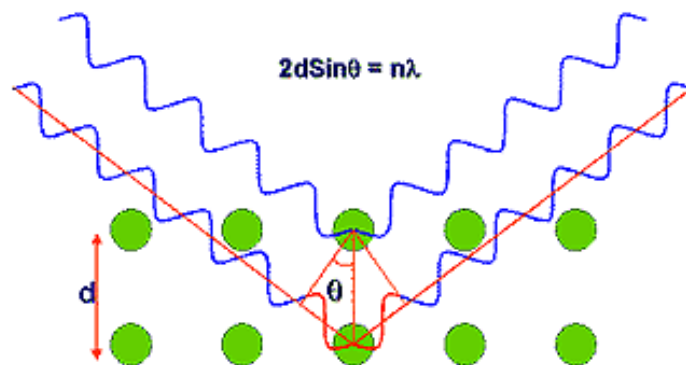


Figure 3.1: Bragg's law for x-ray diffraction.

### 3.1.1 Single Crystal X-ray Diffraction

Most detailed information about crystal structure including unit cell parameters, space groups, positional parameters, atomic occupancies, bond lengths, and bond angles are obtained from single crystal X-ray diffraction. A very small single crystal (about 0.2 mm) is used in a 4- circle goniometer diffractometer which refers to 4 angles (degrees of freedom) relating to the relationship between crystal lattice, incident beam, and detector as shown in Figure 3.2. Three out of four parameters are fixed and the detector scan through the fourth angle to obtain each hkl reflection. The set of data containing thousands of reflections is collected and interpreted for structural information [2].

Single crystal X-ray diffraction data in this work were collected on a Bruker SMART APEXII CCD system and an Oxford Cryostream cooler at 173 K and/or 273 K. A standard focus tube was used with an anode power of 50 kV at 30 mA, a crystal to plate distance of 5.0 cm,  $512 \times 512$  pixels/frame, beam center (256.52, 253.16),  $\phi/\omega$  scan with step of  $0.30^\circ$ , exposure/frame of 10.0 s/frame, and SAINT integration. SADABS program was used to correct for absorption. The crystal structures were solved with direct method using SHELXS program and refined with full-matrix least-squares method using SHELXTL software [3].

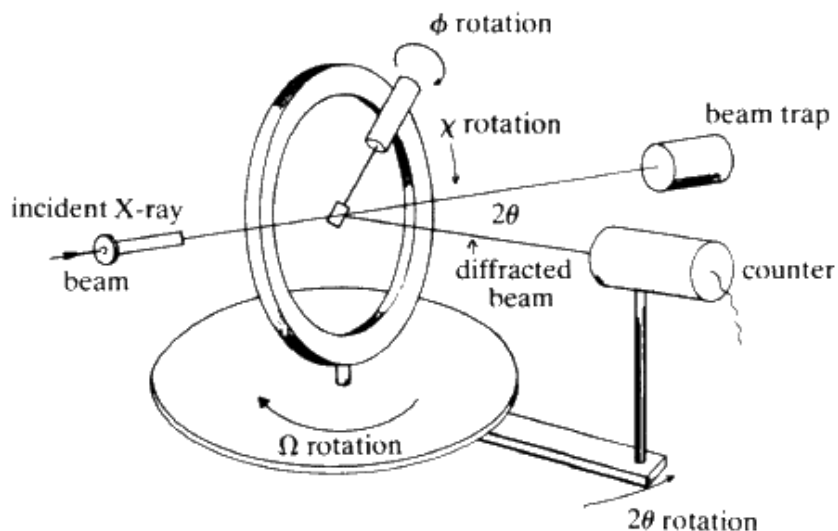


Figure 3.2: Schematic diagram of a four-circle diffractometer [2].

### 3.1.2 Powder X-ray Diffraction

In the powder X-ray diffraction technique, sample is assumed to contain an infinite number of extremely small crystals which randomly orient [2]. Each crystalline material has its own characteristic pattern thus powder X-ray diffraction was used for phase identification and impurity check. More detail on structure can be obtained by refinement; however, fine data collection and sample preparation are required.

All samples in this work were characterized by powder X-ray diffraction on a Rigaku MiniFlex II diffractometer using Cu  $K\alpha$  radiation and a graphite monochromator (Fig. 3.3). The MiniFlex II operates at fixed tube voltage of 30 kV and a fixed tube output current of 15 mA producing characteristic Cu  $K\alpha$  X-ray with 1.5406 Å wavelength [4]. This diffractometer is usually equipped with 6-sample

holder where 6 samples can be loaded at the same time. For phase identification purpose, sample was either dispersed in ethanol on the glass slide on top of the holder and dried in an oven or pressed on two-sided tape on top of the holder. The continuous scan from  $2\theta = 10-60$  was generally used for purity check. However, the step-scan with step size of 0.02 degree / 2 seconds per step from  $2\theta = 12-120$  was used to collect data for refinement purpose.



Figure 3.3: Rigaku MiniFlex II diffractometer (left) and the inner workings with X-ray tube, sample platform and detector labeled (right).

In addition to phase identification, more information on the sample can be interpreted from peak shape and intensity. Peak shape of powder X-ray diffraction pattern is mainly affected by crystallite size and strain in the lattice while the intensity of each reflection depends on scattering factor of the compositional elements and the number of hkl plane contributing to the reflection (multiplicity) [1]. These detailed data were obtained by structural refinement.

### 3.2 Powder Neutron Diffraction

Similar to X-ray, neutron has wavelength that is suitable for diffraction of crystals. Although X-ray is used in most of the crystal structure analyses, neutron diffraction has some advantages and can provide further information. In neutron diffraction, crystal such as Ge is used to filter neutron beam allowing only monochromatic wavelength to interact with the sample [2]. The major differences between X-ray and neutron diffraction is that X-ray is scattered by electron cloud in the elements while neutron interacts with nucleus. Neutron can therefore provide more information for light elements which do not scatter X-ray well enough to be detected especially in the presence of other heavier elements. For example, neutron diffraction is used to confirm oxygen content or oxygen position in many cases [5-6].

Neutron powder diffraction data in this work were collected using the BT-1 32-counter high-resolution diffractometer at the Center for Neutron Research at the National Institute of Standards and Technology (NIST). A Cu (311) monochromator, yielding a wavelength of 1.5401(2) Å, was employed. Collimation of 15' or 7' of arc was used before the monochromator, 20' before the sample, and 7' before the detectors. Samples were loaded into vanadium containers 10.8 mm in diameter and 50 mm in length. Data were collected at room temperature over a  $2\theta$  range of  $3^\circ$  to  $168^\circ$ .

### 3.3 Physical Property Measurement System (PPMS)

Most of the physical properties measured in this work were done on the Quantum Design Physical Property Measurement System (QD-PPMS) (Fig. 3.4). The PPMS provides a work station that can perform variety of measurements including AC/DC resistivity, AC/DC magnetism, and AC transport [7]. The measurement can be performed at temperature range of 1.9-400 K. The accuracy of temperature is about  $\pm 0.5\%$  and all measurements were done in vacuum.

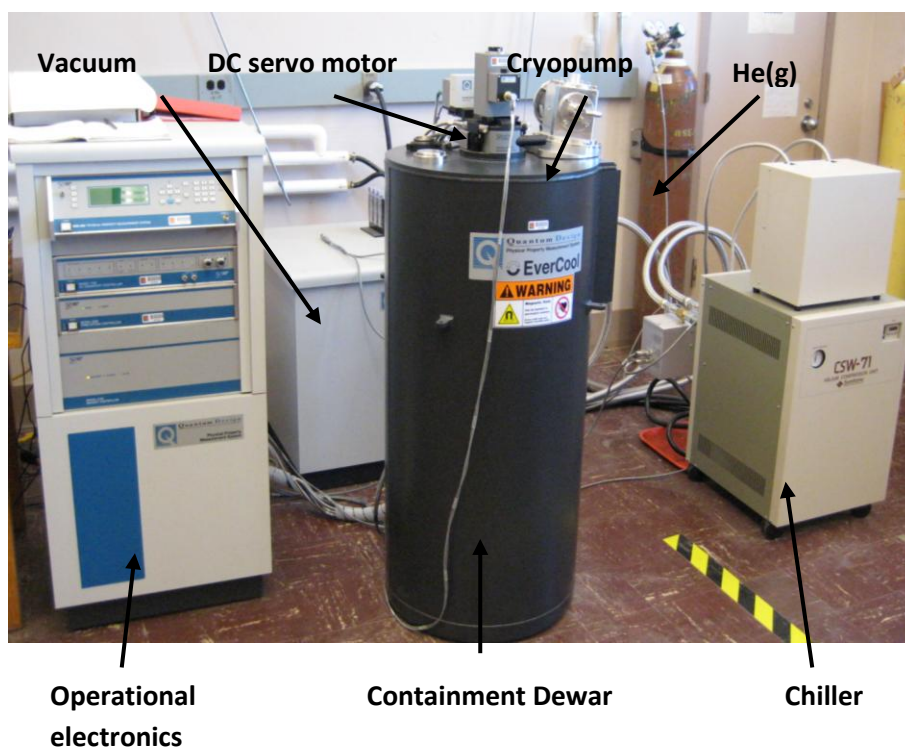


Figure 3.4: Quantum Design Physical Property Measurement System set up for ACMS measurements.

The PPMS used in this work is equipped with an EverCool system which liquefies He gas to He liquid and provides the He liquid to the PPMS for temperature control.

### **3.3.1 DC Electrical Resistivity**

Electrical resistivity is an important bulk property of the oxides. There are two ways to measure this property; two-probe and four-probe measurement. Since the contact resistance is included in two-probe measurement, it is mainly used to get preliminary result and more suitable for relatively resistive materials. On the other hand, four-probe method, where the lead and contact resistance are excluded, is required for more accurate measurements especially for highly conducting samples where the contact resistance could greatly affect real conductivity of the sample [2].

In four-probe method, four copper wires were attached to the bar-shaped samples using conductive silver paste. The other side of the wires was soldered to the puck which was loaded to the PPMS for the measurement (Fig.3.5). The geometry of the bar was input in the program to calculate resistivity from the obtained resistance raw data. Temperature range of about 50-300 K is used to obtain temperature variation of resistivity. Wider temperature range, 5-300 K, was used in some cases especially for superconductivity search.



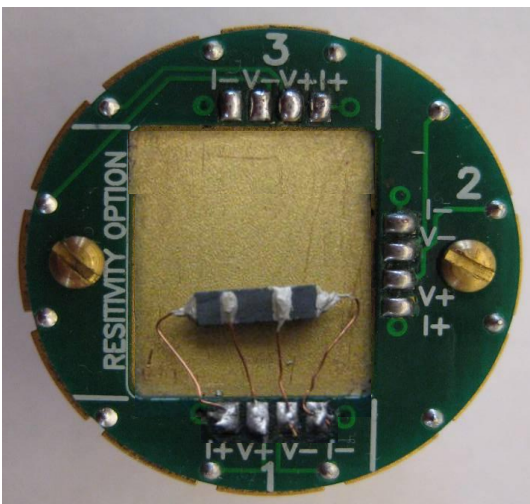


Figure 3.5: PPMS resistivity puck with a bar sample connected to position 1 using the four probe contact technique.

### 3.3.2 Magnetometry

PPMS can perform AC susceptibility and DC magnetization. DC magnetization is the main technique used in this work. Magnetic field is applied to the sample to induce a magnetization within the sample which is detected by magnetometry system as a voltage. A voltage signal depends on the magnetic moment and the vertical movement of the sample. Therefore, the samples are prepared as a sintered piece of pellet or well packed powder in the polycarbonate capsule to avoid any movement. The set up and the sample preparation are demonstrated in Figure 3.6. The other important factor is location of the sample with respect to the detection coils. Thus, it is necessary to locate the sample using a single point DC extraction. This allows the instrument to correct for the sample displacement when the DC servo motor is engaged.

For DC magnetization measurements, an applied field is necessary. Although the PPMS utilizes a superconducting magnet capable of magnetic fields as high as 7 Tesla, an applied field of 0.1 – 1 Tesla is generally sufficient for measurements. Temperature range of the measurement could vary from sample to sample. Therefore, some preliminary information of the magnetic interactions of the sample is recommended or more than one measurement is needed to obtain all useful data.

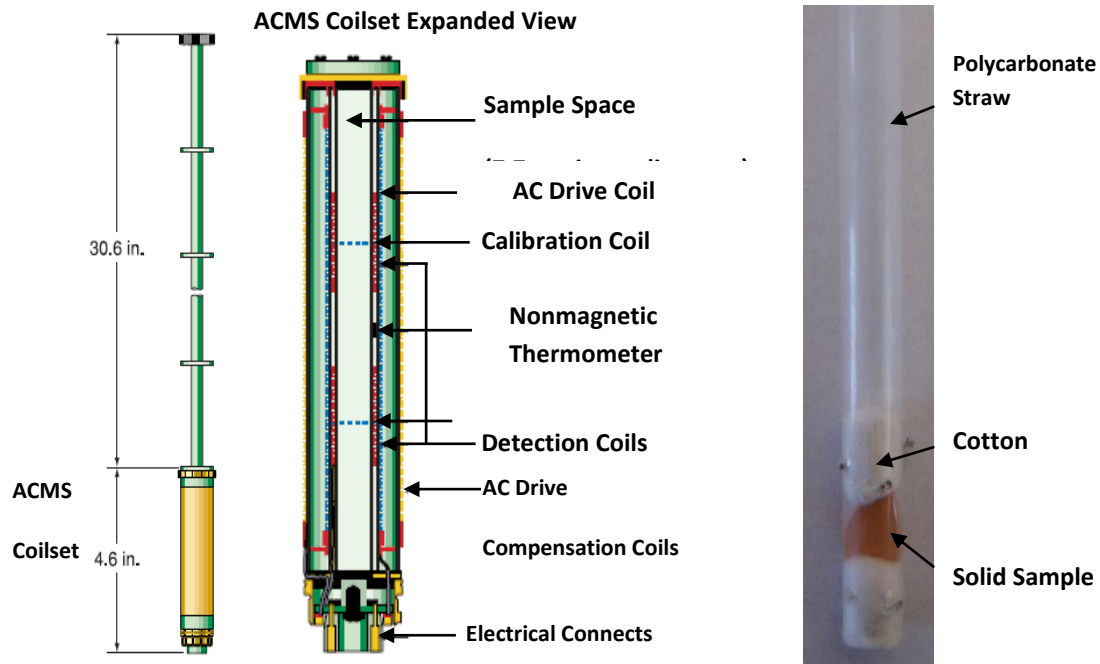


Figure 3.6: Representation of the ACMS coil set and tube assemblage (left), expanded view with labels of the ACMS coil set detection unit (center), and mounted ‘as prepared’ sample (right). ACMS coil set illustrations taken and modified from Quantum Design application notes [7].

### 3.4 Seebeck Coefficient

Seebeck coefficients ( $S$ ) measure the voltage difference when heat gradient is applied between two ends of the sample. The absolute values of Seebeck coefficients, in general, increase with the resistivity of the sample. Since grain boundary of the sample does not affect Seebeck coefficient, this technique is very useful to confirm the trend of resistivity in sintered polycrystalline samples where the resistivity obtained from the pellet could deviate from the accurate values because of the grain boundary and porosity.



Figure 3.7: Set up for Seebeck coefficient measurement. Sample pellet is put in between two silver electrodes.

All Seebeck coefficients in this work were performed on the sintered pellets using static method. The voltage was applied to the hot end of the samples through the metal block, silver in this case, to introduce heat gradient between two ends of the pellet (Fig. 3.7). The voltage across the two ends were measured and the Seebeck

coefficients were calculated using  $S = \Delta V/\Delta T$  relationship when  $\Delta V$  and  $\Delta T$  are voltage difference and temperature difference, respectively.

### 3.5 Thermoelectric Properties

#### 3.5.1 Seebeck Coefficient and Resistivity at High Temperature, ZEM-3

Temperature variations of Seebeck coefficient and electrical resistivity are measured simultaneously under inert atmosphere using the LVAC-RIKO ZEM-3 Thermoanalyzer as shown in Figure 3.8. The instrument consists of a measuring chamber and a controller. Inside a measuring chamber, a bar of sample is placed between two spring loaded Ni electrodes. Power is applied through the electrodes to generate heat gradient. Voltage across the sample as well as temperature are measured by two Pt probes touching the side of the bar (Fig.3.8(b)). Four electrodes; two at the two ends of the sample and two on the side, are used to obtain 4-probe resistivity.

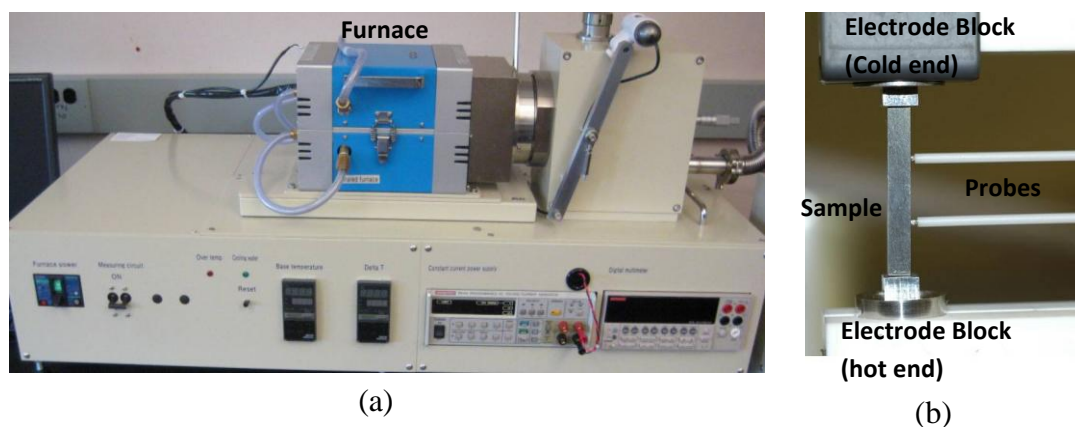


Figure 3.8: ZEM Thermoanalyzer (a) and sample in the measuring chamber (b).

### 3.5.2 Thermal Diffusivity Measurements, Netzsch MicroFlash®

As discussed earlier, figure of merit for thermoelectric materials depends on electrical conductivity, Seebeck coefficient as well as thermal conductivity. Thermal conductivity,  $\lambda$ , is equal to

$$\lambda(T) = a(T) * C_p(T) * \rho(T)$$

where  $a$ ,  $C_p$  and  $\rho$  are thermal diffusivity, specific heat, and density of the sample, respectively. To determine thermal conductivity,  $a$ ,  $C_p$ , and  $\rho$  were measured using various methods.

Thermal diffusivity was measured on sintered pellets using Netzsch MicroFlash® as shown in Figure 3.8. A short laser pulse was used to heat the front side of the sample pellet. The absorbed heat propagates through the sample and increases temperature on the rear surface of the pellet which is measured versus time by an infrared detector. The laser used in this instrument is Nd-YAG with maximum pulse energy of 18.5J and a pulse length of 0.5ms. Measurements at various temperatures can be performed as the instrument is equipped with two interchangeable furnaces which allow the measurements to be done between -125°C-1000°C. The limit range of measurement in Netzsch MicroFlash® is for materials with thermal diffusivity between 0.01mm<sup>2</sup>/s to 1000mm<sup>2</sup>/s.

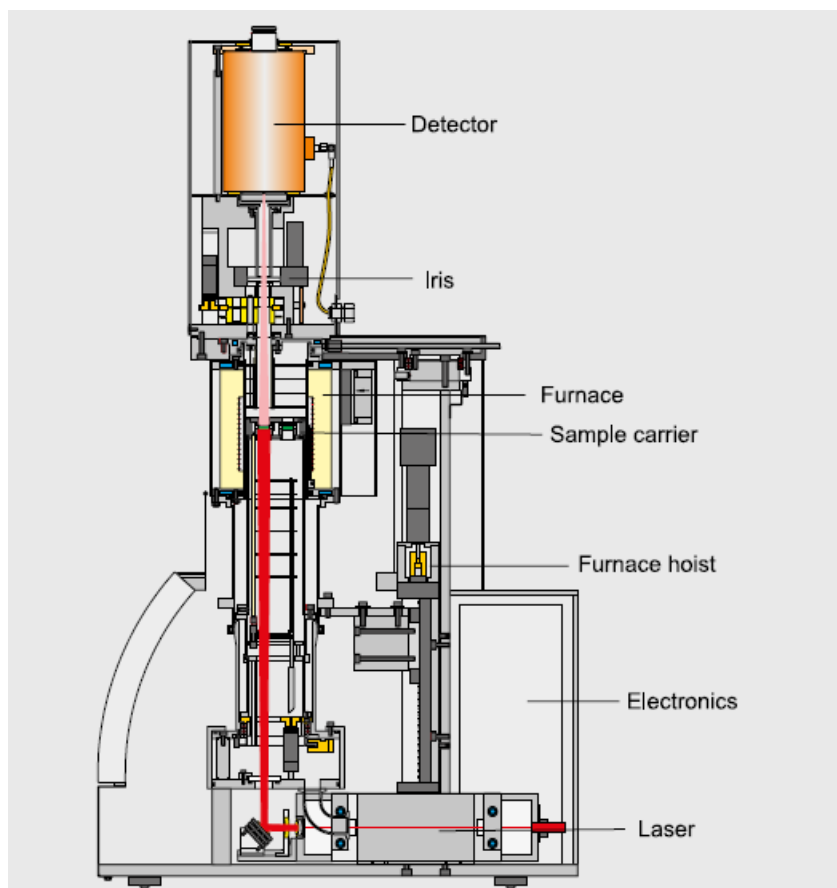


Figure 3.9: Instrument design for Netzsch MicroFlash<sup>®</sup> [8].

### 3.5.3 Specific Heat Measurements, DSC

Differential scanning calorimetry (DSC) measures the difference of heat required to raise temperature of the sample and the reference material as a function of temperature. Sample and the reference are kept in two separate small pans on top of two separate heaters. During the measurement, heating rates of both pans are programmed to be the same. However, amount of heated needed to raise temperature of the two pans to meet the required heating rate are different. This difference is then

interpreted to yield heat capacity. Mettler DSC was used in this work which performed DSC measurement in the range 25°C-400°C using aluminum pans. Sapphire was used as a standard material and STARE program package was used to calculate specific heat of the sample.

### **3.6 Thermogravimetric Analysis; TGA**

Thermogravimetric analysis analyzes the change of weight of the sample with time or temperature [9]. The instrument used in this work is Metler Toledo TGA 850. Only small amount of sample, in the order of mg, is put in a small alumina pan which is put on a micro balance. The initial weight is recorded and the heating profile can be set up to as high as 1100°C with different heating rate. Inert gas, N<sub>2</sub> in this work, is used as a protective gas for all runs to protect the balance. The analysis can be done in air or specific atmosphere by flowing the reactive gas whose rate can also be controlled. The output data are plotted between weight and temperature or running time. Weight loss and decomposing temperature are used for further interpretation. Quantitative analysis can be performed accurately where the weight loss is used to calculate the initial composition or to determine the decomposition reaction.

### **3.7 Dielectric Measurement**

Dielectric property is one of the important electrical properties. In this work, capacitance and loss tangent measurements were taken on HP 4284 LCR meters. Surfaces of the pellets were polished and coated with conductive silver paint. Before measurements, an open (air) and short (copper pellet) correction were performed to

normalize the instrument to the approximate thickness of the samples. The pellets with known surface area and thickness were then put in between parallel plates and capacitance measurements were performed at fixed frequencies of 1, 10, 100, 500, 1000 kHz. The measurements were done in temperature range 25-300°C and the set up is shown in Figure 3.10.



Figure 3.10: Dielectric set up with LCR meter (left) and two parallel electrodes (right).

### 3.8 Optical Measurement

Diffused reflectance of powder samples were measured in Dr. David McIntyre's lab in OSU Physics Department. Light from a light source is passed through a bifurcated Y-shaped optical fiber assembly (Fig. 3.11 inset shows the end of such a wire with blue spheres as the light output) onto the sample and back into the bifurcate optical fiber (Figure 3.11 inset center white circle) where it is taken to a spectrophotometer [10-11]. MgO or BaSO<sub>4</sub> was used a light reference.



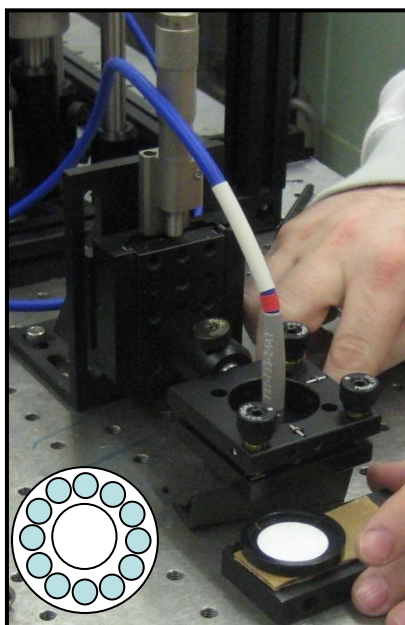


Figure 3.11: Illustration of a fiber optic system used in diffuse reflectance measurements (inset is an illustration of the end of a fiber optic cable). A standard sample of  $\text{BaSO}_4$  can be seen, bottom right.

### 3.9 References

1. B. D. Cullity, S. R. Stock, 'Elements of X-ray Diffraction', 3<sup>rd</sup> ed., Prentice-Hall, Inc., (2001).
2. A. K. Cheetam, P. Day, 'Solid-State Chemistry: techniques', Oxford University Press, (1987).
3. G.M. Sheldrick, SHELEXTL, Version 6.14, Bruker Analytical X-ray Instruments, Inc., Madison, WI, 2003.
4. Rigaku Corporation, 'X-Ray Diffractometer MiniFlex II Instruction Manual', 2<sup>nd</sup> ed., Rigaku Corporation, (2006).
5. J. E. Greedan, A. O'Reilly, C. V. Stager, *Phys. Rev. B*, **35** (1987), 8770.
6. B. C. Tofield, W. R. Scott, *J. Solid State Chem.*, **10** (1974), 183.
7. Quantum Design. 'Physical Property Measurement System Hardware and Operations Manual', 2<sup>nd</sup> Ed., Quantum Design, (1999).
8. <http://www.netzsch-thermal-analysis.com/en/products/detail/pid,26,t,6.html>
9. A. R. West, 'Solid State Chemistry and Its Applications', John Wiley & Sons: New York, (1984).
10. R. Kykyneshi. M.S. Thesis, Oregon State University, Corvallis, OR, 2004

11. Ocean Optics, Inc. "We Make A Fiber For That!" Ocean Optics, Inc. <http://www.oceanoptics.com/Products/opticalfibers.asp>. Accessed May 2010.

## Chapter

### 4. Electronically Conducting Tellurium Oxide Pyrochlores

#### 4.1 Abstract

Our exploratory synthesis of mixed valence oxides of tellurium has produced many new defect pyrochlore-type phases containing  $\text{Te}^{4+}$  and  $\text{Te}^{6+}$ . Compounds with the general formula,  $\text{Cs}(\text{M},\text{Te})_2\text{O}_6$  ( $\text{M} = \text{Al}, \text{Ga}, \text{Cr}, \text{Fe}, \text{Co}, \text{In}, \text{Ho}, \text{Lu}, \text{Yb}, \text{Er}, \text{Ge}, \text{Rh}, \text{Ti}, \text{Zn}, \text{Ni}, \text{and Mg}$ ) have been synthesized by solid state reaction. X-ray diffraction studies indicated that they crystallize in a cubic defect pyrochlore structure (space group:  $Fd\bar{3}m$ ). M and Te cations randomly occupy octahedral sites (16c sites) and Cs occupy O' sites (8b) in  $\text{A}_2\text{B}_2\text{O}_6\text{O}'$  pyrochlore. The samples were highly colored (ranging from black to dark green) indicating a possible mixed valency for Te with appreciable charge transfer between them in the octahedral sites. Electronic conductivity was observed in some phases and could be as high as 2S/cm ( $\text{M}=\text{Ge}$ ). Seebeck coefficients of conducting samples showed negative values which suggested that electrons are the major charge carriers. Temperature dependence of conductivity indicates that the samples are semiconductors with, in some cases, degenerate semiconducting behavior.

In order to investigate this conduction mechanism,  $\text{Cs}(\text{Al},\text{Te})_2\text{O}_6$  with various Al:Te ratio have been studied in detail. Results from structural refinements on powder neutron diffraction, powder X-ray diffraction, and single crystal X-ray diffraction data showed that Al:Te ratio could be varied. The variations in cell edge for Cs/Al/Te/O

phases range from 10.06 Å for the Al rich limit to 10.14 Å for the Te rich phase. A maximum in the electrical conductivity of about 0.1 S/cm was found in the middle of this range close to the ideal composition of  $\text{CsAl}_{0.33}\text{Te}_{1.67}\text{O}_6$ . Changes of cell parameters and conductivities were explained by two mechanisms. When Al content is less than ideal value, some  $\text{Te}^{6+}$  are reduced to  $\text{Te}^{4+}$  where electron transfer between the two species results in the color and conductivity. However, for compositions with  $\text{Al} > 0.33$ , extra  $\text{Te}^{4+}$  occupy the interstitial sites of the structure giving rise to the color but the difference between two sites limits the electron transfer and thus the conductivity.

Polycrystalline samples of  $\text{Rb}(\text{M},\text{Te})_2\text{O}_6$  with cubic pyrochlore structure were prepared and characterized and single crystal of  $\text{RbAl}_{0.33}\text{Te}_{1.67}\text{O}_6$  was grown using  $\text{TeO}_2$  flux. Unit cell parameters of  $\text{Rb}(\text{M},\text{Te})_2\text{O}_6$  are smaller than the Cs analogs as expected. Any present  $\text{Te}^{4+}$  would be more compressed in such small lattices which should result in more conducting samples; however, the observed lighter color and lower electrical conductivity suggest that there is relatively less  $\text{Te}^{4+}$  in these compounds, if any. More studies are required to understand this system.

## 4.2 Introduction

### 4.2.1 Crystallography of the Pyrochlores

Among all ternary oxides, pyrochlore oxides with the general formula  $A_2B_2O_7$  are known. The structure is named after the mineral pyrochlore,  $(NaCa)(NbTa)O_6F/(OH)$  (Fig.4.1), which was first described in 1826 [1]. A wide range of cations can be substituted into A and B sites leading to hundreds different compositions with various properties. Moreover, pyrochlore structure has a high tolerance to vacancies. Therefore, defect pyrochlores with vacancies in A and/or O sites are formed leading to even more variety of compounds in this family.

The general formula of pyrochlore oxides can be written as  $A_2B_2O_6O'$  which clearly represents four different crystallographic sites in the structure. Pyrochlore structure is cubic with  $Fd\bar{3}m$  space group and 8 molecules per unit cell ( $z=8$ ). Since there are four different crystallographic sites, there are four choices of origin. The common origin used in literatures is the B cation which is used here. The crystallographic information is shown in Table 4.1. Oxygen x parameter can be determined by X-ray or neutron structural analysis and the value is limited to 0.3125-0.375 [2].

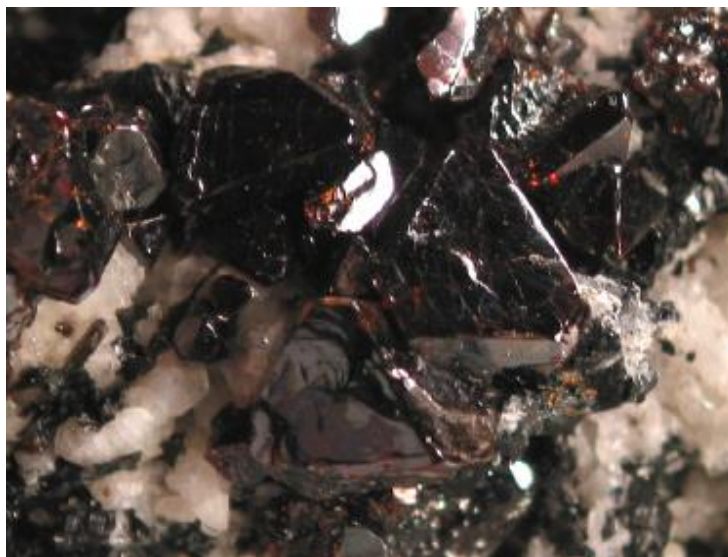


Figure 4.1: Pyrochlore mineral [3].

Table 4.1: Pyrochlore Structure Data (Origin at B site) [after ref.2].

| Ion | Location | Site symmetry       | Coordinates   |
|-----|----------|---------------------|---|
|     |          |                     | $(0,0,0; 0, \frac{1}{2}, \frac{1}{2}; \frac{1}{2}, 0, \frac{1}{2}; \frac{1}{2}, \frac{1}{2}, 0) +$  |
| 16A | 16d      | $\bar{3}m (D_{3d})$ | $\frac{1}{2}, \frac{1}{2}, \frac{1}{2}; \frac{1}{2}, \frac{1}{4}, \frac{1}{4}; \frac{1}{4}, \frac{1}{2}, \frac{1}{4}; \frac{1}{4}, \frac{1}{4}, \frac{1}{2}$  |
| 16B | 16c      | $\bar{3}m (D_{3d})$ | $0,0,0; 0, \frac{1}{4}, \frac{1}{4}; \frac{1}{4}, 0, \frac{1}{4}; \frac{1}{4}, \frac{1}{4}, 0$  |
| 48O | 48f      | $mm(C_{2v})$        | $x, \frac{1}{8}, \frac{1}{8}; \bar{x}, \frac{7}{8}, \frac{7}{8}; \frac{1}{4}-x, \frac{1}{8}, \frac{1}{8}; \frac{3}{4}+x, \frac{7}{8}, \frac{7}{8};$<br>$\frac{1}{8}, x, \frac{1}{8}; \frac{7}{8}, \bar{x}, \frac{7}{8}; \frac{1}{4}-x, \frac{1}{8}, \frac{7}{8}; \frac{3}{4}-x, \frac{7}{8};$<br>$\frac{1}{8}, \frac{1}{8}, x; \frac{7}{8}, \frac{7}{8}, \bar{x}; \frac{1}{8}, \frac{1}{8}, \frac{1}{4}-x; \frac{7}{8}, \frac{7}{8}, \frac{3}{4}+x$ |
| 8O' | 8b       | $\bar{4}3m(T_d)$    | $\frac{3}{8}, \frac{3}{8}, \frac{3}{8}; \frac{5}{8}, \frac{5}{8}, \frac{5}{8}$  |

x value for other origins can be obtained by the following relationships:

$$x(A_0) = \frac{3}{4} - x(B_0), x(\square_0) = \frac{1}{2} - x(O'_0), x(O_0) = x(A_0) - \frac{1}{8}, x(\square_0) = \frac{5}{8} - x(A_0)$$

In any case x may be replaced with  $\frac{1}{4}x$

## 4.2.2 Description of Pyrochlore Structure

There are many ways to describe pyrochlore structure. Three different views based on the defect fluorite structure [4-6], the interpenetrating networks of  $B_2O_6$  and  $A_2O'$  [7], and the interpenetrating networks of tetrahedral  $B_4\Box$  and  $A_4O'$  [8] are discussed in the following sections.

### 4.2.2.1 Description Based on Defect Fluorite Structure [2, 4-6]

In this description, A and B cations in  $A_2B_2O_7$  pyrochlore form a face centered cubic array whose tetrahedral holes are occupied by anions. A and B cations are ordered in alternate  $[110]$  direction in every other  $(001)$  plane and in alternate  $[\bar{1}10]$  direction in the other  $(001)$  plane as shown in Figure 4.2(a). This ordering results in three kinds of tetrahedral interstitial sites for anions: 48f position coordinated by two A and two B cations, 8a position coordinated by four B cations, and 8b position coordinated by four A cations (Fig. 4.2(a)). As shown in Table 4.1, oxygen anions only occupy 48f and 8b sites while 8a positions are left vacant. In order to reduce the electrostatic repulsion between four surrounding B cations, 48f anions displace from the center of their tetrahedral (Fig. 4.2(b)). 48f anions shift from the original position,  $x=0.375$ , toward  $x=0.3125$  position where B cations will be in perfect octahedra sharing corners along  $[110]$  direction (Fig. 4.3). As a result, the B-O-B angle along this direction increases from  $109^\circ 28'$  to about  $132^\circ$ . However, the 8b anions remain in the original tetrahedral position. A sub array,  $A_2O'$ , that is isostructural to one of the

two networks in anticrostobalite structure ( $\text{Cu}_2\text{O}$ ) is formed from the 8b anions and A cations in 16d positions.

This description is suitable when  $x$  value is close to 0.375 which is normally the case for pyrochlore oxides with large B cations. The model also explains the connection between pyrochlore and defect fluorite structure. The close relationship between the two structures is obvious as transition of pyrochlore to defect fluorite is observed in  $\text{A}_2\text{B}_2\text{O}_7$  with large B cations [2].

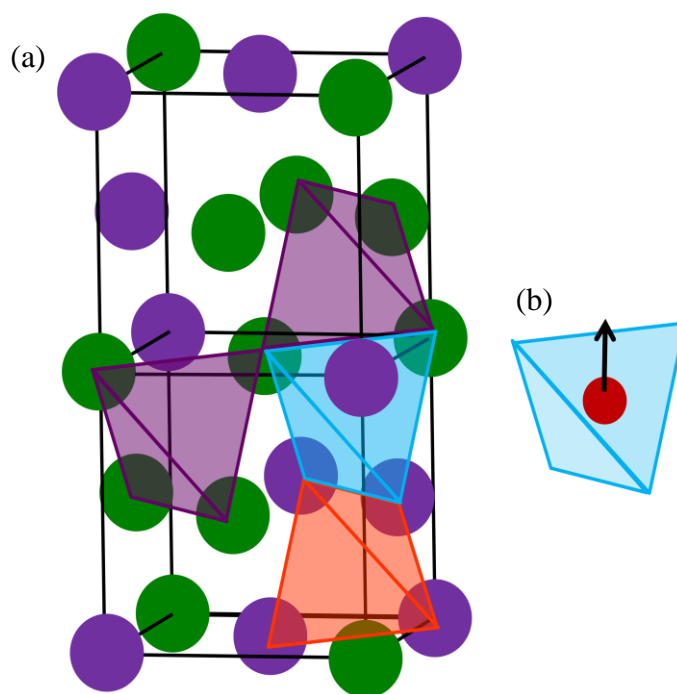


Figure 4.2: (a) Pyrochlore structure as derived from a fluorite lattice (anions are removed for clarity). Purple, blue, and orange tetrahedra represent the 8a, 48f, and 8b anion position, respectively. (b) Example of 48f anion shifting toward 8a vacant site to reduce electrostatic repulsion between four B cations.



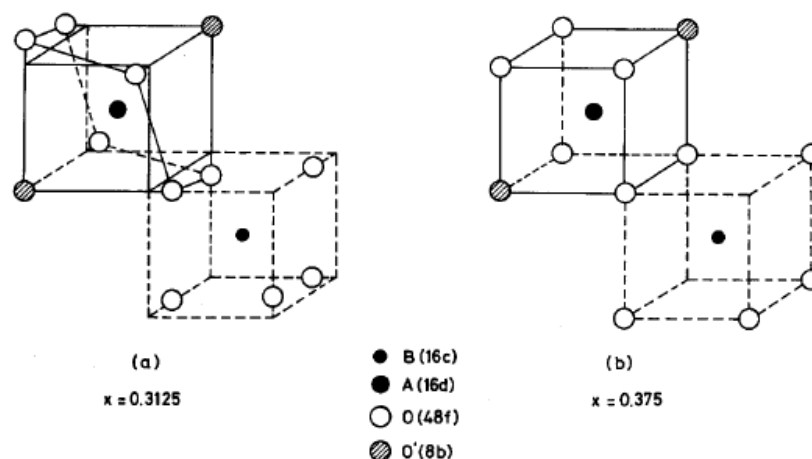


Figure 4.3: Change in shape of coordination polyhedral of A and B ions with 48f oxygen parameter  $x$  in  $A_2B_2O_6O'$  structure. Coordination around B becomes a regular octahedron from  $x=0.3125$  ( $5/16$ ) and for  $x=0.375$  ( $3/8$ ) the coordination around A becomes a regular cube. [2,9]

#### 4.2.2.2 Description Based on Interpenetrating Networks of $B_2O_6$ and $A_2O'$ [2,7]

In pyrochlore oxides, each B cation is surrounded by six oxygen anions forming an octahedron. These octahedra share corners with each other to form tetrahedral groups as shown in Figure 4.4. Each A cation is surrounded by eight oxygen anions which include six of O and two of O'. However, the A-O' distance is always much smaller than A-O distance. As a consequence, A-O interaction can be neglected and the structure is described as the interpenetrating networks of  $B_2O_6$  octahedra and  $A_2O'$  chains.

This  $A_2O'$  network is identical with one observed in  $Cu_2O'$  anticristoballite where A cations is in linear coordination. Two of zig-zag chains formed from A-O' linkage intersect at O'. Therefore, each O' in the chain is coordinated by four A

cations in tetrahedral arrangement with A-O'-A angle of  $109^{\circ}28'$ . The A-O' distance is obtained from unit cell parameters and is unaffected by any positional parameters.

B cations in  $B_2O_6$  network are in distorted octahedral coordination while O anions are linearly coordinated. The octahedra become more regular when x approach 0.3125. The deviation from this value determines the distortion of the octahedral network. There is no significant interaction between the networks since the shortest internetwork distance, A-O, is still much longer than any intranetwork separations. This description is suitable for most pyrochlore compounds and it supports the existences of defect pyrochlore  $\square AB_2O_6\square$  and  $A_2B_2O_{7-x}\square_x$  where  $B_2O_6$  network form the 'back bone' of the structure. However, it neglects the importance of A and O' ions although A cations do affect the formation of the compounds [2].

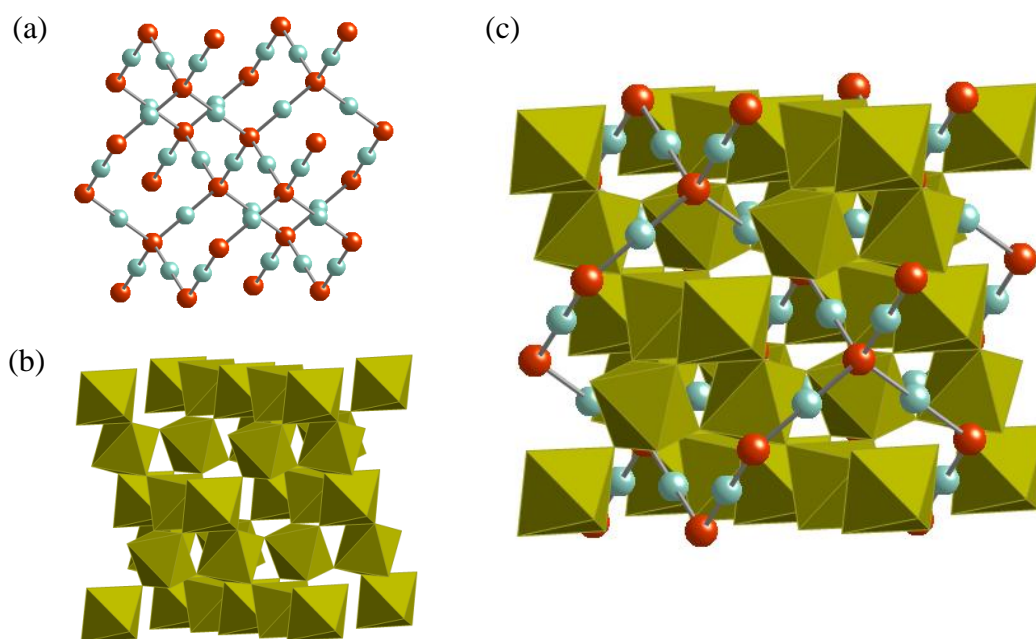


Figure 4.4: (a)  $A_2O'$  chain, (b)  $M_2O_6$  octahedral network, (c) pyrochlore structure

#### 4.2.2.3 Description Based on Anticristobalite [8]

B cations in pyrochlore connect to each other through oxygen in a tetrahedral way with vacant space in the center (Fig. 4.5(a)). Each B cation is coordinated by 6 oxygens to form octahedral arrangement.  $B_4$  tetrahedra share a vertex to form  $B_{4/2}O_6$  network as observed in cristobalite  $SiO_2$  with space group  $Fd\bar{3}m$ . This network interpenetrates with the anticristobalite-like  $A_2O'$  chain. Each A cation is coordinated by four oxygens forming a tetrahedron (Fig. 4.5(b)), each of which share corners to form 3-dimensional network. The interpenetration of these two networks results in pyrochlore structure. Distortion of  $BO_6$  octahedron depends on structural parameter  $x$ . A regular octahedron is formed at  $x=0.3125$  and the compression and dilation toward 3-fold axis occur when  $x>0.3125$  and  $x<0.3125$ , respectively [2]. This description gives importance to  $x$  parameter since it determines coordinations of the two cations. Moreover, the model gives more importance to  $O'$  anion in 8b sites which undergoes  $sp^3$  hybridization and it is therefore coordinated by four A in a tetrahedron. Since the structure is closely related to cristobalite  $SiO_2$ , deviations from overall cubic symmetry might be analogous to the polymorphs of  $SiO_2$ . When A cations are  $d^{10}$ , which often form  $sp^3$  hybridization, the A- $O'$  bonds become stronger and the A-O distance increases to give lower  $x$  value (approaching 0.3125). If A- $O'$  bond strength is still higher, the regular octahedra may distort in other direction (dilation along the 3-fold axis). This distortion will further decrease  $x$  value to less than 0.3125, the value for regular octahedral. The major drawback of this model is that it does not support the formation of defect pyrochlores.

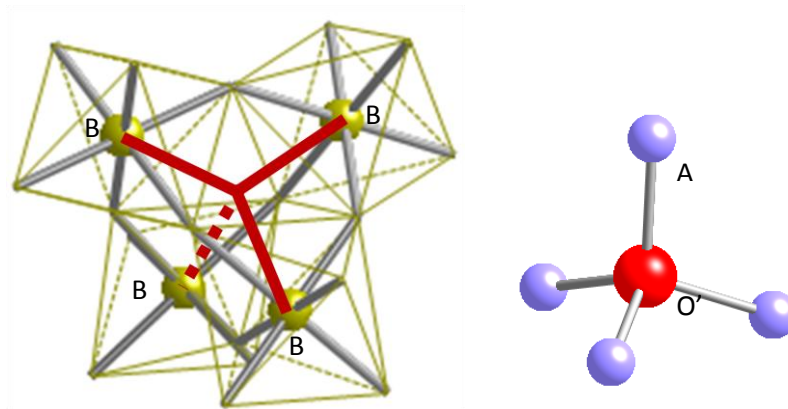


Figure 4.5: The arrangement in  $B_{4/2}O_6$  network (a) and  $A_2O'$  network (b) in pyrochlore structure.

### 4.2.3 Defect Pyrochlores

As mentioned earlier, pyrochlore structure tolerates vacancies and many types of defect pyrochlore oxides are known including  $A_2B_2O_6$  or  $A_2B_2O_{7-y}$  with vacancies at  $O'$  sites and  $AB_2O_6$  with vacancies at both A and  $O'$  sites. Most of  $A_2B_2O_6$  oxides form perovskite structure but pyrochlore structure is preferred when A and B ions are highly polarizable but not very electropositive leading to strong covalent bonds in A-O and/or B-O [2]. Some examples are  $Tl_2Nb_2O_6$  [10],  $Pb_2Ru_2O_6$  [5], and  $Bi_2Rh_2O_6$  [11]. Partial vacancies at  $O'$  sites are possible which will result in  $A_2B_2O_{7-y}$  such as  $Pb_2Ru_2O_{6.5}$  [12] and  $Tl_2Nb_2O_{6.64}$  [13].

$A^{1+}B_2O_6$  defect pyrochlores are well known. To keep the charge balanced, F is substituted into O sites or combination of aliovalent cations are simultaneously substituted in B sites. While there are 3 ions in  $A_2O'$  chain for  $A_2B_2O_6O'$  pyrochlores, two of them are vacant in  $AB_2O_6$ . Consequently, the only A cation can occupy various crystallographic sites depending on its ionic radius and polarizability. These possible sites include 32e, 8b, and 16d as shown in Figure 4.6. Small cation like Na prefers 16d

site [14] while K, Rb, and Cs usually occupy 8b or 32e position [15-16]. H<sub>2</sub>O is frequently found in these interstitial sites when A cation is small [17]. Because the rigid network of B<sub>2</sub>O<sub>6</sub> octahedra prevents the collapse of the structure, A cation can sometimes move through the tunnel resulting in high cation mobility. As a result, the compounds can show high ionic conductivity especially when A is relatively small. For example, K(Al,W)<sub>2</sub>O<sub>6</sub> has ionic conductivity of  $5.2 \times 10^{-3}$  S/cm at 300 °C [18]. The strong interaction within octahedra framework and the high mobility of A cation in AB<sub>2</sub>O<sub>6</sub> are emphasized by the existence of WO<sub>3</sub> with pyrochlore-like structure. The compound was prepared by ionic exchange of (NH<sub>4</sub><sup>+</sup>)<sub>0.5</sub>W<sub>2</sub>O<sub>6</sub> in acidic solution resulting in W<sub>2</sub>O<sub>6</sub>.xH<sub>2</sub>O which was dehydrated to yield the stable W<sub>2</sub>O<sub>6</sub> pyrochlore network [19]. Ion exchange is also used to prepare many other pyrochlores.

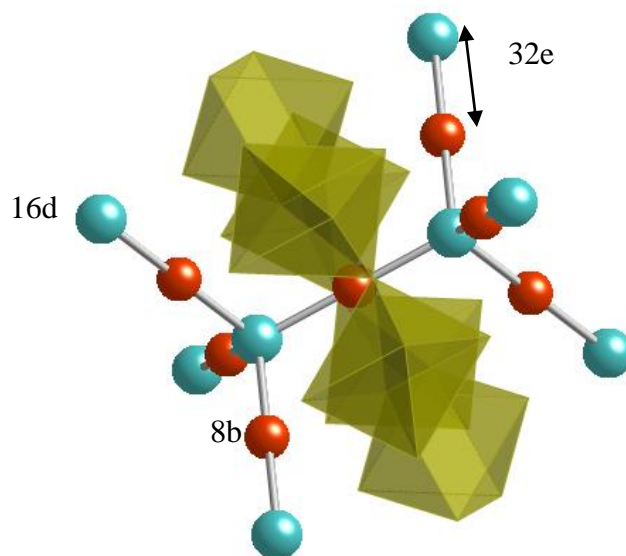


Figure 4.6: Crystallographic sites for A cation in AM<sub>2</sub>O<sub>6</sub> defect pyrochlore. Ball and stick model shows the arrangement of A<sub>2</sub>O' chain where the polyhedral represent B<sub>2</sub>O<sub>6</sub> octahedral network.

#### 4.2.4 Pyrochlore Oxides and Their Applications

The biggest family of pyrochlore oxides is  $A^{3+}_2B^{4+}_2O_7$  where  $A^{3+}$  can be some members of group IIIA elements,  $Bi^{3+}$ ,  $Sc^{3+}$ ,  $Y^{3+}$ , and all the rare earth elements;  $B^{4+}$  can be group IVA except C, most of  $3d$ ,  $4d$ , and  $5d$  elements whose  $4+$  oxidation state are stable [2]. There are fewer compounds with  $A^{2+}_2B^{5+}_2O_7$  formula because there is less availability of suitable  $A^{2+}$  and  $B^{5+}$ . Figure 4.7 represents diagrams of some possible substitutions at A and B sites for  $A^{3+}_2B^{4+}_2O_7$  (Fig. 4.7(a)) and  $A^{2+}_2B^{5+}_2O_7$  (Fig. 4.7(b)) [2]. Several complex substitutions involving many different ions at both cation and anion sites are also reported.

Pyrochlore oxides are used in many applications. Some have been used commercially and some have potential to be applied. Dupont-Birox<sup>®</sup> thick film resistor based on  $Bi_2Ru_2O_7$  is commercially used in many modern microelectronic devices because of its high stability and low temperature coefficient of resistance [20-21].  $Ca(U,Pu)Ti_2O_7$  pyrochlore and  $Ca(ZrTi_2O_7)$  pyrochlore-related oxides are the major components of Synroc, a synthetic rock used to immobilized nuclear waste such as U and Th [22-23]. In immobilization, radio nuclides are incorporated to form stable solid solutions with pyrochlores [16].

In additions, many pyrochlore oxides show interesting properties that can lead to useful applications in the future. For example,  $Pb_2[Ru_{1.5}Pb_{0.5}]O_{7-y}$  has a potential to be an electrode in NO/NO<sub>2</sub> sensor [24] and  $Gd_2Ti_2O_7$  shows suitable properties for a promising electrolyte material in solid oxide fuel cells [25].

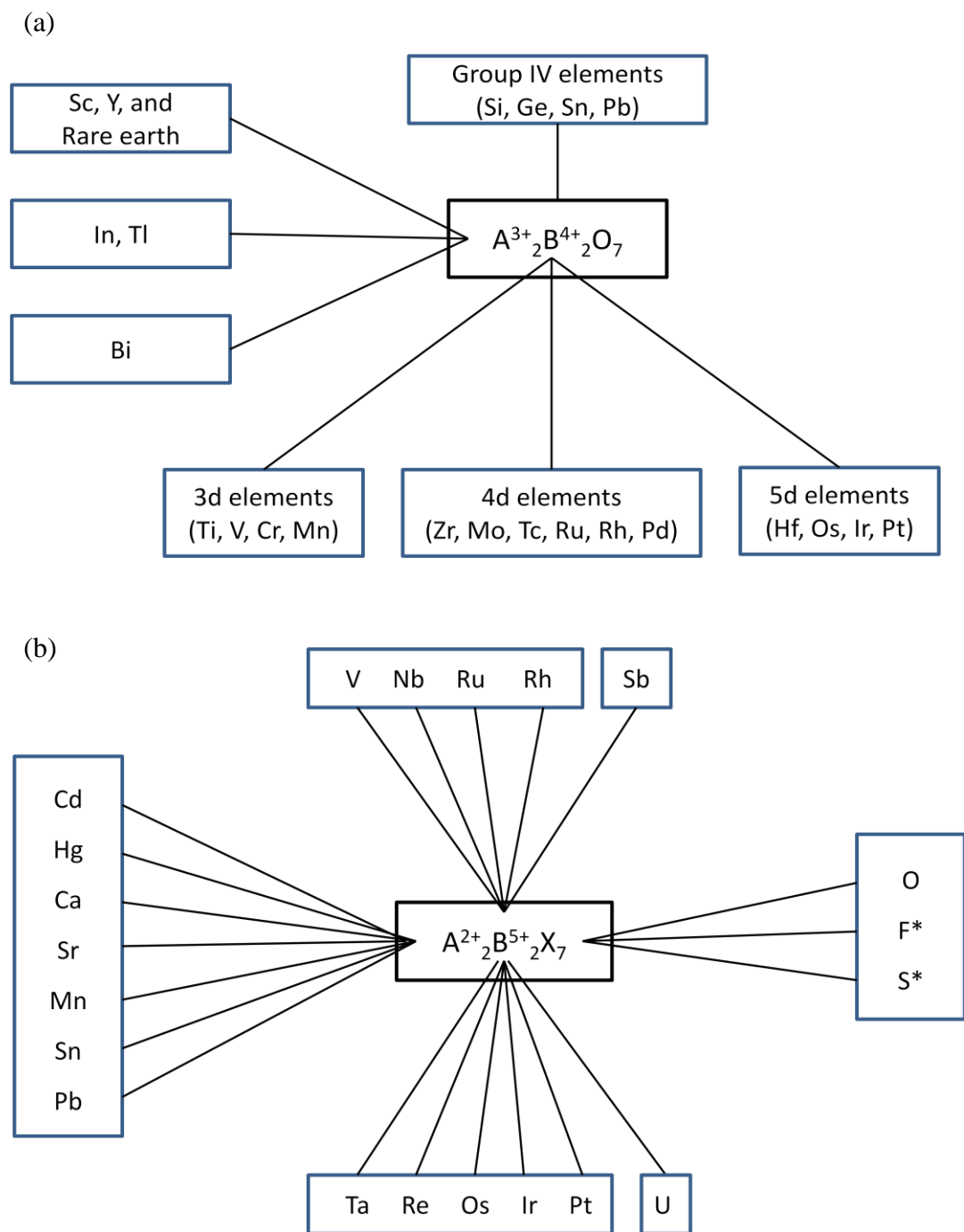


Figure 4.7: Possible substitutions at A and B sites of  $A^{3+}_2B^{4+}_2O_7$  (a) and  $A^{2+}_2B^{5+}_2O_7$  (b). \* indicates that only partial substitution is possible [2].

#### 4.2.5 Tellurium Oxide Pyrochlores

Only few Tellurium oxides with  $A_2B_2O_7$  normal pyrochlore structure are known, all of which contain only  $Te^{4+}$ . Single crystal of  $Pr_2Te_2O_7$  was investigated by Weber and Schleid [26] and  $Ln_2Te_2O_7$  where  $Ln = La, Nd, Eu,$  and  $Gd$  were later reported by Ismunandar *et al.* [27]. The special feature of these compounds is that they form cubic structure despite of the lone pair electrons on  $Te^{4+}$ .

To best of our knowledge, the only Te containing oxide known to crystallize in  $A_2B_2O_6$  pyrochlore is  $M_2GeTeO_6$  where  $M = K, Rb, Cs$ . The refinement from polycrystalline sample showed that M cation is in 32e sites instead of the normal 16d site [28]. Partial vacancies at O' sites results in  $A_2M_2O_{7-x}$  formula such as  $Pb_2(M_{1.5}Te_{0.5})O_{6.5}$ ,  $M = Ti, Zr, Sn,$  and  $Hf$  with O' occupying half of the 8b sites [29].

Most of tellurium containing pyrochlore oxides adopt defect pyrochlore structure with general formula  $AB_2O_6$  where A is univalent cation such as  $K^{1+}, Rb^{1+}, Cs^{1+},$  and  $Tl^{1+}$ . The average charge on M site becomes 5.5 and Te is usually mixed with other aliovalent cations as shown in Table 4.2. Some other variations are  $Rb_{1.5}Cr_{0.5}Te_{1.5}O_6$  where  $Rb^{1+}$  randomly occupies 3/8 of 32e site [40] and  $K_{1.5}Cr_{0.5}Te_{1.5}O_6 \cdot 0.5H_2O$  [42].



Table 4.2: Tellurium oxides with AB<sub>2</sub>O<sub>6</sub> defect pyrochlore structure

| Composition   | Unit cell parameter (Å) | References |
|---|-------------------------|------------|
| <b>AM<sup>4+</sup><sub>0.5</sub>Te<sub>1.5</sub>O<sub>6</sub></b> |                         |            |
| KTi <sub>0.5</sub> Te <sub>1.5</sub> O <sub>6</sub>               | 10.0597(3)              | [30]       |
| RbTi <sub>0.5</sub> Te <sub>1.5</sub> O <sub>6</sub>              | 10.0903(2)              | [30]       |
| CsTi <sub>0.5</sub> Te <sub>1.5</sub> O <sub>6</sub>              | 10.1346(2)              | [30]       |
| TiTi <sub>0.5</sub> Te <sub>1.5</sub> O <sub>6</sub>              | 10.0930(3)              | [30]       |
| <b>AM<sup>5+</sup>TeO<sub>6</sub></b>                             |                         |            |
| (H <sub>3</sub> O)SbTeO <sub>6</sub>                              | 10.1510(1)              | [31,33]    |
| NaSbTeO <sub>6</sub>  | 10.292                  | [32]       |
| KSbTeO <sub>6</sub>   | 10.1133(2)              | [32-34]    |
| RbSbTeO <sub>6</sub>  | 10.156(2)               | [32-34]    |
| CsSbTeO <sub>6</sub>  | 10.22                   | [32-34]    |
| TlSbTeO <sub>6</sub>  | 10.145(5)               | [32-34]    |
| AgSbTeO <sub>6</sub>  | 10.230(2)               | [33]       |
| NaNbTeO <sub>6</sub>  | 10.585                  | [35]       |
| KNbTeO <sub>6</sub>   | 10.24                   | [35-36]    |
| RbNbTeO <sub>6</sub>  | 10.26                   | [35-36]    |
| CsNbTeO <sub>6</sub>  | 10.30                   | [35-36]    |
| TlNbTeO <sub>6</sub>  | 10.26                   | [35-36]    |
| K <sub>0.5</sub> Tl <sub>0.5</sub> NbTeO <sub>6</sub>             | 10.2528                 | [37]       |
| Rb <sub>0.5</sub> Tl <sub>0.5</sub> NbTeO <sub>6</sub>            | 10.2553                 | [37]       |
| Cs <sub>0.5</sub> Tl <sub>0.5</sub> NbTeO <sub>6</sub>            | 10.2791                 | [37]       |
| HTaTeO <sub>6</sub> ·H <sub>2</sub> O                             | 10.287(3)               | [38]       |
| NaTaTeO <sub>6</sub>  | 10.544                  | [35]       |
| KTaTeO <sub>6</sub>   | 10.25                   | [35]       |
| RbTaTeO <sub>6</sub>  | 10.26                   | [35]       |
| CsTaTeO <sub>6</sub>  | 10.29                   | [35]       |
| TlTaTeO <sub>6</sub>  | 10.26                   | [35]       |
| KVTeO <sub>6</sub>  | 10.008(1)               | [39]       |
| RbVTeO <sub>6</sub>   | 10.036(1)               | [39]       |
| CsVTeO <sub>6</sub>   | 10.483(1)               | [39-40]    |

### 4.3 Electronic Conductivity in Some New Tellurium Oxides with the Pyrochlore Structure

#### 4.3.1 Introduction

Superconductivity has been observed in mixed valence oxides with heavy post-transition metals. Sleight *et al.* reported the superconductivity in  $\text{BaBi}_{1-x}\text{Pb}_x\text{O}_3$  perovskites with transition temperatures as high as 13K [43].  $\text{BaBiO}_3$  itself is insulating with distorted perovskite structure because charge disproportionation of  $\text{Bi}^{4+}$  splits the Bi 6s conduction band into a completely filled band ( $\text{Bi}^{3+}$ ) and an empty band ( $\text{Bi}^{5+}$ ). Substitution of Pb disrupts charge disproportionation and the resulted cubic perovskite oxide is superconducting [43]. Similar phenomenon is found in  $\text{BaPb}_{1-x}\text{Sb}_x\text{O}_3$  where the superconductivity was reported with transition temperature of 3.5K by Cava *et al.* [44].

High electronic conductivity is readily obtained on n-type doping of CdO,  $\text{In}_2\text{O}_3$ , and  $\text{SnO}_2$ ; however, such behavior has apparently not been observed on moving further along this row to Sb and Te. The conduction band for CdO,  $\text{In}_2\text{O}_3$ , and  $\text{SnO}_2$  is dominated by cation 5s states; thus, these n-type doped compounds can be viewed as  $s^0/s^1$  mixed valence compounds of class III according to the classification of Robin and Day as discussed in section 1.6 [45]. Although mixed valence oxides of Te are known, all of them belong to class I mixed valency with distinctly different sites for  $\text{Te}^{4+}$  and  $\text{Te}^{6+}$ . Some examples are  $\text{Te}_2\text{O}_5$  ( $\text{Te}^{4+}\text{Te}^{6+}\text{O}_5$ ),  $\text{Ag}_2\text{Te}_2\text{O}_6$  ( $\text{Ag}_2\text{Te}^{4+}\text{Te}^{6+}\text{O}_6$ ), and  $\text{SrTe}_3\text{O}_8$  ( $\text{SrTe}_2^{4+}\text{Te}^{6+}\text{O}_8$ ) [46-48]. The compound  $\text{CsTe}_{1/2}\text{Te}_{3/2}^{6+}\text{O}_6$  can be viewed as a class II mixed valence compound because it is highly colored with both  $\text{Te}^{4+}$  and

$\text{Te}^{6+}$  on octahedral sites [49]. However,  $\text{CsTe}_{1/2}^{4+}\text{Te}_{3/2}^{6+}\text{O}_6$  has no measurable electronic conductivity at room temperature. The only oxide of Te reported to be electronically conducting is  $\text{BaTl}_{1/2}\text{Te}_{1/2}\text{O}_3$  where the conductivity is likely related to Tl/Te valence degeneracy caused by an overlap of the Tl 6s and Te 5s bands [50].

$\text{A}^{1+}\text{B}_2\text{O}_6$  defect pyrochlore oxides (Fig.4.8) are known for many A cations such as K, Rb, Cs, or Tl. The three hexavalent cations found in this structure are  $\text{Mo}^{6+}$ ,  $\text{W}^{6+}$  and  $\text{Te}^{6+}$ , leading to compounds such as  $\text{CsTaWO}_6$ ,  $\text{RbTiTeO}_6$ , and  $\text{CsNbMoO}_6$  [30,51]. These compounds are large band gap materials consistent with their white or light yellow colors. High ionic conductivity of the  $\text{A}^{1+}$  cation is also generally observed in these compositions [18, 52].

The compound  $\text{CsTe}_2\text{O}_6$  has been reported with a rhombohedral distortion of cubic pyrochlore structure [49]. Structural analysis shows cation ordering of  $\text{Te}^{4+}$  and  $\text{Te}^{6+}$  yielding a  $\text{CsTe}_{1/2}^{4+}\text{Te}_{3/2}^{6+}\text{O}_6$  formula. A remarkable feature of  $\text{CsTe}_2\text{O}_6$  is the very high symmetry of the  $\text{Te}^{4+}$  octahedron. This  $\text{Te}^{4+}$  is at a center of symmetry fixing all six Te-O distances to be equal. The O-Te-O angles deviate from  $90^\circ$  by less than  $1^\circ$ . Such high symmetry is unknown for any other oxides of  $\text{Te}^{4+}$  and unknown in oxides for any other  $5s^2$  cations such as  $\text{Sn}^{2+}$  or  $\text{Sb}^{3+}$ . This highly unusual symmetry for  $\text{Te}^{4+}$  suggested that it might be possible to prepare mixed valence Te pyrochlores that were electronically conducting where electrons can easily move between very similar, if not the same, sites of  $\text{Te}^{4+}$  and  $\text{Te}^{6+}$ .

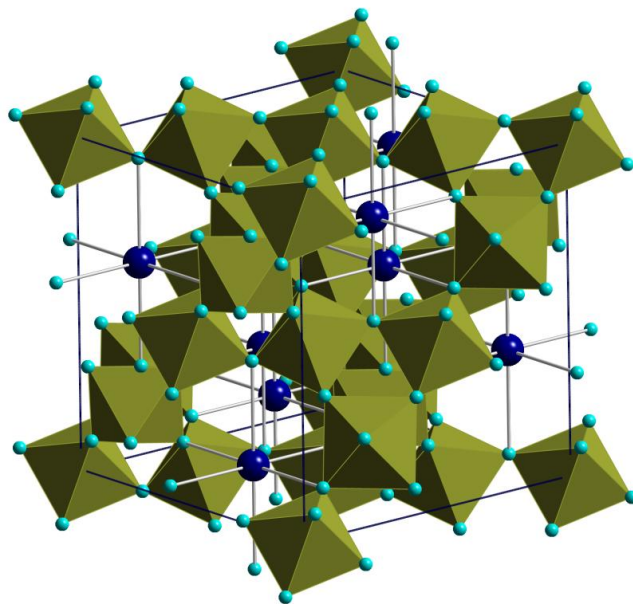


Figure 4.8: Structure of cubic  $AM_2X_6$  pyrochlores as a network of corner shared  $M_2X_6$  octahedra with  $A^{1+}$  (dark blue) in an interstitial site (8b site).

### 4.3.2 Results and Discussion

The nominal compositions of the new  $Cs(M,Te)_2O_6$  pyrochlores prepared in this study are given in Table 4.3 with their cubic cell edges at 25 °C and some electrical properties. The prepared compounds include oxides of the types  $CsM_{1/2}^{4+}Te_{3/2}^{6+}O_6$ ,  $CsM_{1/3}^{3+}Te_{5/3}^{6+}O_6$  and  $CsM_{1/4}^{2+}Te_{7/4}^{6+}O_6$ . Powder X-ray diffraction patterns of all compositions showed cubic  $AM_2O_6$  defect pyrochlore structure. Since there are 2 vacancies at O' (8b) and A (16d) sites, there are various possible sites available for the only A cation in the  $A_2O'$  chain. Figure 4.9 shows a comparison of the observed X-ray diffraction with calculated patterns of representative compound,  $CsAl_{0.33}Te_{1.67}O_6$ , when Cs is in 8b site and 16d site. As shown in the Figure,  $Cs^{1+}$  in these compounds

prefers 8b over 16d sites. This preference is expected as 8b site is larger than 16 site and hence more suitable for large  $\text{Cs}^{1+}$ .

Table 4.3:  $\text{Cs}(\text{M},\text{Te})_2\text{O}_6$  pyrochlores prepared in this work.

| <b>Compound</b>  | <b>a (Å)</b> | <b><math>\rho</math> (<math>\Omega\text{cm}</math>) @RT</b> | <b>S (mV/K)@RT</b> |
|--|--------------|---|--------------------|
| <b><math>\text{CsM}^{3+}_{0.33}\text{Te}_{1.67}\text{O}_6</math></b> |              |   |                    |
| $\text{Cs}(\text{Al}_{0.33}\text{Te}_{1.67})\text{O}_6$              | 10.085       | 10  | -87                |
| $\text{Cs}(\text{Cr}_{0.33}\text{Te}_{1.67})\text{O}_6$              | 10.159       | $>10^6$   | -                  |
| $\text{Cs}(\text{Mn}_{0.33}\text{Te}_{1.67})\text{O}_6$              | 10.186       | $3 \times 10^3$   | -390               |
| $\text{Cs}(\text{Fe}_{0.33}\text{Te}_{1.67})\text{O}_6$              | 10.183       | 42  | -130               |
| $\text{Cs}(\text{Co}_{0.33}\text{Te}_{1.67})\text{O}_6$              | 10.175       | 118   | -206               |
| $\text{Cs}(\text{Ga}_{0.33}\text{Te}_{1.67})\text{O}_6$              | 10.158       | 3   | -50                |
| $\text{Cs}(\text{Sc}_{0.33}\text{Te}_{1.67})\text{O}_6$              | 10.256       | $10^5$  | -                  |
| $\text{Cs}(\text{In}_{0.33}\text{Te}_{1.67})\text{O}_6$              | 10.281       | 33  | -150               |
| $\text{Cs}(\text{Tl}_{0.33}\text{Te}_{1.67})\text{O}_6$              | 10.345       | 3   | -70                |
| $\text{Cs}(\text{Lu}_{0.33}\text{Te}_{1.67})\text{O}_6$              | 10.348       | $>10^6$   | -                  |
| $\text{Cs}(\text{Yb}_{0.33}\text{Te}_{1.67})\text{O}_6$              | 10.357       | $>10^6$   | -                  |
| $\text{Cs}(\text{Tm}_{0.33}\text{Te}_{1.67})\text{O}_6$              | 10.364       | $>10^6$   | -                  |
| $\text{Cs}(\text{Er}_{0.33}\text{Te}_{1.67})\text{O}_6$              | 10.375       | $>10^6$   | -                  |
| $\text{Cs}(\text{Ho}_{0.33}\text{Te}_{1.67})\text{O}_6$              | 10.394       | $>10^6$   | -                  |
| <b><math>\text{CsM}^{4+}_{0.5}\text{Te}_{1.5}\text{O}_6</math></b>   |              |   |                    |
| $\text{Cs}(\text{Ge}_{0.5}\text{Te}_{1.5})\text{O}_6$                | 10.044       | 0.5   | -51                |
| $\text{Cs}(\text{Ti}_{0.5}\text{Te}_{1.5})\text{O}_6$                | 10.150       | $>10^6$   | -                  |
| $\text{Cs}(\text{Rh}_{0.5}\text{Te}_{1.5})\text{O}_6$                | 10.181       | $10^3$  | -90                |
| <b><math>\text{CsM}^{2+}_{0.25}\text{Te}_{1.75}\text{O}_6</math></b> |              |   |                    |
| $\text{Cs}(\text{Mg}_{0.25}\text{Te}_{1.75})\text{O}_6$              | 10.220       | 482   | -180               |
| $\text{Cs}(\text{Zn}_{0.25}\text{Te}_{1.75})\text{O}_6$              | 10.233       | $>10^6$   | -                  |
| $\text{Cs}(\text{Ni}_{0.25}\text{Te}_{1.75})\text{O}_6$              | 10.219       | $>10^6$   | -                  |

A plot of unit cell parameters versus average ionic radius of octahedral cations [53] for all the compounds shows a linear behavior (Fig. 4.10). Magnetism is studied in some samples which contain magnetic elements. The plot of  $1/\chi$  vs. temperature is

shown in Figure 4.11. The magnetic moments obtained from experimental data agree well with spin-only theoretical values calculated by assuming  $M^{3+}$  cations in octahedral environment (Table 4.4).

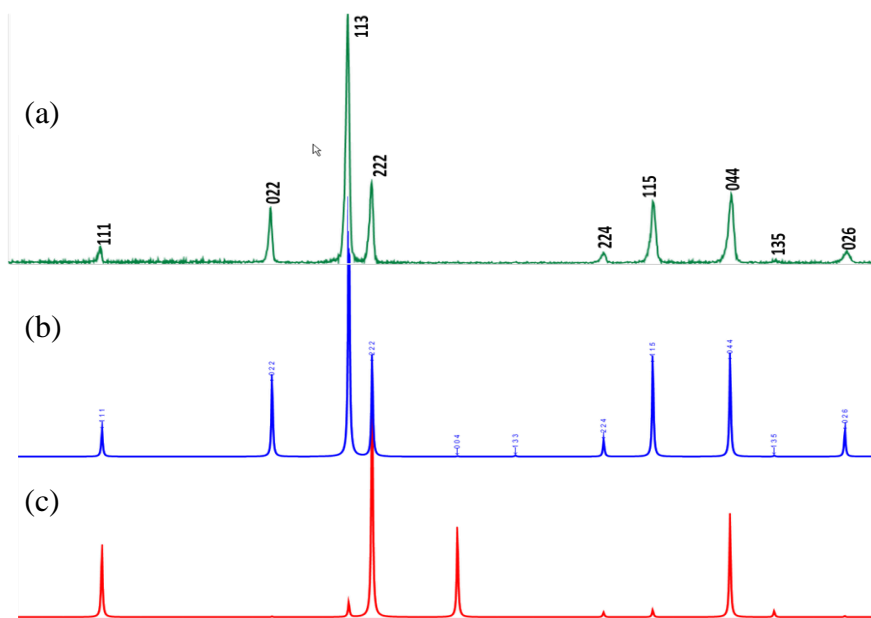


Figure 4.9: Comparison of observed pattern of  $\text{CsAl}_{0.33}\text{Te}_{1.67}\text{O}_6$  (a) with simulated patterns when Cs is in 8b site (b) and 16d site (c).

All the compounds are black. Electronic conductivity cannot be detected in some of these compounds, indicating that the conductivity is less than  $10^{-6}$  S/cm. However, others show electronic conductivity at room temperature that can be as high as 2 S/cm (Table 4.3). For those that conduct, the temperature dependence of the conductivity generally indicates semiconducting behavior (Fig. 4.12). However, the lack of significant temperature dependence for some samples suggests degenerate semiconducting behavior.

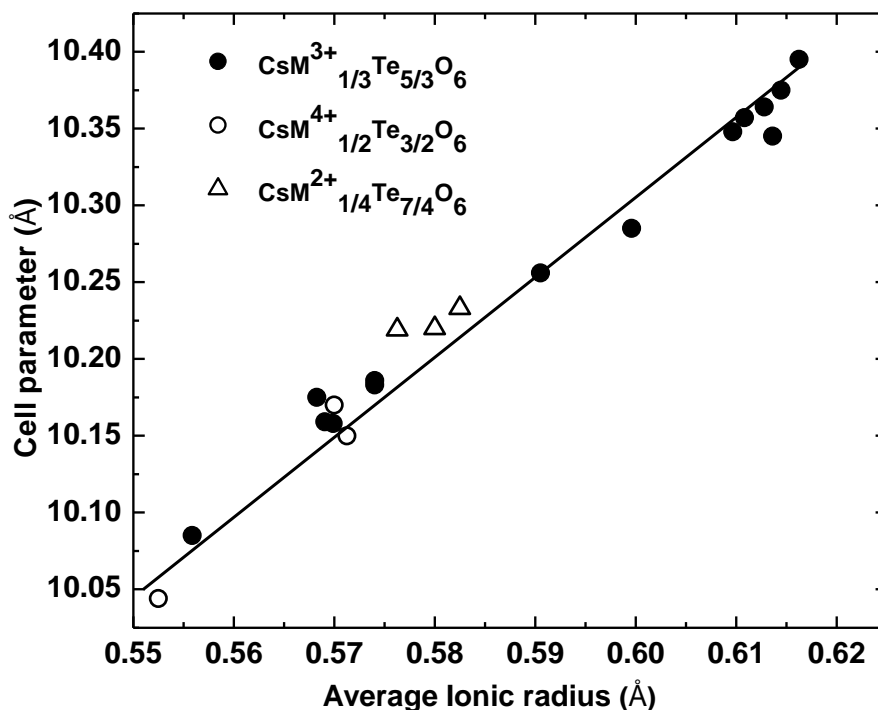


Figure 4.10: Average ionic radius of octahedral cations vs.  $a$  lattice parameter for Cs(M,Te)O<sub>6</sub> phases

The negative Seebeck coefficients (Table 4.3) indicate that the major charge carriers are electrons. Low Seebeck coefficients are observed for the better conductors, as would be expected. The higher Seebeck coefficients for the insulating samples suggest that grain boundaries are not the cause of the high resistance. Plots of  $\log \rho$  vs.  $1/T$  (Fig. 4.13) are not linear which indicates that the gap between the filled  $5s$  states and the conduction band changes with temperature. As this gap decreases when temperature is increased (Fig.4.13), these compounds may be headed to a metallic state at high temperature. Plots of  $\log \rho$  vs.  $1/T^{1/4}$  are, however, linear (Fig. 4.14) which is attributed to a three-dimensional variable range hopping of carriers. The color

and the conductivity of  $\text{CsTl}_{1/3}\text{Te}_{5/3}\text{O}_6$  can be attributed to Tl/Te valence degeneracy as in the case of  $\text{BaTl}_{1/2}\text{Te}_{1/2}\text{O}_3$ . However, the color and electrical properties of the other compounds are inconsistent with their ideal formulas.

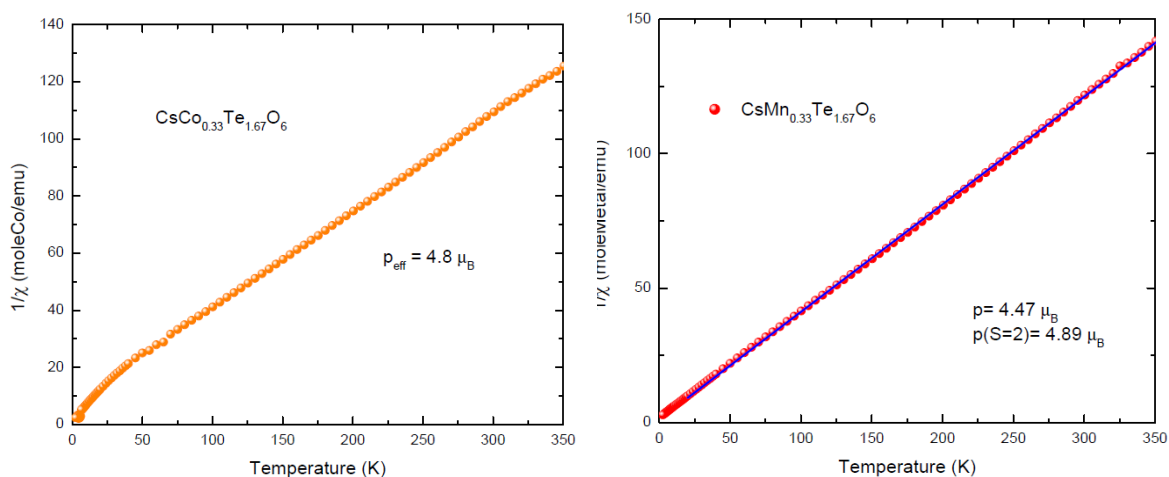


Figure 4.11: Magnetic property of  $\text{Cs}(\text{M},\text{Te})_2\text{O}_6$ ,  $\text{M} = \text{Co}^{3+}$  and  $\text{Mn}^{3+}$ .

Table 4.4: Curie-Weiss analysis of magnetic susceptibility.

| Composition                                    | Theoretical $\mu_{\text{eff}}$ ( $\mu_{\text{B}}$ )<br>(spin-only) | Calculated $\mu_{\text{eff}}$ ( $\mu_{\text{B}}$ )<br>from experimental data |
|--|--|--|
| $\text{CsCo}_{0.33}\text{Te}_{1.67}\text{O}_6$ | 4.90   | 4.8  |
| $\text{CsMn}_{0.33}\text{Te}_{1.67}\text{O}_6$ | 4.90   | 4.89   |

Apparently, there is some mixed valency of Te and therefore some deviations from the ideal stoichiometries, which may be very small. Possible deviations from ideal stoichiometry include concentration of  $\text{Cs}^{1+}$  interstitial cations, M/Te ratio, and oxygen deficiency. Synthesis under pure oxygen still gives black phases. Our experimental variations of the M/Te ratios suggest some range of stoichiometry, but all compositions are black. Normally, significant oxygen vacancies do not exist on the



octahedral network of the pyrochlore structure. An apparent exception is  $\text{TaWO}_{5.5}$ . However, this compound was prepared by an unusual multistep synthesis and oxygen vacancies were not fully confirmed by a neutron diffraction study [54]. Titration could potentially determine the amount of  $\text{Te}^{6+}$  reduction, but our attempts at titration have been thwarted by our inability to dissolve these pyrochlores.

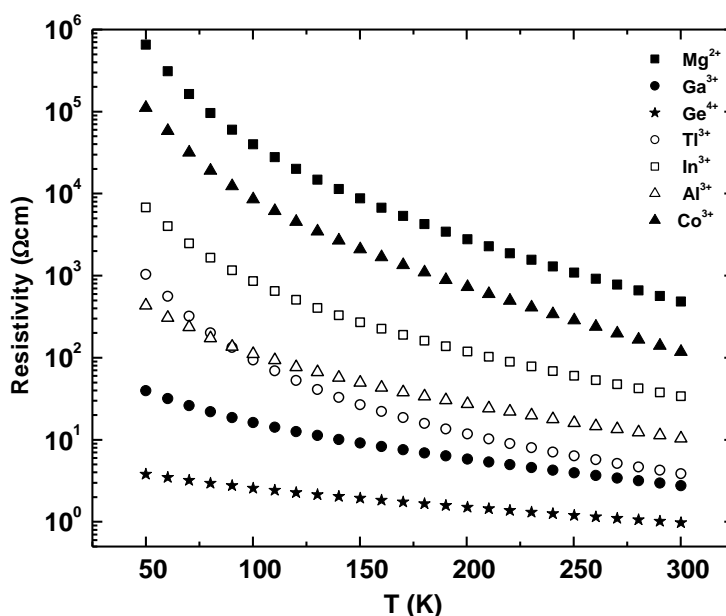


Figure 4.12: Log of resistivity for  $\text{Cs}(\text{M},\text{Te})_2\text{O}_6$  phases plotted vs. temperature.

The structure of  $\text{TeO}_3$  consists of a network of  $\text{Te}^{6+}$  octahedra sharing corners with a Te-O-Te angle of  $138^\circ$ , essentially the same Te-O-Te angle as in  $\text{Cs}(\text{M},\text{Te})_2\text{O}_6$  pyrochlores [55]. Although  $\text{TeO}_3$  is nearly white, its color is actually a very light grey. This indicates a high band gap material with a low level of optical absorption throughout the visible region due to defects. The color centers in  $\text{TeO}_3$  leading to the grey color may well be the same color centers causing the black color in Te

pyrochlores made in this study, and this center would be associated with a slight reduction of  $\text{Te}^{6+}$ .

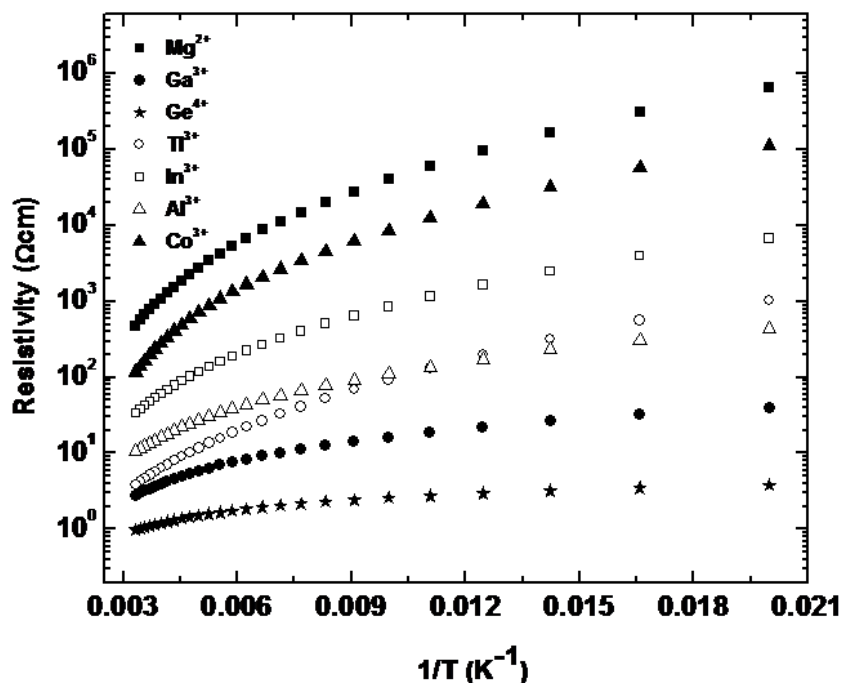


Figure 4.13: Log of resistivity for  $\text{Cs}(\text{M},\text{Te})_2\text{O}_6$  phases plotted vs.  $1/T$ .

Schematic energy diagrams for these compounds are shown in Figure 4.15 with hypothetical cubic  $\text{CsTe}_2\text{O}_6$  (Fig. 4.15(a)) and actual rhombohedral  $\text{CsTe}_2\text{O}_6$  (Fig. 4.15(b)). Similar to other oxides, the valence band is mainly oxygen in character and the conduction band is most contributed by  $5s$  band of Te. If  $\text{CsTe}_2\text{O}_6$  had the ideal cubic pyrochlore structure with all Te atoms on equivalent sites,  $5s$  conducting band would be left one-fourth filled and the compound would be metallic. However, charge ordering results in distinctly different Te sites in rhombohedral  $\text{CsTe}_2\text{O}_6$  (Fig. 4.15(b)) with  $\text{Te}^{4+}$  having longer Te-O distances than  $\text{Te}^{6+}$ . This leads to a splitting of the  $5s$  band to filled  $5s$  states associated with  $\text{Te}^{4+}$  and empty  $5s$  states associated with

$\text{Te}^{6+}$ . For the  $\text{Cs}(\text{M},\text{Te})_2\text{O}_6$  pyrochlores, there is only one empty  $5s$  conduction band without splitting since there is only one  $\text{Te}^{6+}$  species in the structure. However, small reduction of  $\text{Te}^{6+}$  introduces the filled defect level of  $\text{Te}^{4+}$  close to the conduction band. The number of these filled  $5s$  states is much lower than in  $\text{CsTe}_2\text{O}_6$ , but the energy of these states can be higher in the more contracted lattices. Electron transfer between the filled defect states and the conduction band results in black color and the electronic conductivity in some cases.

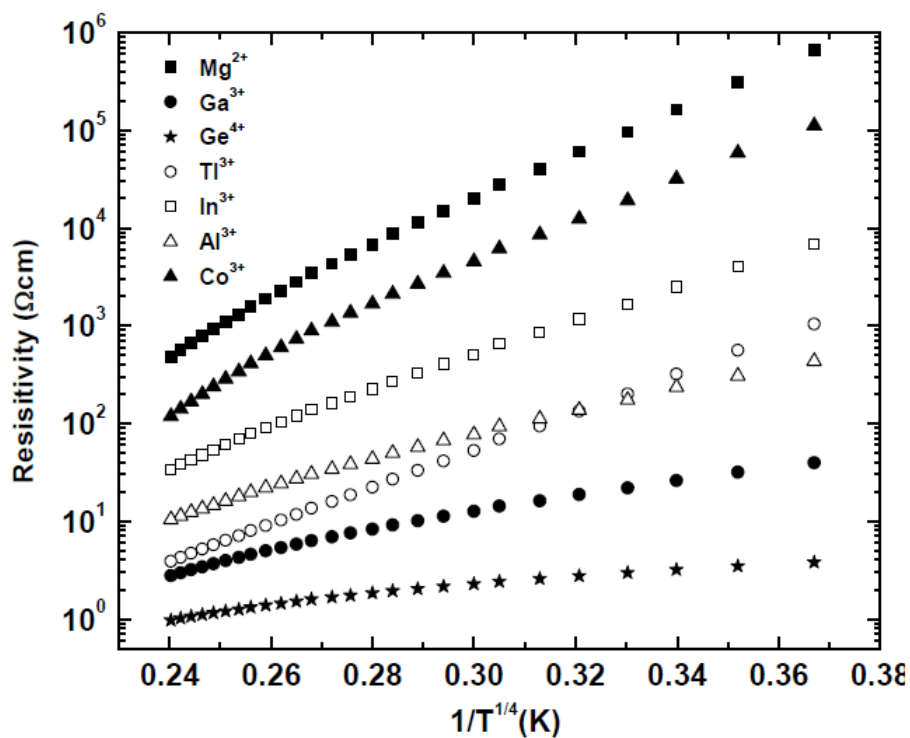


Figure 4.14: Log of resistivity for  $\text{Cs}(\text{M},\text{Te})_2\text{O}_6$  phases plotted vs.  $1/T^{1/4}$

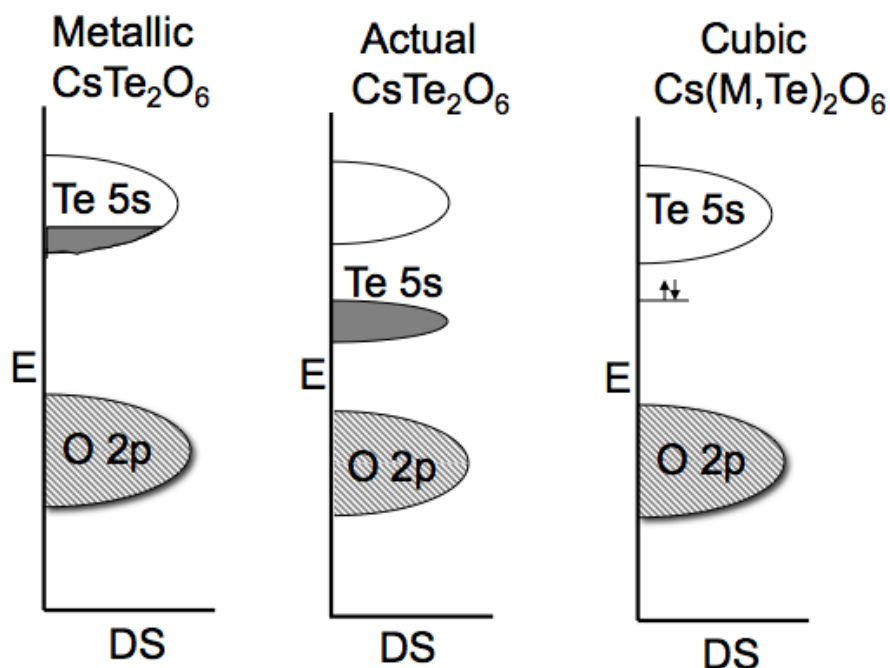


Figure 4.15: Schematic energy diagrams for (a) hypothetical cubic  $\text{CsTe}_2\text{O}_6$  that is metallic due to a  $\frac{1}{4}$  filled  $5s$  band, (b) actual rhombohedral  $\text{CsTe}_2\text{O}_6$ , and (c) cubic  $\text{Cs}(\text{M},\text{Te})_2\text{O}_6$  phases.

Explaining the conductivity variations is a challenge because there would appear to be at least three important variables: the number of occupied  $5s$  states, the energies of these occupied  $5s$  states relative to the conduction band, and the mobility of the conduction electrons. Only the  $\text{CsM}_{1/3}^{3+}\text{Te}_{5/3}\text{O}_6$  series is large enough to expect the emergence of reliable trends. Two trends appear in this series. Conductivity is enhanced by a smaller lattice and by M cations having states of the appropriate energy to mix into the Te  $5s$  band. The higher conductivity we observe for some of our cubic  $\text{Cs}(\text{M},\text{Te})_2\text{O}_6$  pyrochlores must be due to occupied  $5s$  states that are closer to the conduction band than in rhombohedral  $\text{CsTe}_2\text{O}_6$  (Fig. 4.15), which has a conductivity less than  $10^{-6}$  S/cm at room temperature. This is not surprising because in our cubic

$\text{Cs}(\text{M},\text{Te})_2\text{O}_6$  pyrochlores there is no cooperative lattice distortion stabilizing  $\text{Te}^{4+}$  with longer Te-O distances as occurs in rhombohedral  $\text{CsTe}_2\text{O}_6$ . Because none of cubic  $\text{Cs}(\text{M},\text{Te})_2\text{O}_6$  pyrochlores is metallic, it appears that 5s electrons are always trapped in pairs forming  $\text{Te}^{4+}$  through a local lattice distortion with longer Te-O distances.

However, the higher energy of these filled 5s states relative to rhombohedral  $\text{CsTe}_2\text{O}_6$  indicates that the  $\text{Te}^{4+}$ -O distances for at least some of our cubic  $\text{Cs}(\text{M},\text{Te})_2\text{O}_6$  pyrochlores are not as long as in rhombohedral  $\text{CsTe}_2\text{O}_6$ . The higher conductivities in  $\text{CsM}_{1/3}^{3+}\text{Te}_{5/3}\text{O}_6$  pyrochlores with smaller cell edges (Table 4.3) suggest that the more compact lattices weaken the stabilization of the trapped 5s electrons and bring the filled 5s states closer to the conduction band. The  $\text{CsM}_{1/3}^{3+}\text{Te}_{5/3}\text{O}_6$  pyrochlores with the larger cell edges allow a deep trap, resulting generally in no observable conductivity at room temperature. There is, however, another factor involved. Conductivities for this series are also higher when the band gap of the corresponding  $\text{M}_2\text{O}_3$  oxide is smaller. Thus, although the smallest cell edge for the  $\text{CsM}_{1/3}^{3+}\text{Te}_{5/3}\text{O}_6$  series is for  $\text{M} = \text{Al}$ ,  $\text{CsAl}_{1/3}^{3+}\text{Te}_{5/3}\text{O}_6$  does not have the highest conductivity because  $\text{Al}_2\text{O}_3$  is a large band gap material lacking states of appropriate energy to mix into the Te 5s band. The band gaps of  $\text{Ga}_2\text{O}_3$  and  $\text{In}_2\text{O}_3$ , on the other hand, are such that some mixing of their s states into the Te 5s band can be expected. The impact of this mixing is so great for  $\text{M} = \text{Tl}$  that good conductivity occurs despite the relatively large cell edge. Trends within the  $\text{CsM}_{1/2}^{4+}\text{Te}_{3/2}^{6+}\text{O}_6$  and  $\text{CsM}_{1/4}^{2+}\text{Te}_{7/4}\text{O}_6$  series are less clear due to the small number of examples in each series. However, we

do note the highest conductivity we have observed is for  $\text{CsGe}_{1/2}\text{Te}_{3/2}^{\text{6+}}\text{O}_6$ , which also has the smallest cell edge we have observed.

### 4.3.3 Conclusion

Series of novel compounds with the formula  $\text{Cs}(\text{M},\text{Te})_2\text{O}_6$  with  $\text{M} = \text{Al}, \text{Ga}, \text{Cr}, \text{Fe}, \text{Co}, \text{In}, \text{Ho}, \text{Lu}, \text{Yb}, \text{Er}, \text{Ge}, \text{Rh}, \text{Ti}, \text{Zn}, \text{Ni},$  and  $\text{Mg}$  have been synthesized by solid state reaction. The compounds adopt cubic defect pyrochlore structure where  $\text{M}$  and  $\text{Te}$  randomly occupy 16c sites. Dark green to black color is observed in every composition and relatively high electronic conductivity is observed in some phases which can be explained by mixed valence of  $\text{Te}^{4+}/\text{Te}^{6+}$ . Defect states are introduced to band structure by the presence of  $\text{Te}^{4+}$ . Electron transfer between these defect levels and the conduction band give rise to the color and conductivity in some cases. Seebeck coefficients indicate that electrons are the major charge carriers which support the mixed valence mechanism. Although the accurate trend could not be obtained, the conductivity is found, in general, to increase when the cell parameter is decreased.

### 4.3.4 Experimental

$\text{Cs}(\text{M},\text{Te})_2\text{O}_6$  oxides were prepared from appropriate quantities of  $\text{CsNO}_3$ ,  $\text{TeO}_2$ , and an oxide of  $\text{M}$  by solid state reaction in air at 450 to 650 °C. Detailed information of all the reactants is shown in Table 4.5. All prepared compounds were characterized by powder X-ray diffraction collected on a Rigaku MiniFlex II powder diffractometer using  $\text{Cu K}\alpha$  radiation and a graphite monochromator on the diffracted beam. DC electrical resistivity were measured on the pellets by conventional four-

probe method in the temperature range 50-300K using a Quantum Design PPMS.

Seebeck coefficients were determined by static method at room temperature.

Table 4.5: Reactants used in this work.

| <b>Reactant</b>                | <b>Source</b>   | <b>Purity</b> |
|--------------------------------|---|---------------|
| CsNO <sub>3</sub>              | Alfa Aesar  | 99.8%         |
| RbNO <sub>3</sub>              | Alfa Aesar  | 99.8%         |
| TeO <sub>2</sub>               | Aldrich   | 99+%          |
| Al <sub>2</sub> O <sub>3</sub> | Aldrich   | 99.99%        |
| Cr <sub>2</sub> O <sub>3</sub> | Aldrich   | 99%           |
| Mn <sub>2</sub> O <sub>3</sub> | Johnson Matthey   | 98%           |
| Fe <sub>2</sub> O <sub>3</sub> | JMC   | 99.999%       |
| Co <sub>3</sub> O <sub>4</sub> | Alfa Aesar  | 99.7%         |
| Ga <sub>2</sub> O <sub>3</sub> | Aldrich   | 99.99+%       |
| Sc <sub>2</sub> O <sub>3</sub> | Alfa Aesar  | 99.99%        |
| In <sub>2</sub> O <sub>3</sub> | Aldrich   | 99.99%        |
| Tl <sub>2</sub> O <sub>3</sub> | Johnson Matthey   | 99.999%       |
| Lu <sub>2</sub> O <sub>3</sub> | Alfa Aesar  | 99.9%         |
| Yb <sub>2</sub> O <sub>3</sub> | Alfa Aesar  | 99.9%         |
| Tm <sub>2</sub> O <sub>3</sub> | Aldrich   | 99.9%         |
| Er <sub>2</sub> O <sub>3</sub> | Aldrich   | 99.99%        |
| Ho <sub>2</sub> O <sub>3</sub> | Aldrich   | 99.999%       |
| GeO <sub>2</sub>               | Strem Chemicals   | 99.999%       |
| TiO <sub>2</sub>               | JMC   | 99.99%        |
| RhO <sub>2</sub>               | prepared from<br>RhCl <sub>3</sub> ·xH <sub>2</sub> O (99.9%,<br>Alfa, Aesar) |               |
| MgO                            | Alfa Aesar  | 99.95%        |
| ZnO                            | Aldrich   | 99.99%        |
| NiO                            | Alfa Aesar  | 99.99%        |

## 4.4 Structural Studies and Electrical Properties of Cs/Al/Te/O Phases with the Pyrochlore Structure

### 4.4.1 Introduction

Relatively high electronic conductivities have been reported in tellurium oxides with pyrochlore structure as described in section 4.3 [56]. Although the electronic conductivity in  $\text{CsTl}_{0.33}\text{Te}_{1.67}\text{O}_6$  could be explained by a good overlap of Tl  $6s$  and Te  $5s$  band, the same explanation could not be applied for some other phases such as  $\text{CsGe}_{0.5}\text{Te}_{1.5}\text{O}_6$  whose conductivity is as high as 2 S/cm. The observed electronic conductivities, black color, and negative Seebeck coefficients in these compounds suggested mixed valency of  $\text{Te}^{4+}/\text{Te}^{6+}$ . This mixed valency must be accompanied with some deviations from the ideal formula. The possible deviations, which could be very small, include concentration of  $\text{Cs}^{1+}$  cations, the precise M/Te ratio, and oxygen deficiency. We had been unable to determine the deviation from ideal stoichiometry that led to the presumed mixed valency of Te and the related electrical properties.

In this work, single crystals of some representative compounds of conducting  $\text{Cs}(\text{M},\text{Te})_2\text{O}_6$  were investigated. Detailed structural analysis as well as electrical property measurements were done on single crystals and polycrystalline samples of  $\text{CsAl}_x\text{Te}_{2-x}\text{O}_6$ ,  $x=0.25-0.45$ . Cs/Al/Te/O pyrochlore was chosen for investigations because of the large difference of X-ray and neutron atomic scattering factors between Al and Te which leads to more reliable Al/Te ratios from powder diffraction refinement [57]. Moreover, as there is no mixed valence situation possible for



counting ions,  $\text{Cs}^{1+}$ ,  $\text{Al}^{3+}$ , and  $\text{O}^{2-}$ ; the only possible species to have mixed valency is Te ( $\text{Te}^{4+}/\text{Te}^{6+}$ ). In addition, preliminary results showed that the compositions and conductivities of this Cs/Al/Te/O system could be varied.

#### 4.4.2 Results

##### 4.4.2.1 Single Crystals

Octahedral crystals were obtained as the only product from  $\text{CsAl}_x\text{Te}_{2-x}\text{O}_6$ ,  $x = 0.25, 0.33, \text{ and } 0.45$ ;  $\text{CsGa}_{0.33}\text{Te}_{1.67}\text{O}_6$ , and  $\text{CsGe}_{0.50}\text{Te}_{1.50}\text{O}_6$  growth (Fig.4.16). However, attempt to grow  $\text{CsIn}_{0.33}\text{Te}_{1.67}\text{O}_6$  resulted in a mixture of two types of crystals with similar proportions and sizes; octahedral crystals of  $\text{CsIn}_{0.33}\text{Te}_{1.67}\text{O}_6$  and hexagonal pyramidal crystals of  $\text{In}_2\text{TeO}_6$ . All the pyrochlore crystals seemed to be black in color but investigation under microscope indicated that they can be transparent dark grey.  $\text{In}_2\text{TeO}_6$  crystal can be transparent green under microscope especially when the crystals are thin enough.

The obtained  $\text{CsAl}_x\text{Te}_{2-x}\text{O}_6$   $x = 0.34, 0.37, \text{ and } 0.38$ ,  $\text{CsGa}_{0.34}\text{Te}_{1.66}\text{O}_6$ ,  $\text{CsIn}_{0.33}\text{Te}_{1.67}\text{O}_6$  and  $\text{CsGe}_{0.50}\text{Te}_{1.50}\text{O}_6$  crystals crystallize in defect pyrochlore structure of the type  $\text{AM}_2\text{O}_6$ . Table 4.6-4.9 show crystallographic data, structural refinement, atomic coordinates and displacement factors of all crystals. Selected bond lengths and angles are given in Table 4.10.

Table 4.6: Crystal data and structure refinements of Cs(M,Te)<sub>2</sub>O<sub>6</sub>, M = Ga, In, and Ge.

|   |  |  |   |
|---|--|--|---|
| Starting composition                            | CsGa <sub>0.33</sub> Te <sub>1.67</sub> O <sub>6</sub> | CsIn <sub>0.33</sub> Te <sub>1.67</sub> O <sub>6</sub> | CsGe <sub>0.5</sub> Te <sub>1.50</sub> O <sub>6</sub> |
| Refined crystal composition                     | CsGa <sub>0.34</sub> Te <sub>1.66</sub> O <sub>6</sub> | CsIn <sub>0.33</sub> Te <sub>1.67</sub> O <sub>6</sub> | CsGe <sub>0.5</sub> Te <sub>1.50</sub> O <sub>6</sub> |
| Formula weight (g/mol)                          | 464.50   | 479.73   | 456.51  |
| Temperature (K)                                 | 173(2) K   | 173(2)   | 173(2)  |
| Space group                                     | Fd $\bar{3}$ m   | Fd $\bar{3}$ m   | Fd $\bar{3}$ m  |
| a (Å)   | 10.1375(14)  | 10.2697(7)   | 10.0167(14)   |
| V (Å <sup>3</sup> )                             | 1041.8(2)  | 1083.11(13)  | 1005.0 (2)  |
| Z   | 8  | 8  | 8   |
| $\rho_{\text{calculated}}$ (Mg/m <sup>3</sup> ) | 5.923  | 5.884  | 6.034   |
| Absorption coefficient (mm <sup>-1</sup> )      | 17.896   | 16.974   | 18.782  |
| F(000)  | 1599   | 1648   | 1576  |
| Crystal size (mm <sup>3</sup> )                 | 0.06 x 0.04 x<br>0.02                                  | 0.06 x 0.04 x<br>0.02                                  | 0.06 x 0.04 x<br>0.02                                 |
| $\Theta$ range                                  | 3.48 - 27.97   | 3.44 - 26.99   | 3.52 - 27.73  |
| Reflections collected                           | 2743   | 2825   | 1367  |
| Independent reflections                         | 83 [R(int) =<br>0.0232]                                | 79 [R(int) =<br>0.0140]                                | 79 [R(int) =<br>0.0168]                               |
| Completeness to $\theta=27.81^\circ$            | 100.0 %  | 100.0 %  | 100.0 %   |
| Data/restraints/parameters                      | 83 / 1 / 11  | 79 / 0 / 9   | 79 / 0 / 11   |
| Goodness-of-fit on F <sup>2</sup>               | 1.190  | 1.277  | 1.391   |
| Final R indices [I>2 $\sigma$ (I)]              | R <sub>1</sub> = 0.0129,<br>wR <sub>2</sub> = 0.0308   | R <sub>1</sub> = 0.0087,<br>wR <sub>2</sub> = 0.0173   | R <sub>1</sub> = 0.0175,<br>wR <sub>2</sub> = 0.0381  |
| R indices (all data)                            | R <sub>1</sub> = 0.0156,<br>wR <sub>2</sub> = 0.0317   | R <sub>1</sub> = 0.0093,<br>wR <sub>2</sub> = 0.0178   | R <sub>1</sub> = 0.0207,<br>wR <sub>2</sub> = 0.0394  |
| Largest difference peak                         | +0.346 e.Å <sup>-3</sup>                               | +0.522 e.Å <sup>-3</sup>                               | +0.581 e.Å <sup>-3</sup>                              |
| Largest difference hole                         | -0.786 e.Å <sup>-3</sup>                               | -0.355 e.Å <sup>-3</sup>                               | -0.708 e.Å <sup>-3</sup>                              |

Table 4.7: Atomic coordinates and displacement factors of  $\text{Cs}(\text{M},\text{Te})_2\text{O}_6$ ,  $\text{M} = \text{Ga}, \text{In},$  and  $\text{Ge}$ .

| Atom   | Wyckoff position | X     | Y     | Z          | $U_{\text{eq}}$ |
|--|------------------|-------|-------|------------|-----------------|
| $\text{CsGa}_{0.34}\text{Te}_{1.66}\text{O}_6$ |                  |       |       |            |                 |
| Cs   | 8b               | 0.125 | 0.125 | 0.125      | 15(1)           |
| Ga/Te  | 16c              | 0     | 0.5   | 0          | 6(1)            |
| O  | 48f              | 0.125 | 0.625 | -0.0700(4) | 11(1)           |
| $\text{CsIn}_{0.33}\text{Te}_{1.67}\text{O}_6$ |                  |       |       |            |                 |
| Cs   | 8b               | 0.125 | 0.125 | 0.125      | 17(1)           |
| In/Te  | 16c              | 0     | 0.5   | 0          | 7(1)            |
| O  | 48f              | 0.125 | 0.625 | -0.0703(3) | 24(1)           |
| $\text{CsGe}_{0.5}\text{Te}_{1.50}\text{O}_6$  |                  |       |       |            |                 |
| Cs   | 8b               | 0.125 | 0.125 | 0.125      | 13(1)           |
| Ge/Te  | 16c              | 0     | 0.5   | 0          | 8(1)            |
| O  | 48f              | 0.125 | 0.625 | -0.0709(6) | 10(1)           |

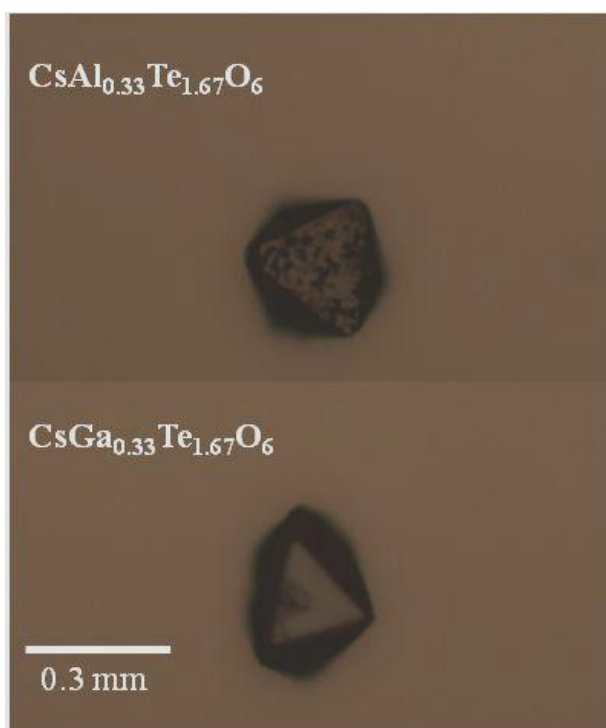


Figure 4.16: Single crystals of  $\text{Cs}(\text{M},\text{Te})_2\text{O}_6$  defect pyrochlores

Table 4.8: Crystal data and structure refinements of CsAl<sub>x</sub>Te<sub>2-x</sub>O<sub>6</sub>, x = 0.25, 0.33, and 0.45

|   |   |   |   |
|---|---|---|---|
| Starting composition                            | CsAl <sub>0.25</sub> Te <sub>1.75</sub> O <sub>6</sub>                  | CsAl <sub>0.33</sub> Te <sub>1.67</sub> O <sub>6</sub>                  | CsAl <sub>0.45</sub> Te <sub>1.55</sub> O <sub>6</sub>                  |
| Crystal composition                             | Cs <sub>0.98</sub> Al <sub>0.38</sub> Te <sub>1.62</sub> O <sub>6</sub> | Cs <sub>0.98</sub> Al <sub>0.37</sub> Te <sub>1.63</sub> O <sub>6</sub> | Cs <sub>0.98</sub> Al <sub>0.33</sub> Te <sub>1.67</sub> O <sub>6</sub> |
| Formula weight (g/mol)                          | 445.37  | 447.01  | 479.73  |
| Temperature (K)                                 | 293(2) K  | 173(2)  | 173(2)  |
| Space group                                     | Fd $\bar{3}$ m  | Fd $\bar{3}$ m  | Fd $\bar{3}$ m  |
| a (Å)   | 10.0684(2)  | 10.071(1)   | 10.1035(3)  |
| V (Å <sup>3</sup> )                             | 1020.66(4)  | 1021.57(19)   | 1031.37(5)  |
| Z   | 8   | 8   | 8   |
| $\rho_{\text{calculated}}$ (Mg/m <sup>3</sup> ) | 5.797   | 5.813   | 5.801   |
| Absorption coefficient (mm <sup>-1</sup> )      | 16.324  | 16.398  | 16.423  |
| F(000)  | 1536  | 1541  | 1551  |
| Crystal size (mm <sup>3</sup> )                 | 0.06 x 0.04 x<br>0.02   | 0.06 x 0.04 x<br>0.02   | 0.06 x 0.04 x<br>0.02   |
| $\Theta$ range                                  | 3.50 - 27.92  | 3.50 - 27.91  | 3.49 - 27.81  |
| Reflections collected                           | 2743  | 2690  | 2688  |
| Independent reflections                         | 80 [R(int) =<br>0.4409]   | 80 [R(int) =<br>0.0255]   | 80 [R(int) =<br>0.0131]   |
| Completeness to $\theta=27.81^\circ$            | 100.0 %   | 100.0 %   | 100.0 %   |
| Data/restraints/parameters                      | 80 / 1 / 11   | 80 / 1 / 11   | 80 / 1 / 10   |
| Goodness-of-fit on F <sup>2</sup>               | 1.160   | 1.579   | 1.402   |
| Final R indices [I>2 $\sigma$ (I)]              | R <sub>1</sub> = 0.0119,<br>wR <sub>2</sub> = 0.0271                    | R <sub>1</sub> = 0.0155,<br>wR <sub>2</sub> = 0.0323                    | R <sub>1</sub> = 0.0133,<br>wR <sub>2</sub> = 0.0325                    |
| R indices (all data)                            | R <sub>1</sub> = 0.0138,<br>wR <sub>2</sub> = 0.0284                    | R <sub>1</sub> = 0.0161,<br>wR <sub>2</sub> = 0.0326                    | R <sub>1</sub> = 0.0140,<br>wR <sub>2</sub> = 0.0329                    |
| Largest difference peak                         | +0.304 e.Å <sup>-3</sup>  | +0.301 e.Å <sup>-3</sup>  | +0.331 e.Å <sup>-3</sup>  |
| Largest difference hole                         | -0.419 e.Å <sup>-3</sup>  | -0.381 e.Å <sup>-3</sup>  | -0.504 e.Å <sup>-3</sup>  |

Table 4.9: Atomic coordinates and displacement factors of  $\text{CsAl}_x\text{Te}_{2-x}\text{O}_6$ ,  $x = 0.25$ ,  $0.33$ , and  $0.45$ .

| Atom   | Wyckoff position | X     | Y     | Z          | $U_{\text{eq}}$ |
|--|------------------|-------|-------|------------|-----------------|
| $\text{Cs}_{0.98}\text{Al}_{0.38}\text{Te}_{1.62}\text{O}_6$ |                  |       |       |            |                 |
| Cs   | 8b               | 0.125 | 0.125 | 0.125      | 21(1)           |
| Al/Te  | 16c              | 0     | 0.5   | 0          | 9(1)            |
| O  | 48f              | 0.125 | 0.625 | -0.0702(4) | 14(1)           |
| $\text{Cs}_{0.98}\text{Al}_{0.37}\text{Te}_{1.63}\text{O}_6$ |                  |       |       |            |                 |
| Cs   | 8b               | 0.125 | 0.125 | 0.125      | 16(1)           |
| Al/Te  | 16c              | 0     | 0.5   | 0          | 7(1)            |
| O  | 48f              | 0.125 | 0.625 | -0.0697(5) | 12(1)           |
| $\text{Cs}_{0.98}\text{Al}_{0.33}\text{Te}_{1.67}\text{O}_6$ |                  |       |       |            |                 |
| Cs   | 8b               | 0.125 | 0.125 | 0.125      | 21(1)           |
| Al/Te  | 16c              | 0     | 0.5   | 0          | 9(1)            |
| O  | 48f              | 0.125 | 0.625 | -0.0697(5) | 14(1)           |

Table 4.10: Bond lengths and bond angles.

|  | M-O1 $\times 6$ | Cs-O1 $\times 6$ | Cs-O2 $\times 12$ | M-O-M     | O-M-O    |
|--|-----------------|------------------|-------------------|-----------|----------|
| $\text{Cs}_{0.98}\text{Al}_{0.33}\text{Te}_{1.67}\text{O}_6$ | 1.919(1)        | 3.086(4)         | 3.6157(6)         | 92.8(2)   | 137.0(2) |
| $\text{Cs}_{0.98}\text{Al}_{0.37}\text{Te}_{1.63}\text{O}_6$ | 1.914(2)        | 3.075(5)         | 3.6041(8)         | 92.8(2)   | 137.0(3) |
| $\text{Cs}_{0.98}\text{Al}_{0.38}\text{Te}_{1.66}\text{O}_6$ | 1.915(1)        | 3.069(4)         | 3.6022(6)         | 93.1(1)   | 136.7(2) |
| $\text{CsGa}_{0.34}\text{Te}_{1.66}\text{O}_6$               | 1.9274(14)      | 3.092(4)         | 3.6273(8)         | 92.96(14) | 136.8(2) |
| $\text{CsIn}_{0.33}\text{Te}_{1.67}\text{O}_6$               | 1.9536(13)      | 3.130(4)         | 3.6741(6)         | 93.07(13) | 136.6(2) |
| $\text{CsGe}_{0.5}\text{Te}_{1.50}\text{O}_6$                | 1.908(2)        | 3.046(6)         | 3.5827(10)        | 93.3(2)   | 136.3(3) |

#### 4.4.2.2 Polycrystalline Samples

Powder X-ray diffraction data showed that the major phase was cubic pyrochlore with space group  $Fd\bar{3}m$  for all samples.  $\text{CsTe}_2\text{O}_6$  impurity was observed in samples with  $x = 0.24$  and  $0.27$  while  $\text{Al}_2\text{O}_3$  impurity was found in samples with  $x = 0.33, 0.38, 0.40$  (Fig. 4.17). Calculated percentage of impurity in each sample from neutron powder diffraction refinement using GSAS software [58] is shown in Table 4.11. The results of the structural refinement for  $\text{CsAl}_x\text{Te}_{2-x}\text{O}_6$  are summarized in Tables 4.12 and 4.13. The typical observed and calculated profiles are shown in Figure 4.18. The value  $x$  for a  $\text{CsAl}_x\text{Te}_{2-x}\text{O}_6$  formula was determined by refining the Al/Te ratio on the 16c site. The high sensitivity of neutron data to oxygen indicated a fully occupied O site for all values of  $x$ . The results from the neutron and X-ray Rietveld refinements were in good agreement.

The range of the cell edges was verified by powder X-ray diffraction with Si as an internal standard. As shown in Table 4.12, the refinements from both neutron and X-ray diffraction show that synthesis method used for polycrystalline samples only gave Al contents about equal to the ideal  $\text{CsAl}_{0.33}\text{Te}_{1.67}\text{O}_6$  composition or less.

All X-ray and neutron powder diffraction patterns of these samples show significant peak broadening and peak asymmetry. Refinement of the size and strain parameters in GSAS software indicates that the broadening is due only to the strain parameter. SEM studies shown in Figure 4.19 indicate the crystallite sizes of several hundred nanometers which are too large to broaden the peaks. The observed broadening is not an indication of strain caused by an external stress. Instead, this

strain is caused by inhomogeneities in the lattice directly related to the presence of two cations with very different sizes in the same crystallographic positions as is commonly observed in solid solution. Figure 4.20 represents a plot of room temperature electrical resistivity and Seebeck coefficient versus  $x$  for  $\text{CsAl}_x\text{Te}_{2-x}\text{O}_6$  phases. With increasing Al content there is first a steady decrease in resistivity down to the lowest value at about  $10 \text{ } \Omega\text{cm}$  for  $\text{CsAl}_{0.33}\text{Te}_{1.67}\text{O}_6$ . Further increases in Al content lead to very high resistivity values. The temperature dependence of resistivity of the more conducting samples is shown in Figure 4.21.

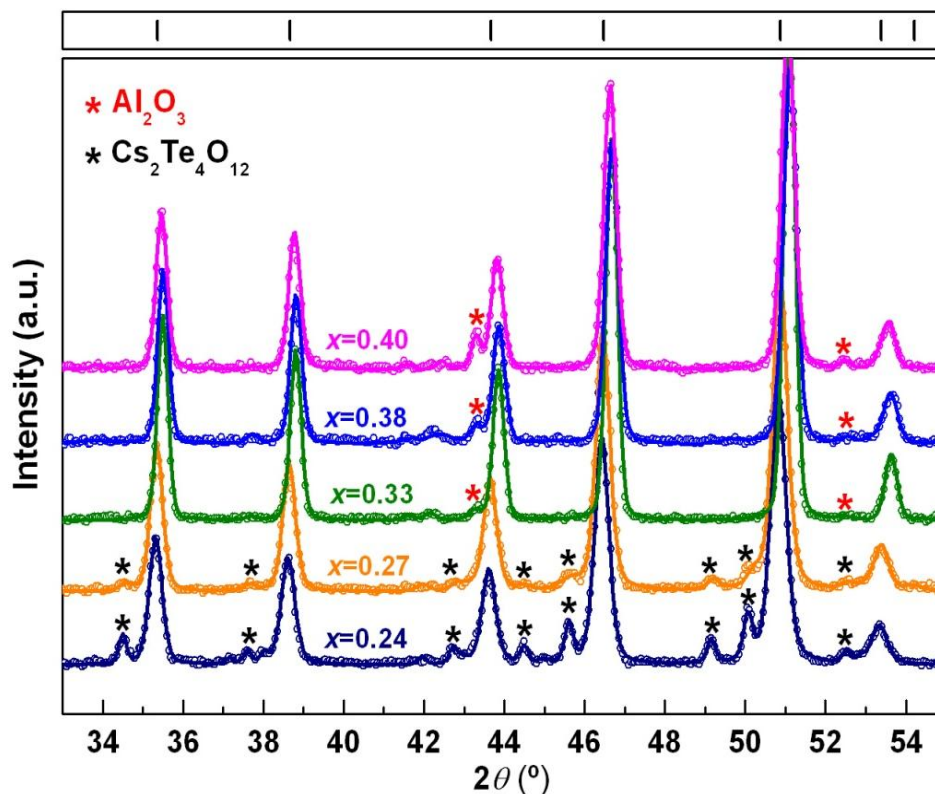


Figure 4.17: Observed (open circles) and calculated (solid line) neutron powder diffraction data of  $\text{CsAl}_x\text{Te}_{2-x}\text{O}_6$  showing the major cubic pyrochlore phase (peak positions denoted as vertical bars on the top), together with minor impurity phases.

Table 4.11: Calculated percentage of impurity from powder refinement

| Composition                                    | Calculated percentage of impurity |
|--|-----------------------------------|
| $\text{CsAl}_{0.24}\text{Te}_{1.76}\text{O}_6$ | 10% $\text{CsTe}_2\text{O}_6$     |
| $\text{CsAl}_{0.27}\text{Te}_{1.73}\text{O}_6$ | 6.9% $\text{CsTe}_2\text{O}_6$    |
| $\text{CsAl}_{0.33}\text{Te}_{1.67}\text{O}_6$ | 0.8% $\text{Al}_2\text{O}_3$      |
| $\text{CsAl}_{0.38}\text{Te}_{1.62}\text{O}_6$ | 0.9% $\text{Al}_2\text{O}_3$      |
| $\text{CsAl}_{0.40}\text{Te}_{1.60}\text{O}_6$ | 1.5% $\text{Al}_2\text{O}_3$      |

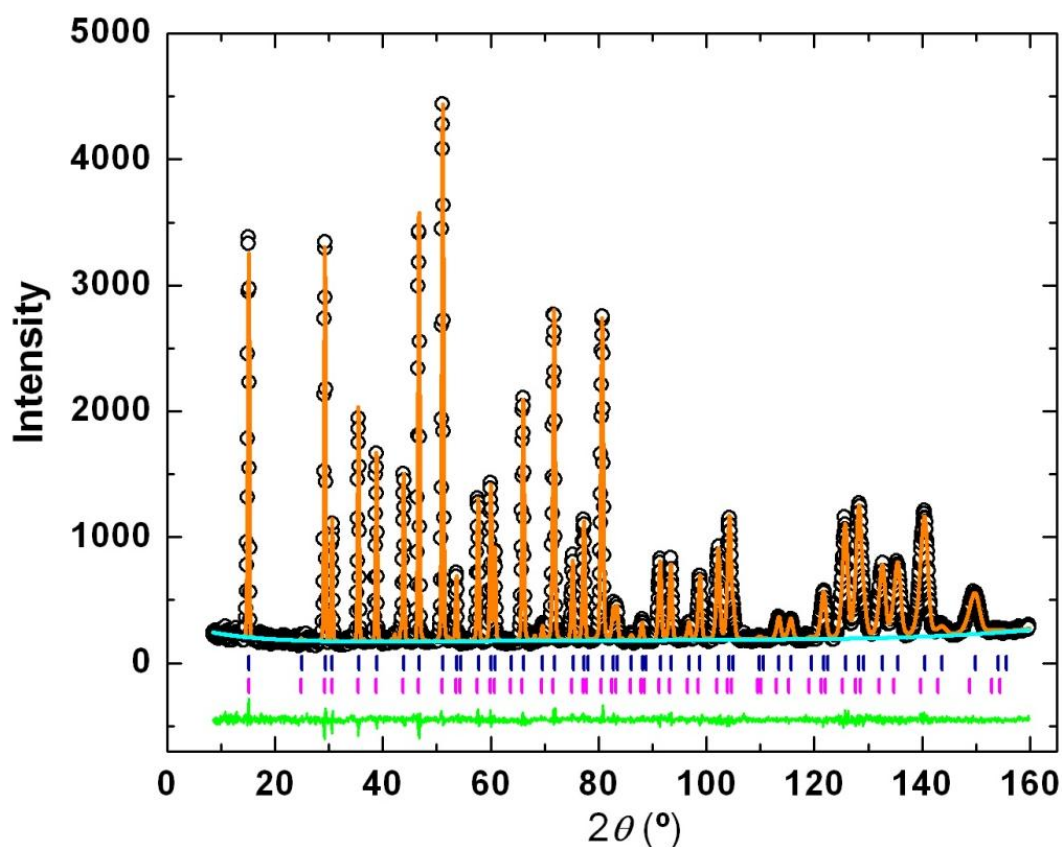


Figure 4.18: Rietveld refinement of neutron powder diffraction data for  $\text{CsAl}_{1/3}\text{Te}_{5/3}\text{O}_6$ . Applied neutron wavelength was  $1.5401(2)$  Å (NIST BT-1). The raw data are plotted as open circles with calculated fit on top. The bottom curve shows the difference between the observed and the calculated data. Vertical bars in the first row indicate the reflection positions of cubic  $\text{CsAl}_{1/3}\text{Te}_{5/3}\text{O}_6$  with cell edge  $10.0889(1)$  Å. Vertical bars in the second row represent the asymmetric strain simulated as a second cubic phase with slightly larger cell edge  $10.1140(1)$  Å.



Table 4.12: Structural refinement results of powder neutron and X-ray (*Italic*) data for  $\text{CsAl}_x\text{Te}_{2-x}\text{O}_6$ .

| Al $x$      | Al $x$<br>(Refined)              | Cs<br>Occupancy                     | Cell $a$<br>(Å)                     | $x(\text{O})$                   | $\chi^2/\text{GOF}$             | wR <sub>p</sub><br>(%)          |
|-------------|----------------------------------|-------------------------------------|-------------------------------------|---------------------------------|---------------------------------|---------------------------------|
| 0.24        | 0.24(1)                          | 0.99(1)                             | 10.1482(1)                          | 0.3193(1)                       | 1.14                            | 5.72                            |
| 0.27        | 0.26(1)                          | 0.99(1)                             | 10.1417(1)                          | 0.3194(1)                       | 1.15                            | 5.86                            |
| 0.33        | 0.30(1)                          | 0.99(1)                             | 10.0889(1)                          | 0.3197(1)                       | 1.43                            | 6.16                            |
| 0.38        | 0.32(1)                          | 0.99(1)                             | 10.0890(1)                          | 0.3196(1)                       | 1.68                            | 6.67                            |
| 0.40        | 0.34(1)                          | 0.99(1)                             | 10.0997(1)                          | 0.3196(1)                       | 0.98                            | 5.12                            |
| <i>0.24</i> | <i>0.24(1)</i>                   | <i>1.02(2)</i>                      | <i>10.1497(1)</i>                   | <i>0.3202(3)</i>                | <i>1.84</i>                     | <i>9.72</i>                     |
| <i>0.27</i> | <i>0.26(1)</i>                   | <i>1.02(2)</i>                      | <i>10.1410(1)</i>                   | <i>0.3187(3)</i>                | <i>1.57</i>                     | <i>8.97</i>                     |
| <i>0.33</i> | <i>0.30(1)</i>                   | <i>1.02(2)</i>                      | <i>10.0891(1)</i>                   | <i>0.3208(3)</i>                | <i>2.58</i>                     | <i>11.5</i>                     |
| <i>0.38</i> | <i>0.32(1)</i>                   | <i>1.02(2)</i>                      | <i>10.0888(1)</i>                   | <i>0.3210(3)</i>                | <i>2.42</i>                     | <i>11.2</i>                     |
| <i>0.40</i> | <i>0.34(1)</i>                   | <i>1.02(2)</i>                      | <i>10.0929(1)</i>                   | <i>0.3214(3)</i>                | <i>1.94</i>                     | <i>9.97</i>                     |
| Al $x$      | Cs<br>$U_{11}$ (Å <sup>2</sup> ) | Al/Te<br>$U_{11}$ (Å <sup>2</sup> ) | Al/Te<br>$U_{12}$ (Å <sup>2</sup> ) | O<br>$U_{11}$ (Å <sup>2</sup> ) | O<br>$U_{22}$ (Å <sup>2</sup> ) | O<br>$U_{23}$ (Å <sup>2</sup> ) |
| 0.24        | 0.0154(5)                        | 0.0059(3)                           | -0.0003(3)                          | 0.0079(3)                       | 0.0135(3)                       | 0.0044(5)                       |
| 0.27        | 0.0175(4)                        | 0.0073(3)                           | -0.0004(3)                          | 0.0094(3)                       | 0.0130(2)                       | 0.0050(4)                       |
| 0.33        | 0.0166(4)                        | 0.0053(2)                           | -0.0004(3)                          | 0.0079(3)                       | 0.0099(2)                       | 0.0040(4)                       |
| 0.38        | 0.0161(5)                        | 0.0047(3)                           | -0.0004(3)                          | 0.0077(3)                       | 0.0103(2)                       | 0.0041(4)                       |
| 0.40        | 0.0176(4)                        | 0.0043(2)                           | 0.00(2)                             | 0.0077(3)                       | 0.0108(2)                       | 0.0040(4)                       |
| <i>0.24</i> | <i>0.0215(3)</i>                 | <i>0.0083(4)</i>                    | —                                   | <i>0.026(3)</i>                 | —                               | —                               |
| <i>0.27</i> | <i>0.0162(3)</i>                 | <i>0.0073(3)</i>                    | —                                   | <i>0.026(3)</i>                 | —                               | —                               |
| <i>0.33</i> | <i>0.0182(3)</i>                 | <i>0.0056(2)</i>                    | —                                   | <i>0.002(1)</i>                 | —                               | —                               |
| <i>0.38</i> | <i>0.0154(3)</i>                 | <i>0.0039(2)</i>                    | —                                   | <i>0.002(2)</i>                 | —                               | —                               |
| <i>0.40</i> | <i>0.0170(3)</i>                 | <i>0.0048(2)</i>                    | —                                   | <i>0.004(1)</i>                 | —                               | —                               |

**Notes:**

- The value of  $x$  in the first column is the nominal Al content in  $\text{CsAl}_x\text{Te}_{2-x}\text{O}_6$ . The same powder samples were used for neutron and X-ray data collection.
- Standard uncertainties for powder neutron refinements, given in parentheses, do not reflect the uncertainty in the neutron wavelength.
- Anisotropic thermal displacement parameters are expressed as  $\exp[-2\pi^2 \times (U_{11}h^2a^{*2} + U_{22}k^2b^{*2} + U_{33}l^2c^{*2} + 2U_{12}hka^*b^* + 2U_{13}hla^*c^* + 2U_{23}klb^*c^*)]$ ;  $U_{11} = U_{22} = U_{33}$ ,  $U_{12} = U_{13} = U_{23} = 0$  for Cs;  $U_{11} = U_{22} = U_{33}$ ,  $U_{12} = U_{13} = U_{23}$  for Al/Te;  $U_{22} = U_{33}$ ,  $U_{12} = U_{13} = 0$  for O. Only isotropic thermal displacement parameters,  $U_{\text{iso}}$ , were refined for powder XRD data.

Table 4.13: Bond lengths, bond angles and bond valence sums calculated from powder neutron structural refinements of  $\text{CsAl}_x\text{Te}_{2-x}\text{O}_6$ .

| Al $x$ | Cs–O<br>$\times 6$ , (Å) | Cs–O<br>$\times 12$ , (Å) | M–O<br>$\times 6$ , (Å) | Cs, BVS<br>(Cs–O $\times 18$ ) | M–O–M<br>(°) | O–M–O<br>(°) |
|--------|--------------------------|---------------------------|-------------------------|--------------------------------|--------------|--------------|
| 0.24   | 3.1000(9)                | 3.6299(1)                 | 1.9259(3)               | 1.40                           | 137.16(5)    | 92.72(3)     |
| 0.27   | 3.0975(8)                | 3.6275(1)                 | 1.9248(3)               | 1.41                           | 137.14(4)    | 92.74(3)     |
| 0.33   | 3.0824(7)                | 3.6126(1)                 | 1.9182(3)               | 1.48                           | 136.98(4)    | 92.84(3)     |
| 0.38   | 3.0824(9)                | 3.6121(1)                 | 1.9176(3)               | 1.47                           | 137.01(5)    | 92.82(3)     |
| 0.40   | 3.0845(7)                | 3.6146(1)                 | 1.9190(3)               | 1.45                           | 137.01(4)    | 92.83(3)     |

**Notes:**

- The value of  $x$  in the first column is the nominal Al content in  $\text{CsAl}_x\text{Te}_{2-x}\text{O}_6$ .
- M stands for Al and Te that share the same 16c (or 16d) site.
- Bond valence sums (BVS) were calculated using the Bond Valence Calculator [59]

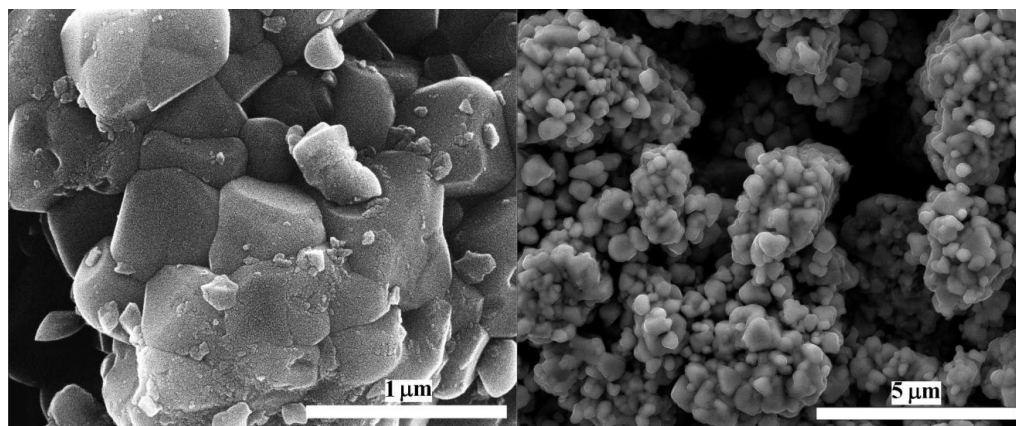


Figure 4.19: Scanning electron microscope images of  $\text{CsAl}_{1/3}\text{Te}_{5/3}\text{O}_6$  ( $x = 0.33$ ) powder at different magnifications.

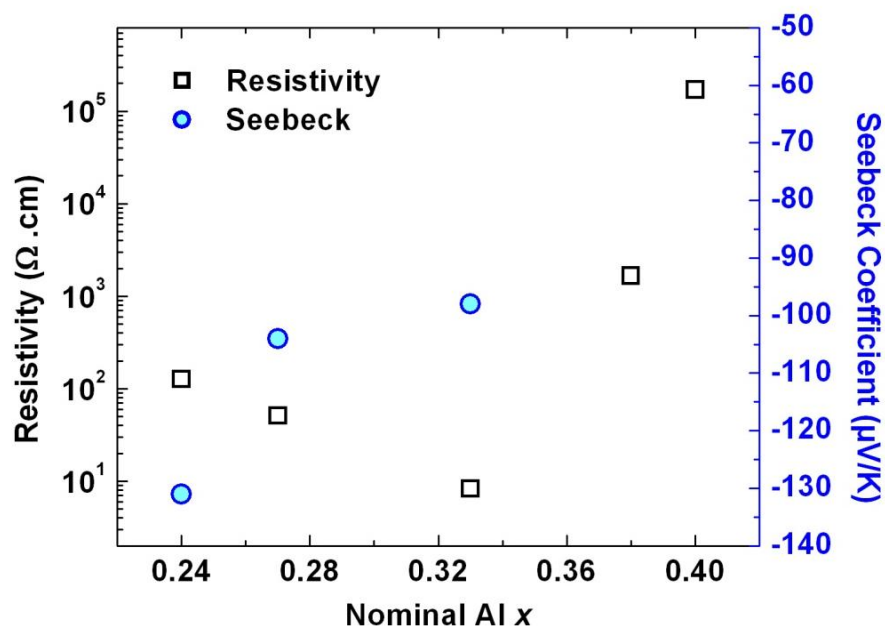


Figure 4.20: Resistivity of  $\text{CsAl}_x\text{Te}_{2-x}\text{O}_6$  neutron samples plotted vs. temperature. The values of  $x$  are nominal Al content. Uncertainties are not indicated, but are commensurate with the scatter of the data.

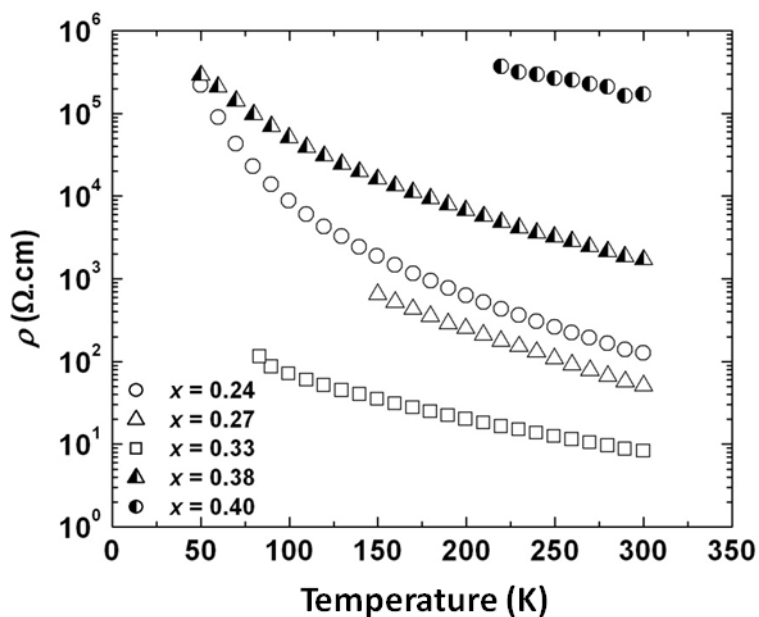


Figure 4.21: Variation of electrical resistivity versus room temperature of  $\text{CsAl}_x\text{Te}_{2-x}\text{O}_6$  neutron samples. Uncertainties are not indicated, but are less than the point size.

Variation of the slopes indicates that  $\text{CsAl}_{0.33}\text{Te}_{1.67}\text{O}_6$  also has the lowest activation energy which increases when Al content is either increased or decreased. Absolute values of Seebeck coefficient are lower in the more conducting samples as expected (Fig. 4.20). A Seebeck coefficient could not be measured in the more insulating samples.

#### 4.4.3 Discussion

Detailed structural analyses from single X-ray diffraction indicated that all crystals form  $\text{AB}_2\text{O}_6$  defect pyrochlore structure with  $Fd\bar{3}m$  space group. As discussed earlier in 4.2, the structure consists of  $\text{B}_2\text{O}_6$  octahedral network with A cations in interstitial sites. Although there are more than one available site for A cation, it is usually restricted by ionic radius and the polarizability of A.

Many previous studies have described Cs in the  $\text{CsM}_2\text{O}_6$  pyrochlores as being in the 32e site, slightly displaced from the ideal 8b site. In recent refinements of the structures of  $\text{CsTi}_{1/2}\text{W}_{3/2}\text{O}_6$ ,  $\text{CsTi}_{1/4}\text{Zr}_{1/4}\text{W}_{3/2}\text{O}_6$ ,  $\text{CsZr}_{1/2}\text{W}_{3/2}\text{O}_6$ , and  $\text{CsHf}_{1/2}\text{W}_{3/2}\text{O}_6$ , Cs atom was always placed in the 32e site. However, the displacements of Cs from the ideal 8b site never exceeded one standard deviation [60]. Thus, there is no evidence for static displacements of Cs from the 8b site. A very recent paper reexamined  $\text{CsTi}_{1/2}\text{W}_{3/2}\text{O}_6$  using both X-ray and neutron powder diffraction data also used the 32e site for Cs [61]. In their study, small displacements of Cs from 8b were reported, but they were in opposite directions for the X-ray versus the neutron data and an average of the two refinements places Cs essentially exactly at the 8b site.

In this work, X-ray diffraction data of 7 different  $\text{CsM}_2\text{O}_6$  crystals were refined. The cubic cell edges ranged from 10.02 to 10.32 Å for these crystals. In no case was it found that Cs in 32e rather than 8b gave a better fit to observed data. There is, however, an explanation for why the 32e site for Cs seems by some workers to be slightly preferred over 8b. There has never been a refinement of any  $\text{CsM}_2\text{O}_6$  pyrochlores using anisotropic thermal parameters for Cs; although, Cs always has the largest thermal parameter value of the three atoms in the structure and Cs has a very high scattering power in X-ray diffraction. If only the usual thermal ellipsoid model based on a harmonic potential well is considered, the thermal motion of Cs is constrained to be isotropic by the symmetry of 8b site.

However, the 8b site has tetrahedral symmetry (Fig.4.22) and thus an anharmonic potential well. Therefore, Cs thermal motion cannot be well described by the commonly used thermal ellipsoid model. Placing Cs in 32e is a way then to approximate the impact of the thermal motion of Cs in the actual anharmonic potential well. Recent studies of  $\text{KOs}_2\text{O}_6$  with the pyrochlore structure have concluded that K is in the 8b site, but it shows anharmonicity along the [111] direction [62-63].

Anharmonic thermal motion has been well studied for ZnS, ZnSe, ZnTe, and GaP [64]. Due to the high symmetry of these structures as well as the A site in the  $\text{AB}_2\text{O}_6$  pyrochlore structure, an anharmonic refinement adds just one more parameter to the refinement for an atom at the site with tetrahedral symmetry. We find that the anharmonic component of the atomic displacement parameters (ADP) is small for Cs but becomes obvious when Rb is substituted for Cs. This difference between the

behavior of Cs and Rb might be expected because the bond valence sum for Cs is about 1.5 (Table 4.13) whereas the Rb value is 1.08. Thus, Cs is compressed by the lattice and more tightly held than Rb. Figure 4.23 shows the result of refining the anharmonic contribution to the ADP of Rb. The resulting tetrahedron centered at the 8b site indicates that the preferred direction of the thermal motion of Rb along the 3-fold axis is toward the nearby 16d site. This might be expected because the empty 16d sites provide the pathway for the ionic conductivity which is more pronounced for Rb relative to Cs due to the smaller size of Rb. The much smaller anharmonic motion of Cs appears to be in the opposite direction which might be expected based on the 8b site potential well calculated by Pannetier [65].

Peak broadening in the diffraction patterns was a common feature of all the  $\text{CsAl}_x\text{Te}_{2-x}\text{O}_6$  polycrystalline samples (Fig. 4.17), and this broadening was analyzed using our neutron diffraction data. Refinement of the size and strain parameters in GSAS software indicates that the broadening is entirely due to the strain parameter. Such broadening is common in systems with variable composition where compositional homogeneity at the unit cell level is impossible. Although lattice planes are flat and regularly spaced in the ideal crystal, in reality they can be bent and result in irregular interplanar distances. As a consequence, diffraction peaks are broadened which can be modeled as strain. Similar phenomenon was observed in LaNi-based alloys where the hybridizing caused peak broadening that could be accounted for solely on the basis of lattice strain [66].

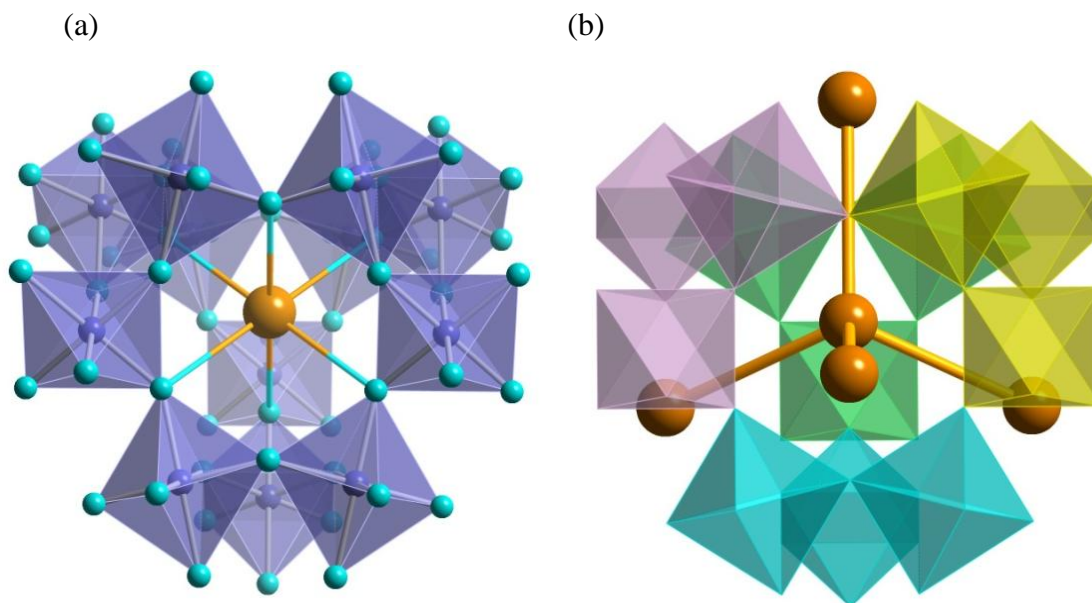


Figure 4.22: (a) Structure of cubic  $\text{Cs}(\text{Al,Te})_2\text{O}_6$  pyrochlores as a network of corner shared  $(\text{Al/Te})\text{O}_6$  octahedra (blue, 16c sites) with Cs (orange) in 8b interstitial sites. Oxygen atoms (48f) are shown in turquoise color. (b) Although the first Cs–O coordination sphere is a perfect octahedron, the symmetry of the Cs (orange, 8b sites) is actually tetrahedral. Apexes of the tetrahedron around Cs can be viewed as centers of the four colored triangles formed by corner shared  $(\text{Al/Te})\text{O}_6$  octahedra. Four neighboring Cs atoms (orange) are also tetrahedrally located around the center Cs. Different colors are used for the same  $(\text{Al/Te})\text{O}_6$  octahedra to show the tetrahedral symmetry, and the Al/Te and O atoms are not shown for clarity.

GSAS software treats strain as if the lattice expansion and contraction are equivalent. Therefore, the peaks remain symmetrical as they broaden. However, the lattice expansion and contraction are not necessary equivalent in the real lattices. In such situation, peaks are not symmetrical. In order to account for this asymmetry, the second phase was added to act as an asymmetry component. Figure 4.24 shows an example of a typical  $\text{CsAl}_x\text{Te}_{2-x}\text{O}_6$  peak. Using the refined strain value for this sample, three peaks can be used to approximate this broad peak. The peak widths in

the main three calculated peaks (Fig.4.24 peak 1-3) have been constrained to the instrumental parameters for this instrument; i.e., these calculated peaks have the shapes expected with no size or strain broadening. This demonstrates that this peak with an average cubic cell edge of 10.09 Å actually has a range of cubic cell edges from 10.07 to 10.12 Å. The fourth peak (Fig.4.24) was included to account for the asymmetry of the strain has a cell edge of 10.13 Å.

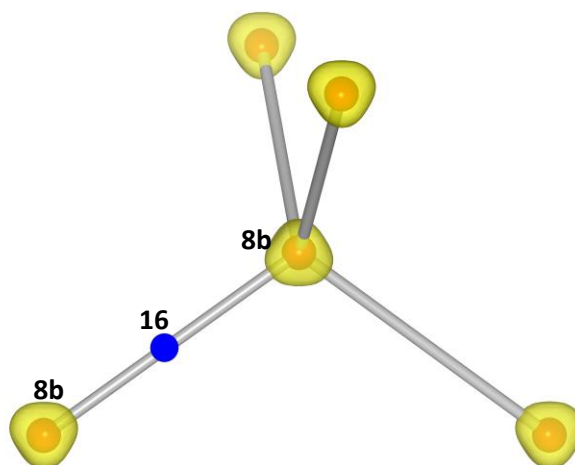


Figure 4.23: Neighboring Rb atoms (red) in pyrochlore  $\text{RbAl}_{1/3}\text{Te}_{5/3}\text{O}_6$  are tetrahedrally arranged (lines drawn between adjacent Rb atoms to guide the eye). The Rb probability density function (PDF) cannot be described as an ellipsoid due to the tetrahedral symmetry. The application of anharmonic refinement of the PDF leads to tetrahedral-shaped probability density isosurfaces (yellow) centered in Rb atoms at 8b sites. The electron density is moving toward the empty 16d sites (blue). The lines joining the 8b sites are 3-fold axes, which extend through the 8b sites. The 32e sites lie on this 3-fold axis. Placing atoms in 32e sites close to the 8b sites approximates an anharmonic motion.

Although ionic conductivity is detected in some pyrochlore oxides with similar composition, it is very low, usually undetectable at room temperature [68]. A typical ionic conductivity of  $\text{CsM}_2\text{O}_6$  pyrochlores at 300°C is only about  $10^{-6}$  S/cm. However,



significant electronic conductivity and color of some  $\text{CsM}_{1/3}^{3+}\text{Te}_{5/3}\text{O}_6$  and  $\text{CsM}_{1/2}^{4+}\text{Te}_{3/2}\text{O}_6$  pyrochlores prepared in this work (4.3) indicate the deviations from ideal formula which was presumed to be related to mixed valency of Te.

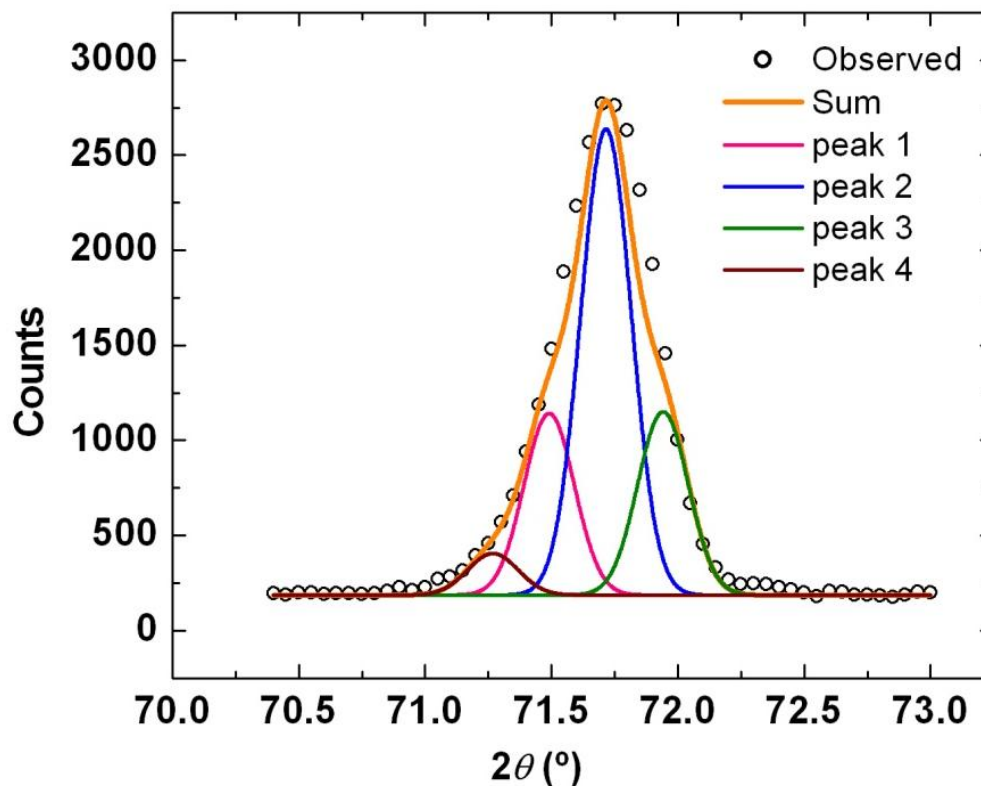


Figure 4.24: Asymmetric peak broadening in  $\text{CsAl}_x\text{Te}_{2-x}\text{O}_6$  neutron powder diffraction patterns showing the impact of internal strain.

Employing two different synthesis methods; crystal growth and solid state reaction, cubic cell edge of the Cs/Al/Te/O pyrochlore phases could be varied from 10.06 to 10.14 Å (Fig.4.25). In general, the unit cell parameter increases with Te content. Both synthesis methods resulted in products very close to the ideal  $\text{CsAl}_{1/3}\text{Te}_{5/3}\text{O}_6$  composition. Te rich phases could be obtained as polycrystalline

sample from solid state reaction while crystal growths always resulted in Al rich phases.

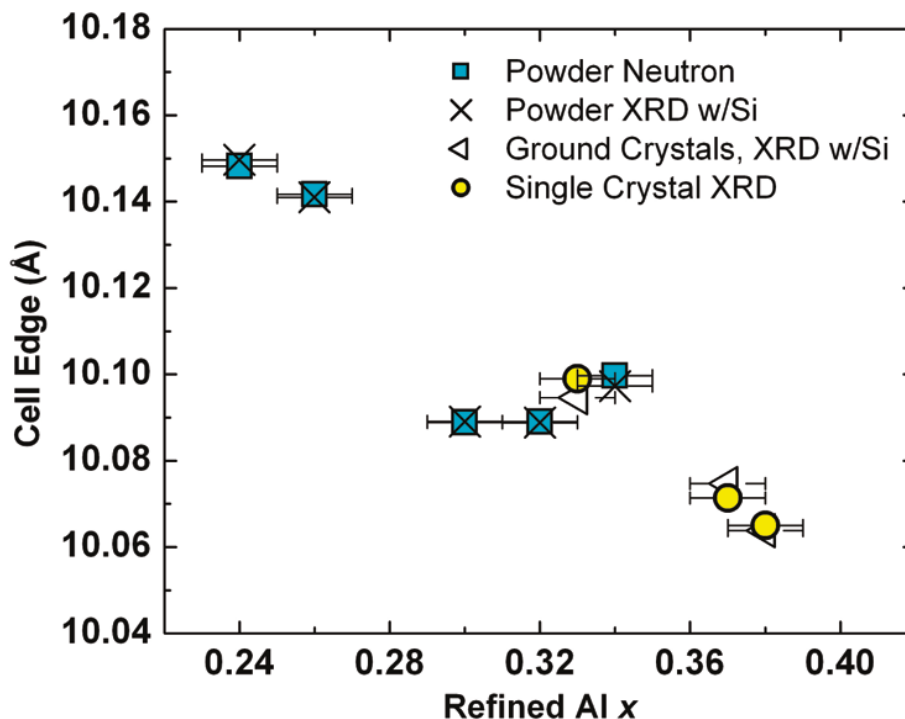


Figure 4.25: Variation of cell edge with refined Al content in  $\text{CsAl}_x\text{Te}_{2-x}\text{O}_6$ . Cell edges for ground crystals (from the same batch of the single crystal analyzed) were calculated by LeBail fit of powder XRD data with Si as an internal standard. The refined Al  $x$  values for the ground crystals were taken from the corresponding single crystal refinements. The errors in cell edge are smaller than the points (see Table 4.12), and error bars for  $x$  represent  $1\sigma$ .

In order to keep the charge balanced in the Te rich phases with Al content less than 0.33, some  $\text{Te}^{6+}$  is reduced to  $\text{Te}^{4+}$  giving  $\text{CsAl}_{1/3-y/3}\text{Te}_{y/2}^{4+}\text{Te}_{5/3-y/6}^{6+}\text{O}_6$  composition.  $\text{CsAl}_{1/3-y/3}\text{Te}_{y/2}^{4+}\text{Te}_{5/3-y/6}^{6+}\text{O}_6$  can be viewed as a solid solution between  $\text{CsAl}_{1/3}\text{Te}_{5/3}\text{O}_6$  and  $\text{CsTe}_2\text{O}_6$  [49]. Given the radii in 6-fold coordination of  $0.535\text{ \AA}$  for  $\text{Al}^{3+}$ ,  $0.56\text{ \AA}$  for  $\text{Te}^{6+}$ , and  $0.97\text{ \AA}$  for  $\text{Te}^{4+}$  [53], the increase in cubic cell edge is expected as  $y$

increases. It is primarily the very large  $\text{Te}^{4+}$  that causes the lattice expansion and strain. Although  $\text{Te}^{4+}$  will be compressed by the lattice, lattice relaxation in the vicinity of  $\text{Te}^{4+}$  will cause some local lattice expansion. Furthermore, there will very likely be some clustering of  $\text{Te}^{4+}$  as a precursor to phase separation of  $\text{CsTe}_2\text{O}_6$  from the  $\text{CsAl}_{1/3}\text{Te}_{5/3}\text{O}_6/\text{CsTe}_2\text{O}_6$  solid solution. Solubility limit of about 30%  $\text{CsTe}_2\text{O}_6$  in  $\text{CsAl}_{1/3}\text{Te}_{5/3}\text{O}_6$  is found. On cooling this solubility limit might decrease, if equilibrium were achieved. Diffusion of  $\text{Te}^{4+}$  is not likely to impede phase segregation because this is in fact only an electron hopping process from Te to Te. However, Al diffusion will be slow and will impede phase segregation. The result may then be some clustering of  $\text{Te}^{4+}$  with no actual phase segregation. There will be lattice expansion in the areas of  $\text{Te}^{4+}$  clustering, relative to the remainder of the lattice. This will broaden peaks according to the usual strain function. The broadening decreases as  $y$  goes to 0.0 because the  $\text{Te}^{4+}$  content on 16c sites is decreasing.

The small amount of  $\text{Te}^{4+}$  introduces filled defect states lying just below the conduction band (Fig. 4.26). The transition of electrons from defect level to conduction band increases number of free electrons which consequently increase the conductivity. However, the energy of this level is very sensitive to the dimensions of the lattice. Since  $\text{Te}^{4+}$  is much larger than  $\text{Al}^{3+}$  and  $\text{Te}^{6+}$ , this  $\text{Te}^{4+}$  is compressed in the lattice. However, when the lattice expands the compression of  $\text{Te}^{4+}$  is relieved which stabilizes the  $\text{Te}^{4+}$  5s state and decreases its energy level. Although the number of electrons in defect states increases with  $y$  ( $\text{Te}^{4+}$  content), the energy level of the defect state is decreased. As a result, the conductivity decreases when  $y$  increases. The

temperature dependence of resistivity (Fig. 4.20) supports that this filled Te 5s state is dropping in energy as  $y$  increases. As  $y$  goes to zero,  $x=0.33$  and  $y=0$ , the filled Te 5s states are lost, and there is a steep rise in resistivity. The actual point of minimum resistivity is uncertain. Based on nominal compositions, the minimum is very close to the ideal  $\text{CsAl}_{0.33}\text{Te}_{1.67}\text{O}_6$  composition, as would be expected in this model. Refinement of the Al/Te ratio indicates that the minimum may be at an  $x$  value in  $\text{CsAl}_x\text{Te}_{2-x}\text{O}_6$  of about 0.30 rather than 0.33 (Fig. 4.25). However, although the Al/Te ratios from analysis of diffraction data are a good way of estimating the range of the compositions, this method is not accurate enough to be certain just how close it is to the ideal composition.

Al rich phases can be represented as  $(\text{Cs}_{1-z}\text{Te}_z^{4+})(\text{Al}_{1/3+z}\text{Te}_{5/3-z}^{6+})\text{O}_6$ . This formula is consistent with their preparation utilizing an excess of  $\text{TeO}_2$  as a flux. Less amount of large  $\text{Te}^{4+}$  is presented in octahedral sites resulting in less strain in the lattice and less broadening of the diffraction peaks. The cavities of the network in pyrochlore structure can be highly disordered. For example, Cd in  $\text{Cd}_2\text{Nb}_2\text{O}_7$  and  $\text{Cd}_2\text{Ta}_2\text{O}_7$  pyrochlores could be significantly substituted with Mg, Mn, Fe, Co, Ni, Cu and Zn although these cations are much smaller for the Cd site. They are presumed to be displaced off this site in a disordered manner [68]. In the case of the  $\text{Sn}_2\text{Nb}_2\text{O}_7$  pyrochlore, the  $\text{Sn}^{2+}$  is found to be displaced about 0.4 Å from the ideal position [69]. Similarly, a likely site for  $\text{Te}^{4+}$  in  $(\text{Cs}_{1-z}\text{Te}_z^{4+})(\text{Al}_{1/3+z}\text{Te}_{5/3-z}^{6+})\text{O}_6$  phases is 32e because it gives 3 short Te–O distances on one side of Te which is a normal situation for  $\text{Te}^{4+}$ . For example, in the case of the perovskite  $\text{TeCuO}_3$ , the  $\text{Te}^{4+}$  has 3 short Te–O bonds

on one side of Te with an average distance of 1.945 Å [70]. Therefore, Te 5s defect states still exist in these phases but less compression in the lattice lower their energy level. These filled 5s states contribute to the observed color but not to conductivity.

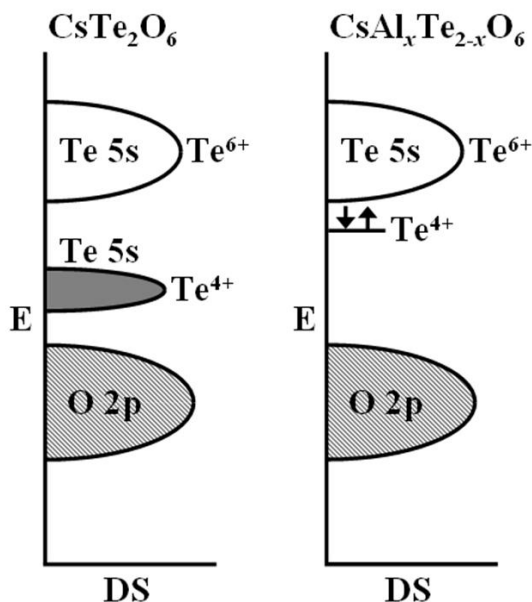


Figure 4.26: Schematic energy level diagrams for rhombohedral  $\text{CsTe}_2\text{O}_6$  and cubic  $\text{CsAl}_x\text{Te}_{2-x}\text{O}_6$  phases showing O 2p and Te 5s states only. The filled 5s states for  $\text{Te}^{4+}$  in  $\text{CsTe}_2\text{O}_6$  are at lower energy than the empty 5s states due to the longer  $\text{Te}^{4+}\text{-O}$  distances relative to the  $\text{Te}^{6+}\text{-O}$  distances. In cubic  $\text{CsAl}_x\text{Te}_{2-x}\text{O}_6$  phases the  $\text{Te}^{4+}$  states are pushed up in energy as the lattice compresses the  $\text{Te}^{4+}\text{-O}$  distances with increasing  $x$ . At  $x = 0.33$  the  $\text{Te}^{4+}$  donor states disappear.

The cubic cell edge increases as the M–O bond distance increases for all the  $\text{CsM}_2\text{O}_6$  pyrochlores prepared and evaluated in this study (Fig. 4.27(a)). Such dependence is expected, and this plot substantiates the reliability of determination of the oxygen positional parameters for these phases in the present work. Figure 4.27(a) also shows that the Cs–O distance increases as the unit cell and M–O distance increase which is not necessary. As the M–O distance changes, one can adjust the oxygen

positional parameter and the unit cell edge such that there is no change in the Cs–O distance. Consider the largest cell edge in Figure 4.27,  $a = 10.321 \text{ \AA}$  and  $x(\text{O}) = 0.3201$ . This gives an M–O distance of  $1.963 \text{ \AA}$  and a Cs–O distance of  $3.147 \text{ \AA}$ . When the M–O distance is  $1.908 \text{ \AA}$ , by adjusting  $a$  to  $10.155 \text{ \AA}$  and  $x(\text{O})$  to  $0.314$ , Cs–O distance can be constant at  $3.147 \text{ \AA}$ . Instead, Cs–O distance decreases to  $3.046$  with a cell edge of  $10.017 \text{ \AA}$ , and  $x(\text{O})$  of  $0.3209$ . So why has the Cs–O distance changed so much when it could have remained constant? Some understanding comes from examination of the M–O–M and O–M–O bond angles (Fig. 4.27(b)) which show a very small variation compared to the range known for all  $\text{AM}_2\text{O}_6$  ( $A = \text{K, Rb, Cs, Tl}$ ) compounds with the pyrochlore structure [2]. Keeping the Cs–O distance constant with decreasing M–O in the above example would cause the O–M–O angle to drop to  $90.61^\circ$  and the M–O–M angle to increase to  $140.20^\circ$ . These angles are far outside the range observed for our  $\text{Cs}(\text{M,Te})_2\text{O}_6$  pyrochlores but well within the range found for all  $\text{AM}_2\text{O}_6$  ( $A = \text{K, Rb, Cs, Tl}$ ) compounds with the pyrochlore structure, where the M–O–M angle can increase to  $145.4^\circ$  and the O–M–O angle can decrease to  $86.9^\circ$  (Fig. 4.27(b)).

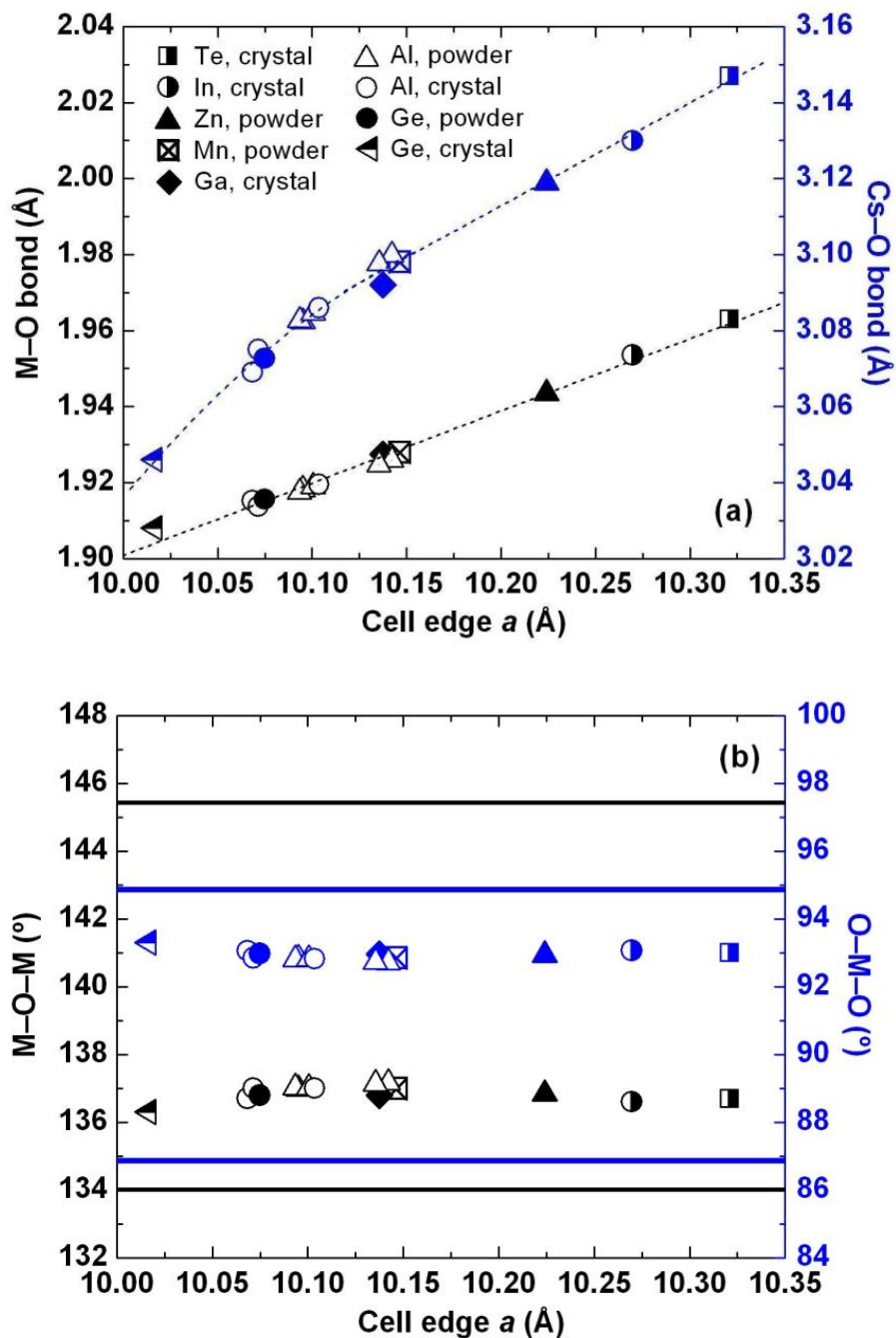


Figure 4.27: Bond distances (a) and angles (b) vs. cell edge for all the  $\text{Cs}(\text{M},\text{Te})_2\text{O}_6$  ( $\text{M} = \text{Te}, \text{In}, \text{Zn}, \text{Mn}, \text{Ga}, \text{Al}$  and  $\text{Ge}$ ) pyrochlore samples prepared in this and previous work. Black and blue solid lines in (b) indicate the ranges of M-O-M and O-M-O bond angles, respectively, found for all the  $\text{A}(\text{M},\text{M}')_2\text{O}_6$  ( $\text{A} = \text{K}, \text{Rb}, \text{Cs}, \text{TI}$ ) pyrochlores [2]. Uncertainties are not indicated, but are less than the point size.

For the  $\text{CsM}_2\text{O}_6$  pyrochlores, the framework is resisting these angle changes even though the  $\text{MO}_6$  octahedra would become less distorted. The bond valence sum (Fig. 4.28) for Cs (CN = 18) is above 1.0 for even the largest Cs–O distance, and only decreases slightly after adjustment to consider the softness of the Cs–O bond is made [71]. It continues to increase with the decreasing M–O distance even though this increase is not necessary.

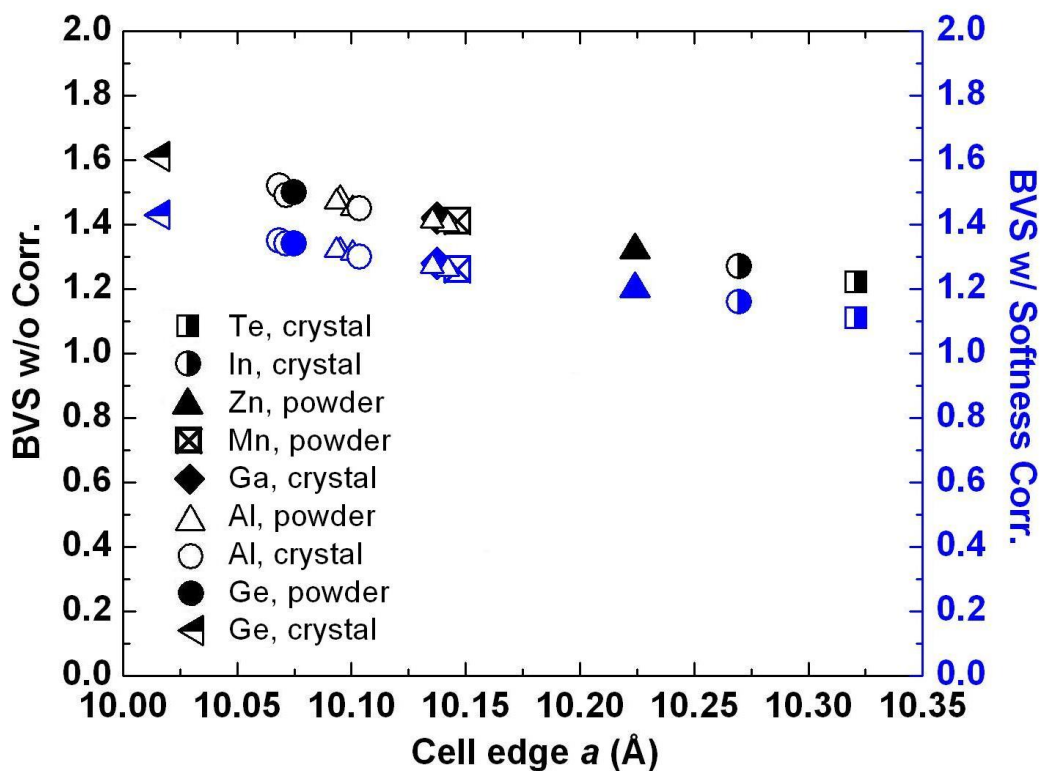


Figure 4.28: Bond valence sums of Cs (CN = 18, 6 short bonds and 12 long bonds) for all the  $\text{Cs}(\text{M},\text{Te})_2\text{O}_6$  (M = Te, In, Zn, Mn, Ga, Al and Ge) pyrochlore samples prepared in this and previous work. BVS adjusted to the softness of the Cs–O bond (blue) are slightly smaller than BVS not corrected with bond softness (black).



A partial explanation is that the Cs–O distance is highly compressible. The compressibility of an A–O bond increases as the oxidation state of A decreases and the size of A increases. Thus, the Cs–O bond is the most compressible of all metal-oxygen bonds [72]. This does not, however, really explain the behavior of the Cs–O distance shown in Fig. 4.27(a). The explanation may be related to the anharmonicity of the Cs thermal motion or it may be related to interstitial species other than Cs.

#### 4.4.4 Conclusion

A Cs/Al/Te/O pyrochlore phases have been prepared with a cubic cell edge ranging from 10.06 Å for the Al rich limit to 10.14 Å for the Te rich limit. Rietveld structural analyses based on both X-ray and neutron diffraction data were performed on 5 different compositions. Single crystals of 6 compositions were prepared and studied by X-ray diffraction. A maximum in the electrical conductivity of about 0.1 S/cm is found in the middle of this range close to the ideal composition of  $\text{CsAl}_{1/3}\text{Te}_{5/3}\text{O}_6$ . Changes of cell parameters and conductivities were explained by two mechanisms. When Al content is less than ideal value, some  $\text{Te}^{6+}$  is reduced to  $\text{Te}^{4+}$  where electron transfer between the two species results in the color and conductivity. However, for compositions with  $\text{Al} > 0.33$ , extra  $\text{Te}^{4+}$  occupy the interstitial sites of the structure giving rise to the color but the difference between two sites of mixed valency limits the electron transfer and thus the conductivity.

#### 4.4.5 Experimental

Compositions of the  $\text{CsAl}_x\text{Te}_{2-x}\text{O}_6$  type with  $x = 0.25, 0.27, 0.30, 0.33, 0.36, 0.40, 0.45,$  and  $0.5$  were prepared by solid state reaction using  $\text{CsNO}_3$  (Alfa Aesar, 99.8%),  $\text{TeO}_2$  (Aldrich, 99+%), and  $\text{Al}_2\text{O}_3$  (Aldrich, 99.99%) as reactants. Stoichiometric mixtures of starting materials were ground and heated twice at  $600\text{ }^\circ\text{C}$  for 12 h in gold crucibles with intermediate grinding. Powders were black for all values of  $x$ . Higher heating temperatures resulted in the formation of a glass. Crystals were grown using  $\text{TeO}_2$  as a flux. A 1:1 weight ratio of a  $\text{CsM}_x\text{Te}_{2-x}\text{O}_6$  ( $M = \text{Te, In, Ga, Ge}$ ) and  $\text{CsAl}_x\text{Te}_{2-x}\text{O}_6$  phase and  $\text{TeO}_2$  were mixed and heated in air at  $800\text{ }^\circ\text{C}$  for 3 h in a gold crucible. The crucible was then cooled at  $3^\circ\text{C/h.}$  to  $600\text{ }^\circ\text{C}$  whereupon the furnace was turned off and allowed to cool to room temperature. The flux was dissolved in 50%v/v HCl solution to free the crystals. Attempts to use a 1:4 flux ratio led to glass formation under these conditions. Examination of the “black” crystals under a microscope shows that they can be transparent grey.

Our structural studies are based on powder X-ray and neutron diffraction data and on single crystal X-ray diffraction data. Neutron diffraction data were obtained at the NIST Center for Neutron Research for samples with nominal  $x$  values of 0.24, 0.27, 0.33, 0.38, and 0.40. Neutron powder diffraction data were collected using the BT-1 32-counter high-resolution diffractometer at the NIST Center for Neutron Research at the National Institute of Standards and Technology. A Cu (311) monochromator, yielding a wavelength of  $1.5401(2)\text{ \AA}$ , was employed. Collimation of  $15'$  of arc was used before the monochromator,  $20'$  before the sample, and  $7'$  before the

detectors. The samples were loaded into vanadium containers 15.8 mm in diameter and 50 mm in length. Data were collected at room temperature over a  $2\theta$  range of  $3^\circ$  to  $168^\circ$ . X-ray diffraction data on the same samples were collected on a Rigaku MiniFlex II diffractometer using Cu  $K\alpha$  radiation and a graphite monochromator. A Si internal standard was used in some cases. The neutron and XRD data were refined by the Rietveld method using GSAS software. Single-crystal X-ray diffraction data were collected using a Bruker SMART APEXII CCD system. A standard focus tube was used with an anode power of 50 kV at 30 mA. A subsequent SADABS correction was applied. The crystal structure was solved with the direct method program SHELXS and refined with full-matrix least-squares program SHELXTL [73]. These single crystal refinements confirmed the pyrochlore structure in space group  $Fd\bar{3}m$ . One has a choice of 4 different settings within space group  $Fd\bar{3}m$ . Unless otherwise indicated, in the discussion we have placed Cs in 8b at  $3/8, 3/8, 3/8$ , Al/Te in 16c at  $0, 0, 0$ , and O in 48f at  $x, 1/8, 1/8$ . Electrical conductivity data were obtained on sintered pellets by the four-probe method using a QD PPMS system. Seebeck coefficients were determined by a static method and could not be determined on the samples with very low conductivities.

## 4.5 Synthesis and Characterization of Novel $\text{Rb}(\text{M},\text{Te})_2\text{O}_6$ Pyrochlores

### 4.5.1 Introduction

The interesting electrical properties in conducting  $\text{Cs}(\text{M},\text{Te})_2\text{O}_6$  as discussed in 4.3-4.4 have led to the interest in similar phases with Rb as  $\text{A}^+$  cation,  $\text{Rb}(\text{M},\text{Te})_2\text{O}_6$ . In this work, synthesis and preliminary characterizations of novel  $\text{Rb}(\text{M},\text{Te})_2\text{O}_6$  are discussed. Moreover, crystal growth and structural analysis of  $\text{RbAl}_{0.33}\text{Te}_{1.67}\text{O}_6$  are also reported.

### 4.5.2 Results

#### 4.5.2.1 Polycrystalline Samples

New pyrochlore oxides  $\text{Rb}(\text{M},\text{Te})_2\text{O}_6$ ,  $\text{M} = \text{M}^{2+}$ ,  $\text{M}^{3+}$ , and  $\text{M}^{4+}$  prepared in this work are shown in Table 4.14 with cell parameters at room temperature, color, and preliminary data on electrical conductivity. Powder x-ray diffraction patterns indicated cubic defect pyrochlore structure for all compositions. Although  $\text{Cs}(\text{M},\text{Te})_2\text{O}_6$  phases are black as discussed in 4.3-4.4, the Rb analog have lighter color and none of them show detectable electrical conductivity.

#### 4.5.2.2 $\text{RbAl}_{0.33}\text{Te}_{1.67}\text{O}_6$ Single Crystal

Transparent orange-red octahedral crystal of  $\text{RbAl}_{0.33}\text{Te}_{1.67}\text{O}_6$  was obtained. Structural analysis indicated cubic defect pyrochlore structure with  $Fd\bar{3}m$  space group where Al and Te randomly occupy octahedral 16c site. Similar to  $\text{Cs}(\text{M},\text{Te})_2\text{O}_6$  series,  $\text{Rb}^{1+}$  occupy 8b sites while 16d sites are left vacant. Crystallographic data are shown

in Table 4.15. Table 4.16 and 4.17 summarize atomic coordinates, displacement factors, and selected bond lengths and angles, respectively.

Table 4.14: Rb(M,Te)<sub>2</sub>O<sub>6</sub> pyrochlores prepared in this work

| Compound   | a (Å) | Resistance (Ω) @RT | Color         |
|--|-------|--------------------|---------------|
| <b>RbM<sup>3+</sup><sub>1/3</sub>Te<sub>5/3</sub>O<sub>6</sub></b> |       |                    |               |
| Rb(Al <sub>1/3</sub> Te <sub>5/3</sub> )O <sub>6</sub>             | 10.02 | >10 <sup>6</sup>   | Greenish grey |
| Rb(Cr <sub>1/3</sub> Te <sub>5/3</sub> )O <sub>6</sub>             | 10.08 | >10 <sup>6</sup>   | Dark brown    |
| Rb(Mn <sub>1/3</sub> Te <sub>5/3</sub> )O <sub>6</sub>             | 10.08 | >10 <sup>6</sup>   | Black         |
| Rb(Fe <sub>1/3</sub> Te <sub>5/3</sub> )O <sub>6</sub>             | 10.07 | >10 <sup>6</sup>   | Brown         |
| Rb(Co <sub>1/3</sub> Te <sub>5/3</sub> )O <sub>6</sub>             | 10.11 | >10 <sup>6</sup>   | Dark grey     |
| Rb(Ga <sub>1/3</sub> Te <sub>5/3</sub> )O <sub>6</sub>             | 10.09 | >10 <sup>6</sup>   | Dark green    |
| Rb(Sc <sub>1/3</sub> Te <sub>5/3</sub> )O <sub>6</sub>             | 10.19 | >10 <sup>6</sup>   | Dark grey     |
| Rb(In <sub>1/3</sub> Te <sub>5/3</sub> )O <sub>6</sub>             | 10.22 |                    |               |
| Rb(Tl <sub>1/3</sub> Te <sub>5/3</sub> )O <sub>6</sub>             | 10.19 |                    |               |
| <b>RbM<sup>4+</sup><sub>1/2</sub>Te<sub>3/2</sub>O<sub>6</sub></b> |       |                    |               |
| Rb(Ge <sub>1/2</sub> Te <sub>3/2</sub> )O <sub>6</sub>             | 9.95  | >10 <sup>6</sup>   | Grey-brown    |
| Rb(Rh <sub>1/2</sub> Te <sub>3/2</sub> )O <sub>6</sub>             | 10.09 | >10 <sup>6</sup>   | Black         |
| <b>RbM<sup>2+</sup><sub>1/4</sub>Te<sub>7/4</sub>O<sub>6</sub></b> |       |                    |               |
| Rb(Mg <sub>1/4</sub> Te <sub>7/4</sub> )O <sub>6</sub>             | 10.11 | >10 <sup>6</sup>   | Brown         |
| Rb(Zn <sub>1/4</sub> Te <sub>7/4</sub> )O <sub>6</sub>             | 10.13 | >10 <sup>6</sup>   | Reddish-brown |
| Rb(Ni <sub>1/4</sub> Te <sub>7/4</sub> )O <sub>6</sub>             | 10.14 | >10 <sup>6</sup>   | Dark-grey     |

### 4.5.3 Discussion

The single crystal obtained from TeO<sub>2</sub> flux growth resulted in Al rich phase, similar to what was observed in crystal growth of Cs(Al,Te)<sub>2</sub>O<sub>6</sub>. Powder X-ray diffraction of Rb(M,Te)<sub>2</sub>O<sub>6</sub> phases indicate the same cubic pyrochlore structure as observed in Cs(M,Te)<sub>2</sub>O<sub>6</sub>. Cell parameters are smaller than the Cs compounds as

expected with the smaller ionic radii of  $\text{Rb}^+$ . As discussed in 4.4, more compact cell compresses  $\text{Te}^{4+}$ , increases its energy level and in general results in higher conductivity. Although cell parameters are smaller in  $\text{Rb}(\text{M},\text{Te})_2\text{O}_6$  compounds, the lighter colors and much lower conductivities were observed. Therefore, it is most likely that there is less amount of  $\text{Te}^{4+}$  in the lattice of these compounds, if any. However, detailed studies are needed to clearly explain these phenomena.

Table 4.15: Crystallographic data of  $\text{RbAl}_{0.33}\text{Te}_{1.67}\text{O}_6$

|   |  |
|---|--|
| Starting composition                            | $\text{RbAl}_{0.33}\text{Te}_{1.67}\text{O}_6$ |
| Crystal composition                             | $\text{RbAl}_{0.39}\text{Te}_{1.61}\text{O}_6$ |
| Formula weight (g/mol)                          | 396.93   |
| Temperature (K)                                 | 293(2)   |
| Space group                                     | $\text{Fd}\bar{3}\text{m}$                     |
| a (Å)   | 10.0026(6)                                     |
| V (Å <sup>3</sup> )                             | 1000.78 (10)                                   |
| Z   | 8  |
| $\rho_{\text{calculated}}$ (Mg/m <sup>3</sup> ) | 5.269  |
| Absorption coefficient (mm <sup>-1</sup> )      | 19.087   |
| F(000)  | 1389   |
| $\Theta$ range                                  | 3.53-27.77                                     |
| Reflections collected                           | 2628   |
| R(int)  | 0.0157   |
| Independent reflections                         | 79   |
| Completeness to $\theta = 27.81^\circ$          | 100.0 %  |
| Goodness-of-fit on $F^2$                        | 1.333  |
| Final R indices [ $I > 2\sigma(I)$ ]            | $R_1 = 0.0130,$<br>$wR_2 = 0.0303$             |
| R indices (all data)                            | $R_1 = 0.0133,$<br>$wR_2 = 0.0304$             |
| Largest difference peak                         | +0.321 e.Å <sup>-3</sup>                       |
| Largest difference hole                         | -0.506 e.Å <sup>-3</sup>                       |

Table 4.16: Atomic coordinates and displacement factors of  $\text{RbAl}_{0.33}\text{Te}_{1.67}\text{O}_6$ 

| Atom   | Wyckoff position | x     | y     | z          | $U_{\text{eq}}$ |
|--|------------------|-------|-------|------------|-----------------|
| $\text{RbAl}_{0.39}\text{Te}_{1.61}\text{O}_6$ |                  |       |       |            |                 |
| Rb   | 8b               | 0.125 | 0.125 | 0.125      | 30(1)           |
| Al/Te  | 16c              | 0     | 0.5   | 0          | 8(1)            |
| O  | 48f              | 0.125 | 0.625 | -0.0712(3) | 15(1)           |

Table 4.17: Selected bond lengths and angles of  $\text{RbAl}_{0.33}\text{Te}_{1.67}\text{O}_6$ 

|  | M-O1 $\times 6$ | Rb-O1 $\times 6$ | Rb-O2 $\times 12$ | M-O-M     | O-M-O    |
|--|-----------------|------------------|-------------------|-----------|----------|
| $\text{RbAl}_{0.39}\text{Te}_{1.61}\text{O}_6$ | 1.9063(13)      | 3.039(4)         | 3.5771(6)         | 93.44(13) | 136.1(2) |

#### 4.5.4 Conclusion

Polycrystalline sample of  $\text{Rb}(\text{M},\text{Te})_2\text{O}_6$  with cubic pyrochlore structure were prepared and characterized. Single crystal of  $\text{RbAl}_{0.33}\text{Te}_{1.67}\text{O}_6$  was grown using  $\text{TeO}_2$  flux. Unit cell parameters of  $\text{Rb}(\text{M},\text{Te})_2\text{O}_6$  are smaller than the Cs analogs as expected. Any present  $\text{Te}^{4+}$  would be more compressed in such small lattices which should result in more conducting samples; however, the observed lighter color and lower electrical conductivities suggest that there is relatively less  $\text{Te}^{4+}$  in these compounds, if any. More studies are required to understand this system.

#### 4.5.5 Experimental

Polycrystalline samples of  $\text{Rb}(\text{M},\text{Te})_2\text{O}_6$  were synthesized by solid state reaction using  $\text{RbNO}_3$ ,  $\text{TeO}_2$ , and oxides of M as shown in table 4.5. Stoichiometric mixture of starting materials were ground, pressed into pellet and heat at 500-600°C for 24h in gold containers with an intermediate grinding. X-ray diffraction data on the samples were collected on a Rigaku MiniFlex II diffractometer using  $\text{Cu K}\alpha$  radiation and a graphite monochromator. Single crystals of  $\text{RbAl}_{0.33}\text{Te}_{1.67}\text{O}_6$  were grown by flux method using polycrystalline sample of  $\text{RbAl}_{0.33}\text{Te}_{1.67}\text{O}_6$  and  $\text{TeO}_2$  flux with 1:1 weight ratio in a gold crucible. The crucible was heated at 800°C for 3 hours before being cooled at 3°C/hour to 600°C where the furnace was turned off. Flux was dissolved in 50% v/v HCl solution to free the crystals. Single-crystal X-ray diffraction data were collected using a Bruker SMART APEXII CCD system. A standard focus tube was used with an anode power of 50 kV at 30 mA. A subsequent SADABS correction was applied. The crystal structure was solved with the direct method program SHELXS and refined with full-matrix least-squares program SHELXTL [73].

#### 4.6 References

1. F. Wöhler, *Ann. Phys. Chem. Pogg.*, **7** (1826), 417.
2. M.A. Subramanian, G. Aravamudan and G. V. Subba Rao, *Prog. Solid State Chem.*, **15** (1983), 55.
3. [http://www.khyberminerals.com/tucson09\\_1.htm](http://www.khyberminerals.com/tucson09_1.htm), Accessed February 2011.
4. E. Aleshin, R. Roy, *J. Am. Ceram. Soc.*, **45** (1962), 18.
5. J. M. Longo, P. M. Raccach, J. B. Goodenough, *Mat. Res. Bull.*, **4** (1969), 191
6. H. S. Horowitz, J. M. Longo, J. T. Lewardowski, *ibid.*, **16** (1981), 489.
7. A. W. Sleight, *Inorg. Chem.*, **7** (1968), 1704.
8. J. Pannetier, J. Lucas, *Mat. Res. Bull.*, **5** (1970), 797.
9. M. Faucher, P. Caro, *J. Solid State Chem.*, **12** (1975), 1.



10. I.N. Belyaev, D.S. Lesnykh and T.G. Lupeiko, *Zh. Neorg. Khim.*, **14** (1969), 648.
11. J. M. Longo, P.M. Racciah, J. A. Kafalas, J. W. Pierce, *Mater. Res. Bull.*, **7** (1971), 137.
12. A. W. Sleight, *Mat. Res. Bull.*, **6** (1971), 775.
13. S. Uma, S. Kodialam, A. Yokochi, N. Khosrovani, M. A. Subramanian, A. W. Sleight, *J. Solid State Chem.*, **155** (2000), 225.
14. D. W. Murphy, J. L. Dye, S. M. Zahurak., *Inorg. Chem.*, **22** (1983), 3679.
15. P. W. Barnes, P. M. Woodward, Y. Lee, T. Vogt, J. A. Hriljac, *J. Am. Chem. Soc.*, **125** (2003), 4573.
16. K. R. Whittle, G. R. Lumpkin, S. E. Ashbrook, *J. Solid State Chem.*, **179** (2006), 512.
17. C. Michel, D. Groult, B. Raveau, *J. Inorg. Nucl. Chem.*, **37** (1975), 247.
18. M.A. Subramanian, R. Subramanian, A. Clearfield, *Solid State Ionics*, **15** (1985), 15.
19. A. Coucou, M. Figlarz, *Solid state ionics*, **28-30** (1988), 1762.
20. R. J. Bouchard, J. L. Gilson, *Mat. Res. Bull.*, **6** (1971), 669.
21. B. Rehak, K. Horcic, M. Frumar, L. Koudelka, *J. Cryst. Growth*, **68** (1984), 647.
22. H. Zu, Y. Wang, P. Zhao, W. L. Bourcier, R. V. Konyonenburg, H. F. Shaw, *Environ. Sci. Technol.*, **38** (2004), 1480.
23. R. G. Dosch, T. J. Headley, C. J. Northrup, P. F. Hlava, *Sandia National Laboratories Report*, **82-2980** (1982), 1.
24. Y. Shimizu, K. Maeda, *Sensor Actuat. B-Chem.*, **52** (1998), 84.
25. V. V. Kharton, E. V. Tsipis, A. A. Yarenchenko, N. P. Vyshatko, A. L. Shaula, E. N. Naumovich, J. R. Frade, *J. Solid State Electrochem.*, **7** (2003), 468.
26. F. A. Weber, T. Schleid, *Z. Anorg. Allg. Chem.*, **626** (2000), 1285.
27. Ismunandar, I. Haryanto, S. Dewi, *Jurnal Matematika dan Sains*, **8** (2003), 27.
28. M. Amarilla, M. L. Veiga, C. Pico, M. Gaitan, A. Jerez, *Inorg. Chem.*, **28** (1989), 1701
29. J. A. Alonso, C. Cascales, I. Rasines, *Z. Anorg. Allg. Chem.*, **537** (1986), 213.
30. A. Castro, I. Rasines, X. M. Turrillas, *J. Solid State Chem.*, **80** (1989), 227.
31. J. A. Alonso, X. Turrillas, *Dalton Trans.*, (2005), 865.
32. N. P. Egorov, N. G. Chermorukov, I. A. Korshunov, *Zh. Neorg. Khim.*, **34** (1989), 827.
33. X. Turrillas, G. Delabouglise, J. C. Joubert, *Solid State Ionics*, **21** (1986), 195
34. J. A. Alonso, A. Castro, I. Rasines, X. M. Turrillas, *J. Matter. Sci.*, **23** (1988), 4103.
35. N. G. Chernorukov, N. P. Egorov, E. V. Suleimanov, *Zh. Neorg. Khim.*, **34** (1989), 2995.
36. B. Darriet, M. Rat, J. Galy, P. Hagenmuller, *Mat. Res. Bull.*, **6** (1971), 1305.
37. S. Garcia-Martin, M. L. Veiga, A. Jerez, C. Pico, *Mat. Res. Bull.*, **26** (1991), 789.
38. M. Catti, C. M. Mari, E. Cazzanelli, G. Mariotto, *Solid State Ionics*, **40** (1990), 900.
39. S. Garcia-Martin, M. L. Veiga, A. Jerez, M. Gaitan, C. Pico, *J. Chem. Soc., Dalton Trans.*, **8** (1988), 2141.

40. Y.-S. Hong, M. Zakhour, M. A. Subramanian, J. Darriet, *J. Mater. Chem.*, **8** (1998), 1889.
41. J. Isasi, M. L. Lopez, M. L. Veiga, C. Pico, *Solid State Ionics*, **89** (1996), 321
42. J. Isasi, M. L. Lopez, M. L. Veiga, E. Ruiz-Hitzky, C. Pico, *J. Solid State Chem.*, **116** (1995), 290.
43. A.W. Sleight, J.L. Gilson, P.E. Bierstedt, *Solid State Commun.*, **17** (1975) 27.
44. R. J. Cava, B. Batlogg, G. P. Ramirez, J. J. Krajewski, W. F. Peck Jr., L. W. Rupp Jr., A. S. Cooper. *Nature*, **339** (1989), 291.
45. M. B. Robin, P. Day, *Adv. Inorg. Chem. and Radiochem.*, **10** (1967), 247.
46. O. Lindqvist, J. Moret, *Acta Cryst. Sect. B*, **29** (1973), 643.
47. W. Klein, J. Curda, E.-M. Peters, M. Z. Jansen, *Anorg. Allg. Chem.*, **631** (2005), 2893.
48. N. Barrier, S. Malo, O. Hernandez, M. Hervieu, B. Raveau, *J. Solid State Chem.*, **179** (2006), 3484.
49. B. O. Loopstra, K. Goubitz, *Acta Cryst. C*, **42** (1986), 520.
50. M. A. Subramanian, R. L. Harlow, A. P. Ramirez, *Inter. J. Inorg. Mater.*, **2** (2000), 131.
51. T. Kar, R. N. P. Choudhary, *Mater. Sci. Eng. B*, **90** (2002), 224.
52. A. W. Sleight, J. E. Gulley, T. Berzins, *Adv. Chem.*, **183** (1977), 195..
53. R. D. Shannon, *Acta Crystallogr., Sect. A*, **32** (1976), 751.
54. D. Groult, J. Pannetier, B. Raveau, *J. Solid State Chem.*, **41** (1982), 277.
55. D. Dumora, P. Hagenmuller, *C. R. Acad. Sci. Paris, Ser. C*, **266** (1968), 276.
56. T. Siritanon, G. Laurita, R. T. Macaluso, J. N. Millican, A.W. Sleight, M.A. Subramanian, *Chem. Mater.*, **21** (2009), 5572.
57. B. D. Cullity, S. R. Stock, 'Elements of X-ray Diffraction', 3rd ed., Prentice-Hall, Inc., (2001).
58. A.C. Larson and R.B. Von Dreele, "General Structure Analysis System (GSAS)," Los Alamos National Laboratory Report LAUR, 2004, 86-784; B.H. Toby, EXPGUI, a graphical user interface for GSAS, *J. Appl. Cryst.*, **34** (2001), 210.
59. C. Hormillosa, S. Healy, T. Stephen and I.D. Brown, Bond Valence Calculator, Version 2.0, 1993. <http://www.ccp14.ac.uk>
60. K.R. Whittle, G.R. Lumpkin, S.E. Ashbrook, *J. Solid State Chem.*, **179** (2006) 512.
61. G.J. Thorogood, P.J. Saines, B.J. Kennedy, R.L. Withers, M.M. Elcombe, *Mat. Res. Bull.*, **43** (2008), 787.
62. J.-I. Yamaura, S. Yonezawa, Y. Muraoka, Z. Hiroi, *J. Solid State Chem.*, **179** (2006), 336.
63. T. Hasegawa, N. Ogita, Y. Nagao, J.-I. Yamaura, Z. Hiroi, M. Udagawa, *Physica C*, in press.
64. M. Rh. Rabadanov, A. A. Loshmanov, Yu. V. Shaldin, *Crystal. Rep.*, **42** (1997), 592.
65. J. Pannetier, *J. Phys. Chem. Solids*, **34** (1973), 583.
66. Y. Nakamura, K. Oguro, I.Uehara, E. Akiba, *J. Alloys Compd.*, **298** (2000), 138.
67. A.W. Sleight, J.E. Gulley, T. Berzins, *Adv. Chem. Ser.*, **163** (1977), 195.

68. A.W. Sleight, *Mater. Res. Bull.*, **9** (1974), 1437.
69. T. Birchall and A.W. Sleight, *J. Solid State Chem.*, **13** (1975), 118.
70. E. Philippot, M. Maurin, *Revue de Chimie Minerale*, 1976, 13, 162.
71. S. Adams, softBV, Version 0.96, 2004. <http://kristall.uni-mki.gwdg.de/softbv/>
72. R. M. Hazen, C. T. Prewitt, *Am. Mineral.*, **62** (1977), 309.
73. G.M. Sheldrick, SHEXEXTL, Version 6.14, Bruker Analytical X-ray Instruments, Inc., Madison, WI, 2003.

## Chapter

### 5. Effects of Oxygen Deficiency and Tungsten Substitution on the Structure and Properties of CsTe<sub>2</sub>O<sub>6</sub>

#### 5.1 Abstract

Systematic studies of cesium tellurates, CsTe<sub>2</sub>O<sub>6-x</sub> where x = 0, 0.15, 0.25, 1.5, have been investigated. Structures of CsTe<sub>2</sub>O<sub>6-x</sub> phases were analyzed by single crystal X-ray diffraction and neutron powder diffraction. Stoichiometric CsTe<sub>2</sub>O<sub>6</sub> is a mixed valence Cs<sub>2</sub>Te<sup>4+</sup>Te<sup>6+</sup><sub>3</sub>O<sub>12</sub> compound adopting rhombohedral pyrochlore-type structure with a complete order of the Te<sup>4+</sup> and Te<sup>6+</sup>. On heating at slightly above 600°C, CsTe<sub>2</sub>O<sub>6</sub> lost oxygen resulting in cubic structure with disordered Te<sup>4+</sup>/Te<sup>6+</sup> and oxygen vacancies. Two novel phases of CsTe<sub>2</sub>O<sub>6-x</sub> were prepared with orthorhombic structure. The first phase with x of about 0.2-0.3 crystallizes in *Pnma* symmetry. At higher values of x, a new compound was discovered with a structure related to that reported for Rb<sub>4</sub>Te<sub>8</sub>O<sub>23</sub>.

Series of compounds with formula CsTe<sub>2-x</sub>W<sub>x</sub>O<sub>6</sub> where x=0.2-0.5 have been prepared. The compounds can be considered as solid solution of CsTe<sub>2</sub>O<sub>6</sub> and CsTe<sub>0.5</sub>W<sub>1.5</sub>O<sub>6</sub>. Although the two end members adopt rhombohedral and trigonal structure, these solid solution phases crystallize in cubic defect pyrochlore structure with W<sup>6+</sup>, Te<sup>6+</sup>, and Te<sup>4+</sup> randomly occupy 16c octahedral site. Optical properties of the compounds can be explained by intervalence charge transfer between Te<sup>4+</sup> and Te<sup>6+</sup>.

## 5.2 Introduction

### 5.2.1 Cation Ordering in Pyrochlores

As discussed in 4.2, B cations in pyrochlore connect to each other through oxygen to form tetrahedral arrangement each of which share corners to the neighbors to form 3-dimensional networks. If all octahedra are identical the compounds adopt cubic structure with  $Fd\bar{3}m$  space group. Mixtures of different B cations do not necessarily distort the structure. For example,  $\text{Cs}(\text{M},\text{Te})_2\text{O}_6$  discussed in 4.3 [1],  $\text{CsNbWO}_6$ , and  $\text{Pb}_2\text{FeReO}_6$  [2] crystallize in cubic structure. However, dissimilar B cations can sometimes result in distortion and hence non-cubic pyrochlore-related structures.

There are only two possible ways to order cations in pyrochlore network: 1:3 ordering and 1:1 ordering (Fig.5.1). 1:3 ordering in B site results in rhombohedral pyrochlore structure with space group  $R\bar{3}m$ .  $\text{CsTe}_2\text{O}_6$  is one example which contains the ordering of  $\text{Te}^{4+}$  and  $\text{Te}^{6+}$  in 1:3 ratios [3]. Although both Tellurium species are in octahedral coordination, the longer  $\text{Te}^{4+}$ -O bond distinguish the two octhedra. Similar ordering is found in Parabarionmicrolite,  $\text{BaTa}_4\text{O}_{10}(\text{OH})_2 \cdot 2\text{H}_2\text{O}$  which crystallizes in the same rhombohedral  $R\bar{3}m$  space group [4].  $Fd\bar{3}m$  to  $R\bar{3}m$  transformation lowers the symmetry and splits most sites of the cubic pyrochlore into two nonequivalent sites.

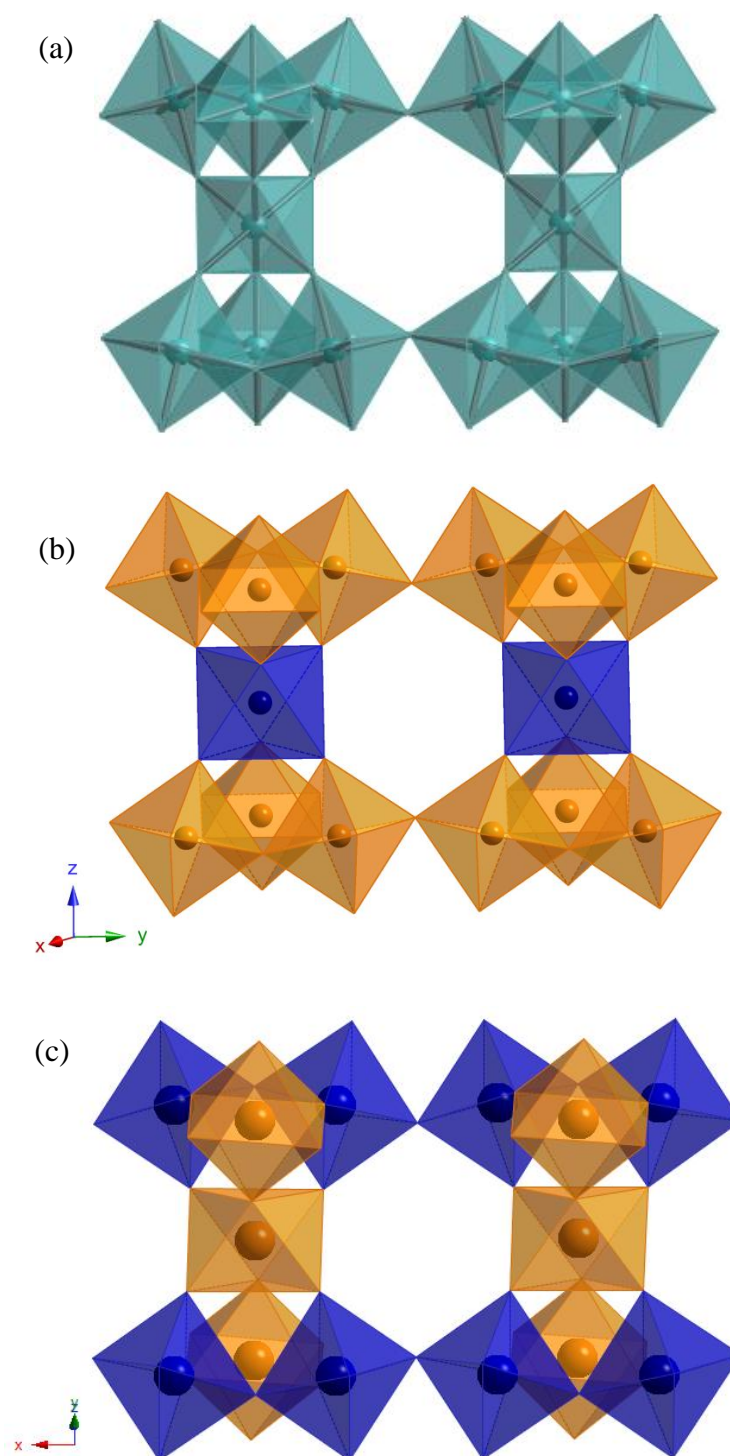


Figure 5.1: Tetrahedral arrangement of  $\text{BO}_6$  octahedra in cubic pyrochlore (a), rhombohedral pyrochlore showing 1:3 ordering (b), and tetragonal pyrochlore with 1:1 ordering. Different colors represent different octahedral.

1:1 ordering in pyrochlore network results in orthorhombic structure. Subramanian *et al.* prepared  $\text{NH}_4\text{CoAlF}_6$  which can adopt both cubic pyrochlore structure,  $Fd\bar{3}m$ , and orthorhombic pyrochlore-related structure,  $Pnma$ , depending on the preparation method [5]. Both structures consist of  $\text{MO}_6$  octahedra network of Co/Al sharing corners and  $\text{NH}_4$  in interstitial sites but Co and Al cations are ordered in orthorhombic structure leading to the distortion. According to Madelung energy calculation, it was found that the ordered orthorhombic phase is more stable due to the large difference between ionic radius of  $\text{Co}^{2+}$  and  $\text{Al}^{3+}$  [5]. Similar ordered pyrochlore phases have been observed in  $\text{AMM}'\text{F}_6$  with  $A = \text{Rb}$  or  $\text{Cs}$ ,  $M = \text{Cu}$  or  $\text{Ag}$ ,  $M' = \text{Al}$ ,  $\text{Ga}$  [6-7].

### 5.2.2 Oxygen Deficiency in Pyrochlores

Anion deficiency in  $\text{A}_2\text{B}_2\text{O}_6\text{O}'$  pyrochlore is common at A and O' sites because  $\text{B}_2\text{O}_6$  network forms the main framework of the structure. However, oxygen deficiency in  $\text{AB}_2\text{O}_6$  is very rare. Groult *et al.* reported  $\text{TaWO}_{5.5}$  which the refinement showed vacancies in 48f oxygen position. These vacancies are disordered and do not affect cubic symmetry of the structure. Therefore, the space group remains unchanged and the compound can be viewed as  $\text{TaWO}_{5.5}\square_{0.5}$  [8]. The other example is  $\text{A}_{1.1}\text{W}_{1.65}\text{O}_{5.5}$ ,  $A = \text{Rb}$ ,  $\text{Cs}$  prepared by Driouiche *et al.* where analysis of powder X-ray diffraction data gave cubic pyrochlore structure with 20% of cation vacancies in  $\text{W}_2\text{O}_6$  network [9]. However, confirmation of actual oxygen content in this compound has not been reported.

### 5.3 Oxygen Deficient Phases of CsTe<sub>2</sub>O<sub>6</sub>

#### 5.3.1 Introduction

In 1986 Loopstra and Goubitz [3] reported the structures of four Cs-Te oxides. Three of these compounds contain only Te<sup>4+</sup>: Cs<sub>2</sub>TeO<sub>3</sub>, Cs<sub>2</sub>Te<sub>2</sub>O<sub>5</sub>, and Cs<sub>2</sub>Te<sub>4</sub>O<sub>9</sub>. The fourth compound, CsTe<sub>2</sub>O<sub>6</sub>, contains mixed valence Te and can be written as Cs<sub>2</sub>Te<sup>4+</sup>Te<sup>6+</sup><sub>3</sub>O<sub>12</sub>. In this compound, Te<sup>4+</sup> and Te<sup>6+</sup> occupy different crystallographic sites leading to distortion from cubic symmetry (Fig.5.2). Such an ordering has never been observed for other A<sub>2</sub>M<sup>4+</sup>M<sup>6+</sup><sub>3</sub>O<sub>12</sub> pyrochlores such as Cs<sub>2</sub>Ti<sup>4+</sup>W<sup>6+</sup><sub>3</sub>O<sub>12</sub> [4]. More remarkably, the Te<sup>4+</sup> site is an inversion center. This is apparently the only example of a 5s<sup>2</sup> cation at such high symmetry in an oxide. Ordinarily, one expects to see a low symmetry site that provides space on one side of the cation for the lone pair electrons. Cesium tellurite, CsTe<sub>2</sub>O<sub>4.5</sub>, with all Te in 4+ oxidation state is also remarkable because the connection of polyhedral framework is the same as for a cubic pyrochlore except that the O vacancies are ordered, which reduces the symmetry to tetragonal (Fig.5.3). This compound apparently is the only example of an AM<sub>2</sub>O<sub>6-x</sub> pyrochlore with ordered O vacancies. These O vacancies provide the asymmetric coordination expected for Te<sup>4+</sup>. In 2001 a second modification of CsTe<sub>2</sub>O<sub>6</sub> was reported [10]. Single crystal investigation resulted in cubic pyrochlore structure with only one crystallographic site for the mixed valence Te. A primary motivation of this study was to understand the existence of this cubic form of “CsTe<sub>2</sub>O<sub>6</sub>”.



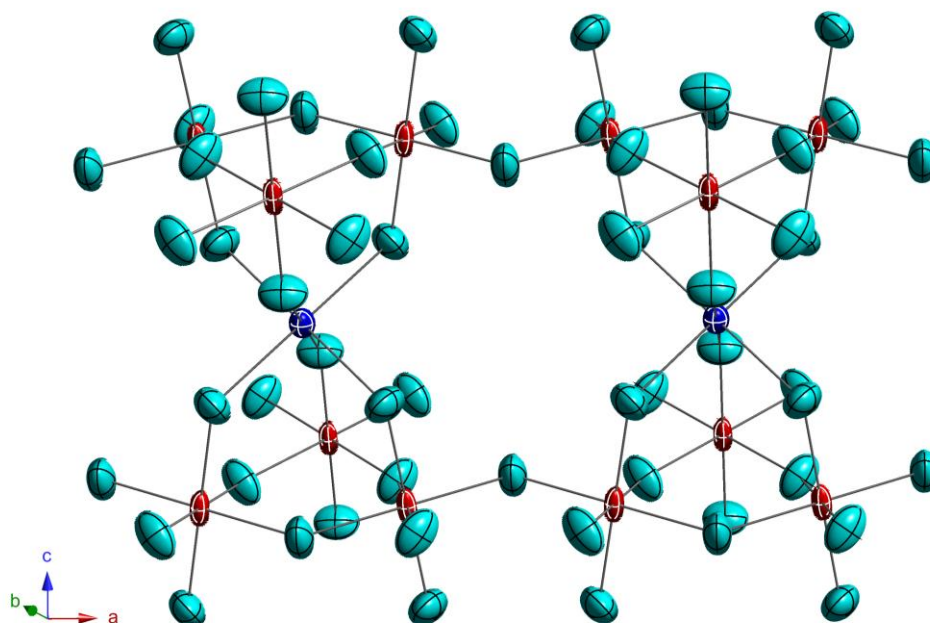


Figure 5.2:  $\text{CsTe}_2\text{O}_6$  structure showing ordering of  $\text{Te}^{4+}$  (blue) and  $\text{Te}^{6+}$  (brown) and anisotropic thermal ellipsoids of Te and O (turquoise).

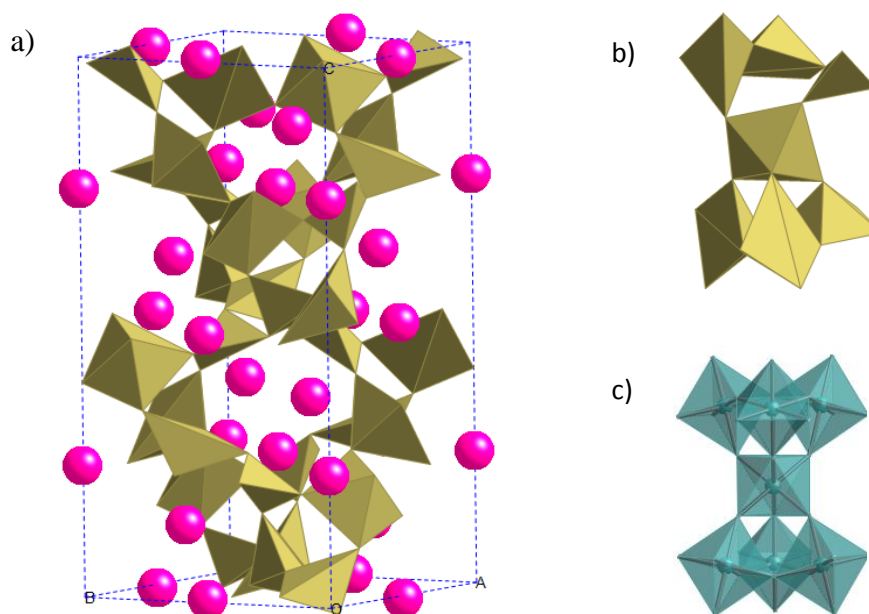


Figure 5.3:  $\text{CsTe}_2\text{O}_{4.5}$  structure (a) showing arrangement of  $\text{Te}^{4+}$  polyhedral (yellow polyhedral) with  $\text{Cs}^+$  in interstitial sites (pink ball). Tetrahedral arrangement is shown separately for clarification in (b) comparing with that of cubic pyrochlore (c).

### 5.3.2 Results

Thermogravimetric analysis of  $\text{CsTe}_2\text{O}_6$  in air is shown in Figure 5.4.  $\text{CsTe}_2\text{O}_6$  started to lose weight at about  $600^\circ\text{C}$ . The discontinuity of the plot indicates that intermediate phase might be formed in between which continued to lose weight when heat was further applied. Since weight loss start at relatively low temperature, it is most likely that the weight loss represents oxygen content released from  $\text{CsTe}_2\text{O}_6$ . Weight of the sample became constant at about 95% which was calculated to give oxygen content of 4.5, consistent with powder X-ray diffraction of the TGA residual,  $\text{CsTe}_2\text{O}_{4.5}$ .

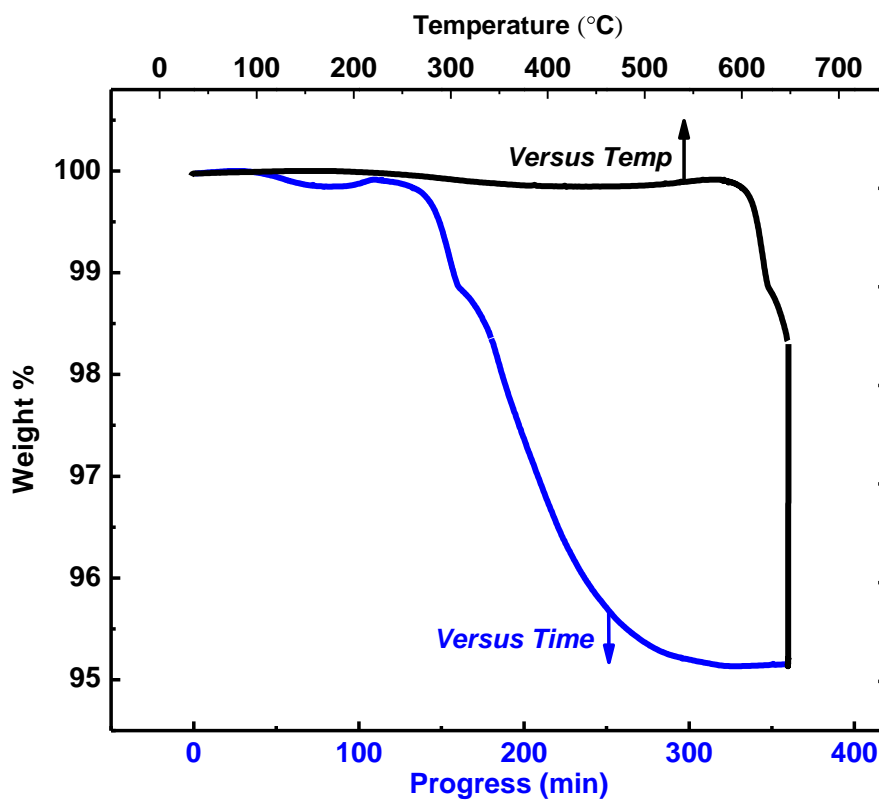


Figure 5.4: Thermogravimetric analysis of  $\text{CsTe}_2\text{O}_6$ .

Figure 5.5 shows the powder X-ray diffraction patterns of  $\text{CsTe}_2\text{O}_{6-x}$  compositions prepared in silica ampoules. A pseudo-cubic phase with a pyrochlore-type structure exists over an apparent range of about  $\text{CsTe}_2\text{O}_{5.8}$  to  $\text{CsTe}_2\text{O}_{5.7}$ . Peak splitting and broadening is observed indicating that the symmetry is actually not cubic (Fig. 5.6). The  $\text{CsTe}_2\text{O}_{5.9}$  composition is a mixture of rhombohedral and pseudocubic thus showing the miscibility gap between these two phases.

Diffraction patterns of  $\text{CsTe}_2\text{O}_6$  and  $\text{CsTe}_2\text{O}_{4.5}$  prepared in this work agree well with the reported ones [3]. Dark brown  $\text{CsTe}_2\text{O}_6$  crystallizes in  $R\bar{3}m$  space group with  $\text{Te}^{4+}$  and  $\text{Te}^{6+}$  ordered in pyrochlore-related structure. White  $\text{CsTe}_2\text{O}_{4.5}$  adopts  $I\bar{4}2d$  space group containing only  $\text{Te}^{4+}$ . As shown in Figure 5.5, four different diffraction patterns were observed which belong to  $\text{CsTe}_2\text{O}_6$ ,  $\text{CsTe}_2\text{O}_{5.75}$ ,  $\text{CsTe}_2\text{O}_{4.85}$ , and  $\text{CsTe}_2\text{O}_{4.5}$  nominal formula. The other starting compositions resulted in mixtures of two or more of these phases. Although  $\text{CsTe}_2\text{O}_6$  and  $\text{CsTe}_2\text{O}_{4.5}$  are known, the other phases have never been reported before.

### 5.3.2.1 Rhombohedral $\text{CsTe}_2\text{O}_6$

Powder X-ray diffraction indicated that single phase of  $\text{CsTe}_2\text{O}_6$  can be obtained from standard solid state reaction. We have refined this structure from both single crystal X-ray diffraction data collected at 110 K and from powder neutron diffraction data collected at room temperature.

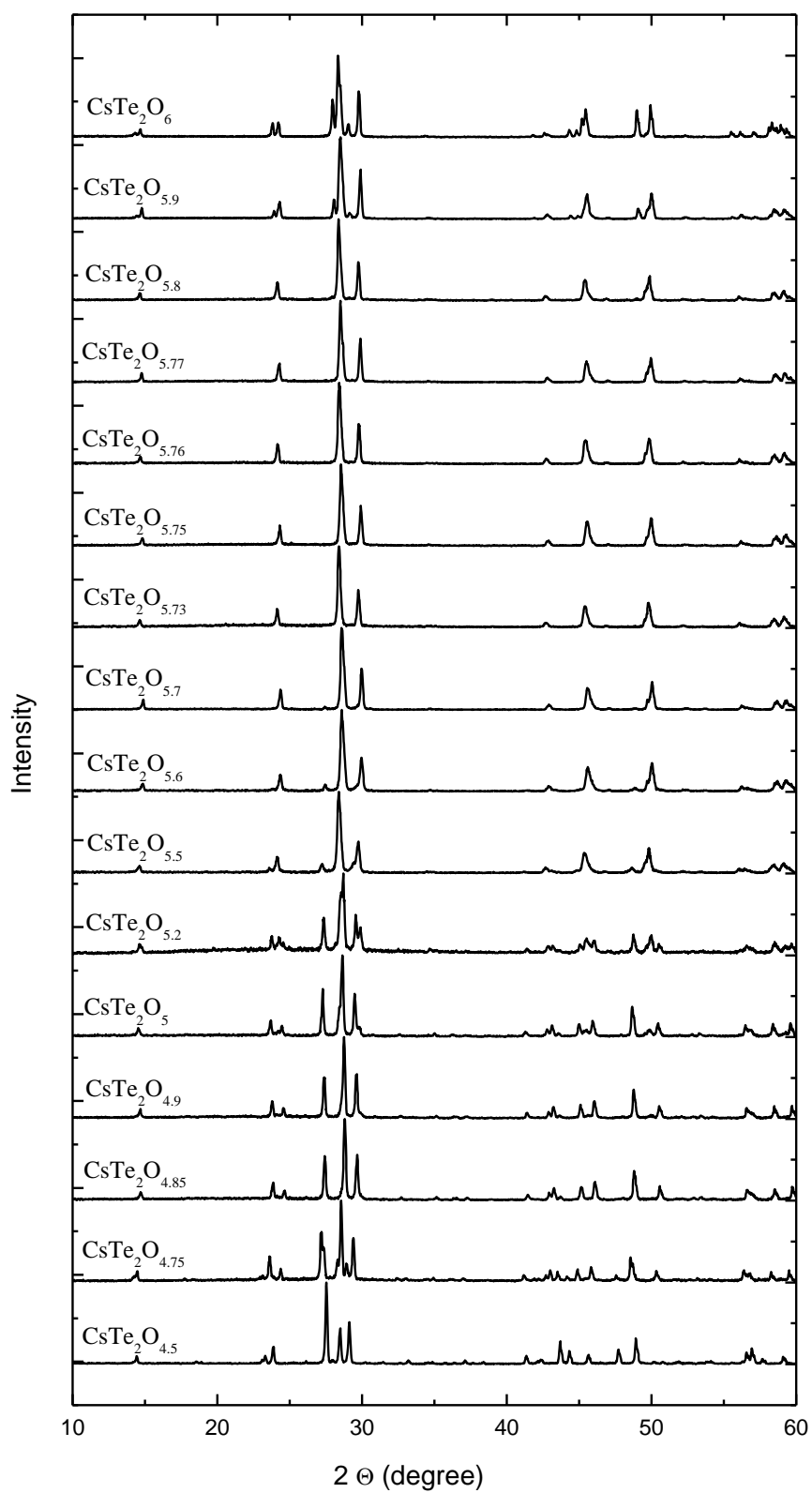


Figure 5.5: Powder x-ray diffraction pattern of CsTe<sub>2</sub>O<sub>6-x</sub> phases.

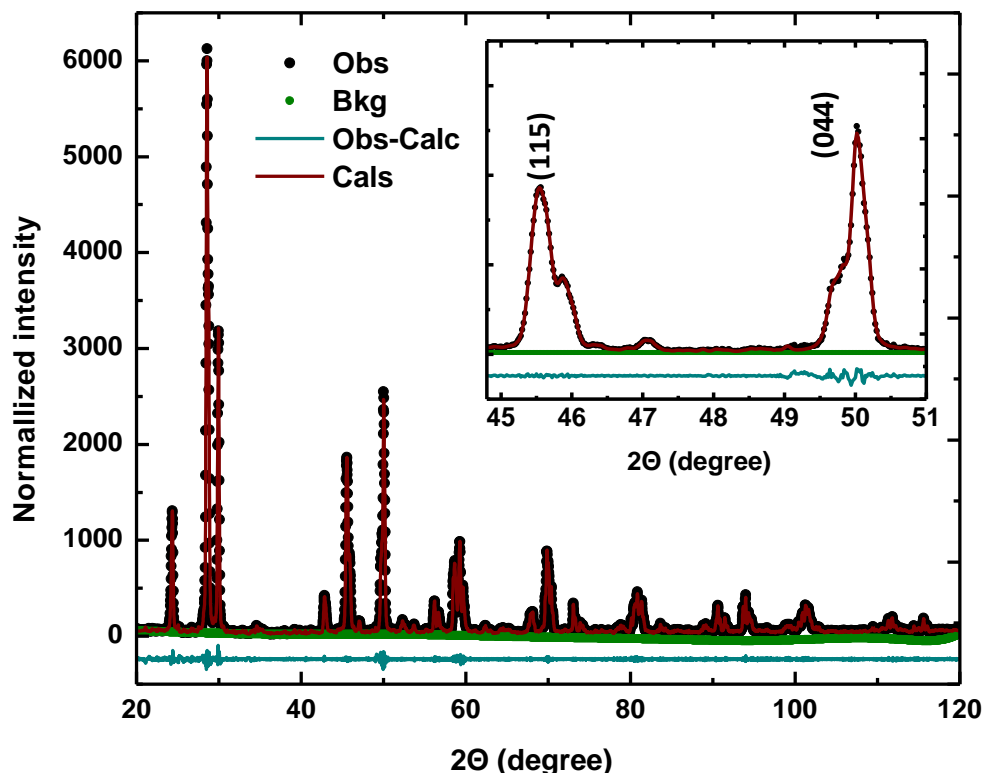


Figure 5.6: LeBail fit of neutron powder diffraction data for orthorhombic  $\text{CsTe}_2\text{O}_{5.75}$  prepared in silica ampoules at  $500^\circ\text{C}$ . Peak splitting and broadening in higher angles indicate that the symmetry is not cubic. The inset shows the close up view of the two peaks (cubic hkl values: 115 and 044) showing peak splitting due to orthorhombic symmetry.

In both cases the original structure reported was fully supported. However, refinement of anisotropic displacement factors was not given in the previous report on the structure of  $\text{CsTe}_2\text{O}_6$  [3]. Such thermal ellipsoids could potentially give information about a tendency for  $\text{Te}^{4+}$  to exhibit the typical lone pair distortion. Despite the high symmetry of the  $\text{Te}^{4+}$  site, a thermal ellipsoid at this site is allowed to either elongate or flatten along the 3-fold axis. In fact, the ellipsoid for  $\text{Te}^{4+}$  is close to spherical, being only slightly flattened along the 3-fold axis (Fig. 5.2). All thermal ellipsoids are unremarkable indicating a completely normal structure. The neutron

data are especially sensitive to the contribution from oxygen. Refinement of occupancies indicates that both O sites are fully occupied. Although the electrical conductivity of a  $\text{CsTe}_2\text{O}_6$  pellet was too low to measure at room temperature, it became measurable above 300 °C (Fig 5.7).

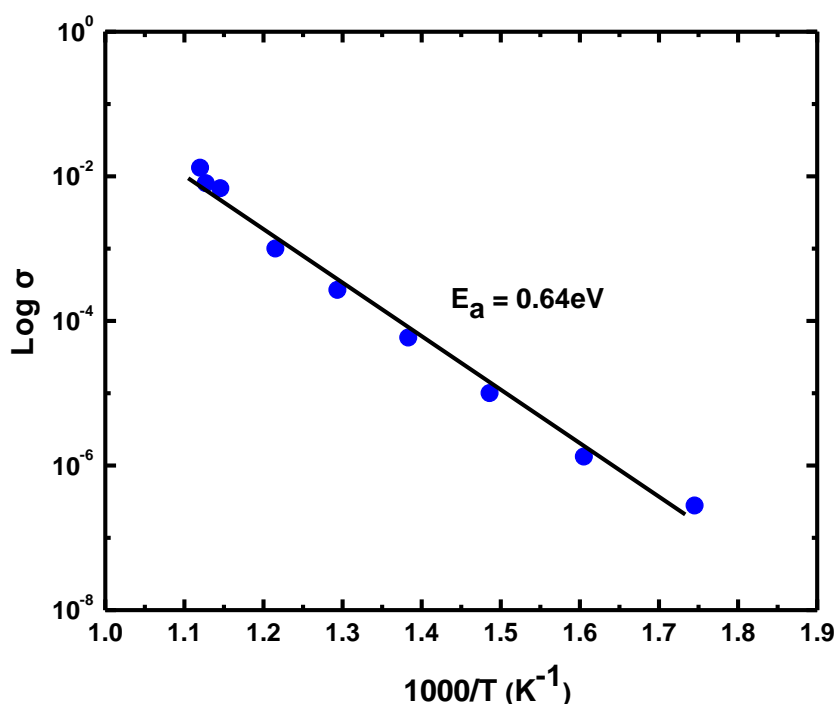


Figure 5.7: Electrical conductivity (log scale) vs.  $1000/T$  for  $\text{CsTe}_2\text{O}_6$ .

### 5.3.2.2 $\text{CsTe}_2\text{O}_{6-x}$

A pseudo-cubic phase was observed for  $\text{CsTe}_2\text{O}_{6-x}$  when  $x = 0.2-0.3$ . Several lower symmetries were evaluated and the best Rietveld fits of powder X-ray diffraction and neutron patterns were obtained with an orthorhombic cell based on *Imma* or *Pnma* space group. Many fluorides of the type  $\text{A}^{1+}\text{M}^{2+}\text{M}^{3+}\text{F}_6$  ( $\text{A}^{1+} = \text{Cs, Rb, K, NH}_4^+$ ;  $\text{M}^{2+} = \text{Mg, Zn, Fe, Ni, Co, Cu, Ag}$ ;  $\text{M}^{3+} = \text{Fe, Ni, Cu, V, Co, Cr, Al, In}$ ) have

been reported with an orthorhombically distorted pyrochlore-type structure [5,15-17].

Most have the *Pnma* space group, but some have the *Imma* space group.

Table 5.1: Crystal data and structure refinements of CsTe<sub>2</sub>O<sub>6</sub>

|   |   |
|---|---|
| Starting composition                            | CsTe <sub>2</sub> O <sub>6</sub>                  |
| Crystal composition from refinement             | CsTe <sub>2</sub> O <sub>6</sub>                  |
| Formula weight (g/mol)                          | 484.11  |
| Temperature (K)                                 | 110(2) K  |
| Space group                                     | R $\bar{3}$ m                                     |
| a (Å)   | 7.2692(3)   |
| c (Å)   | 18.3029(13)                                       |
| V (Å <sup>3</sup> )                             | 837.57(8)   |
| Z   | 6   |
| $\rho_{\text{calculated}}$ (Mg/m <sup>3</sup> ) | 5.759   |
| Absorption coefficient (mm <sup>-1</sup> )      | 16.831  |
| F(000)  | 1242  |
| Crystal size (mm <sup>3</sup> )                 | 0.03 x 0.03 x 0.02                                |
| $\Theta$ range                                  | 3.34- 27.96                                       |
| Reflections collected                           | 2401  |
| Independent reflections                         | 283 [R(int) = 0.0174]                             |
| Completeness to $\theta=27.81^\circ$            | 99.6%   |
| Data/restraints/parameters                      | 283 / 0 / 23                                      |
| Goodness-of-fit on F <sup>2</sup>               | 1.220   |
| Final R indices [ $I > 2\sigma(I)$ ]            | R <sub>1</sub> = 0.0166, wR <sub>2</sub> = 0.0401 |
| R indices (all data)                            | R <sub>1</sub> = 0.0177, wR <sub>2</sub> = 0.0407 |
| Largest difference peak                         | +1.124 e.Å <sup>-3</sup>                          |
| Largest difference hole                         | -1.345e.Å <sup>-3</sup>                           |

Table 5.2: Atomic coordinates and Displacement factor of CsTe<sub>2</sub>O<sub>6</sub>

| Atom  | X          | Y          | Z          | U <sub>eq</sub> |
|-------|------------|------------|------------|-----------------|
| Cs    | 0          | 0          | 0.1220(1)  | 9(1)            |
| Te(1) | -0.3333    | -0.3333    | 0.1667     | 4(1)            |
| Te(2) | -0.5       | 0          | 0          | 3(1)            |
| O(1)  | -0.2033(3) | -0.4065(7) | -0.0175(2) | 8(1)            |
| O(2)  | 0.1955(3)  | -0.1955(3) | 0.230(2)   | 7(1)            |

Table 5.3: Selected bond lengths and angles of CsTe<sub>2</sub>O<sub>6</sub>

|               |            |                 |           |
|---------------|------------|-----------------|-----------|
| Te(1)-O(2) ×6 | 2.107(4)   | O(2)-Te(1)-O(2) | 88.99(14) |
| Te(2)-O(2) ×2 | 1.890(3)   | O(1)-Te(2)-O(1) | 85.9(2)   |
| Te(2)-O(1) ×4 | 1.9370(14) | O(1)-Te(2)-O(2) | 87.94(13) |

In both cases the structure can be viewed as chains of M<sup>2+</sup> cations running perpendicular to M<sup>3+</sup> chains. This orthorhombic pyrochlore-type structure has apparently never been reported for an oxide. The *Pnma* structure is a minor distortion of the *Imma* structure. Thus, the peaks violating the body centered absence condition are weak, and we cannot be absolutely certain of their presence due to weak impurity peaks in our pattern. When the structure was first refined in *Pnma*, the positions of Cs and Te1 remain very close to the positions they would have in *Imma*. However, some O positions deviate significantly from the positions they would be constrained to in *Imma*. Thus, the structure is represented in *Pnma*. However, Rietveld refinements in *Imma* produce the same conclusions concerning the O site with O vacancies and the strong displacement of Te toward this vacancy. Neutron diffraction data were collected on a sample with a nominal composition of CsTe<sub>2</sub>O<sub>5.75</sub>. Resulting



interatomic distances and site occupancies are summarized in Table 5.4-5.5. One Te site has a significantly larger average Te-O distance than the other site, 2.00 Å for Te2 vs. 1.92 Å for Te1. The smaller average Te-O distance is typical of Te<sup>6+</sup> and is essentially the same average distance we find for Te<sup>6+</sup> in CsTe<sub>2</sub>O<sub>6</sub> (1.921 Å). The larger distance is indicative of some larger Te<sup>4+</sup> on this site along with Te<sup>6+</sup>. The O vacancies are predominantly only on the O2 site, and the O occupancy for O2 refined to 74% in good agreement with the nominal composition of CsTe<sub>2</sub>O<sub>5.75</sub>. Based on the hypothesis that Te atoms next to an O vacancy would be displaced from their ideal site, this Te atom was split. The Te2 atom with no adjacent O vacancies remained fixed at its ideal position of 0, 1/2, 0. The added Te3 atom was allowed to move off this inversion center with x, y, and z all being variable. A displacement of 0.34 Å for Te3 from the inversion center occurred. Refinement of the Te2/Te3 ratio gave equal amounts of Te2 and Te3. This is the expected value for 25% vacancies on the O2 site. A section of this chain with Te<sup>4+</sup> and O vacancies is shown in Figure 5.8. The bond valence sum for Te3 is 4.47 whereas it is 4.17 for Te<sup>4+</sup> in rhombohedral CsTe<sub>2</sub>O<sub>6</sub> [3]. Refinements of anisotropic U values are successful for Cs, Te1, O1, O3, and O4. However, such refinement is unsuccessful for Te2, Te3, and O2. These atoms make up the chain where there is a high degree of disorder. The displacement of Te3 is presumed to be the largest displacement caused by this disorder, but smaller static displacements will also occur for Te2 and O2. Unsurprisingly, these displacements are not well modeled by a thermal ellipsoid. The unit cell parameters and volumes for the CsTe<sub>2</sub>O<sub>6-x</sub> phases prepared at 500°C are plotted vs. x in Figure 5.8. The increase in

volume with increasing  $x$  is expected based on a  $\text{Cs}_2\text{Te}^{4+}_{1-x}\text{Te}^{6+}_{3-x}\text{O}_{6-x}$  formula due to increase of  $\text{Te}^{4+}$ , which is much larger than  $\text{Te}^{6+}$ .

Table 5.4: Neutron structural refinement of  $\text{CsTe}_2\text{O}_{5.75}$  (prepared at 500 °C)

| <b>General information</b>                 |                      |                      |                      |                      |                      |                           |
|--|----------------------|----------------------|----------------------|----------------------|----------------------|---------------------------|
| Space group                                |                      | <i>Pnma</i>          |                      |                      |                      |                           |
| <i>a</i> (Å)                               |                      | 7.3270(3)            |                      |                      |                      |                           |
| <i>b</i> (Å)                               |                      | 7.3012(3)            |                      |                      |                      |                           |
| <i>c</i> (Å)                               |                      | 10.2689(4)           |                      |                      |                      |                           |
| V (Å <sup>3</sup> )                        |                      | 549.34(3)            |                      |                      |                      |                           |
| $\chi^2/\text{GOF}$                        |                      | 2.87                 |                      |                      |                      |                           |
| $R_p$ (%)                                  |                      | 6.27                 |                      |                      |                      |                           |
| $wR_p$ (%)                                 |                      | 8.04                 |                      |                      |                      |                           |
| <b>Atomic coordinates and occupancy</b>    |                      |                      |                      |                      |                      |                           |
|  |                      | <i>x</i>             | <i>y</i>             | <i>z</i>             | occupancy            | $U(\text{Å}^2)$           |
| Cs   | Cs1                  | -0.0029(25)          | 1/4                  | 0.6192(15)           | 1.0                  |                           |
| Te   | Te1                  | 0.246(2)             | 1/4                  | 0.2457(15)           | 1.0                  |                           |
|  | Te2                  | 0                    | 1/2                  | 0                    | 0.50(2)              | $U_{\text{iso}}$ 0.011(6) |
|  | Te3                  | 0.013(4)             | 0.514(3)             | 0.031(3)             | 0.25(1)              | $U_{\text{iso}}$ 0.005(5) |
| O  | O1                   | 0.4956(25)           | 1/4                  | 0.192(1)             | 1.0                  |                           |
|  | O2                   | 0.014(2)             | 1/4                  | 0.928(1)             | 0.74(2)              | $U_{\text{iso}}$ 0.023(3) |
|  | O3                   | 0.2056(15)           | 0.4454(15)           | 0.131(1)             | 1.0                  |                           |
|  | O4                   | 0.803(1)             | 0.435(2)             | 0.122(2)             | 1.0                  |                           |
| <b>Anisotropic displacement parameters</b> |                      |                      |                      |                      |                      |                           |
|  | $U_{11}(\text{Å}^2)$ | $U_{22}(\text{Å}^2)$ | $U_{33}(\text{Å}^2)$ | $U_{12}(\text{Å}^2)$ | $U_{13}(\text{Å}^2)$ | $U_{23}(\text{Å}^2)$      |
| Cs1  | 0.016(3)             | 0.016(3)             | 0.054(4)             | 0.0                  | -0.011(7)            | 0.0                       |
| Te1  | 0.001(2)             | 0.010(3)             | 0.026(5)             | 0.0                  | 0.0017(25)           | 0.0                       |
| O1   | 0.005(3)             | 0.20(2)              | 0.017(5)             | 0.0                  | -0.009(6)            | 0.0                       |
| O3   | 0.050(6)             | 0.051(5)             | 0.044(5)             | -0.036(4)            | -0.038(4)            | 0.040(5)                  |
| O4   | 0.021(4)             | 0.13(1)              | 0.13(1)              | 0.027(6)             | -0.007(6)            | 0.08(1)                   |

Table 5.5: Selected interatomic distances ( $\text{\AA}$ ) for  $\text{CsTe}_2\text{O}_{5.75}$ 

|                   |          |                  |          |
|-------------------|----------|------------------|----------|
| Te1-O1            | 1.91(2)  | Cs-O1 $\times$ 2 | 3.727(4) |
| Te1-O1            | 1.94(2)  | Cs-O1            | 3.20(2)  |
| Te1-O3 $\times$ 2 | 1.89(1)  | Cs-O2            | 3.17(2)  |
| Te1-O4 $\times$ 2 | 1.97(2)  | Cs-O2            | 3.57(2)  |
| Te2-O2 $\times$ 2 | 1.972(5) | Cs-O2            | 3.82(2)  |
| Te2-O3 $\times$ 2 | 2.053(9) | Cs-O3 $\times$ 2 | 3.12(2)  |
| Te2-O4 $\times$ 2 | 1.97(1)  | Cs-O3 $\times$ 2 | 3.71(2)  |
| Te3-O2            | 2.20(3)  | Cs-O3 $\times$ 2 | 3.63(2)  |
| Te3-O3            | 1.81(3)  | Cs-O4 $\times$ 2 | 3.18(20) |
| Te3-O3            | 2.32(3)  | Cs-O4 $\times$ 2 | 3.80(2)  |
| Te3-O4            | 1.89(3)  | Cs-O4 $\times$ 2 | 3.61(2)  |
| Te3-O4            | 2.10(3)  |                  |          |

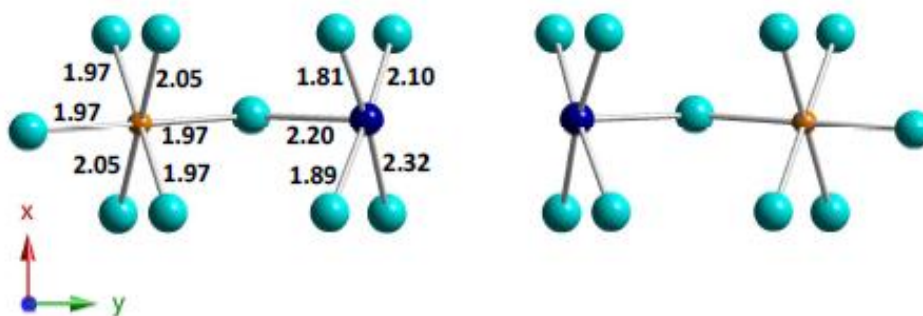


Figure 5.8: A segment of the chain containing the  $\text{Te}^{4+}$  and O vacancies and the important bond distances are marked in  $\text{\AA}$ . The difference in the Te-O distances for the two Te atoms results from a shift of  $0.34 \text{ \AA}$  for Te3 toward the O vacancy (midpoint of chain). The Te3 atoms (dark blue) are assumed to all be  $\text{Te}^{4+}$ , and the Te2 atoms (orange) are a mixture of  $\text{Te}^{4+}$  and  $\text{Te}^{6+}$ .

Thermogravimetric analysis (TGA) of  $\text{CsTe}_2\text{O}_{5.75}$  prepared in silica ampoules was performed under  $\text{O}_2$  atmosphere at  $580^\circ\text{C}$  to approximate oxygen content in the compound as shown in Figure 5.10. Residual sample after TGA had the same color and diffraction pattern as  $\text{CsTe}_2\text{O}_6$ . While there is 0.5 of  $\text{Te}^{4+}$  in  $\text{CsTe}_2\text{O}_6$ , there is

about 0.75 of  $\text{Te}^{4+}$  in  $\text{CsTe}_2\text{O}_{5.75}$ . When heated under  $\text{O}_2$  atmosphere, some of  $\text{Te}^{4+}$  present in  $\text{CsTe}_2\text{O}_{5.75}$  was oxidized to  $\text{Te}^{6+}$ . Consequently, oxygen content of the sample was increased which resulted in the weight gain. The calculation from TGA data gives oxygen content of about 5.75-5.78.

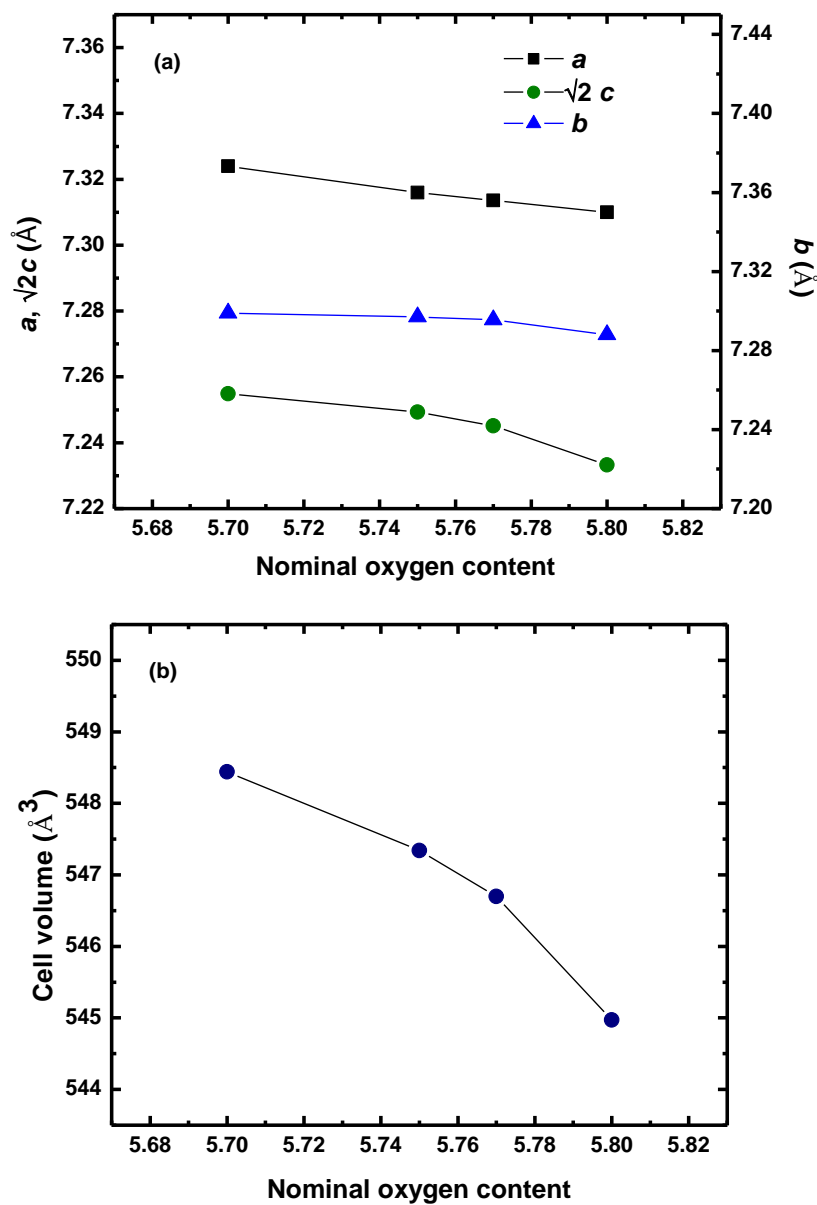


Figure 5.9: Lattice parameters (a) and unit cell volumes (b) of  $\text{CsTe}_2\text{O}_{6-x}$  phases. Standard uncertainties are not indicated, but are less than the point size.

Neutron diffraction data obtained on the  $\text{CsTe}_2\text{O}_{6-x}$  sample prepared by quenching from  $610^\circ\text{C}$  to room temperature showed a cubic pyrochlore-type structure (Table 5.6). Refinement of the occupancy of the O site indicates a formula of  $\text{CsTe}_2\text{O}_{5.8}$ . Structural analysis of a  $\text{CsTe}_2\text{O}_{6-x}$  crystal grown at temperature  $> 600^\circ\text{C}$  also indicated cubic symmetry (Table 5.7). Refinement of the occupation of the O site for this crystal gives a formula of  $\text{CsTe}_2\text{O}_{5.8}$ . We conclude that the higher temperature synthesis can yield pyrochlore-type phases with  $x$  values similar to that obtained in sealed ampoules at  $500^\circ\text{C}$ , but these phases can have a cubic symmetry which never been observed for the samples prepared at  $500^\circ\text{C}$ .

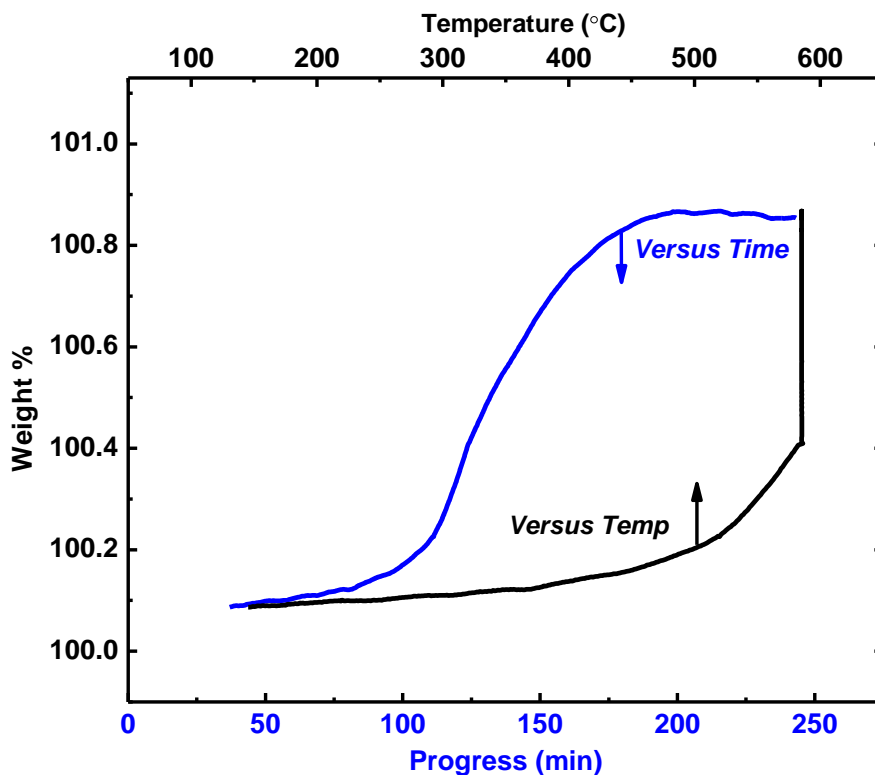


Figure 5.10: Thermogravimetric analysis (TGA) of nominal  $\text{CsTe}_2\text{O}_{5.75}$  phase under  $\text{O}_2$  atmosphere showing weight gain corresponding to  $x=0.25$  in  $\text{CsTe}_2\text{O}_{6-x}$ .  
Table 5.6: Neutron structural refinement of  $\text{CsTe}_2\text{O}_{5.8}$  (quenched from  $610^\circ\text{C}$ )

Table 5.7: Neutron structural refinement of CsTe<sub>2</sub>O<sub>5.8</sub> (quenched from 610 °C)

| <b>General information</b>                      |                            |                            |                            |                            |                            |                            |
|---|----------------------------|----------------------------|----------------------------|----------------------------|----------------------------|----------------------------|
| Space group                                     |                            | $Fd\bar{3}m$               |                            |                            |                            |                            |
| $a$ (Å)   |                            | 10.3410(1)                 |                            |                            |                            |                            |
| $V$ (Å <sup>3</sup> )                           |                            | 1105.83(5)                 |                            |                            |                            |                            |
| $\chi^2/\text{GOF}$                             |                            | 2.39                       |                            |                            |                            |                            |
| $R_p$ (%)                                       |                            | 6.42                       |                            |                            |                            |                            |
| $wR_p$ (%)                                      |                            | 8.19                       |                            |                            |                            |                            |
| <b>Atomic coordinates and occupancy</b>         |                            |                            |                            |                            |                            |                            |
|   | $x$                        | $y$                        | $z$                        | Occupancy                  |                            |                            |
| Cs  | 3/8                        | 3/8                        | 3/8                        | 1.0                        |                            |                            |
| Te  | 0                          | 0                          | 0                          | 1.0                        |                            |                            |
| O   | 0.3196(1)                  | 1/8                        | 1/8                        | 0.97(1)                    |                            |                            |
| <b>Anisotropic displacement parameters</b>      |                            |                            |                            |                            |                            |                            |
|   | $U_{11}$ (Å <sup>2</sup> ) | $U_{22}$ (Å <sup>2</sup> ) | $U_{33}$ (Å <sup>2</sup> ) | $U_{12}$ (Å <sup>2</sup> ) | $U_{13}$ (Å <sup>2</sup> ) | $U_{23}$ (Å <sup>2</sup> ) |
| Cs  | 0.0226(7)                  | 0.0226(7)                  | 0.0226(7)                  | 0.0                        | 0.0                        | 0.0                        |
| Te  | 0.0102(4)                  | 0.0102(4)                  | 0.0102(4)                  | -0.0010(4)                 | -0.0010(4)                 | -0.0010(4)                 |
| O   | 0.0240(8)                  | 0.0606(8)                  | 0.0606(8)                  | 0.0                        | 0.0                        | 0.030(1)                   |
| <b>Selected bond lengths (Å) and angles (°)</b> |                            |                            |                            |                            |                            |                            |
| Cs-O × 6  |                            | 3.158(2)                   |                            | Te-O-Te                    |                            | 136.99(9)                  |
| Cs-O × 12                                       |                            | 3.7006(2)                  |                            | O-Te-O                     |                            | 92.84(6)                   |
| Te-O × 6  |                            | 1.9648(6)                  |                            |                            |                            |                            |

### 5.3.2.3 Orthorhombic CsTe<sub>2</sub>O<sub>4.85-y</sub>

Powder x-ray diffraction of CsTe<sub>2</sub>O<sub>4.85</sub> phase shows that it is isostructural to Rb<sub>4</sub>Te<sub>8</sub>O<sub>23</sub> [18] with  $Pna2_1$  space group as shown in Figure 5.11 comparing with calculated pattern. The Cs phase apparently has less oxygen than that reported for the Rb and K analogues (ATe<sub>2</sub>O<sub>5.75</sub>). The orthorhombic unit cell dimensions of CsTe<sub>2</sub>O<sub>4.85</sub> refined by a LeBail fit of the pattern in Figure 5.11 are  $21.783 \times 14.404 \times 7.190$  Å. The Rb and K analogues are reported to have unit cell parameters of  $19.793 \times 14.664 \times 7.292$  Å and  $19.573 \times 14.448 \times 7.273$  Å, respectively. Only the  $a$  cell parameter

of the Cs cell is larger than that reported for the Rb and K compounds. This unexpected behavior of  $b$  and  $c$  is a further indication that the stoichiometry of the Cs compound may not be the same as the Rb and K compounds. A reliable structure determination of  $\text{CsTe}_2\text{O}_{4.85}$  would likely require a single crystal, as there are 105 variable positional parameters to determine.

Table 5.8: Crystallographic data of  $\text{CsTe}_2\text{O}_{5.8}$  single crystal

|   |                                  |                            |                            |                            |                            |                            |
|---|----------------------------------|----------------------------|----------------------------|----------------------------|----------------------------|----------------------------|
| Temperature (K)                                 | 233(2)                           |                            |                            |                            |                            |                            |
| Space group                                     | $Fd\bar{3}m$                     |                            |                            |                            |                            |                            |
| $a$ (Å)   | 10.3207(15)                      |                            |                            |                            |                            |                            |
| $V$ (Å <sup>3</sup> )                           | 1099.3(3)                        |                            |                            |                            |                            |                            |
| Absorption coefficient (mm <sup>-1</sup> )      | 12.823                           |                            |                            |                            |                            |                            |
| $F(000)$  | 1242                             |                            |                            |                            |                            |                            |
| $\Theta$ range (°)                              | 3.42-26.84                       |                            |                            |                            |                            |                            |
| Data/restraints/parameters                      | 79/0/9                           |                            |                            |                            |                            |                            |
| Goodness-of-fit on $F^2$                        | 1.514                            |                            |                            |                            |                            |                            |
| Final R indices [ $I > 2\sigma(I)$ ]            | $R_1 = 0.0297$ , $wR_2 = 0.0642$ |                            |                            |                            |                            |                            |
| R indices (all data)                            | $R_1 = 0.0297$ , $wR_2 = 0.0642$ |                            |                            |                            |                            |                            |
| <b>Atomic coordinates and occupancy</b>         |                                  |                            |                            |                            |                            |                            |
|   | $x$                              | $y$                        | $z$                        | Occupancy                  |                            |                            |
| Cs  | 3/8                              | 3/8                        | 3/8                        | 1.0                        |                            |                            |
| Te  | 0                                | 1/2                        | 0                          | 1.0                        |                            |                            |
| O   | 0.320(2)                         | 1/8                        | 1/8                        | 0.96(2)                    |                            |                            |
| <b>Anisotropic displacement parameters</b>      |                                  |                            |                            |                            |                            |                            |
|   | $U_{11}$ (Å <sup>2</sup> )       | $U_{22}$ (Å <sup>2</sup> ) | $U_{33}$ (Å <sup>2</sup> ) | $U_{12}$ (Å <sup>2</sup> ) | $U_{13}$ (Å <sup>2</sup> ) | $U_{23}$ (Å <sup>2</sup> ) |
| Cs  | 0.0249(9)                        | 0.0249(9)                  | 0.0249(9)                  | 0.0                        | 0.0                        | 0.0                        |
| Te  | 0.0163(7)                        | 0.0163(7)                  | 0.0163(7)                  | -0.0029(4)                 | -0.0029(4)                 | -0.0029(4)                 |
| O   | 0.082(8)                         | 0.082(8)                   | 0.034(9)                   | -0.04(1)                   | 0.0                        | 0.0                        |
| <b>Selected bond lengths (Å) and angles (°)</b> |                                  |                            |                            |                            |                            |                            |
| Cs-O $\times$ 6                                 | 3.15(2)                          |                            | Te-O-Te                    | 136.7(9)                   |                            |                            |
| Cs-O $\times$ 12                                | 3.693(3)                         |                            | O-Te-O                     | 93.0(6)                    |                            |                            |
| Te-O $\times$ 6                                 | 1.963(6)                         |                            |                            |                            |                            |                            |

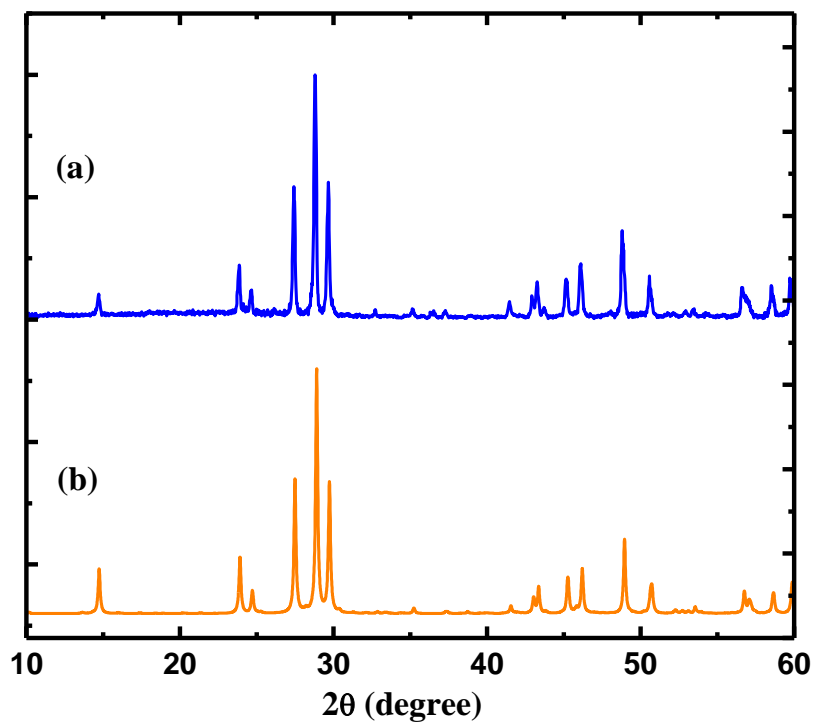


Figure 5.11: Observed powder XRD of nominal  $\text{CsTe}_2\text{O}_{4.85}$  (a) compared with simulated pattern which was calculated based on Cs analog of  $\text{Rb}_4\text{Te}_8\text{O}_{23}$  (b)

### 5.3.3 Discussion

Possible ordering schemes for different M cations in the pyrochlore structure can be visualized considering just the tetrahedral units of the M cation network. Every M cation is a member of two different tetrahedra; thus, it has six M near neighbors in an octahedral arrangement. Based on the  $\text{M}_4$  tetrahedral unit, there are just two ordering schemes to consider for two different cations:  $\text{A}_3\text{B}$  and  $\text{A}_2\text{B}_2$ . Both are known to exist (Fig. 5.12).



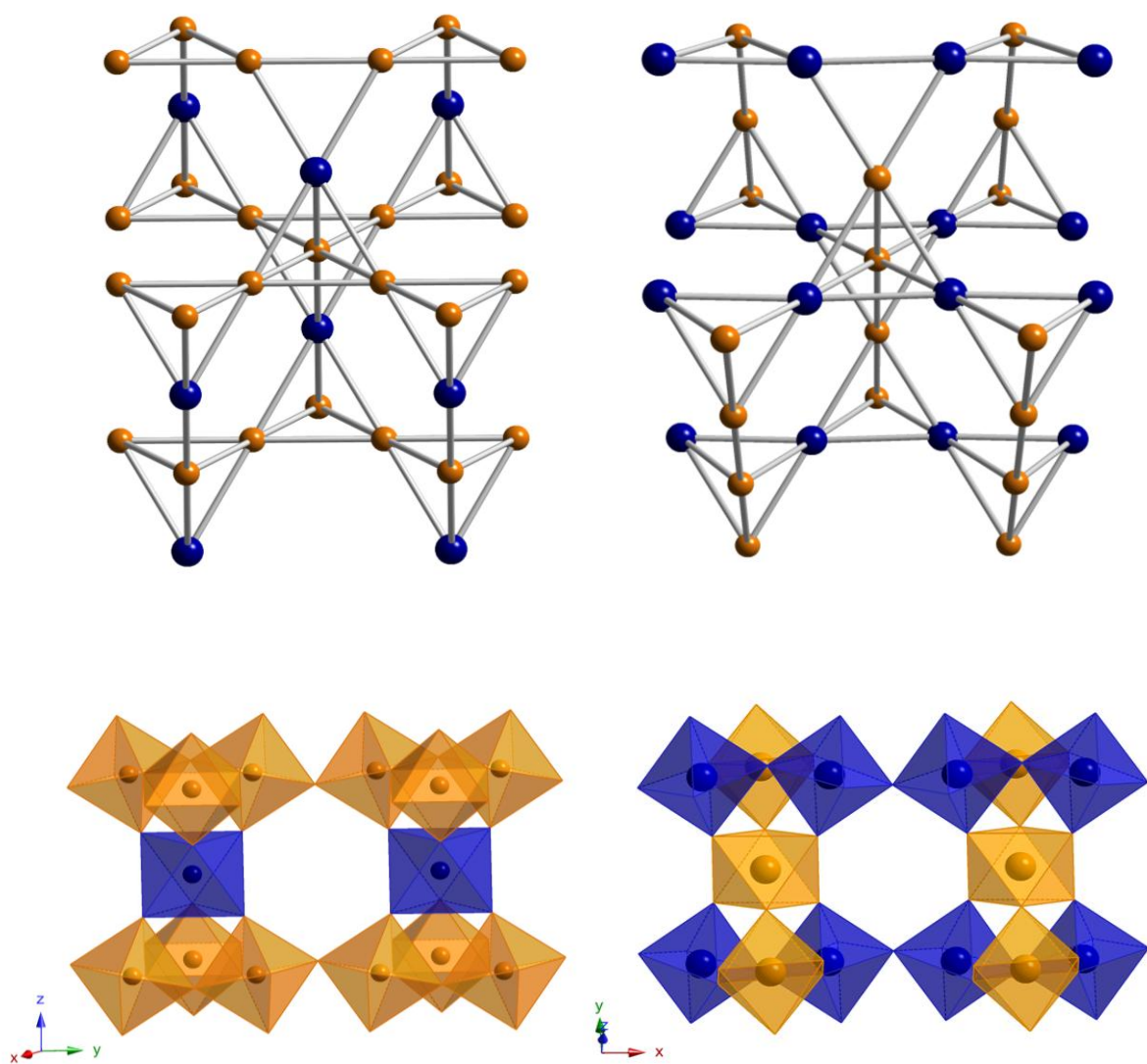


Figure 5.12: The arrangement of M and M' cations in the pyrochlore structure with 1:3 (top left) and 1:1 ordering (top right). Each of the 6 edges of a tetrahedron define a chain extended through the lattice. In the case of 1:3 ordering, 3 chains become all M cations and 3 chains become alternating M and M' cations. In the case of 1:1 ordering, one chain is all M cations, one is all M' cations, and the other 4 chains are alternating M and M' cations. Bottom left and right show polyhedral arrangement of 1:3 and 1:1, respectively.

The  $A_3B$  ordering has been observed only for  $CsTe_2O_6$ . The  $A_2B_2$  ordering scheme had been known for many  $A^{1+}M^{2+}M^{3+}F_6$  phases [5,15-17]. Now we find a variation of the  $A_2B_2$  scheme for  $CsTe_2O_{5.75}$ . In the  $A_3B$  structure the B cations have no B near neighbors; all six near neighbors of B are A atoms. The A cations have four A near neighbors and two B near neighbors. Three of the six chains defined by tetrahedral edges contain only A cations. The other three chains contain alternating A and B cations. For the  $A_2B_2$  network there is no possible ordered arrangement leading to either cation having all neighbors of the other type. Each of the A and B cations has two like and four unlike near neighbors. Now we have A chains running along the a axis and B chains running along the b axis. The direction of these chains is defined by the edges of the basic  $A_2B_2$  tetrahedron. The other four edges of this  $A_2B_2$  tetrahedron define chains with alternating A and B cations. Cubic symmetry cannot be maintained with either the  $A_3B$  or  $A_2B_2$  type ordering. The symmetry drops to rhombohedral for the  $A_3B$  ordering and to orthorhombic for  $A_2B_2$  the ordering. In the ideal pyrochlore structure the A cations are at an inversion center. An inversion center is maintained only for the B cation in the rhombohedral structure. Inversion centers are maintained for both A and B in the *Imma* structure but for only one of these cations in the *Pnma*.

When  $CsTe_2O_6$  becomes oxygen deficient by heating to high temperatures in air, the long-range order of  $Te^{4+}$  and  $Te^{6+}$  is disrupted, and the overall lattice symmetry becomes cubic. However, one expects considerable local distortion in the vicinity of  $Te^{4+}$  and O vacancies. When  $CsTe_2O_{6-x}$  phases are prepared at 500 °C, the  $Te^{4+}$  and O

vacancies collect along one of the six chains. For orthorhombic  $\text{CsTe}_2\text{O}_{5.75}$  there are Te1-O1 chains running along a, and this Te is all 6+. The other Te-O chains run along the b axis. The Te in these chains is close to 75%  $\text{Te}^{4+}$  and 25%  $\text{Te}^{6+}$ . About 25 % of the O2 sites of this chain are vacant. It is O3 and O4 that bond the two chains together. The  $\text{Te}^{4+}$  is attracted to the O vacancies to provide local charge balance and to provide a space for the lone pair of electrons. The ideal site for Te on this chain is an inversion center. However, the  $\text{Te}^{4+}$  cations on either side of this O vacancy are displaced 0.34 Å off this inversion center in the general direction of the O vacancy. This provides Te-O distances more appropriate for  $\text{Te}^{4+}$ . In this model the lone pair of electrons associated with  $\text{Te}^{4+}$  cations would become very close to one another in the region of the O vacancy. This is common behavior for lone pair cations. Close proximity of lone pairs occurs in PbO as well as in ternary oxides of  $\text{Pb}^{2+}$  [19,20]. This behavior is also well known in ternary oxides of  $\text{Te}^{4+}$ , with  $\text{CaTeO}_3$  being a particularly good example [21]. In  $\text{CsTe}_2\text{O}_{5.75}$  there are not enough O vacancies to accommodate all the  $\text{Te}^{4+}$  in positions adjacent to an O vacancy. The Te on this chain not adjacent to an O vacancy is a 1:1 mixture of  $\text{Te}^{4+}$  and  $\text{Te}^{6+}$ , and it is not so strongly displaced from the center of symmetry. However, it is likely that the environment of  $\text{Te}^{4+}$  at this site is strongly distorted relative to that of  $\text{Te}^{6+}$ . The large thermal ellipsoid of O4 (Table 5.1) is likely related to static displacements of O4 to provide a suitable asymmetric site for the  $\text{Te}^{4+}$  that is not adjacent to an O vacancy. If x could be increased to 0.5 for this orthorhombic pyrochlore-type structure, we would have  $\text{CsTe}^{4+}\text{Te}^{6+}\text{O}_{5.5}$  where all  $\text{Te}^{4+}$  could be adjacent to an O vacancy. Oxygen vacancies

are very rare in  $AM_2O_6$  compounds with the pyrochlore structure. However, it appears that the presence of a lone pair cation, such as  $Te^{4+}$ , can stabilize O vacancies in this structure because lone pairs will effectively occupy these vacancies. In fact,  $Cs_2Te_4O_9$  (or  $CsTe_2O_{4.5}$ ) can be regarded as an example of a  $AM_2O_{6-x}$  pyrochlore with ordered O vacancies where all Te is  $Te^{4+}$  [3].

The  $Te^{4+}$  cation in  $Cs_2Te^{4+}Te^{6+}_3O_{12}$  is apparently the only example of a  $5s^2$  cation at an inversion center in an oxide. However, the  $5s^2$  cation  $Sb^{3+}$  is at an inversion center in compounds of the type  $A_4Sb^{3+}Sb^{5+}X_{12}$  ( $A = Rb$  or  $Cs$ ;  $X = Cl$  or  $Br$ ) [11]. The only example of the  $6s^2$  cation  $Bi^{3+}$  at an inversion center with octahedral coordination is  $BaBi^{3+}Bi^{5+}O_6$  [12]. These are all class II mixed valence compounds according to the Robin and Day classification [13]. For class II mixed valence compounds we consider  $s^2 + s^0 \rightarrow 2s^1$  to be a low energy transition due to the similarity of the environments of the  $s^2$  and  $s^0$  cations. All of these compounds absorb light through most of the entire visible region due to this low transition energy. It would appear that in class II mixed valency the mixing of the  $s^2$  and  $s^0$  states enhances an  $s^2$  state that does not show the expected lone-pair distortion. Appreciable electronic conductivity for  $Cs_2Te^{4+}Te^{6+}_3O_{12}$  develops with increasing temperature as expected for a class II mixed-valence compound (Fig. 5.7). We have recently reported that even higher electrical conductivity can be obtained in  $Cs(Te,M)_2O_6$  pyrochlores that contain  $Te^{4+}$  [1,14]. This is caused by small M cations that compress the lattice and destabilize the  $s^2$  state.

$\text{Rb}_4\text{Te}_8\text{O}_{23}$  structure as reported by Minimol *et al.* contains 5  $\text{Te}^{6+}$  and 3  $\text{Te}^{4+}$  all of which are in distinct crystallographic sites. All  $\text{Te}^{6+}$  are in octahedral coordination while  $\text{Te}^{4+}$  cation is in square pyramidal and disphenoid coordinations. Polyhedra of all Te share corners to form 3-dimensional network. This network is similar to the arrangement in pyrochlore where tetrahedral units of cations connect to the neighboring units to form the framework (Fig. 5.13).

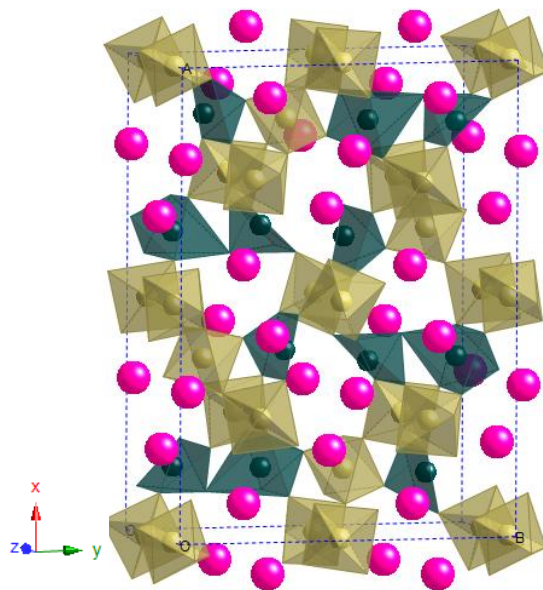


Figure 5.13:  $\text{Rb}_4\text{Te}_8\text{O}_{23}$  structure. Blue and yellow polyhedra represent polyhedra of  $\text{Te}^{4+}$  and  $\text{Te}^{6+}$ , respectively. Pink balls represent Rb.

The color and diffuse reflectance spectra of  $\text{CsTe}_2\text{O}_{6-x}$  samples are shown in Figure 5.14. The red color of the  $\text{CsTe}_2\text{O}_{6-x}$  phases and yellow color of  $\text{Cs}_4\text{Te}_8\text{O}_{23-x}$  indicate that they are class I mixed valence compounds with a much higher energy  $s^2 + s^0 \rightarrow 2s^1$  transition as the symmetry environment for  $\text{Te}^{4+}$  is significantly lower than

that for  $\text{Te}^{6+}$ . For  $\text{CsTe}_2\text{O}_{4.5}$ , only  $\text{Te}^{4+}$  is present; the mixed valence transition is gone, and the color is white.

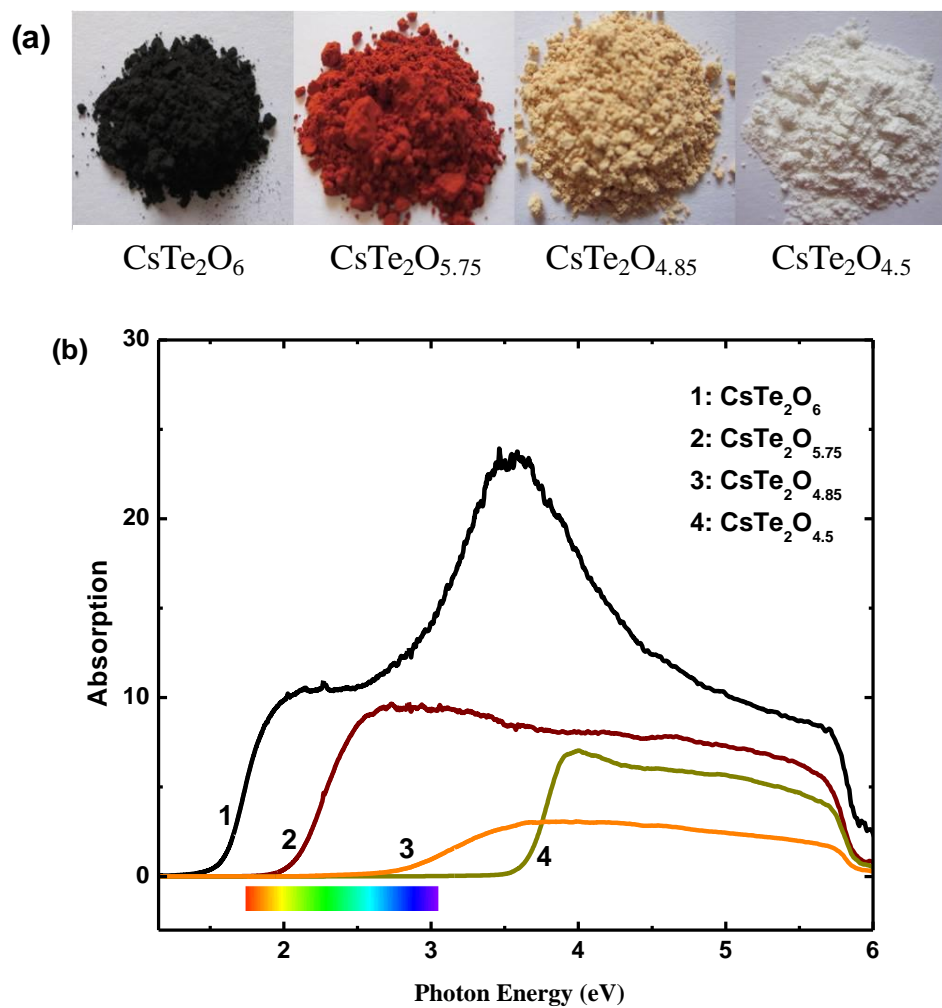


Figure 5.14: Optical properties (b) and appearance (a) of  $\text{CsTe}_2\text{O}_{6-x}$

### 5.3.4 Conclusion

Systematic studies of cesium tellurates,  $\text{CsTe}_2\text{O}_{6-x}$  where  $x = 0, 0.15, 0.25, 1.5$ , have been investigated. Structures of  $\text{CsTe}_2\text{O}_{6-x}$  phases were analyzed by single crystal X-ray diffraction and neutron powder diffraction. Stoichiometric  $\text{CsTe}_2\text{O}_6$  is a mixed

valence  $\text{Cs}_2\text{Te}^{4+}\text{Te}^{6+}_3\text{O}_{12}$  compound adopting rhombohedral pyrochlore-type structure with a complete order of the  $\text{Te}^{4+}$  and  $\text{Te}^{6+}$ . On heating at slightly above  $600^\circ\text{C}$ ,  $\text{CsTe}_2\text{O}_6$  lost oxygen resulting in cubic structure with disordered  $\text{Te}^{4+}/\text{Te}^{6+}$  and oxygen vacancies. Two novel phases of  $\text{CsTe}_2\text{O}_{6-x}$  were prepared with orthorhombic structure. The first phase with  $x$  of about 0.2-0.3 crystallizes in *Pnma* symmetry. At higher values of  $x$ , a new compound was discovered with a structure related to that reported for  $\text{Rb}_4\text{Te}_8\text{O}_{23}$ .

### 5.3.5 Experimental

$\text{CsTe}_2\text{O}_6$  was prepared by heating a stoichiometric mixture of  $\text{CsNO}_3$  (Alfa Aesar, 99.8%) and  $\text{TeO}_2$  (Aldrich, 99+%) in air at  $600^\circ\text{C}$  for 12 hours.  $\text{Cs}_2\text{CO}_3$  (Alfa Aesar, 99.9%) and  $\text{TeO}_2$  were used to prepare  $\text{CsTe}_2\text{O}_{4.5}$  by solid state reaction at  $500^\circ\text{C}$  for 12 hours under Ar atmosphere. To prepare polycrystalline samples of  $\text{CsTe}_2\text{O}_{6-x}$  with  $x = 0.25-1.15$ , appropriate amounts of  $\text{CsTe}_2\text{O}_6$  and  $\text{CsTe}_2\text{O}_{4.5}$  were reacted in evacuated and sealed silica tubes at  $500^\circ\text{C}$  for 12 hours. All samples were characterized by powder X-ray diffraction collected on a Rigaku MiniFlex II powder diffractometer using  $\text{Cu K}\alpha$  radiation and a graphite monochromator on the diffracted beam. Thermogravimetric analyses were performed on a Mettler Toledo TGA 850. The diffuse reflectance spectra were obtained in the range of 200-1100 nm using Xe lamp with a grating double monochromator.  $\text{BaSO}_4$  was used to as a reference to normalize the data. The Kubelka-Munk function was used to transform reflectance data to absorbance. High temperature resistivity was measured by the 2-probe method using platinum electrodes. The pellet was sandwiched between two sheets of Pt, which

were connected to a multimeter through platinum wire. A temperature programmable furnace was used to heat the sample.

A single crystal of cubic  $\text{CsTe}_2\text{O}_{6-x}$  was obtained from a partially melted pellet of  $\text{CsTe}_2\text{O}_6$  that had been heated above  $600^\circ\text{C}$ . Crystals of rhombohedral  $\text{CsTe}_2\text{O}_6$  were prepared by chemical vapor transport using  $\text{TeCl}_4$  as a transporting agent. Reactants were weighted in an Ar-filled glove box and loaded into a silica tube (1 cm diameter and 15 cm length) that was evacuated and sealed. The zones of the two-zone furnace were set at  $620^\circ\text{C}$  and  $590^\circ\text{C}$ . The tube was kept at these temperatures for 120 hours before being cooled to  $450^\circ\text{C}/480^\circ\text{C}$  at  $0.1^\circ\text{C}/\text{min}$  and then cooled to room temperature at  $5^\circ\text{C}/\text{min}$ . Rhombohedral  $\text{CsTe}_2\text{O}_6$  crystals formed in the hot end of the tube.

Single crystal X-ray diffraction data were collected on a Bruker SMART APEXII CCD system using an Oxford Cryostream cooler at 173 or 273 K. A standard focus tube was used with an anode power of 50 kV at 30 mA, a crystal to plate distance of 5.0 cm,  $512 \times 512$  pixels/frame, beam center (256.52, 253.16),  $\phi/\omega$  scan with step of  $0.30^\circ$ , exposure/frame of 10.0s/frame, and SAINT integration. SADABS program was used to correct for absorption. The crystal structures were solved by the direct method using the SHELXS program and refined by the full-matrix least-squares method using SHELXTL software [22].

Neutron diffraction data were collected on three samples. A sample of  $\text{CsTe}_2\text{O}_6$  was prepared in air as described above, and a sample of  $\text{CsTe}_2\text{O}_{5.75}$  was prepared in a silica ampoule as described above. The third sample was prepared by



placing CsTe<sub>2</sub>O<sub>6</sub> in the furnace previously heated to 610°C, holding for 2 hours, and then quenching to room temperature. This procedure was repeated for 2.5 hours and again for 2 hours. Neutron powder diffraction data were collected using the BT-1 32-counter high-resolution diffractometer at the NIST Center for Neutron Research at the National Institute of Standards and Technology. A Cu (311) monochromator, yielding a wavelength of 1.5401(2) Å, was employed. Collimation of 15' of arc was used before the monochromator, 20' before the sample, and 7' before the detectors. The samples were loaded into vanadium containers 15.8 mm in diameter and 50 mm in length. Data were collected at room temperature over a 2θ range of 3° to 168°. The neutron diffraction data were refined by the Rietveld method using GSAS software [23]

## 5.4 W-Substitued CsTe<sub>2</sub>O<sub>6</sub>

### 5.4.1 Introduction

CsW<sub>2</sub>O<sub>6</sub> was first prepared as a major phase from solid state reaction of Cs<sub>2</sub>WO<sub>4</sub>, WO<sub>3</sub>, and WO<sub>2</sub> by Cava *et al.* [24]. Reitveld refinement from powder X-ray diffraction showed cubic defect pyrochlore structure,  $Fd\bar{3}m$  space group [24]. Although the average oxidation state of W in this compound is 5.5, the cubic symmetry suggests no ordering of W. Cs<sub>2</sub>TeW<sub>3</sub>O<sub>12</sub> single crystal was grown by hydrothermal method. The compound crystallizes in  $P6_3$  space group where WO<sub>6</sub> octahedra share corners to form hexagonal layers [25]. Each layer is connected by trigonal pyramidal TeO<sub>3</sub> groups [25]. Figure 5.15 shows Cs<sub>2</sub>TeW<sub>3</sub>O<sub>12</sub> structure

comparing with  $\text{CsTe}_2\text{O}_6$  which can be written as  $\text{Cs}_2\text{Te}^{4+}\text{Te}^{6+}_3\text{O}_{12}$  [3]. Although they crystallize in different space group, the two structures are closely related. Both structures consist of similar corner sharing octahedral networks of  $\text{M}^{6+}\text{O}_6$  but the connecting group in  $\text{Cs}_2\text{TeW}_3\text{O}_{12}$  is trigonal pyramidal  $\text{Te}^{4+}\text{O}_3$  while  $\text{Te}^{6+}\text{O}_6$  layers in  $\text{CsTe}_2\text{O}_6$  are linked by octahedral  $\text{Te}^{4+}\text{O}_6$  (Fig 5.15). Here, we report the synthesis and characterizations of solid solutions between  $\text{Cs}_2\text{Te}^{4+}\text{Te}^{6+}_3\text{O}_{12}$  and  $\text{Cs}_2\text{TeW}_3\text{O}_{12}$ ,  $\text{CsTe}_{2-x}\text{W}_x\text{O}_6$  when  $x=0-3$ .

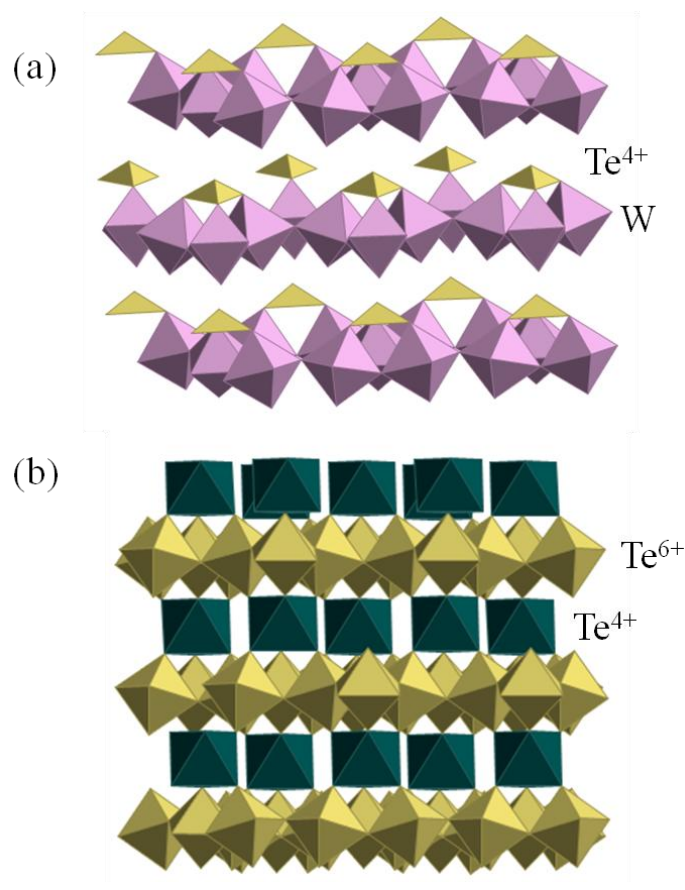


Figure 5.15: Crystal structure of  $\text{Cs}_2\text{TeW}_3\text{O}_{12}$  (a) and  $\text{Cs}_2\text{Te}_4\text{O}_{12}$  ( $\text{CsTe}_2\text{O}_6$ ). Cs has been removed for clarity.

### 5.4.2 Results and Discussion

Powder X-ray diffraction of representative compounds from  $\text{CsTe}_{2-x}\text{W}_x\text{O}_6$  series are shown in Figure 5.16 comparing with the end members,  $\text{CsTe}_2\text{O}_6$  and  $\text{CsTe}_{0.5}\text{W}_{1.5}\text{O}_6$ . The abrupt structural change was observed at W content as low as 0.1 where the major phase could be indexed as defect cubic pyrochlore although small peaks of  $\text{CsTe}_2\text{O}_6$  were still present. Pure cubic phase was achieved at  $x=0.2$  to  $x=0.5$ . As discussed earlier, rhombohedral  $\text{CsTe}_2\text{O}_6$  and cubic  $\text{CsTe}_{2-x}\text{W}_x\text{O}_6$  are closely related. Both structures have  $\text{Te}^{4+}$  in octahedral coordination which is not known for any other oxides. While  $\text{Te}^{4+}$  and  $\text{Te}^{6+}$  are ordered in  $\text{CsTe}_2\text{O}_6$  by occupying distinct crystallographic sites because of the longer  $\text{Te}^{4+}\text{-O}$  bond, substitution of W disorder all species,  $\text{Te}^{4+}/\text{Te}^{6+}/\text{W}^{6+}$ , giving rise to cubic symmetry.  $\text{CsTe}_{0.5}\text{W}_{1.5}\text{O}_6$  peaks were first detected at  $x=0.6$ . Cell parameter of each pure phase was refined by least-square method in the presence of internal standard (NaCl) using GSAS software package [23]. Figure 5.17 shows a plot of refined cell parameters and cell volumes versus tungsten content. As ionic radii of  $\text{W}^{6+}$  is higher than that of  $\text{Te}^{6+}$  (0.6Å versus 0.56Å) [26], cell parameters and cell volumes increase with tungsten content as expected.

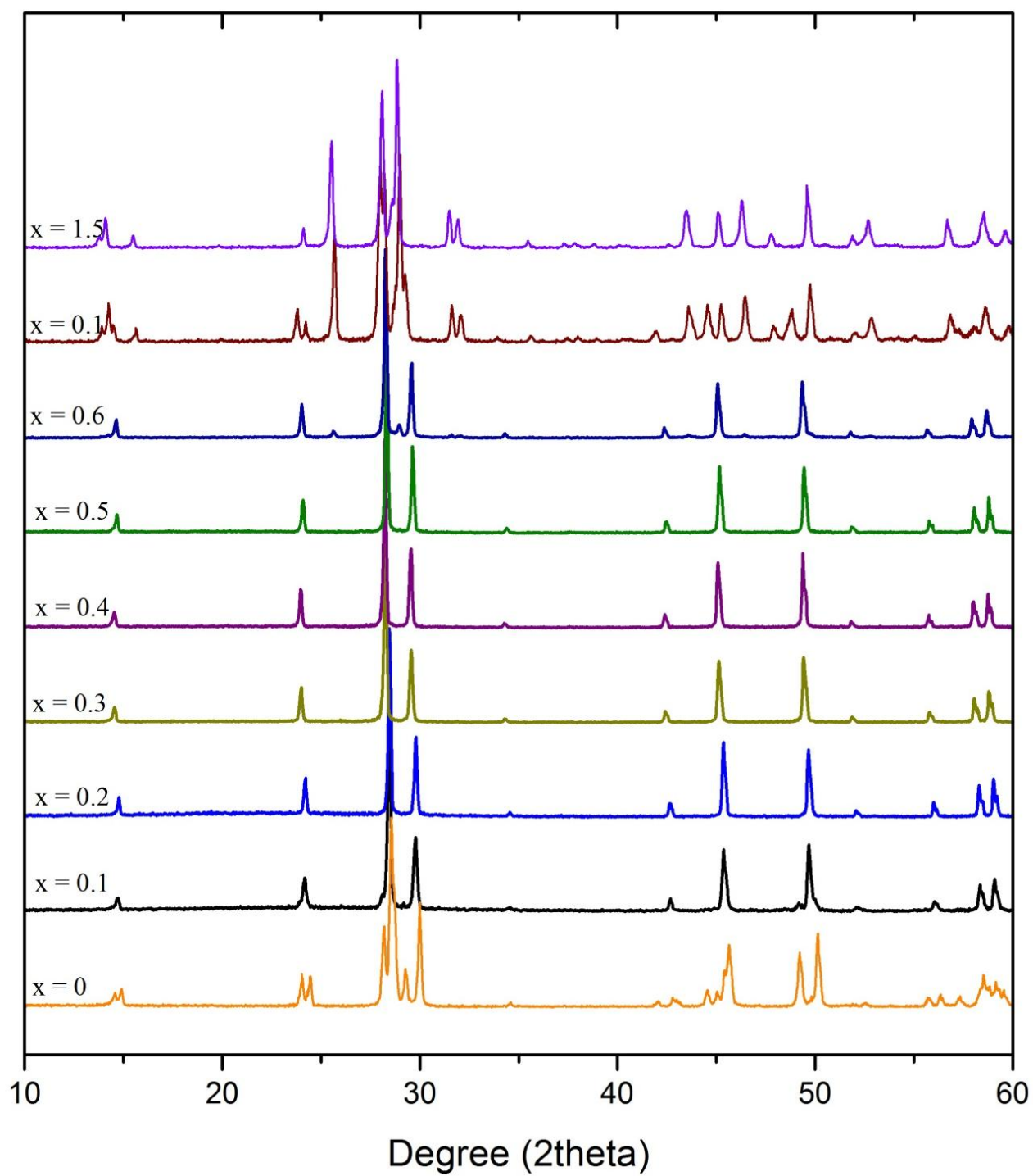


Figure 5.16: Powder X-ray patterns of  $\text{CsTe}_{2-x}\text{W}_x\text{O}_6$

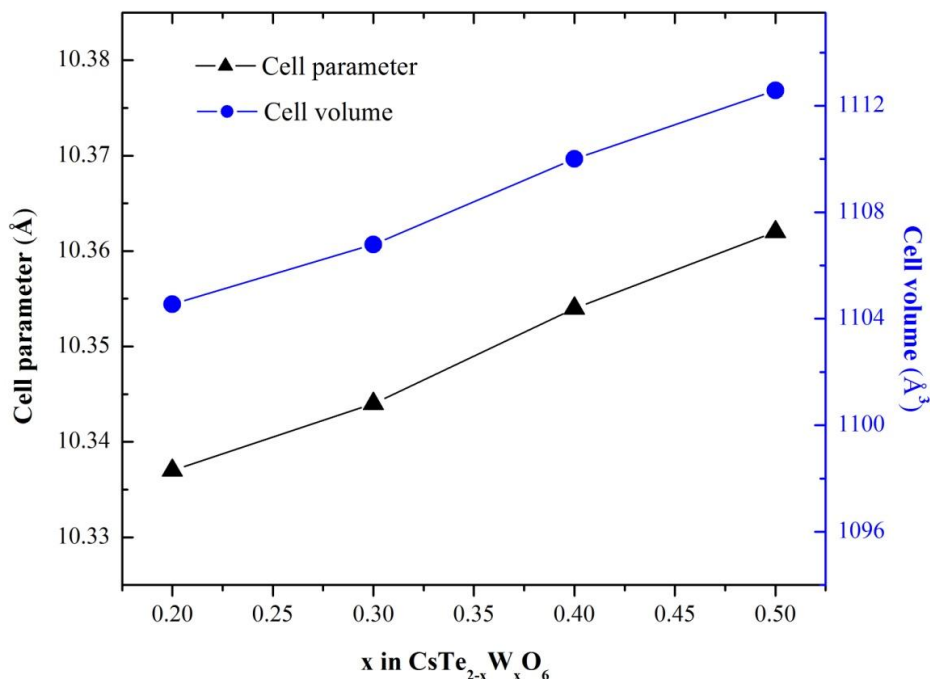


Figure 5.17: Plots of cell parameters and cell volumes versus tungsten content,  $x$ , in  $\text{CsTe}_{2-x}\text{W}_x\text{O}_6$ .

None of the compounds show detectable conductivity at room temperature. Colors of the materials change from white in  $\text{CsTe}_{0.5}\text{W}_{1.5}\text{O}_6$  to very dark brown in  $\text{CsTe}_2\text{O}_6$ . Figure 5.18 shows the physical appearances and optical properties of the samples in UV-Visible region. Absorption in the visible region explains the color appearance of the samples.  $\text{CsTe}_{0.5}\text{W}_{1.5}\text{O}_6$  has no absorption in visible region resulting in the white color.  $\text{CsTe}_2\text{O}_6$  absorbs most wavelengths of the visible region but the edge in red-orange region gives small fraction of red-orange to color of the compound resulting in a very dark brown color. The solid solution  $\text{CsTe}_{2-x}\text{W}_x\text{O}_6$  with  $x=0.2-0.4$  show continuous change in color with absorption edge shift toward higher energy when W content is increased.

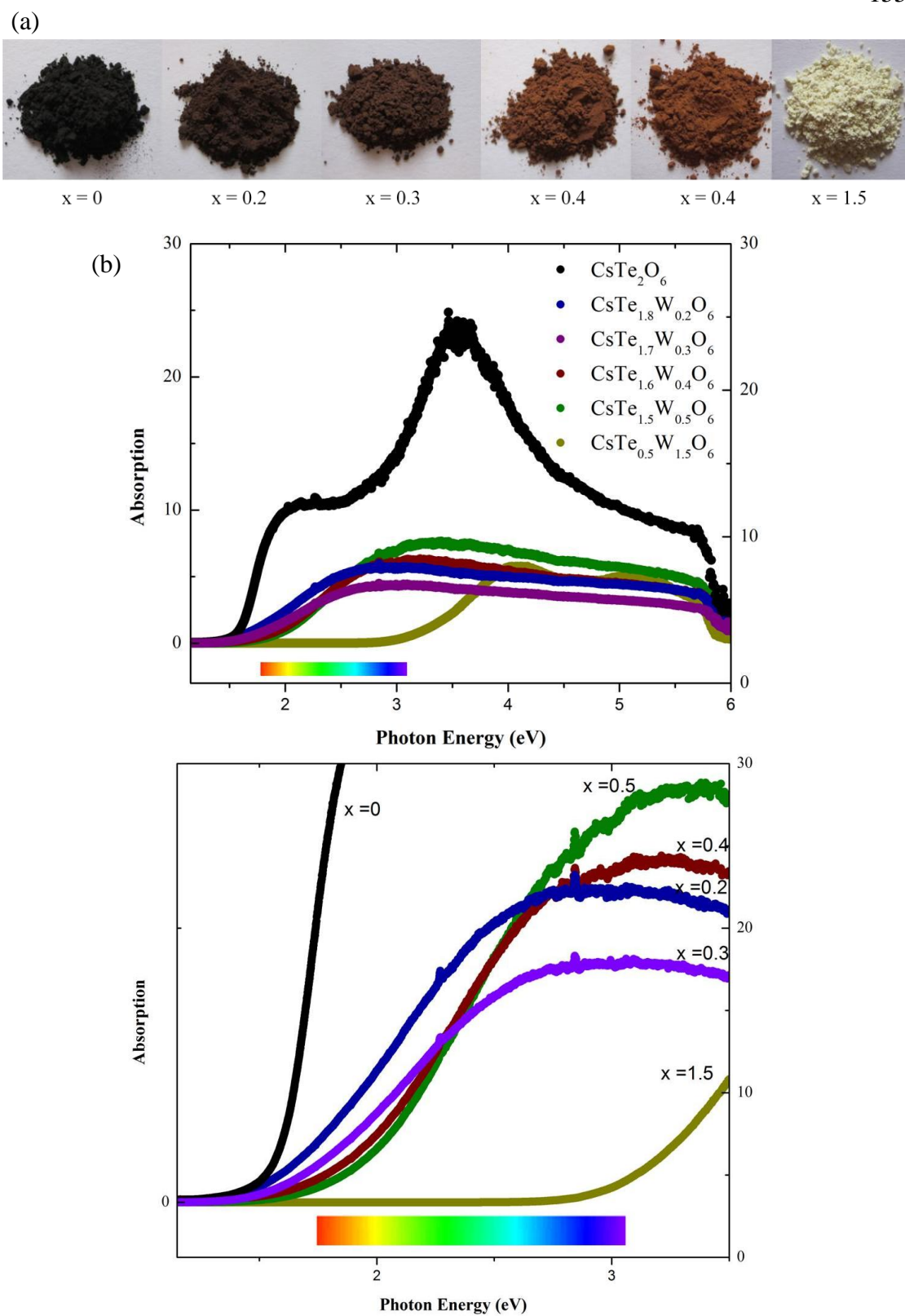


Figure 5.18: Color (a) and optical property (b) of  $\text{CsTe}_{2-x}\text{W}_x\text{O}_6$

Most of  $\text{Te}^{6+}$  and/or  $\text{Te}^{4+}$  compounds are white. Although intervalence charge transfer (IVCT) between  $\text{Te}^{4+}$  and  $\text{Te}^{6+}$  in the mixed valence compounds can give rise to optical absorption, it usually results in absorption of higher energy as  $\text{Te}^{4+}$  and  $\text{Te}^{6+}$  are usually in very different environments.  $\text{CsTe}_2\text{O}_6$  is an exception since both  $\text{Te}^{4+}$  and  $\text{Te}^{6+}$  are in octahedral coordination and the charge transfer between them originates the color. There is no mixed valence situation in  $\text{CsTe}_{0.5}\text{W}_{1.5}\text{O}_6$  and  $\text{Te}^{4+}$  -  $\text{W}^{6+}$  charge transfer require photon with higher energy than the visible region. Samples with  $x=0.2-0.5$  contain Te with both oxidation state and therefore, possess the color. Comparing to  $\text{CsTe}_2\text{O}_6$ , lower intensity of absorption and higher absorption edge are observed in the solid solution because there is relatively less amount of mixed valency and  $\text{Te}^{4+}/\text{Te}^{6+}$  charge transfer is possibly hindered by W in the lattice.

### 5.4.3 Conclusion

Series of compounds with formula  $\text{CsTe}_{2-x}\text{W}_x\text{O}_6$  with  $x=0.2-0.5$  have been made which can be considered as solid solution of  $\text{CsTe}_2\text{O}_6$  and  $\text{CsTe}_{0.5}\text{W}_{1.5}\text{O}_6$ . Although the two end members adopt rhombohedral and trigonal structure, these solid solution phases crystallize in cubic defect pyrochlore structure with  $\text{W}^{6+}$ ,  $\text{Te}^{6+}$ , and  $\text{Te}^{4+}$  randomly occupy 16c octahedral site. Optical properties of the compounds can be explained by intervalence charge transfer between  $\text{Te}^{4+}$  and  $\text{Te}^{6+}$  in the structure which are in the same octahedral coordination. However, this charge transfer between the Te species in two different crystallographic sites requires relatively large activation energy and the compounds show no electronic conductivity at room temperature.

#### 5.4.4 Experimental

Polycrystalline samples of  $\text{CsTe}_{2-x}\text{W}_x\text{O}_6$  with  $x=0.2-0.5$  were prepared by standard solid state reaction. Stoichiometric mixtures of  $\text{CsNO}_3$  (Alfa Aesar, 99.8%),  $\text{TeO}_2$  (Acros Organics, 99+%), and  $\text{WO}_3$  (Aldrich, 99+%) were ground, pressed into pellet, and heat at  $600^\circ\text{C}$  for 24 hours in air using gold containers. All samples were characterized by powder X-ray diffraction using a Rigaku MiniFlex II powder diffractometer using  $\text{Cu K}\alpha$  radiation and a graphite monochromator on the diffracted beam. The diffuse reflectance spectra were obtained in the range of 200-1100 nm using Xe lamp with a grating double monochromator.  $\text{BaSO}_4$  was used to as a reference to normalize the data. Kubelka-Munk function was used to transform reflectance data to absorbance.

#### 5.5 References:

1. T. Siritanon, G. Laurita, R. T. Macaluso, J. N. Millican, A.W. Sleight, M.A. Subramanian, *Chem. Mater.*, **21** (2009), 5572.
2. K. Ramesha, L. Sebastian, B. Eichhorn, J. Gopalakrishnan, *J. Mater. Chem.*, **13** (2003), 2011.
3. B. O. Loopstra, K. Goubitz, *Acta Cryst. C*, **42** (1986), 520.
4. T. Scott Ercit, F. C. Hawthorne, P. Cerny, *Can. Mineral.*, **24** (1986), 655.
5. M. A. Subramanian, W. J. Marshall, R. L. Harlow, *Mat. Res. Bull.*, **31** (1996), 585.
6. B. G. Müller, *J. Fluorine Chem.*, **17** (1981), 317.
7. K. Wieghardt, H. Siebert, *J. Mol. Structure*, **7** (1971), 305.
8. D. Groult, J. Pannetier, B. Raveau, *J. Solid State. Chem.*, **41** (1982), 277.
9. A. Driouiche, F. Abraham, M. Touboul, M. Figlarz, *Mat. Res. Bull.*, **26** (1991), 901.
10. F. A. Weber, S. F. Meier, T. Schleid, *Z. Kristallogr. Suppl.*, **180** (2001), 149.
11. K. Prassides, P. Day, A.K. Cheetham, *Inorg. Chem*, **24** (1985), 545.
12. D.E. Cox, A.W. Sleight, *Solid State Commun.*, **19** (1976), 969.
13. M. B. Robin, P. Day, *Adv. Inorg. Chem. and Radiochem.*, **10** (1967), 247.
14. J. Li, T. Siritanon, J. K. Stalick, A. W. Sleight, M. A. Subramanian, *Inorg. Chem.*, **50** (2011), 5747.



15. K. Friese, J.-Y. Gesland, A. Grzechnik, *Z. Kristallogr.*, **220** (2005) 614.
16. A. Tressaud, R. De Pape, J. Portier, P. Hagemuller, *Bull. Soc. Chim. Fr.*, **10** (1970) 3411.
17. G. Ferey, M. Leblanc, R. de Pape., *J. Solid State Chem.*, **40** (1981), 1.
18. M. P. Minimol, K. Vidyasagar, *Inorg. Chem.*, **44** (2005), 9369.
19. H. Mizoguchi, A. P. Ramirez, T. Siegrist, L. N. Zakharov, A. W. Sleight, M. A. Subramanian, *Chem. Mater.*, **21** (2009), 2300.
20. B. Darriet, M. Devalette, B. Latourrette, *Acta. Cryst.*, **B34** (1978), 3528.
21. B. Stöger, W. Matthias, E. Zobetz, G. Giester, *Acta Cryst.*, **B65** (2009), 167.
22. G.M. Sheldrick, SHELEXTL, Version 6.14, Bruker Analytical X-ray Instruments, Inc., Madison, WI, 2003.
23. A.C. Larson, R.B. Von Dreele, "General Structure Analysis System (GSAS)," Los Alamos National Laboratory Report LAUR, 86-784 (2004); B.H. Toby, *J. Appl. Crystallogr.*, **34** (2001) 210.
24. R. J. Cava, R. S. Roth, T. Siegrist, B. Hessen, J. J. Krajewski, W. F. Peck Jr., *J. Solid State Chem.*, **103** (1993), 359.
25. J. Goodey, K. M. Ok, J. Broussard, C. Hofmann, F. V. Escobedo, P. S. Halasyamani, *J. Solid State Chem.*, **175** (2003), 3.
26. R. D. Shannon, *Acta Crystallogr., Sect. A*, **32** (1976), 751.

## Chapter

### 6. New pyrochlore of the type $\text{CdBi}(\text{M},\text{Te})_2\text{O}_7$

#### 6.1 Abstract

Novel cubic pyrochlores with the formula  $(\text{CdBi})(\text{MTe})\text{O}_7$ ,  $\text{M} = \text{Al}, \text{Cr}, \text{Ga}, \text{In}, \text{Fe}, \text{Mn},$  and  $\text{Sc}$  were synthesized by solid state reaction using oxides of the constituent elements. Magnetic properties analysis show paramagnetism in  $\text{M} = \text{Cr}$  and  $\text{Mn}$  but antiferromagnetism with short-range correlation in  $\text{M} = \text{Fe}$  phase. All compositions are insulating. Dielectric measurements show relatively low dielectric constants which were independent of temperature and frequency.

#### 6.2 Introduction

##### 6.2.1 Quaternary pyrochlores

As discussed earlier in chapter 4, pyrochlore oxides have a general formula  $\text{A}_2\text{B}_2\text{O}_7$  where various cations can be substituted in A and B sites. Many examples of Te-containing pyrochlore oxides are known with  $\text{AB}_2\text{O}_6$  defect pyrochlore but much less are known with the normal  $\text{A}_2\text{B}_2\text{O}_7$ .  $\text{Pr}_2\text{Te}_2\text{O}_7$  and  $\text{Ln}_2\text{Te}_2\text{O}_7$ ,  $\text{Ln} = \text{La}, \text{Nd}, \text{Eu},$  and  $\text{Gd}$  are the only examples [1-2]. These compounds adopt cubic structure despite of  $4s^2$  lone pair electrons on  $\text{Te}^{4+}$ . To our best knowledge, there are no reports on  $\text{Te}^{6+}$ -containing oxides with  $\text{A}_2\text{B}_2\text{O}_7$  normal pyrochlore. However, other cations with 6+ oxidation state are known with this composition.

Pyrochlore oxides of the formula  $A^{1+}_2B^{6+}_2O_7$  are not known [3].  $A^{1+}_2B^{6+}_2O_7$  compounds can be prepared but none of them form pyrochlore structure.  $Na_2Mo_2O_7$  and  $Na_2W_2O_7$  crystallize in orthorhombic structure [4-5]. On the other hand,  $K_2Mo_2O_7$  and  $K_2W_2O_7$  adopt triclinic and monoclinic structure, respectively [6-7].  $Rb_2W_2O_7$  is isostructural to  $K_2W_2O_7$  [8] while  $Rb_2Mo_2O_7$  crystallizes in orthorhombic structure [9] and  $Cs_2Mo_2O_7$  is monoclinic [9].

Partial substitutions of hexavalent cations in B sites of pyrochlore are more common. Cubic pyrochlores of  $(A^{1+}Ln^{3+})(Zr^{4+}Mo^{6+})O_7$  when  $A = Li, Na$  and  $Ln = La, Sm$  were prepared by Mccauley *et al.* [10]. Subramanian *et al.* synthesized and reported electrical properties of  $Ln_2(V^{3+}_{4/3}W^{6+}_{2/3})O_7$  pyrochlore when  $Ln = Gd \rightarrow Lu$  and  $Y$  by solid state reaction under vacuum [11].  $(CdBi)(MW)O_7$ ,  $M = Cr, Ga, V, Mn, Fe, Rh, Sc,$  and  $In$  were prepared by solid state reaction and some phases were reported to have interesting dielectric properties where dielectric constants are independent of temperature and frequency [12].

## 6.2.2 Magnetic pyrochlore oxides

Because pyrochlore structure composes of tetrahedral arrangement of corner shared  $BO_6$  octahedra, the compounds exhibit interesting magnetic properties due to magnetic frustration [13].

At high temperature, most magnetic materials exhibit paramagnetism where the spins are randomly oriented. The spins tend to align in an order manner at lower temperature to lower their energy. The most common magnetic orderings are parallel (ferromagnetic) and antiparallel (antiferromagnetic and ferromagnetic). However, in

some cases, the system cannot minimize its total classical energy because of some limitations leading to frustration [13].

Magnetic frustration can be divided into two classes; geometric and random frustration. Geometry and symmetry of the structure can sometimes forbid certain alignment of the spins. Some examples of such situations are shown in Figure 6.1. Only two out of three spins at corners of a triangle can be aligned antiparallel (Fig. 6.1(a)). Similarly, only two out of four spins at the corners of a tetrahedron can simultaneously be antiparallel to each other (Fig. 6.1(b)). [13]. Random frustration arises from the competing interactions among degrees of freedom in equilibrium or when the randomness is quenched [13].

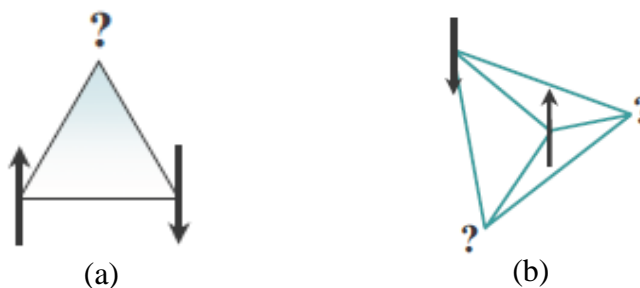


Figure 6.1: Geometric frustration of antiferromagnetic alignment on a triangle (a) and tetrahedron (b) [13].

Many pyrochlore oxides exhibit interesting magnetic behaviors. A review by Gardner summarized magnetism in pyrochlore oxides including long-range ordering, spin-glass, spin-ice, and spin-liquid [13].

In this work, series of compounds with formula  $(\text{CdBi})(\text{MTe})\text{O}_7$ ,  $\text{M} = \text{Al}, \text{Cr}, \text{Ga}, \text{In}, \text{Sc}, \text{Mn},$  and  $\text{Fe}$  adopting cubic pyrochlore structure were prepared by solid state reaction. Magnetic properties in some phases were studied and dielectric properties of the compounds were reported.

## 6.3 Results and Discussion

### 6.3.1 Structure

Figure 6.2 shows observed powder X-ray diffraction patterns of  $\text{CdBiMTeO}_7$  pyrochlore with  $\text{M} = \text{In}, \text{Sc}, \text{Mn}, \text{Fe}, \text{Al}, \text{Ga},$  and  $\text{Cr}$ . All compositions gave single phase oxides which all diffraction peaks can be indexed based on  $\text{A}_2\text{M}_2\text{O}_7$  pyrochlore structure. There is no indication of ordering in either A sites or B sites. Therefore,  $\text{Cd/Bi}$  and  $\text{M/Te}$  randomly occupy 16d and 16c position, respectively. Comparing to perovskite oxides, disordering of cations in pyrochlore oxides is more common [12]. The most frequently found cation ordering in perovskite is 1:1 ordering in  $\text{A}(\text{B},\text{B}')\text{O}_3$  where B and B' systematically order in NaCl-type arrangement as shown in Figure 6.3. In such an arrangement, oxygens move toward the smaller cations to satisfy bond lengths for both smaller and larger cations [14]. Moreover, this ordering puts 'like' cations at the opposite face diagonals of the cube which reduces the electrostatic repulsion between them [12]. On the other hand, such benefits from cation ordering cannot be achieved in pyrochlore structure. Therefore, cation ordering is not expected way to reduce electrostatic repulsion [12].

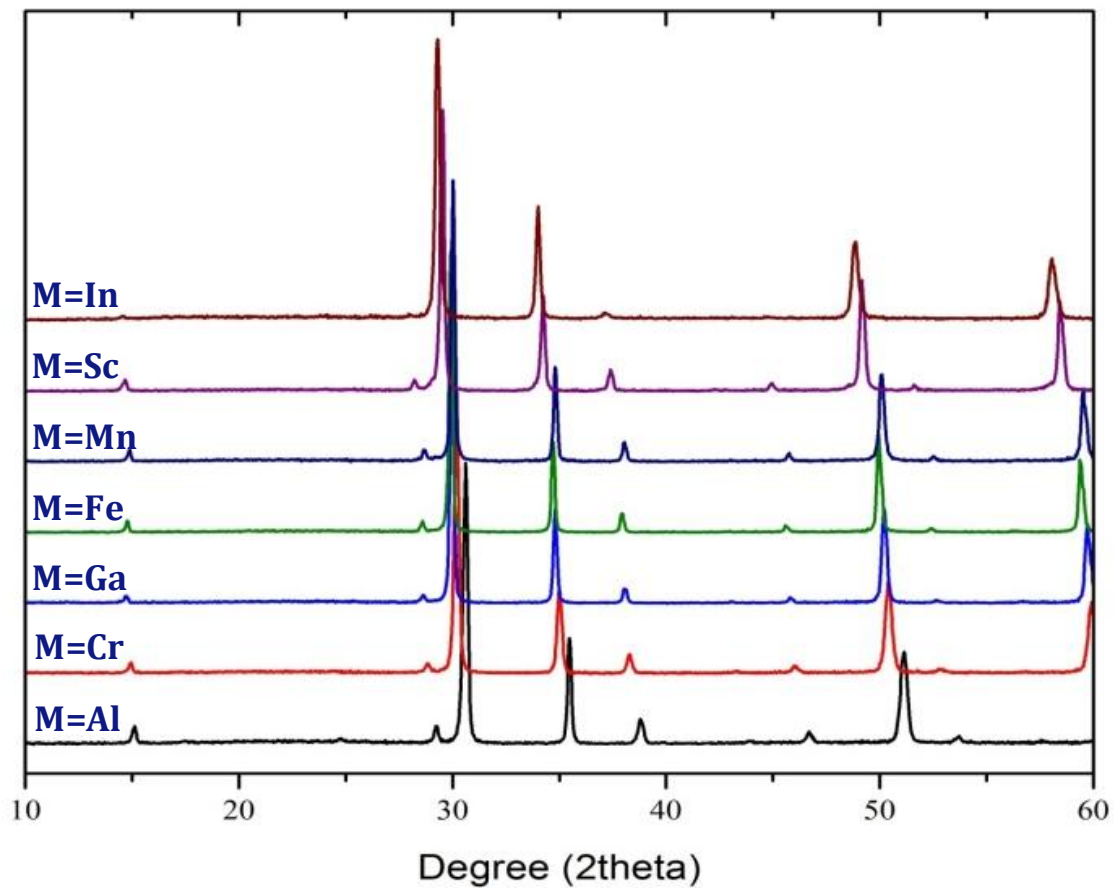


Figure 6.2: Powder X-ray diffraction pattern of  $\text{CdBiMTeO}_7$ .

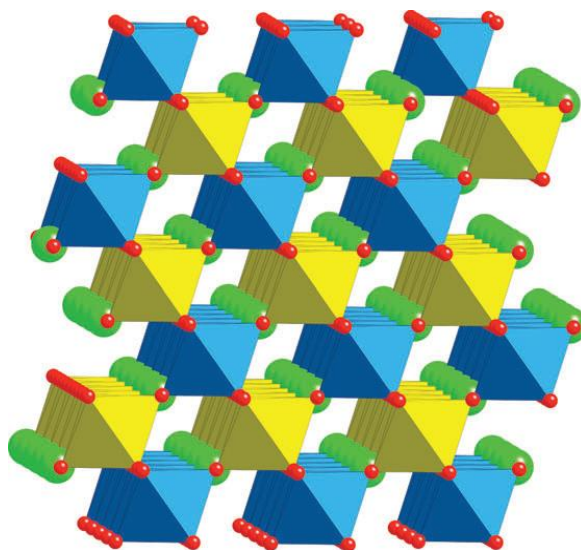


Figure 6.3: 1:1 cation ordering with NaCl-type arrangement in perovskite [14].

Table 6.1 shows the cell parameters and dielectric constant of  $\text{CdBiMTeO}_7$  prepared in this work. Unit cell parameters were refined by least squares method using UnitCell program [15]. Figure 6.4 represents plots of refined unit cell parameters and cell volumes versus average ionic radius in B sites. Both of them show linear behavior as expected [16].

Table 6.1: Novel pyrochlore oxides of the type  $(\text{CdBi})(\text{MTe})\text{O}_7$  made in this study

| Composition          | Avg. radius at B sites ( $\text{\AA}$ ) | Cell parameter ( $\text{\AA}$ ) | Cell volume ( $\text{\AA}^3$ ) | Dielectric constant at RT ( $10^6$ Hz) | Color       |
|----------------------|---|---------------------------------|--------------------------------|--|-------------|
| $\text{CdBiAlTeO}_7$ | 0.5475                                  | 10.0909                         | 1027.52                        | 11                                     | Pale yellow |
| $\text{CdBiCrTeO}_7$ | 0.5875                                  | 10.2449                         | 1075.30                        | 73                                     | Dark green  |
| $\text{CdBiGaTeO}_7$ | 0.59                                    | 10.2906                         | 1089.74                        | 20                                     | Pale yellow |
| $\text{CdBiFeTeO}_7$ | 0.6025                                  | 10.3254                         | 1100.84                        | 44                                     | Red         |
| $\text{CdBiMnTeO}_7$ | 0.6025                                  | 10.2980                         | 1092.10                        | 59                                     | Black       |
| $\text{CdBiScTeO}_7$ | 0.6525                                  | 10.4707                         | 1147.97                        | 40                                     | Pale yellow |
| $\text{CdBiInTeO}_7$ | 0.68                                    | 10.5360                         | 1169.58                        | 28                                     | Pale yellow |

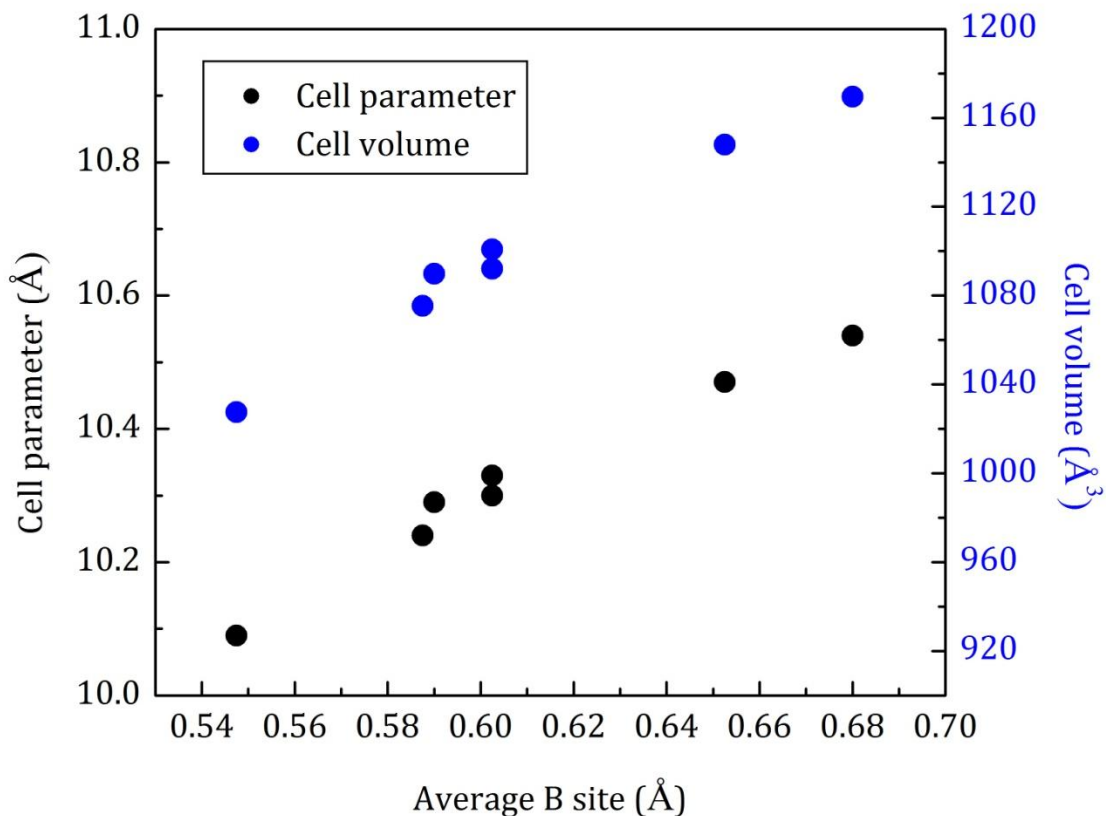


Figure 6.4: Plots of unit cell parameters and cell volumes versus average ionic radii at B site

### 6.3.2 Magnetic properties

Magnetic measurements were done on compositions which contain magnetic species; M= Cr, Mn, and Fe. Paramagnetic behavior was found in M= Cr and Mn. Temperature dependence of inverse magnetic susceptibility follows the Curie-Weiss law in temperature range 5-320K (Fig. 6.5-6.6). The obtained Curie constant (C) and Weiss constant ( $\theta_w$ ) are shown in Table 6.2 comparing with theoretical values of spin-only magnetic moments which were calculated by assuming 3+ oxidation state for all Cr and Mn. The calculated values (Table 6.2) agree well with the observed magnetic



moments. As paramagnetism requires no ordered interaction between cations, this also supports the disordering of the cations in B sites of the structure although negative Weiss constants indicate prevailing antiferromagnetic interaction.

Table 6.2: Magnetic properties of  $\text{CdBiMTeO}_7$ ,  $M = \text{Cr, Mn}$

| Composition          | Temperature range (K) | $\mu_{\text{obs}}$ ( $\mu_{\text{B}}$ ) | $\mu_{\text{calc}}$ ( $\mu_{\text{B}}$ ) | $\Theta_{\text{w}}$ (K) | C (emu.K/mol) |
|----------------------|-----------------------|---|--|-------------------------|---------------|
| $\text{CdBiCrTeO}_7$ | 5-320                 | 3.81                                    | 3.87                                     | -16.490                 | 1.8161        |
| $\text{CdBiMnTeO}_7$ | 5-320                 | 4.85                                    | 4.90                                     | -3.833                  | 3.0075        |

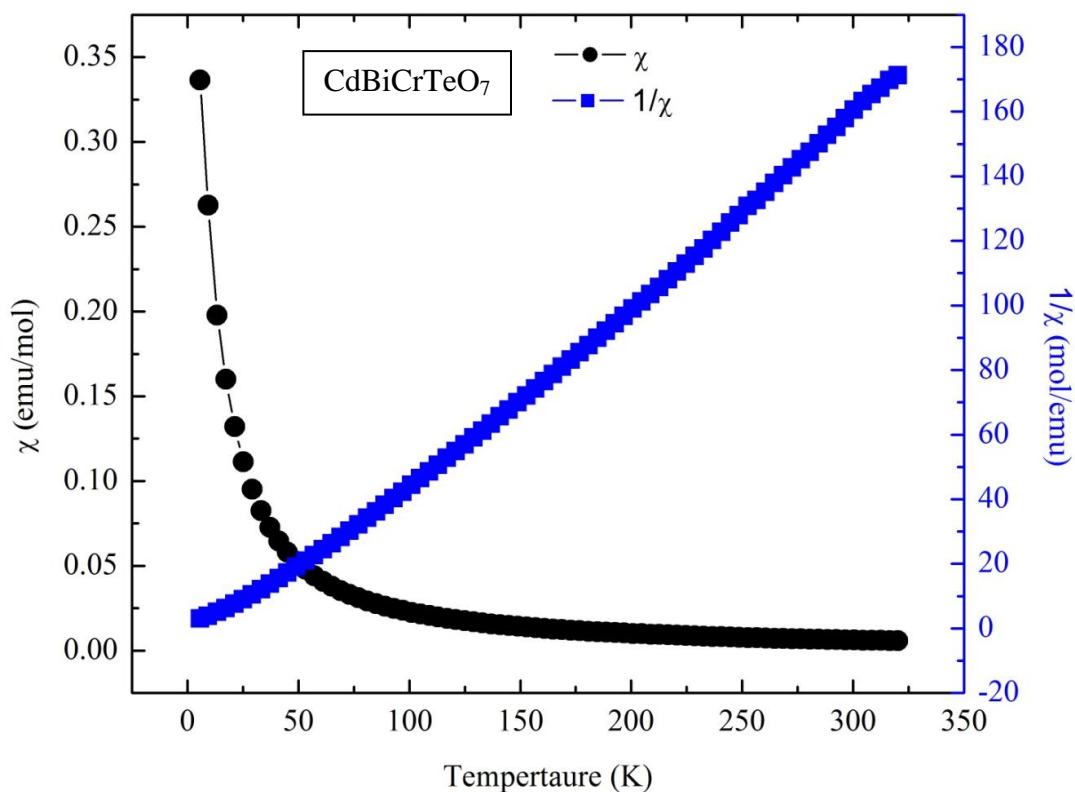


Figure 6.5: Temperature dependence of magnetic susceptibility and inverse magnetic susceptibility of  $\text{CdBiCrTeO}_7$

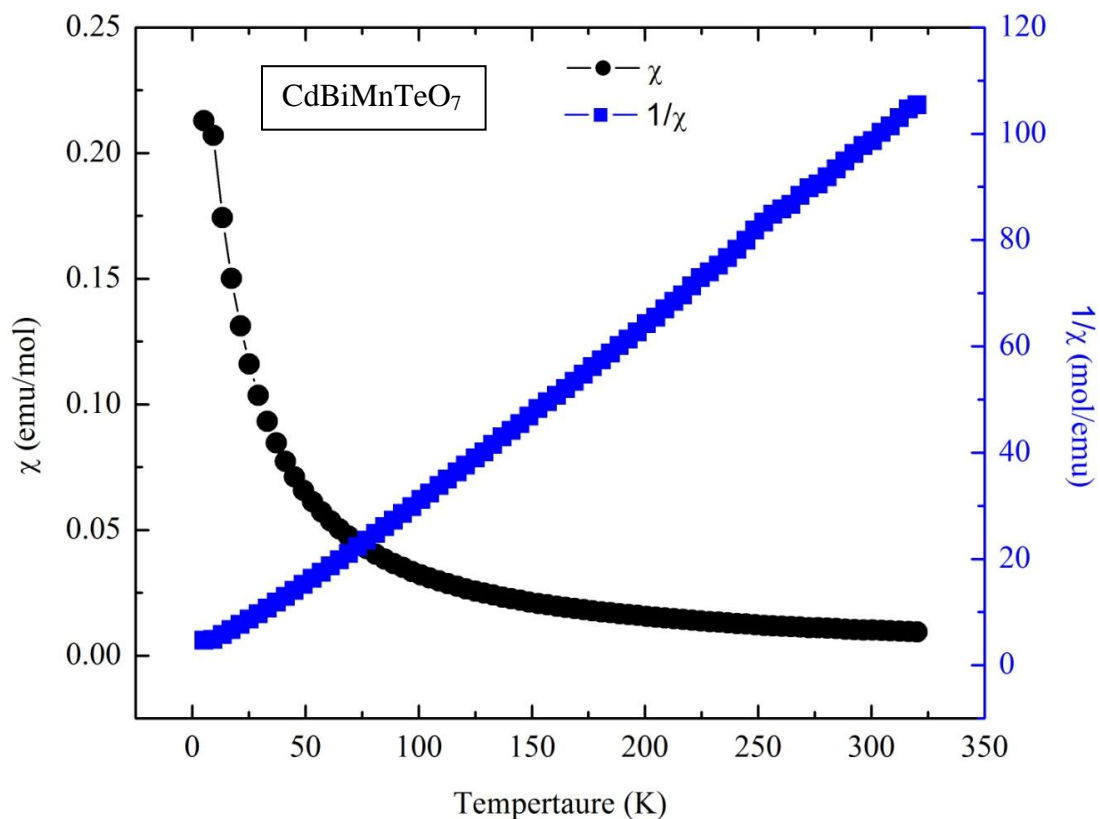


Figure 6.6: Temperature dependence of magnetic susceptibility and inverse magnetic susceptibility of CdBiMnTeO<sub>7</sub>

Temperature dependence of magnetic susceptibility of CdBiFeTeO<sub>7</sub> indicates antiferromagnetic behavior with Neel temperature of 12K (Fig. 6.7). At higher temperature, the compound show paramagnetic-like behavior where magnetic moments of Fe<sup>3+</sup> have no interaction to each other. At low temperature, 12K, long-range ordering of the spins is achieved resulting in antiferromagnetism. Although long-range interaction is suppressed at higher temperature, small deviation from linear line in paramagnetic region indicates short-range interaction. Geometric frustration

could be the main effect that suppresses long-range correlation, however it should be noted that  $\text{Fe}^{3+}$  only occupy half of the B sites which make it even more difficult to align.

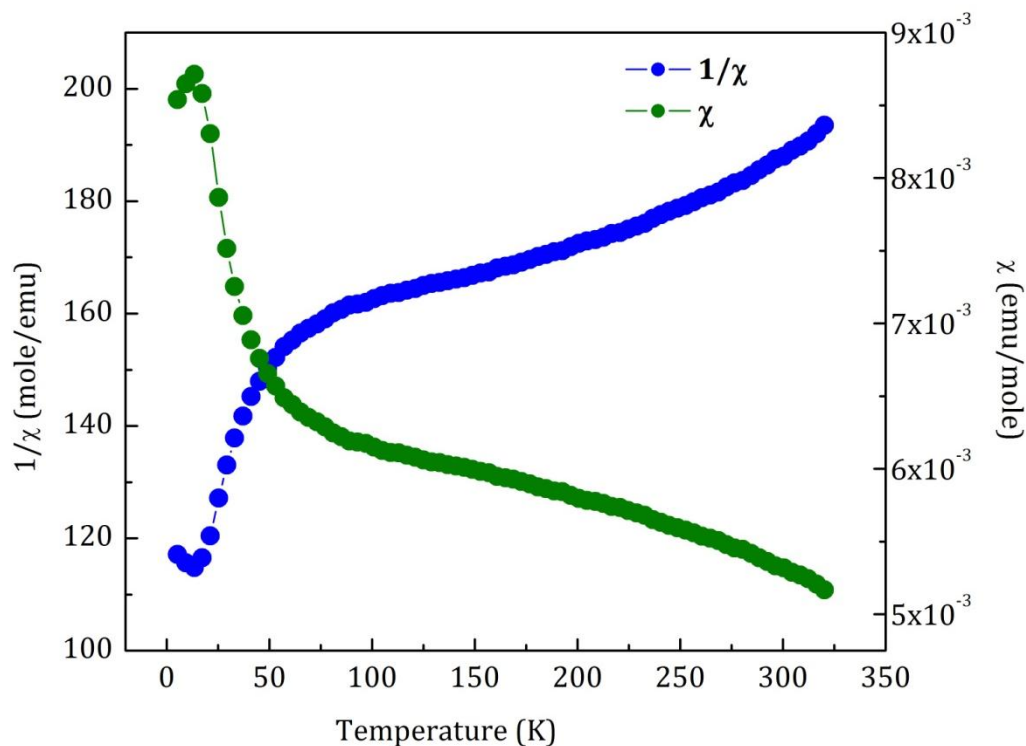


Figure 6.7: Temperature dependence of magnetic susceptibility and inverse magnetic susceptibility of  $\text{CdBiFeTeO}_7$ .

### 6.3.3 Dielectric properties

Dielectric measurements were performed on the sintered pellets of the samples with density of about 60-70%. Attempts to prepare more dense pellets were not successful due to the decomposition of the samples at relatively low temperature (750-800°C). Logarithmic mixing rule is used to correct for porosity. Table 6.1 shows the

corrected dielectric constants ( $10^6$  Hz) of the materials which were not very high. However, they were relatively independent of temperature and frequency as shown in Figure 6.8 and 6.9, respectively.

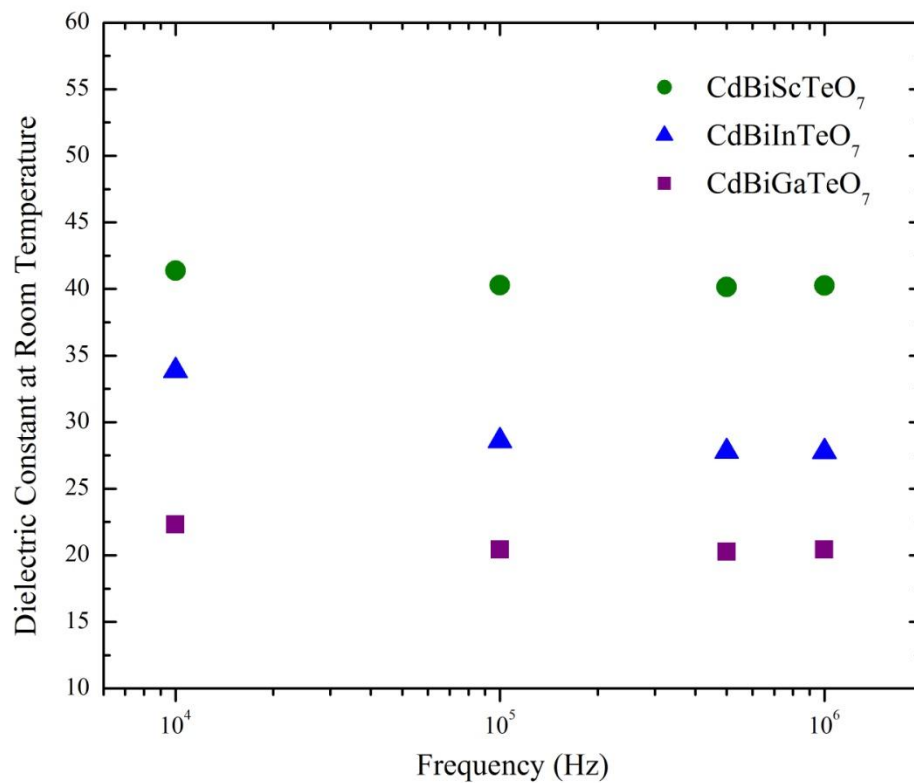


Figure 6.8: Temperature dependence of dielectric constants of some representative compounds.

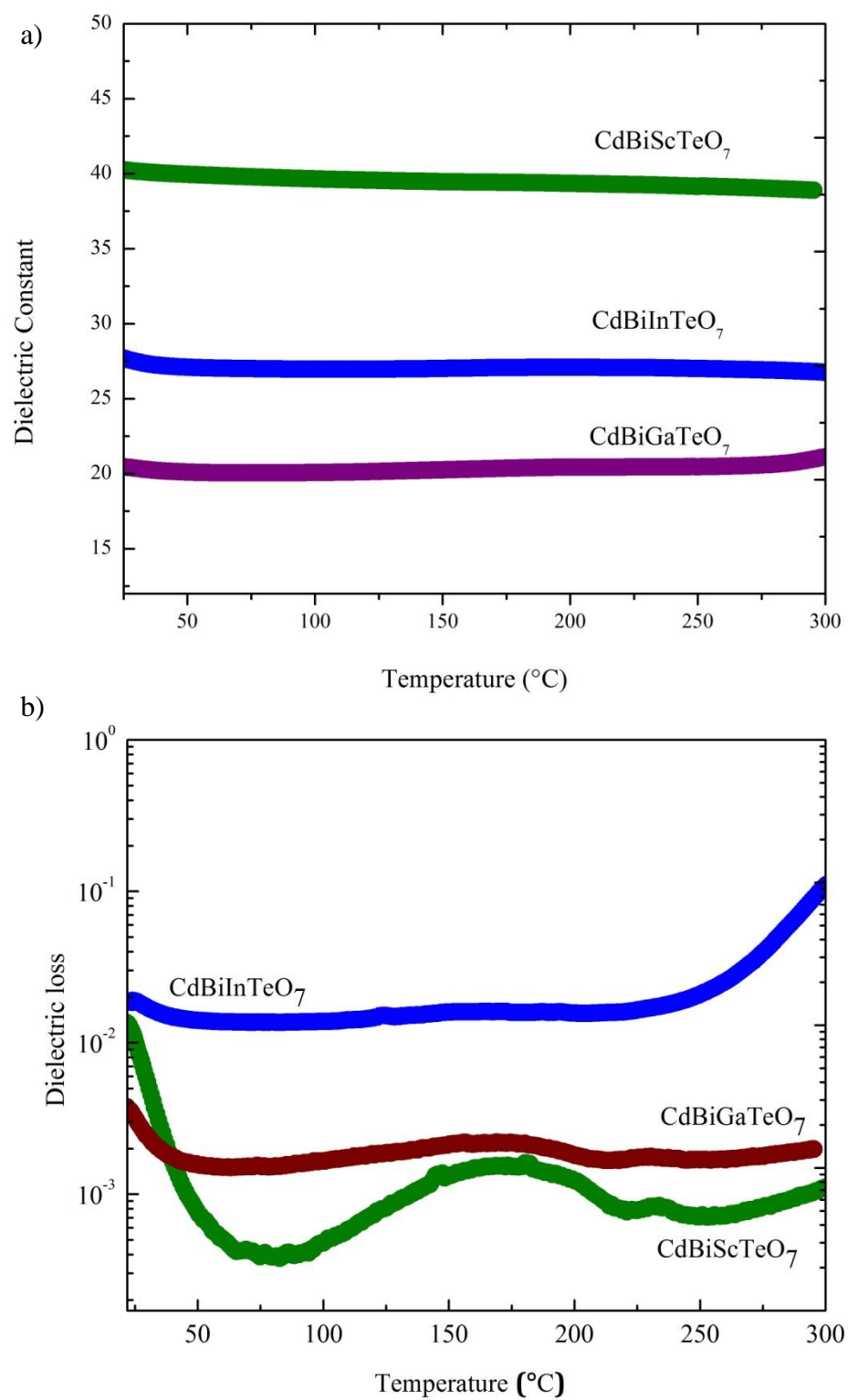


Figure 6.9: Temperature dependence of dielectric constant (a) and dielectric loss (b) of some representative compounds.

## 6.4 Conclusion

The first example of  $\text{Te}^{6+}$ -containing oxides with normal pyrochlore structure,  $\text{CdBi}(\text{MTe})\text{O}_7$ ,  $\text{M} = \text{Al, Cr, Ga, In, Fe, Mn, and Sc}$ , were successfully synthesized by solid state reaction.  $\text{M} = \text{Cr}$  and  $\text{Mn}$  phases were paramagnetic in temperature range 5-320K. Ferromagnetism ( $T_N = 12\text{K}$ ) with short-range correlation was found in  $\text{M} = \text{Fe}$  phase. Dielectric measurements show relatively low dielectric constants which were independent of temperature and frequency.

## 6.4 Experimental

Polycrystalline samples of  $(\text{CdBi})(\text{MTe})\text{O}_7$ ,  $\text{M} = \text{Al, Cr, Ga, In, Fe, Mn, and Sc}$ , were prepared by solid state reactions.  $\text{CdO}$  (Baker analyzed, 99.1%),  $\text{Bi}_2\text{O}_3$  (Aldrich, 99.99%), and oxides of  $\text{M}$  including  $\text{Al}_2\text{O}_3$  (Cerac, 99.99%),  $\text{Cr}_2\text{O}_3$  (Aldrich, 99%),  $\text{Ga}_2\text{O}_3$  (Aldrich, 99.99%),  $\text{In}_2\text{O}_3$  (Aldrich, 99.99%),  $\text{Sc}_2\text{O}_3$  (Standford Materials Corporation, 99.999%),  $\text{Mn}_2\text{O}_3$  (Johnson Matthey, 98%), and  $\text{Fe}_2\text{O}_3$  (Alfa, 99.99%) were used as reactants. Stoichiometric mixtures of reactants were ground, pressed into pellets and heated at  $600^\circ\text{C}$  for 12 hours,  $700^\circ\text{C}$  for 12 hours,  $800^\circ\text{C}$  for 12 hours, and  $850^\circ\text{C}$  for 12 hours in gold containers with intermediate grinding. Powder X-ray diffraction data were obtained by a Rigaku MiniFlex II diffractometer using  $\text{Cu K}\alpha$  radiation and a graphite monochromator. DC magnetization was measured by QD PPMS in temperature range 5-320K with 0.5T applied magnetic field. Dielectric properties measurements were taken on HP 4284 LCR meters at fixed frequencies of 1, 10, 100, 500, 1000 kHz in temperature range 25-300°C.

## 6.5 References

1. F. A. Weber, T. Schleid, *Z. Anorg. Allg. Chem.*, **626** (2000), 1285.
2. Ismunandar, I. Haryanto, S. Dewi, *Jurnal Matematika dan Sains*, **8** (2003), 27.
3. E. Aleshin, R. Roy, *J. Amer. Ceram. Soc.*, **45** (1962), 18.
4. I. Lidqvist, *Acta Chem. Scand.*, **14** (1960), 960.
5. K. Okada, H. Morikawa, F. Marumo, S. Iwai, *Acta Cryst.*, **B31** (1975), 1200.
6. S. A. Magarill, R. F. Klevtsova, *Sov. Phys. Crystallogr.*, **16** (1972), 645.
7. K. J. Range, W. Hegenbart, A. M. Heyns, F. Rau, K. Klement, *Z. Naturforsch.*, **B45** (1990), 107.
8. K. J. Range, U. Klement, F. Rau, U. Schiessl, A. M. Heyns, *Z. Kristallogr.*, **203** (1993), 318.
9. Z. A. Solodovnikova, S. F. Solodovnikov, *Acta Cryst.*, **C62** (2006), i53.
10. R. A. Macculey, F. A. Hummel, *J. Solid State Chem.*, **33** (1980), 99.
11. M. A. Subramanian, G. Aravamudan, G. V. Subba Rao, *Mat. Res. Bull.*, **14** (1979), 1457.
12. M. A. Subramanian, A. W. Sleight, *Mat. Res. Bull.*, **21** (1986), 727.
13. J. S. Gardner, M. J. P. Gingras, J. E. Greedan, *Rev. Mod. Phys.*, **82** (2010), 53.
14. P. K. Davies, H. Wu, A. Y. Borisevich, I. E. Molodetsky, L. Farber, *Annu. Rev. Mater. Res.*, **38** (2008), 369.
15. T. J. B. Holland, S. A. T. Redfern, *Mineralogical Magazine*, **61** (1997), 65.
16. R. D. Shannon, *Acta Crystallogr., Sect. A*, **32** (1976), 751.

## Chapter

### 7. Compositionally Controlled Metal-Insulator Transition in $\text{Tl}_{2-x}\text{In}_x\text{TeO}_6$

#### 7.1 Abstract

Metallic  $\text{Tl}_2\text{TeO}_6$  and insulating  $\text{In}_2\text{TeO}_6$  are both known to crystallize in the  $\text{Na}_2\text{SiF}_6$ -type structure. We have now prepared a complete  $\text{Tl}_{2-x}\text{In}_x\text{TeO}_6$  series in a search for a compositionally controlled metal-insulator transition that might be expected if a complete solid solution can be obtained. Unit cell edges and volume vary monotonically with no indication of miscibility gap. The metal-insulator transition occurs at an  $x$  value of about 1.4, which can be rationalized on a percolation model. No superconductivity could be detected down to 5K.

#### 7.2 Introduction

Superconductivity frequently appears at a metal-insulator boundary as one varies the composition. One of the classical examples is the discovery of superconductivity in  $\text{BaBi}_{1-x}\text{Pb}_x\text{O}_3$  perovskites where the dilution of an  $s^1$  by an  $s^0$  cation disrupts the Bi disproportionation resulting in metallic properties at an  $x$  value of about 0.25. Superconductivity with a  $T_c$  as high as 13 K occurs on the metallic side of this metal-insulator boundary [1]. This approach can be used as one of the ways to find new superconductors.



### 7.2.1 $M_2TeO_6$ structure

Ternary tellurium oxides with the general formula  $M_2TeO_6$  where M is a trivalent cation are reported to adopt various crystal structures depending on the ionic radius of M. Small M cations whose radii is in between  $0.5\text{\AA}$  and  $0.7\text{\AA}$  (e.g., Cr, Fe, Rh) tend to form the trirutile structure (space group  $P4_2/mnm$ ) [2]. The  $Na_2SiF_6$  structure (space group  $P321$ ) is formed when the radii of M cations is in the range  $0.75\text{\AA} < R_M < 0.87\text{\AA}$  [3]. For larger M cations ( $R_M > 0.87\text{\AA}$ ), the orthorhombic  $La_2TeO_6$ -type structure (space group  $P2_12_12_1$ ) is formed [4]. Figure 7.1 show all the three structures adopted by  $M_2TeO_6$ . Exceptions are  $Bi_2TeO_6$ ,  $Tl_2TeO_6$ , and  $Yb_2TeO_6$ .  $Bi_2TeO_6$  forms layer structure due to presence of a stereo active lone pair  $6s^2$  electrons on  $Bi^{3+}$  [5]. The ionic radius of  $Yb^{3+}$  ( $0.868\text{\AA}$ ) and  $Tl^{3+}$  ( $0.885\text{\AA}$ ) [6] are at the borderline, and it is reported that  $Yb_2TeO_6$  can form both  $Na_2SiF_6$  [7] and  $La_2TeO_6$  [8] structure while  $Tl_2TeO_6$  only forms  $Na_2SiF_6$  structure [9].

$Tl_2TeO_6$  and  $In_2TeO_6$  adopt the same  $NaSiF_6$ -type structure (Fig. 7.1(c)) where  $M^{3+}$  and  $Te^{6+}$  are coordinated by 6 oxygens forming octahedra. Octahedra of Te have no connection to each other but they share edges and corners with  $MO_6$  octahedra. On the other hand,  $MO_6$  directly connect to each other and form 3-dimensional network by sharing their corners.

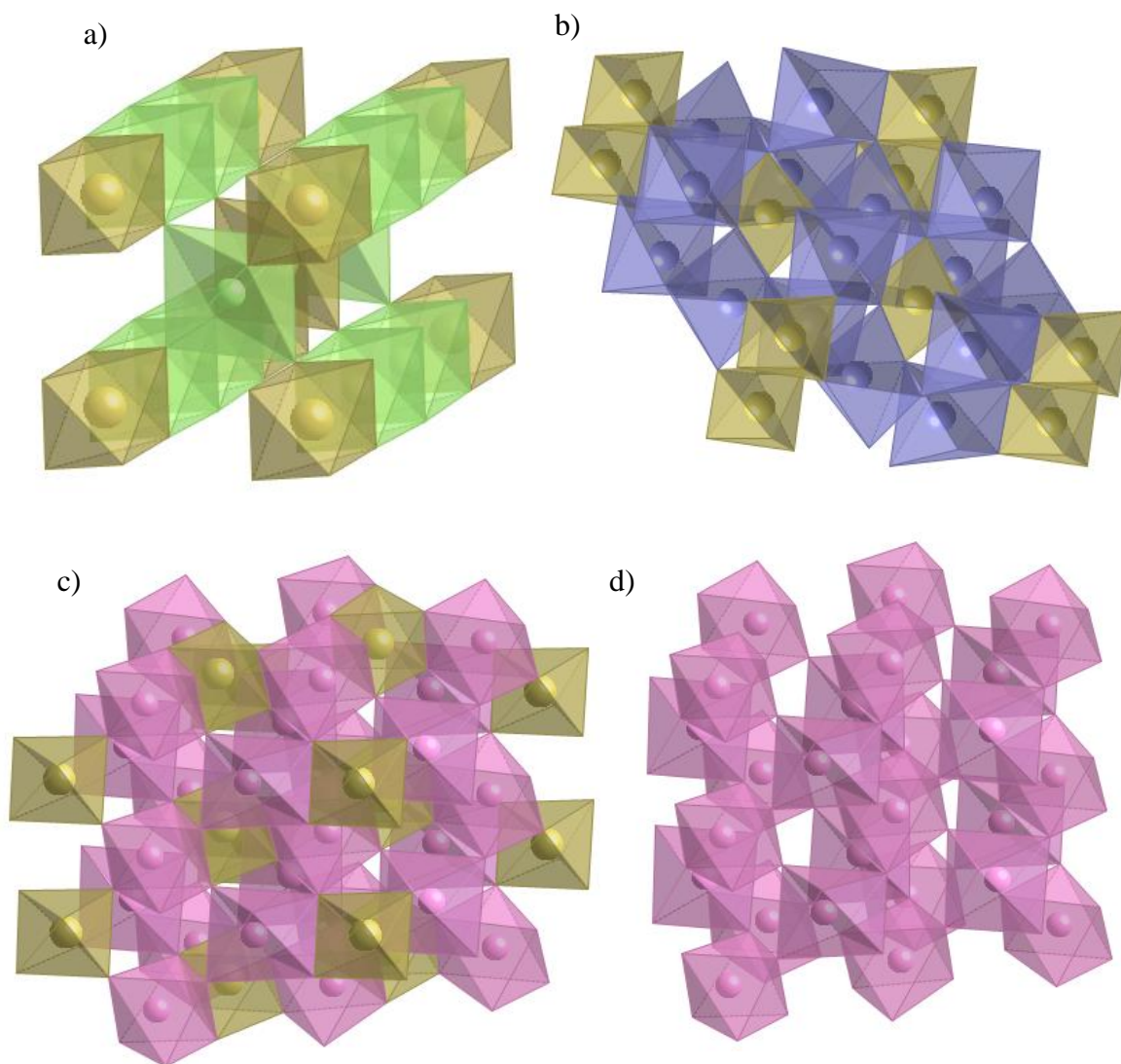


Figure 7.1:  $M_2TeO_6$  structure (olive octahedra represent  $Te^{6+}$  and the other colors represent  $M^{3+}$  octahedra)

- a) Trirutile structure is formed when  $0.5\text{\AA} < R_M < 0.7\text{\AA}$
- b) Orthorhombic  $La_2TeO_6$  structure formed when  $R_M > 0.87\text{\AA}$
- c) Structure of  $In_2TeO_6$  and  $Tl_2TeO_6$
- d) Corner shared octahedral network of  $M^{3+}O_6$

Electrical properties of these tellurates are not well studied. Shannon *et al.* [10] reported that  $In_2TeO_6$  single crystals grown under high pressures ( $\sim 58\text{Kbar}$ ) exhibited

degenerate semiconducting behavior with conductivity on the order of  $10^{-2} \Omega\text{cm}$ , but the preparation at ambient pressure resulted in an insulating compound. It was assumed in their work that the high pressure phase may be oxygen-deficient, but no evidence was given [10]. Insulating behavior for polycrystalline  $\text{In}_2\text{TeO}_6$  has been investigated by Shemirani and Koffyberg. The band gap of 1.56 eV was reported and n-type semiconductivity in Sn-doped  $\text{In}_2\text{TeO}_6$  was studied [11]. The crystal structure of the corresponding thallium analogue,  $\text{Tl}_2\text{TeO}_6$ , has been investigated [9] but there are no reports on its electrical properties.

### **7.2.2 Metal- Insulator transition in Oxides**

Based on electronic property, materials can be roughly divided into three categories; metal, semiconductor, and insulator. In some cases, the transitions from insulator to metal are observed as a result of various parameters. Typical transitions found in oxides are shown in Table 7.1 [12].

Compositionally controlled metal-insulator transitions occur through various mechanisms. Substitution of aliovalent ions to the materials can increase number of charge carriers which consequently increases electronic conductivity. When small amount of charge carriers is first introduced to materials, they create impurity orbitals. Impurity band is formed by the overlap of these impurity orbitals at high concentration of doping [24]. The impurity band does not immediately result in metallic state. However, when the width of this band is greater than the repulsion energy called Hubbard U, metallic state is reached [24]. Some examples are the metal-insulator transition in  $\text{LaNi}_{1-x}\text{M}_x\text{O}_3$  ( $\text{M}=\text{Cr}, \text{Mn}, \text{Fe}, \text{Co}$ ) solid solutions [25].

Table 7.1: Typical metal-insulator transitions in oxides [12]

| <b>Types of transitions</b>              | <b>Example</b>                                     | <b>References</b> |
|--|--|-------------------|
| Pressure-induced                         | NiO  | [13]              |
| Charge ordering                          | Fe <sub>3</sub> O <sub>4</sub>                     | [14]              |
| Spin configuration-induced               | LaCoO <sub>3</sub>                                 | [15-16]           |
| Spin polarization band splitting effects | EuO  | [17]              |
| Compositionally induced                  | La <sub>1-x</sub> Sr <sub>x</sub> CoO <sub>3</sub> | [18-19]           |
| Charge density wave                      | K <sub>0.3</sub> MoO <sub>3</sub>                  | [20]              |
| Temperature-induced                      | Ti <sub>2</sub> O <sub>3</sub> , VO <sub>2</sub>   | [21-23]           |

Aliovalent substitution is not always required for compositionally-controlled metal-insulator transition. Band-width controlling and band-filling can also induce such a transition in materials. Many studies especially in perovskite systems have been done to investigate these mechanisms [26]. Frand *et al.* studied metal-insulator transition in Sm<sub>1-x</sub>Nd<sub>x</sub>NiO<sub>3</sub> solid solutions where size of the rare earth controls the Ni-O-Ni angle and consequently controls the bandwidth [27]. For  $x < 0.45$ , Ni-O-Ni angle is small and the compounds are insulating because of the large gap. The bandwidth increases with  $x$  since Ni-O-Ni angle increases with Nd content. As the Nd content continues to increase, valence band and conduction band start to overlap which results in semimetal state with no band gap as shown in Figure 7.2.

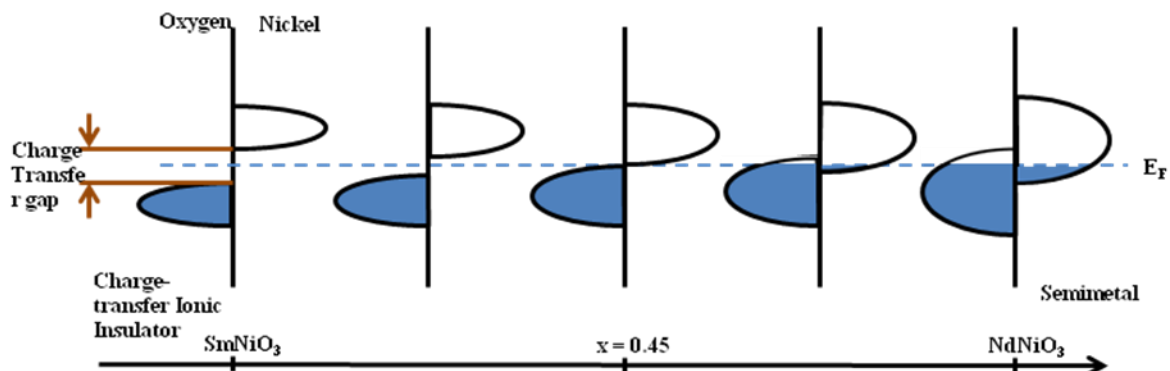


Figure 7.2: Schematic band diagram for  $\text{Sm}_{1-x}\text{Nd}_x\text{NiO}_3$  showing transition from insulator (a) to semimetal state (b) [after 27].

Another explanation for metal-insulator transition is based on a percolation model [28]. Consider a lattice consists of several sites some of which are occupied, some are not. When small number of sites is occupied, there is no connection between the sites or they might form some isolated small clusters as shown in Figure 7.3(a). However, if number of occupied sites reaches certain value, called percolation threshold, they will form a large cluster which extends through the lattice (Fig. 7.3(b) [29]. In comparison, bulk electronic conductivity of some composite materials containing a mixture of insulating and metallic phases transforms from insulating state to metallic state when a number of metallic composition reaches percolation threshold. At this point, they will form a single cluster for electrons to pass through from one side to the other.

Such a model is used to explain transition in  $\text{SrTi}_{1-x}\text{Ru}_x\text{O}_3$  where the energy separation of Ti  $3d$  and Ru  $4d$  band is too large to couple. The system is described as a composite of metallic  $\text{SrRuO}_3$  in insulating matrix of  $\text{SrTiO}_3$  [30].

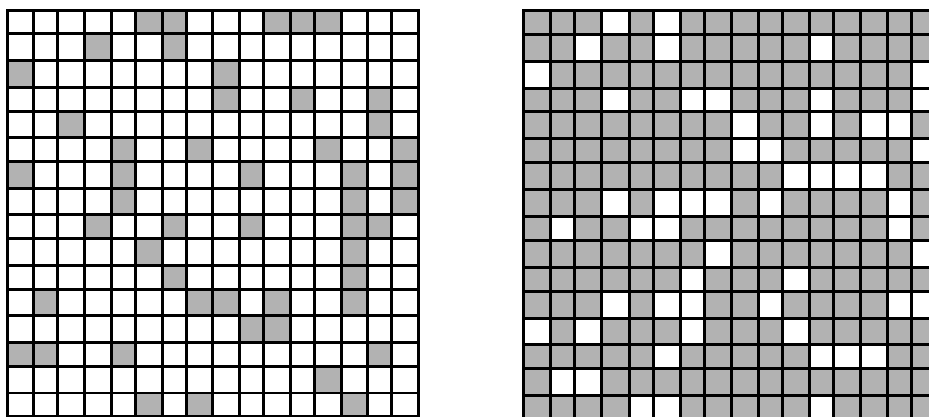


Figure 7.3: Percolation model when few sites are occupied (a) and when the cluster is formed through the lattice (b) [29].

In this work, we report on the synthesis, characterization and electrical properties of the complete  $\text{Tl}_{2-x}\text{In}_x\text{TeO}_6$  solid solutions where metal-insulator transition is observed and rationalized by percolation model.

### 7.3 Results

To obtain single phase solid solution compositions, thallium-rich samples were heated at a relatively lower temperature ( $550^\circ\text{C}$ ) to avoid melting and Tl volatilization whereas indium-rich samples were heated at a higher temperature ( $650^\circ\text{C}$ ) because a  $\text{In}_2\text{Te}_3\text{O}_9$  phase was formed when heating at lower temperatures [31].

Powder X-ray diffraction data showed that the complete solid solution between  $\text{In}_2\text{TeO}_6$  and  $\text{Tl}_2\text{TeO}_6$  could be obtained (Fig. 7.4). All of the powder X-ray diffraction patterns of the  $\text{Tl}_{2-x}\text{In}_x\text{TeO}_6$  series could be indexed assuming the  $\text{Na}_2\text{SiF}_6$  structure (space group:  $P321$ ) where each In/Tl and Te cation is coordinated by six oxygen anions forming distorted octahedra (Fig. 7.1(b)). The  $(\text{In/Tl})_2\text{O}_6$  octahedra share corners with each other, and they shares edges with the  $\text{TeO}_6$  octahedra. Although the  $(\text{In/Tl})_2\text{O}_6$  octahedra are connected in three dimensions, there is no direct connectivity between tellurium octahedra. Powder X-ray diffraction patterns of intermediate compositions show some peak broadening due to lattice strain caused by the large size difference of the two M cations (Fig. 7.4). Unit cell parameters were refined by the least squares method using the UnitCell program [32]. Cell parameters of  $\text{Tl}_2\text{TeO}_6$  and  $\text{In}_2\text{TeO}_6$  agree well with the reported values [9,11]. Figure 7.5 shows plots of the refined unit cell parameters and cell volumes versus x in  $\text{Tl}_{2-x}\text{In}_x\text{TeO}_6$ . Cell parameters and cell volumes decreased when In content is increased as the ionic radii of  $\text{In}^{3+}$  (0.800Å, 6-fold) is smaller than that of  $\text{Tl}^{3+}$  (0.885Å, 6-fold) [6]. Colors of the samples continuously change from dark brown for  $\text{Tl}_2\text{TeO}_6$  to pale yellow for  $\text{In}_2\text{TeO}_6$ .

Figure 7.6 shows plots of room temperature resistivity and Seebeck coefficients. Samples with x = 1.8 and 2 were too insulating for a determination of resistivity or Seebeck coefficient. In general, resistivity increases with In content which is consistent with the variation in Seebeck coefficients. All measured Seebeck coefficients are negative indicating that the majority of carriers are electrons rather than holes. To exclude the effect of porosity, normalized resistivity  $\rho/\rho_{300\text{K}}$  is plotted

versus temperature in Figure 7.7. Resistivity and AC magnetic susceptibility measurements of highly conducting compositions ( $x < 1.5$ ) show no superconductivity down to 5K.

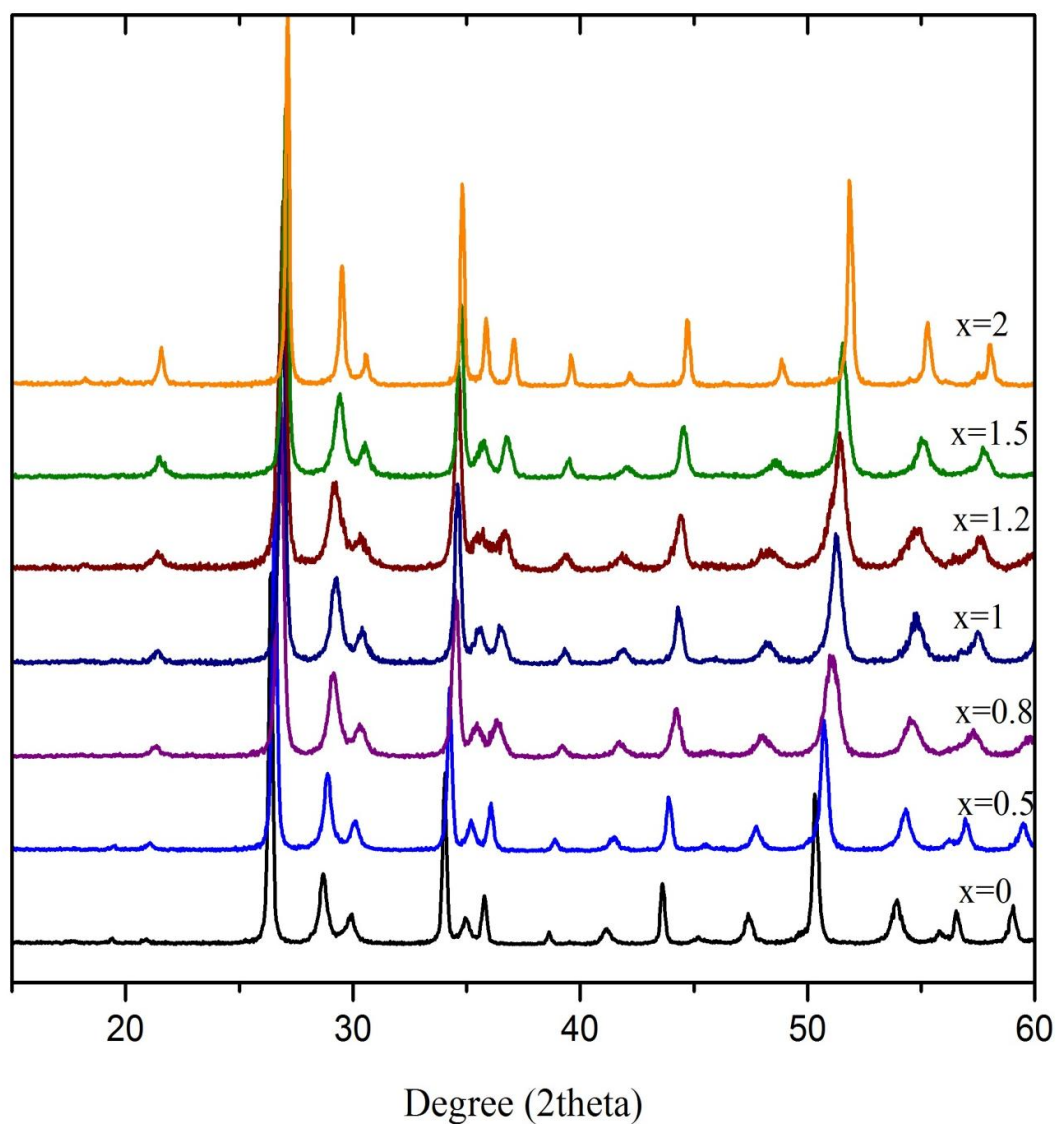


Figure 7.4: Powder X-ray diffraction of  $\text{Tl}_{2-x}\text{In}_x\text{TeO}_6$  solid solutions.



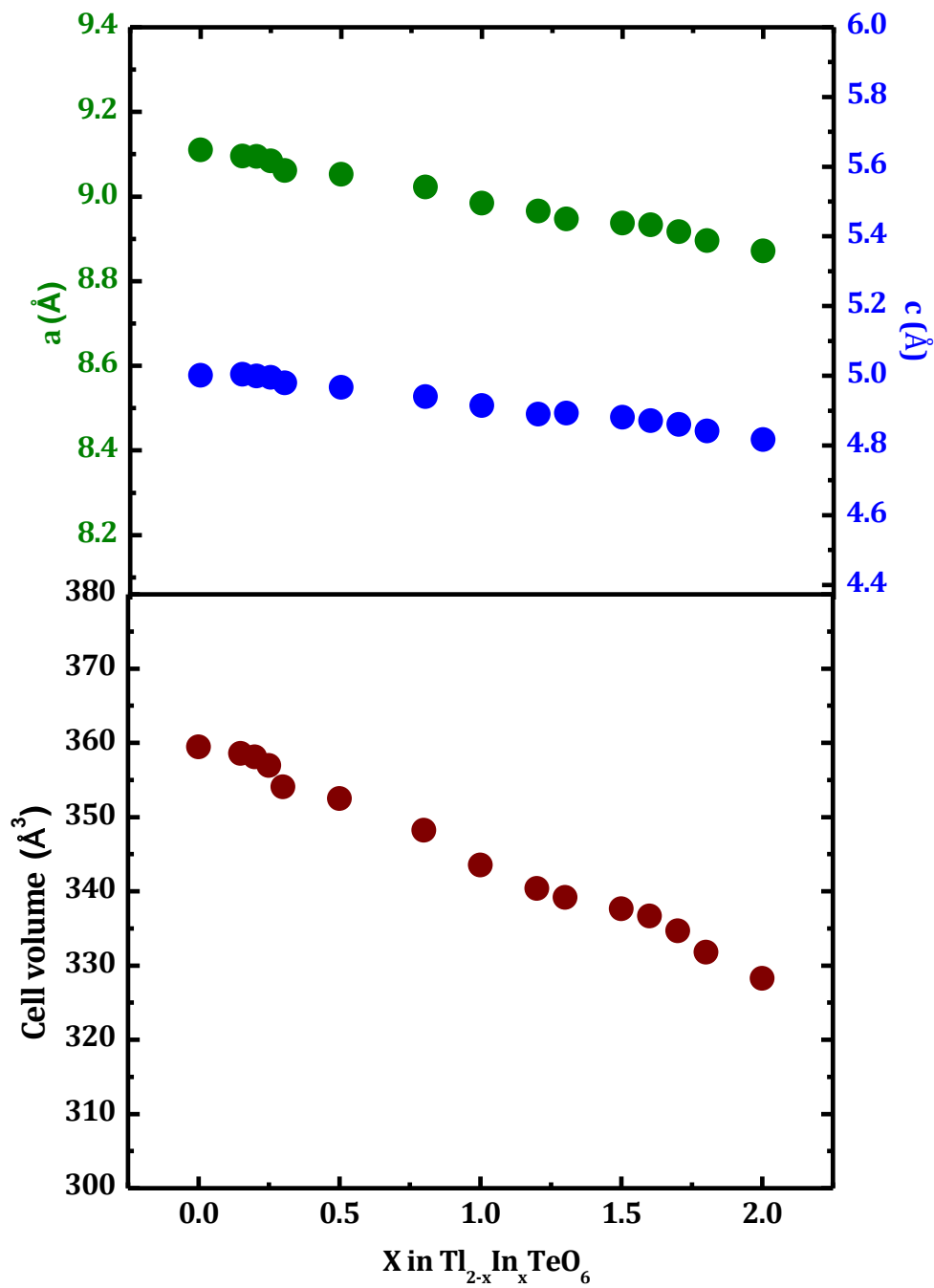


Figure 7.5: Lattice parameters (upper) and unit cell volumes (lower) of  $\text{Tl}_{2-x}\text{In}_x\text{Te}_2\text{O}_6$  solid solution

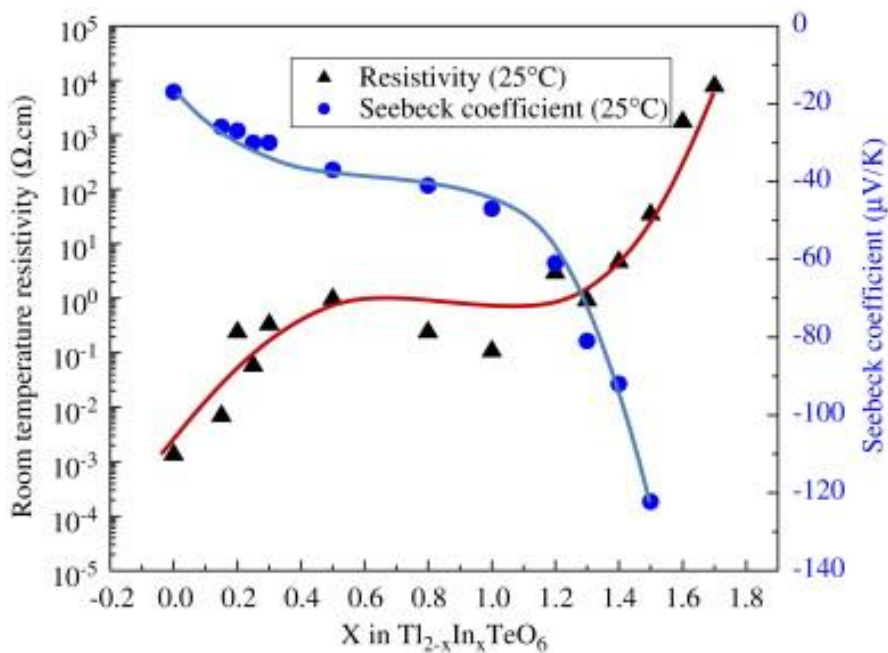


Figure 7.6: Room temperature resistivities and Seebeck coefficients of  $\text{Tl}_{2-x}\text{In}_x\text{TeO}_6$

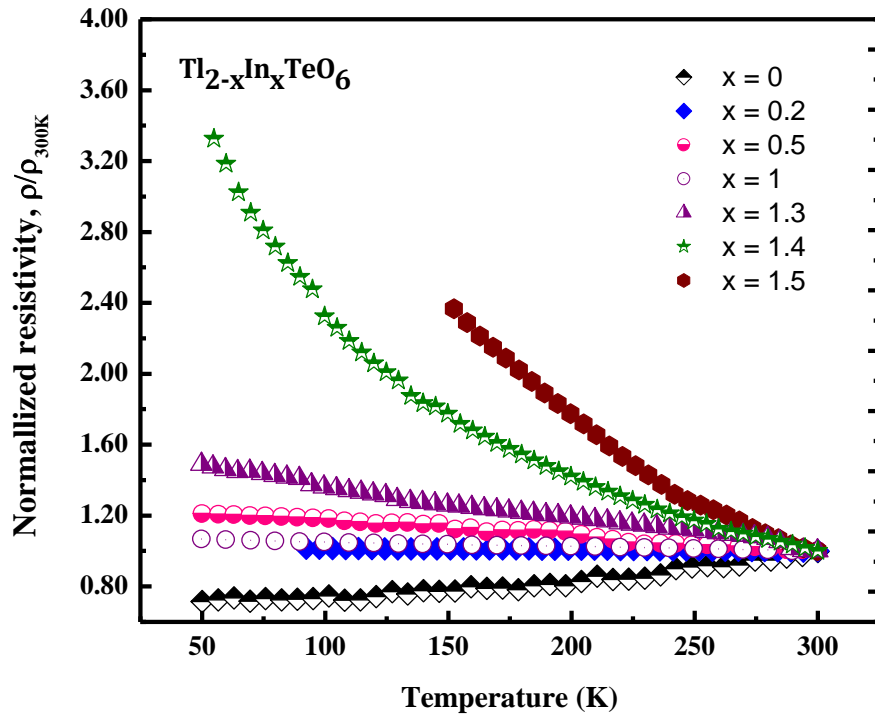


Figure 7.7: Normalized resistivities,  $\rho/\rho_{300\text{K}}$  of some representative compositions

## 7.4 Discussion

The electronic properties of  $\text{In}_2\text{O}_3$  are well understood. This oxide is intrinsically an insulator with a direct band gap of 3.75 eV and a smaller indirect gap of 2.6 eV [33-34]. As with CdO, the indirect gap appears to arise from strong mixing between shallow core  $d$  states and O  $2p$  states [35-36].  $\text{In}_2\text{O}_3$  is easily doped  $n$ -type either by oxygen deficiency [33] or by substitution of Sn on In sites [37] to give a highly degenerate transparent conducting oxide. For the simple binary oxides with the cation in the group oxidation state, a very pronounced decrease in band gap occurs on dropping from the In row to the Tl row.  $\text{In}_2\text{O}_3$  and  $\text{SnO}_2$  are transparent insulators, but both  $\text{Tl}_2\text{O}_3$  and  $\text{PbO}_2$  are black and show metallic properties. Single crystals of  $\text{Tl}_2\text{O}_3$  were reported to have a resistivity of  $9 \times 10^{-5} \Omega\text{cm}$  at room temperature dropping to  $5 \times 10^{-5} \Omega\text{cm}$  at 4 K [38]. The magnitude of the resistivity is typical of a metal, but such a weak temperature dependence of resistivity is not expected for a normal metal. It would appear that the band gap in  $\text{Tl}_2\text{O}_3$  has decreased to zero, that the valence band (O  $2p$ ) and conduction band (Tl  $6s$ ) have become overlapped, and that  $\text{Tl}_2\text{O}_3$  is actually a semimetal. Electronic structure calculations and photoemission studies of  $\text{Tl}_2\text{O}_3$  confirm this description [39]. In the case of  $\text{Tl}_2\text{TeO}_6$  it appears that the O  $2p$  valence band and the Tl  $6s$  conduction band touch as in the case of  $\text{Tl}_2\text{O}_3$ . The resistivity of  $\text{Tl}_2\text{TeO}_6$  decreases from  $1.88 \times 10^{-3} \Omega\text{cm}$  at room temperature to  $1.34 \times 10^{-3} \Omega\text{cm}$  at 50K, again a weak temperature dependence indicates a semimetal rather than a normal metal. The situation for oxides of  $\text{Pb}^{4+}$  is very similar. Both  $\text{PbO}_2$  and perovskite  $\text{BaPbO}_3$  are black and metallic. Band structure calculations

indicate that both compounds are semimetals due to an overlap of the O 2*p* valence band and the Pb 6*s* conduction band [40-41]. However in the case of Ba<sub>2</sub>PbO<sub>4</sub>, the additional Ba has sufficiently stabilized the O 2*p* states such that a small band gap emerges [41]. Stoichiometry may be an issue for PbO<sub>2</sub> and BaPbO<sub>3</sub>, and it has been very recently suggested that stoichiometric PbO<sub>2</sub> would be a semiconductor with a band gap of 0.7eV [42]. There apparently is no chemical evidence, such as titration, for such a partial reduction of Pb<sup>4+</sup>.

A complete solid solution between isostructural oxides is not necessarily expected when one end member is metallic and the other end member is insulating. For example, isostructural metallic RuO<sub>2</sub> and insulating TiO<sub>2</sub> form only a very limited solid solution under equilibrium conditions [43] despite the fact that the radii of Ru<sup>4+</sup> and Ti<sup>4+</sup> are nearly the same, 0.62 and 0.605 Å, respectively [6]. However, complete solubility between metallic and insulating compounds is common for ternary oxides. For example, insulating R<sub>2</sub>Ru<sub>2</sub>O<sub>7</sub> compounds (R = rare earth cation) with the pyrochlore structure form complete solid solutions with metallic A<sub>2</sub>Ru<sub>2</sub>O<sub>7-x</sub> pyrochlores where A is Pb or Bi [44-45]. Complete solid solutions are also observed between insulating and metallic compounds with the perovskite structure. Examples include SrTiO<sub>3</sub> - SrRuO<sub>3</sub>, ACu<sub>3</sub>(Ti<sub>1-x</sub>Ru<sub>x</sub>)<sub>4</sub>O<sub>12</sub> (A = Na, Ca, or La), and R<sub>1-x</sub>A<sub>x</sub>MnO<sub>3</sub> phases where R is a rare earth cation and A is Ca or Sr [46-47]. One might attempt to rationalize the change from an insulator to a metal as a monotonically decreasing band gap until the gap reaches zero for the metallic state. However, a more realistic model to describe some compositionally controlled metal-insulator transitions comes from

percolation phenomenon since energy levels of Tl 6s and In 5s orbitals are most likely too large to overlap and form a single band. A percolation model has been used extensively to describe compositionally controlled metal-insulator transitions in composites. Such composites are typically composed of metal particles dispersed in a polymer matrix. When the loading of metallic particles reaches a certain concentration, the bulk properties change from insulating to metallic. The loading necessary for the transition is described by percolation theory [48]. The volume fraction of conducting phase required for high conductivity can be very accurately calculated for ideal systems. For example, assuming the conducting phase to be spheres gives a value of 28.9% as the amount of conducting phase required for complete connectivity and high conductivity [48]. In the real systems this critical volume percent can be somewhat higher or lower. The compositionally controlled metal-insulator transitions in  $A_xWO_3$  tungsten bronzes can be described using percolation theory. The value of x can be varied over a large range, and it is generally observed that this value must be greater than 0.25 for metallic properties [49]. At lower values of x we can assume that the 5d electrons of W produced by the intercalation of the A cations are delocalized over some W atoms, but these electrons remain in the vicinity of the A cations. Thus, the bulk does not exhibit metallic properties. As the concentration of A cations increases, these clusters of delocalized electrons make contact with one another and a change in bulk properties from insulating to metallic occurs. Such a model has been used to explain the

compositionally controlled metal-insulator transitions in  $\text{SrTiO}_3$  -  $\text{SrRuO}_3$  and  $\text{R}_{1-x}\text{A}_x\text{MnO}_3$  perovskites [46,48].

In the  $\text{Tl}_{2-x}\text{In}_x\text{TeO}_6$  solid solutions we could assume that metallic conductivity will occur only through Tl–O–Tl linkages. According to the percolation theory we can expect that continuous Tl–O–Tl linkages will begin to appear at about 30% Tl ( $x=1.4$ ). The exact value depends on assumptions made, such as the nature of likely short range ordering or clustering of In and Tl. In any case, for such a heterogeneous system, an abrupt metal-insulator transition is not expected at a precise composition. From a percolation model we expect that resistivity will show a dramatic increase as  $x$  increases above about 1.4, and this is observed (Fig. 7.6). The absolute values of the Seebeck coefficient also show a rapid increase as resistivity increases. Unlike resistivity, the Seebeck coefficient is relatively immune to the impact of grain boundaries. We have a very good fit to a smooth function of the Seebeck coefficient, but there is considerable scatter of the resistivity values. This strongly suggests that grain boundary effects, as well as pellet porosity, have a significant impact on the resistivity values. This grain boundary contribution is then likely the reason for the very small negative slopes of resistivity vs. temperature for samples with  $x=1.3$  and 1.0 (Fig. 7.7).

## 7.5 Conclusion

Complete solid solutions of  $\text{Tl}_{2-x}\text{In}_x\text{TeO}_6$  have been made where unit cell edges and volume vary monotonically with no indication of miscibility gap. Compositionally controlled metal-insulator transition is observed at  $x=1.4$ . Percolation model is used to

explain the transition where materials behave like composites which contain metallic  $Tl_2TeO_6$  phase distribute in the insulating  $In_2TeO_6$  phase. No superconductivity could be detected down to 5K.

## 7.6 Experimental

Polycrystalline samples of  $Tl_{2-x}In_xTeO_6$  with  $x=0$  to 2 were prepared by solid state reactions. Stoichiometric mixtures of  $In_2O_3$  (Aldrich, 99.99%),  $Tl_2O_3$  (Johnson Matthey, 99.999%), and  $TeO_2$  (Acros organics, 99%) or  $H_6TeO_6$  (Analar, 99.5%) were ground, pressed into pellets and heated at 550-650°C in covered gold containers for 24 h with an intermediate grinding. Powder X-ray diffraction data were obtained by a Rigaku MiniFlex II diffractometer using Cu  $K\alpha$  radiation and a graphite monochromator. DC electrical resistivities were measured on the pellets by conventional four-probe method in the temperature range 50-300K using a Quantum Design PPMS. Seebeck coefficients were determined by static method at room temperature. Highly conducting samples were tested for superconductivity using down to 5 K.

## 7.7 References

1. A.W. Sleight, J.L. Gilson, P.E. Bierstedt. *Solid State Commun.*, **17** (1975), 27.
2. G. Bayer, *Fortschr. Miner.* **46** (1969), 41.
3. J. A. Malone, J. F. Dorrian, O. Muller, R. E. Newnham, *J. Am. Ceram. Soc.*, **52** (1969), 570.
4. F.W. Hützler, H.-G. Burckhardt and M. Trömel., *Z. Kristallogr.*, **172** (1984), 116.
5. B. Frit, M. Jaymes, *Bull. Soc. Chim. Fr.*, **1974** (1974), 402.
6. R. D. Shannon, *Acta Crystallogr., Sect. A*, **32** (1976), 751.
7. S. Nathanson, *J. Inorg. Nucl. Chem.*, **30** (1968), 741.

8. M. Troemel, F.W. Huetzler, H.G. Burckhardt, C. Platte, E. Muench, *Z. Anorg. Allg. Chem.*, **551** (1987), 95.
9. F. Bernard, P. Rose, M. Daniele, *Mat. Res. Bull.*, **10** (1975), 1305.
10. R. D. Shannon, J. L. Gillson, R. J. Bouchard, *J. Phys. Chem. Solids.*, **38** (1977), 877.
11. B. Shemirani, F. P. Koffyberg, *Mat. Res. Bull.*, **27** (1992), 693.
12. P. P. Edwards, T. V. Ramakrishnan, C. N. R. Rao, *J. Phys. Chem.*, **99** (1995), 5228.
13. X. B. Feng, N. M. Harrison, *Phys Rev. B*, **69** (2004), 35114.
14. E. J. W. Verwey, *Nature*, **144** (1939), 327.
15. M. Imada, A. Fujimori and Y. Tokura. *Rev. Mod. Phys.*, **70** (1998), 1039.
16. C. N. R. Rao, M. Motin Seikh, C. Narayana, *Top. Curr. Chem.*, **234** (2004), 786.
17. M. Oliver, J. O. Dimmock, A. L. Mcwhorter, T. B. Reed, *Phys. Rev. B*, **5** (1972), 1078.
18. A. Mineshige, M. Kobune, S. Fujii, Z. Ogumi, M. Inaba, T. Yao, K. Kikuchi, *J. Solid State Chem.*, **142** (1999), 374.
19. A. Mineshige, M. Inaba, T. Yao, Z. Ogumi, K. Kikuchi, M. Kawase, *J. Solid State Chem.*, **121** (1996), 423.
20. J. P. Pouget, C. Noguera, A. H. Moudden, R. Moret, *J. Physique*, **46** (1985), 1731.
21. J. B. Goodenough, *J. Solid State Chem.*, **3** (1971), 490.
22. M. Marezio, D. B. McWhan, J. P. Remeika, P. D. Dernier, *Phys. Rev. B*, **5** (1972), 2541.
23. J. M. Honig, L. L. van Zandt, *Annu. Rev. Mater. Sci.*, **5** (1975), 225.
24. P. A. Cox, *'The electronic Structure and Chemistry of Solids'*, Oxford University Press, (1987).
25. P. Ganguly, N. Y. Vasanthacharya, C. N. R. Rao, *J. Solid State Chem.*, **54** (1984), 400.
26. J. B. Goodenough, S. L. Cooper, *Struct. Bond.*, 'Localized to itinerant electronic transition in perovskite oxides', Springer, (1965).
27. G. Frand, O. Bohnke, P. Lacorre, J. L. Fourquet, A. Carre, B. Eid, J. G. Theobald, A. Gire, *J. Solid State Chem.*, **120** (1995), 157.
28. H. Gould, J. Tobochnik, W. Christian, 'Handout for Physics 125/225: Chapter 13 percolation', 2001, 443.
29. M. Abbate, J. A. Guevara, S. L. Cuffini, Y. P. Mascarenhas, E. Morikawa, *Eur. Phys. J. B*, **25** (2002), 203.
30. M. J. Redman, W. P. Binnie, W. J. Mallio, *J. Less Common Metals.*, **23** (1971), 313.
31. T. J. B. Holland, S. A. T. Redfern, *Mineralogical Magazine*, **61** (1997), 65.
32. I. Hamberg, C. G. Granqvist, K. F. Berggren, B. E. Sernelius, and L. Engstrom, *Phys. Rev. B*, **30**, (1984), 3240.
33. R. L. Weiher and R. P. Ley, *J. Appl. Phys.*, **37**, (1966), 299.
34. J. E. Jaffe, R. Pandey, and A. B. Kunz, *Phys. Rev. B*, **43** (1991), 4030.



35. Y. Dou, R. G. Egdell, D. S. L. Law, N. M. Harrison, and B. G. Searle, *J. Phys.: Cond. Matter.*, **10** (1988), 8447.
36. P. A. Cox, W. R. Flavell, and R. G. Egdell, *J. Solid State Chem.*, **68** (1987) 340.
37. A. W. Sleight, J. L. Gillson, B. L. Chamberland, *Mater. Res. Bull.*, **5** (1970), 807.
38. P. Glans, T. Learmonth, K. E. Smith, J. Guo, A. Walsh, G. W. Watson, F. Terzi and R. G. Egdell, *Phys. Rev. B*, **71** (2005), 235109.
39. M. Heinemann, H. J. Terpstram, C. Haas, and R. A. deGroot, *Phys. Rev. B*, **52** (1995), 11740.
40. V. R. R. Medicherla, T. Shripathi, N. P. Lalla, *J. Condens. Matter*, **20** (2008), 035219.
41. D.J. Payne, R.G. Egdell, D.S.L. Law, P-A. Glans, T. Learmonth, K.E. Smith, J. Guo, A. Walsh, G.W. Watson, *J. Mater. Chem.*, **17** (2007), 267.
42. K.T. Jacob and R. Subramanian, *J Phase Equil. Diff.*, **29** (2008), 136.
43. Y. Yamamoto, R. Kanno, Y. Takeda, O. Yamamoto, Y. Kawamoto, M. Takano, *J. Solid State Chem.*, **109** (1994), 372.
44. H. Kobayash R. Kanno, Y. Kawamoto, T. Kamiyama, R Izumi and A.W. Sleight, *J. Solid State Chem.*, **114** (1995), 15.
45. A.P. Ramirez, G. Lawes, D. Li, M.A. Subramanian, *Solid State Commun.* , **131** (2004), 251.
46. L. Gor'kov, V. Kresin, *J. Super.*, **13** (2000), 239.
47. D. R. Baker, G. Paul, S. Sreenivasan, H. E. Stanley, *Phys Rev.*, **E66** (2002), 046136.
48. H.R. Shanks, P.H. Sidles, G.C. Danielson, *Adv. Chem. Ser.*, **39** (1963), 237.

## Chapter

### 8. Thermoelectric Properties of $\text{Rh}_2\text{MO}_6$ , $\text{M}=\text{Mo}$ , $\text{Te}$ , and $\text{W}$

#### 8.1 Abstract

$\text{Rh}_2\text{MO}_6$ ,  $\text{M} = \text{Mo}$ ,  $\text{W}$ , and  $\text{Te}$  were synthesized by solid state reaction. Electronic properties as well as thermoelectric properties were investigated and discussed. The compounds crystallized in rutile-related structure and all show relatively high electronic conductivities with  $\text{Rh}_2\text{TeO}_6$  showed highest electronic conductivity ( $\sim 500$  S/cm at room temperature) despite of localized electron in  $\text{Rh}^{3+}$  and  $\text{Te}^{6+}$ . Measurable magnetic moments also indicate valence degeneracy between  $\text{Rh}$  and the  $\text{M}$  cation. The measured Seebeck coefficients are relatively low and positive indicating hole-type conduction.

#### 8.2 Introduction

Transition metal oxides containing cobalt have increasingly gained attention in thermoelectrics field since  $\text{NaCo}_2\text{O}_4$  was reported to show good thermoelectric properties with  $ZT$  as high as 0.7-0.8 at 1000K [1]. Interesting thermoelectric properties were later found in other cobalt oxides such as  $\text{Ca}_3\text{Co}_4\text{O}_9$  [2] and  $\text{Bi}_2\text{Sr}_3\text{Co}_2\text{O}_y$  [1] as well. It was proposed that large entropy of low-spin-state of  $\text{Co}^{4+}$  in the background of low-spin  $\text{Co}^{3+}$  enhances thermoelectric power and electrical conductivity in such compounds [3]. Since  $\text{Rh}^{3+}/\text{Rh}^{4+}$  are isoelectronic to  $\text{Co}^{3+}/\text{Co}^{4+}$ , mixed valence  $\text{Rh}$  compounds have potential to show similar properties. As a result,

many rhodium oxides have been investigated as potential candidates for thermoelectric applications [3-4].

The  $\text{Rh}_2\text{MO}_6$  compounds with  $M = \text{Mo}, \text{W},$  and  $\text{Te}$  have been reported with either the rutile or the trirutile structure [5-8]. As shown in Figure 8.1, Rh and M cations are disordered in rutile but ordered in trirutile phase. As a result, the  $a$  unit cell parameter remains constant, while the  $c$  unit cell parameter becomes three times larger when the trirutile structure is adopted.

$\text{Rh}_2\text{WO}_6$  can adopt two different structures; rutile and trirutile. Rutile  $\text{Rh}_2\text{WO}_6$ ,  $P4_2/mnm$ , was first reported by Badaud and Omary with Rh and W disordering in the structure [5]. The compound showed relatively high conductivity of about 22 S/cm. Magnetic and electronic properties of rutile  $\text{Rh}_2\text{WO}_6$  could be explained by the overlap of Rh  $4d$  and W  $5d$  orbitals [6]. Synthesis and characterization of trirutile  $\text{Rh}_2\text{WO}_6$  were investigated by V. B. Lazarev *et al.* where the compound was much less conducting ( $10^{-4}$  S/cm) due to the ordering of Rh and W [7-8]. Similarly,  $\text{Rh}_2\text{MoO}_6$  were reported with two different structures. Rutile  $\text{Rh}_2\text{MoO}_6$  showed electrical conductivity of  $3.33 \times 10^{-2}$  S/cm while the trirutile phase is much less conducting ( $10^{-4}$  S/cm) [9-10]. To best of our knowledge,  $\text{Rh}_2\text{TeO}_6$  was only reported with trirutile structure and has a low electrical conductivity ( $\sim 10^{-4}$  S/cm) [7,11]. Apparently, the Seebeck coefficients and thermal conductivity of these  $\text{Rh}_2\text{MO}_6$  phases has not previously been studied.

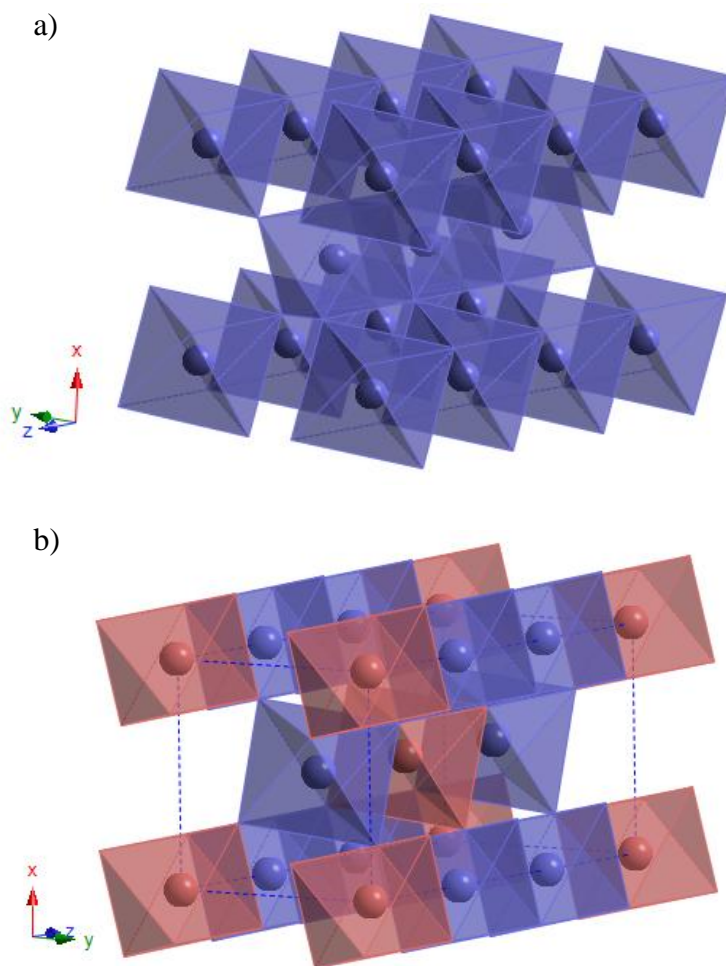


Figure 8.1: Rutile (a) and trirutile (b) structure. Different colors represent different types of cations.

### 8.3 Results

Table 8.1 shows the final temperature of solid state synthesis where single phase of  $\text{Rh}_2\text{MO}_6$ ,  $M = \text{W}, \text{Mo}, \text{and Te}$  were achieved. To obtain single phase of  $\text{Rh}_2\text{MoO}_6$ ,  $\text{RhCl}_3 \cdot x\text{H}_2\text{O}$  was reacted with excess  $\text{MoO}_3$  and the final product was obtained by washing the sample in hot  $\text{NH}_4\text{OH}$  to remove  $\text{MoO}_3$ . Direct solid state reaction of stoichiometric mixture of reactants resulted in  $\text{Rh}_2\text{O}_3$  impurity due to the

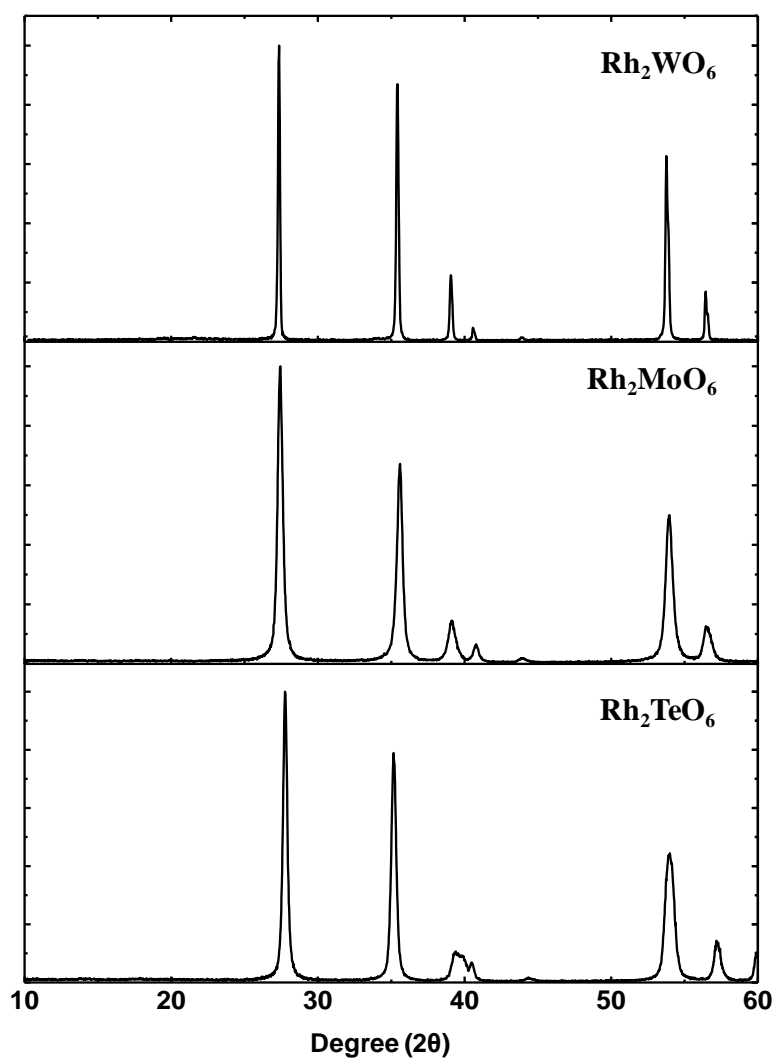
loss of  $\text{MoO}_3$  at relatively low temperature. Attempts to obtain rutile-type phases varying the Rh:M ratio away from 2:1 for M= W or Te did not produce single phase products.

Figure 8.2 shows X-ray diffraction pattern of the  $\text{Rh}_2\text{MO}_6$  phases. Unit cell parameters were obtained by LeBail fit using GSAS software [12] and are summarized in Table 8.1. All the prominent peaks could be indexed based on disordered rutile structure. However, very weak superstructure peaks are observed in the case of  $\text{Rh}_2\text{WO}_6$ . A superstructure peak relative to a primary peak is shown in an expanded view in Figure 8.3. This superstructure peak ( $hkl = 112$ ) is much weaker than expected for complete ordering of Rh and W, and it is broader than the primary peak. Such broadening of superstructure peaks is expected when the ordered domains are much smaller than the crystallite size [13]. It is the integrated peak intensity that must be used to estimate the actual degree of order. Based on relative integrated intensities, we estimate the site occupation for sample b in Figure 8.3 to be about  $(\text{Rh}_{1.6}\text{W}_{0.4})(\text{W}_{0.6}\text{Rh}_{0.4})\text{O}_6$ . No indications of superstructure peaks were observed in the diffraction patterns for either  $\text{Rh}_2\text{MoO}_6$  or  $\text{Rh}_2\text{TeO}_6$ . However due to the scattering powers of Mo and Te relative to that of Rh, the expected superstructure peaks for complete ordering would be very weak for both cases. We conclude that long-range ordering of Rh and W is incomplete in  $\text{Rh}_2\text{WO}_6$  and that some long-range order of the cations may be present but undetected when M is Mo or Te.

Table 8.1: Cell parameters of  $\text{Rh}_2\text{MO}_6$ 

| Compound                  | Final temperature (°C) | a (Å) | c (Å)        | Cell volume (Å <sup>3</sup> ) |
|---------------------------|------------------------|-------|--------------|-------------------------------|
| $\text{Rh}_2\text{MoO}_6$ | 650                    | 4.59  | 3.01         | 63.41                         |
| $\text{Rh}_2\text{WO}_6$  | 1000                   | 4.60  | 3.02 (9.07*) | 63.97 (191.92*)               |
| $\text{Rh}_2\text{TeO}_6$ | 750                    | 4.54  | 3.08         | 63.48                         |

\* trirutile parameters

Figure 8.2: Powder X-ray diffraction patterns of  $\text{Rh}_2\text{MO}_6$  phases.

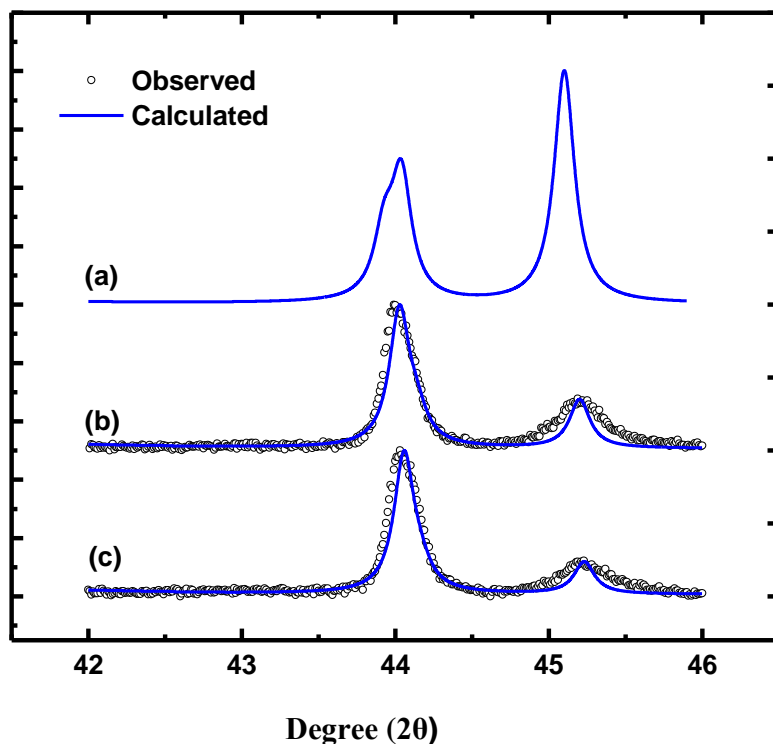
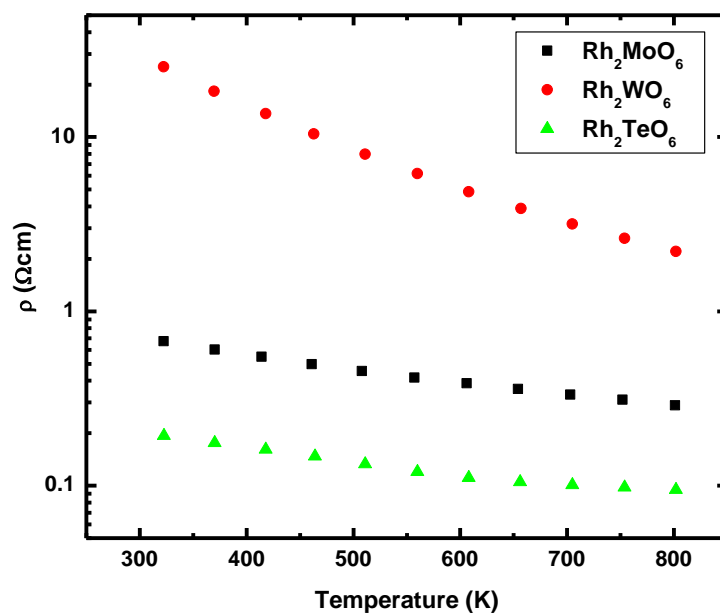
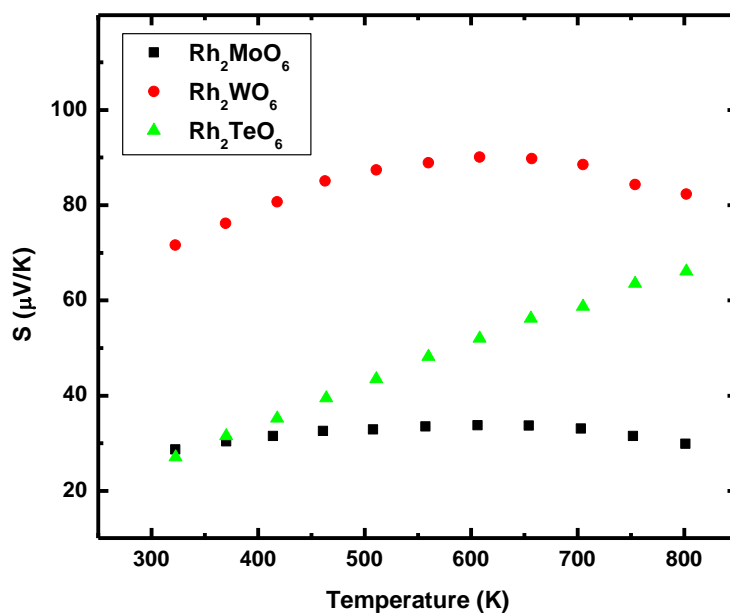


Figure 8.3: XRD patterns for Rh<sub>2</sub>WO<sub>6</sub> with line for calculated patterns and open circles for observed patterns. (a) Calculated pattern for fully ordered Rh<sub>2</sub>WO<sub>6</sub> where the higher angle peak is a superstructure peak. (b) Observed pattern and pattern calculated for (Rh<sub>1.54</sub>W<sub>0.46</sub>)(W<sub>0.54</sub>Rh<sub>0.46</sub>)O<sub>6</sub> (c) Observed pattern of a second sample slightly less ordered and a pattern calculated for (Rh<sub>1.5</sub>W<sub>0.5</sub>)(W<sub>0.5</sub>Rh<sub>0.5</sub>)O<sub>6</sub>.

Temperature variation of electronic resistivities and Seebeck coefficients of all samples are shown in Figure 8.4(a) and 8.4(b), respectively. All samples show semiconducting behavior as resistivity decreases when temperature is increased. Rh<sub>2</sub>TeO<sub>6</sub> shows lowest resistivity of about  $2 \times 10^{-3} \Omega\text{cm}$  at room temperature while Rh<sub>2</sub>WO<sub>6</sub> and Rh<sub>2</sub>MoO<sub>6</sub> are about three orders of magnitude more resistive. Electronic conductivities of Rh<sub>2</sub>WO<sub>6</sub> and Rh<sub>2</sub>MoO<sub>6</sub> obtained in this work are similar with the reported value for rutile phase [9-11] which confirm our structural determinations. The electrical resistivity of Rh<sub>2</sub>TeO<sub>6</sub> has not been previously reported.



(a)



(b)

Figure 8.4: Plots of resistivity (a) and Seebeck coefficient (b) of  $\text{Rh}_2\text{MO}_6$  vs. temperature.

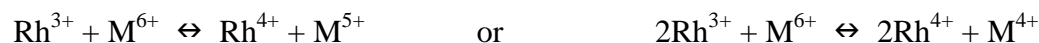


## 8.4 Discussion

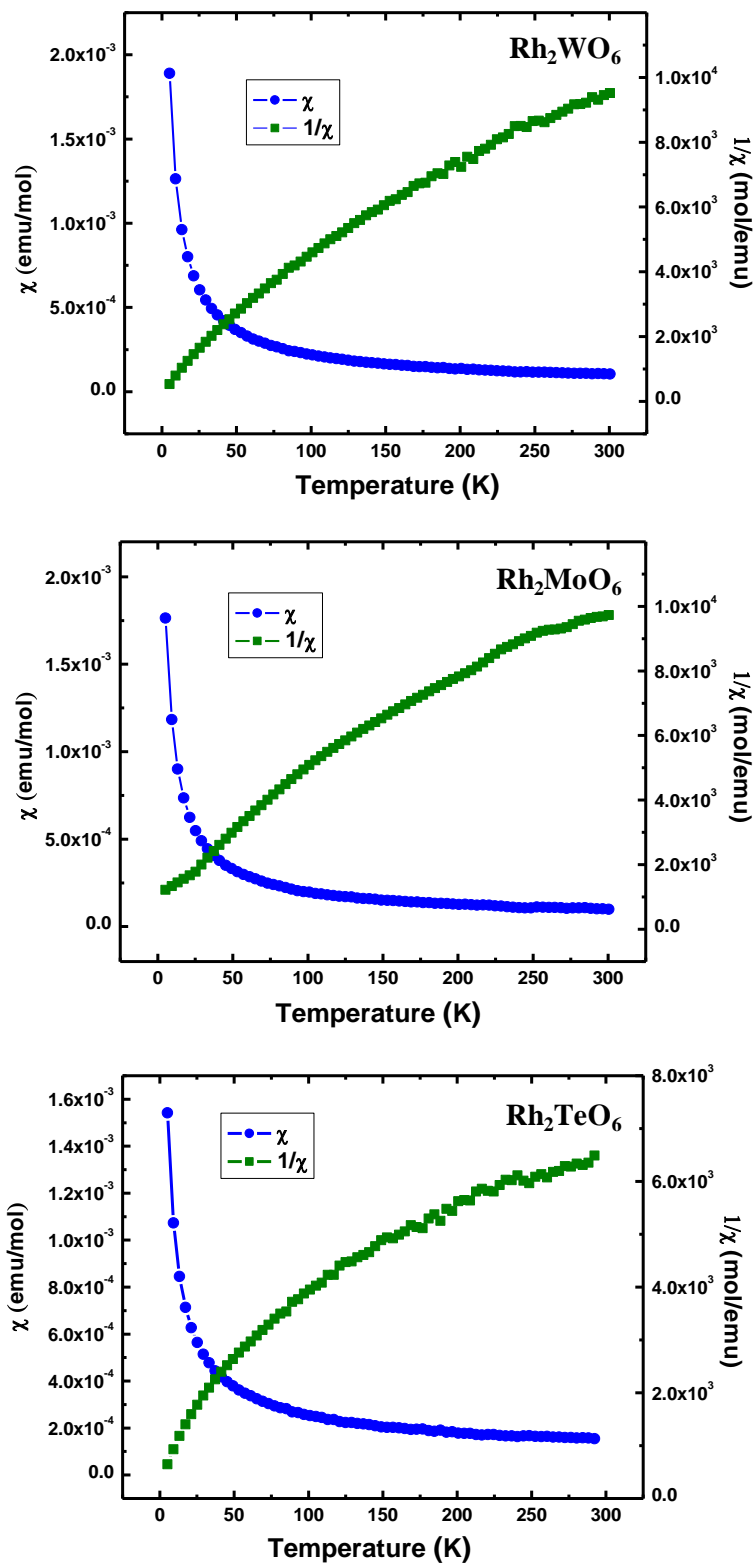
These  $\text{Rh}_2\text{MO}_6$  compounds would be expected to be diamagnetic insulators if the oxidation states were  $\text{Rh}^{3+}$  and  $\text{M}^{6+}$ . The relatively high conductivities and low Seebeck coefficients indicate the presence of valence degeneracy resulting in some oxidation of  $\text{Rh}^{3+}$  by  $\text{M}^{6+}$ . Rutile-type  $\text{RhO}_2$  is known but requires high pressure for its synthesis. However, many rhodates prepared in air contain a mixture of  $\text{Rh}^{3+}$  and  $\text{Rh}^{4+}$  [3,14]. Thus, the presence of  $\text{Rh}^{4+}$  in rutile-type  $\text{Rh}_2\text{MO}_6$  phases is not unexpected. Given that the Rh concentration is twice that of the M cation, there is complete three-dimensional connectivity of Rh through Rh-O-Rh bonds, regardless of the degree of ordering. The Rh  $t_{2g}$  band is filled when all Rh is  $\text{Rh}^{3+}$ , but holes are introduced into this band as  $\text{Rh}^{3+}$  is oxidized to  $\text{Rh}^{4+}$ . Thus, we expect p-type behavior as observed. There will also be partially occupied  $d$  states at the Fermi level associated with reduced Mo and W. These will add an n-type component to the electrical conductivity. This contribution will be less than the p-type contribution due to the poor connectivity between M cations. The oxidizing power of  $\text{Mo}^{6+}$  is greater than that of  $\text{W}^{6+}$ . Therefore, we might expect more oxidation of  $\text{Rh}^{3+}$  to  $\text{Rh}^{4+}$  in  $\text{Rh}_2\text{MoO}_6$  relative to  $\text{Rh}_2\text{WO}_6$ . Thus, we have somewhat higher conductivity for  $\text{Rh}_2\text{MoO}_6$  relative to  $\text{Rh}_2\text{WO}_6$ . The oxidizing power of  $\text{Te}^{6+}$  is even greater than that of  $\text{Mo}^{6+}$ . Thus in  $\text{Rh}_2\text{TeO}_6$ , we have even more holes in the Rh  $t_{2g}$  band and even higher conductivity. The Seebeck coefficient increases steadily with temperature in the case of  $\text{Rh}_2\text{TeO}_6$ . However, for  $\text{Rh}_2\text{MoO}_6$  and  $\text{Rh}_2\text{WO}_6$  there is a maximum in the Seebeck coefficient as temperature increases. This suggests that for  $\text{Rh}_2\text{MoO}_6$  and

$\text{Rh}_2\text{WO}_6$  there is more than one conduction mechanism involving more than one type of charge carriers. For these compounds the two charge carriers would be hole carriers in the Rh  $4dt_{2g}$  band and electrons in  $4d$  or  $5d$  orbitals of Mo or W. In the case of  $\text{Rh}_2\text{TeO}_6$  the only carriers present would be holes in the Rh  $t_{2g}$  band if the reduced Te was present as  $\text{Te}^{4+}$  with a localized pair of  $5s$  electrons.

Interpretation of transport and magnetic measurement become very complicated when valence degeneracy occurs. The situation for  $\text{Rh}_2\text{MO}_6$  phases can be represented as:



These equilibriums are increasingly shifted to the right in the order W, Mo, Te. These equilibriums can also be expected to shift as a function of temperature. Thus, the number of carriers and the number of unpaired electrons can change significantly as temperature changes. Observed magnetic moments are low (Fig.8.5) but are somewhat higher for  $\text{M} = \text{Mo}$  and  $\text{W}$ , presumably due to the presence of unpaired electrons associated with Mo or W. The Rh cation site has a lower charge and a greater size relative to the M cation site. Thus, we can speculate that M cations on the Rh site will have reduced charge leading to an increase in their size. This is compensated by the Rh on the M site being oxidized to increase its charge and decrease its size for a better fit on this site. For  $\text{M} = \text{W}$  this leads to  $(\text{Rh}_{1.6}^{3+}\text{W}_{0.4}^{5+})(\text{W}_{0.6}^{6+}\text{Rh}_{0.4}^{4+})\text{O}_6$ .

Figure 8.5: Magnetism of  $\text{Rh}_2\text{MO}_6$  phases.

A situation somewhat analogous to the  $\text{Rh}_2\text{MO}_6$  phases occurs for  $\text{V}_2\text{MO}_6$  phases. The trirutile structure is observed for  $\text{V}_2\text{WO}_6$  where the oxidation states are well defined as  $\text{V}^{3+}$  and  $\text{W}^{6+}$ , and these two cations are well ordered [15]. However, in the case of  $\text{V}_2\text{MoO}_6$ , the  $\text{Mo}^{6+}$  has oxidized the  $\text{V}^{3+}$ , and the trirutile structure does not form [16].

Thermal conductivity of all samples increases with temperature as expected due to the increase in electronic contribution given by Weidman-Franz equation:  $\lambda_{\text{el}} = L\sigma T$  when  $L$  is Lorentz factor,  $\sigma$  is the electronic conductivity and  $T$  is absolute temperature (Figure 8.6). Calculated Power Factor [ $\text{PF} = (S^2\sigma)$ ] and  $ZT$  are low for all the compounds (Figure 8.7a and b). Observed relatively higher Power Factor (Figure 8.7a) and  $ZT$  (Figure 8.7b) for  $\text{Rh}_2\text{TeO}_6$  are attributed to enhanced electrical conductivity apparently due to a higher concentration of holes.

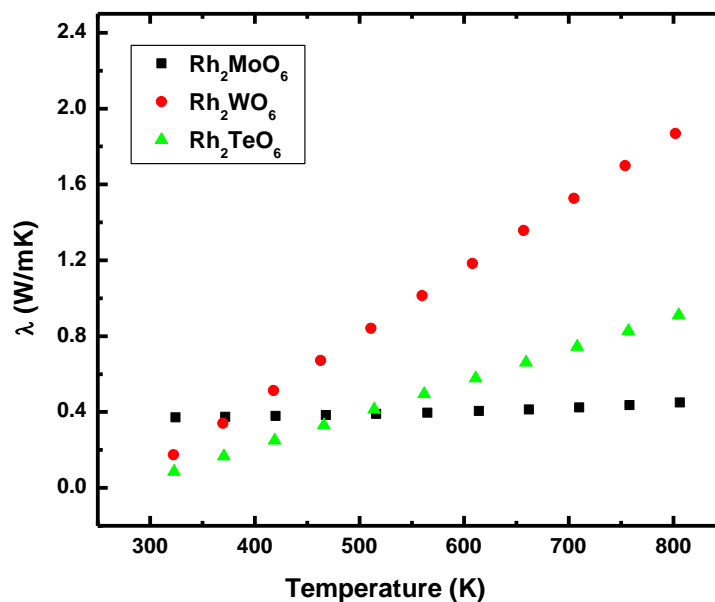


Figure 8.6: Thermal conductivity of  $\text{Rh}_2\text{MO}_6$ .

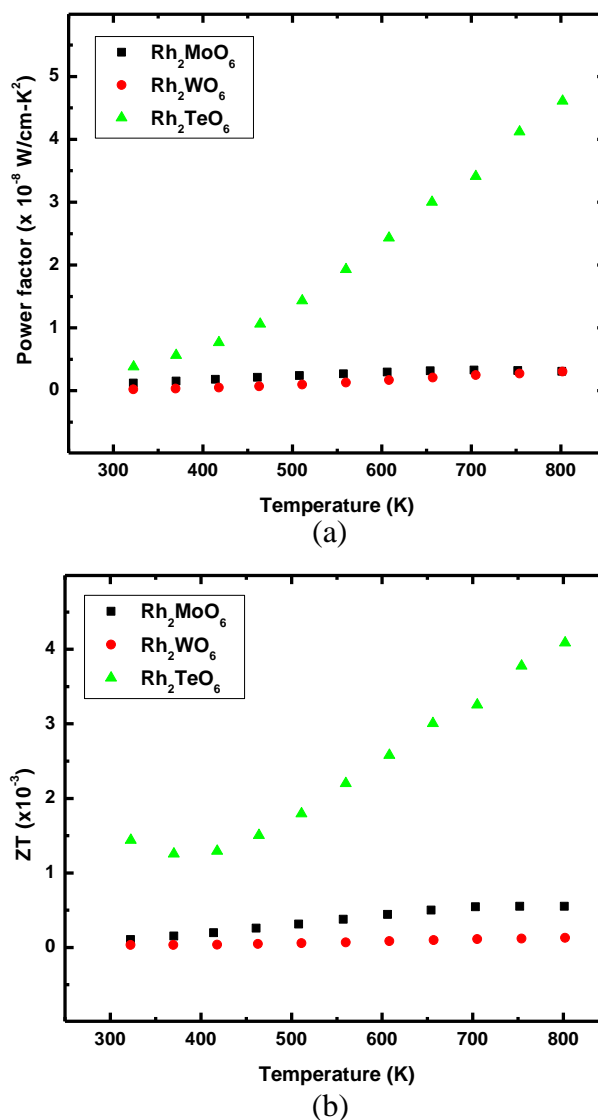


Figure 8.7: Power Factor (a) and ZT (b) plots for  $\text{Rh}_2\text{MO}_6$  phases.

## 8.5 Conclusions

The  $\text{Rh}_2\text{MO}_6$  compounds with  $M = \text{Mo}, \text{W},$  and  $\text{Te}$  crystallize in a rutile-type structure and show relatively high electronic conductivity due to valence degeneracy. This valence degeneracy impedes the cation order required for development of the trirutile structure. Variations of Seebeck coefficients and electronic conductivities as a

function of temperature suggest that both holes and electron carriers contribute to the electrical properties in the case of  $\text{Rh}_2\text{MoO}_6$  and  $\text{Rh}_2\text{WO}_6$ . The calculated ZTs are low for all the compounds.

## 8.6 Experimental

$\text{Rh}_2\text{TeO}_6$  was prepared by solid state reaction from  $\text{RhCl}_3 \cdot x\text{H}_2\text{O}$  and  $\text{TeO}_2$ . Stoichiometric mixture of starting materials was mixed, ground, pressed and heated at 500-750°C for 100-150 hours with several intermediate grindings. Mixture of  $\text{RhCl}_3 \cdot x\text{H}_2\text{O}$  and  $\text{MoO}_3$  with about 1:1 weight ratio was ground and heated as a pellet in air at 500-650°C for 100-150 hours with several intermediate grindings. The sample was then washed in hot  $\text{NH}_4\text{OH}$  to dissolve excess  $\text{MoO}_3$ . The washed powder was filtered, wash with  $\text{H}_2\text{O}$  and ethanol and dry at 120°C. Polycrystalline  $\text{Rh}_2\text{MoO}_6$  was pressed into pellet and sintered at 650°C for 24 hours and was used to measure all properties.  $\text{Rh}_2\text{WO}_6$  was synthesized by solid state reaction of  $\text{Rh}_2\text{O}_3$  (prepare from  $\text{RhCl}_3 \cdot x\text{H}_2\text{O}$ ) and  $\text{WO}_3$  (Aldrich, 99+%) at 1000°C for 100-150 hours with intermediate grindings. Powder X-ray diffraction data were obtained by a Rigaku MiniFlex II diffractometer using Cu K $\alpha$  radiation and a graphite monochromator. The Seebeck coefficient and electrical resistivity measurements were carried out on ZEM-3 (within an error limit of 5%) and the thermal diffusivity measurements (within an error limit of 10%) were carried out on Netzsch micro flash instrument. Specific heat measurements were performed using a METTLER differential scanning calorimeter (DSC).

## 8.7 References

1. I. Terasaki, N. Murayama, eds., *Oxide Thermoelectrics* (Research Signpost, Trivandrum, India, 2002).
2. H. Ohta, K. Sugiura, K. Koumoto, *Inorg. Chem.*, **47** (2008), 8429.
3. H. Mizoguchi, L.N. Zakharov, W.J. Marshall, A.W. Sleight, M.A. Subramanian, *Chem. Mater.*, **21** (2009), 994.
4. W. Kobayashi, S. Hebert, D. Pelloquin, O. Perez, A. Maignan, *Phys. Rev. B*, **76** (2007), 245102.
5. J. P. Badaud, J. Omaly, *C. R. Acad. Sci. Paris*, **278** (1974), 521.
6. H. Leiva, R. Kershaw, K. Dwight, A. Wold, *J. Solid State Chem.*, **47** (1983), 293.
7. L. Degueldre, Y. Gobillon, L. Clerbols, L. Bourgeois, U.S. Patent #3,736,270, 1973.
8. V. B. Lazarev, I.I. Prosychev, I.S. Shaplygin, *Zh. Neorg. Khim.*, **24** (1979) 313.
9. I. I. Prosychev, V. B. Lazarev, I.S. Shaplygin, *Zh. Neorg. Khim.*, **25** (1980) 1159.
10. I. I. Prosychev, V. B. Lazarev, I.S. Shaplygin, *Zh. Neorg. Khim.*, **26** (1981) 3154.
11. L. Degueldre, L. Clerbols, Y. Gobillon, L. Bourgeois, Ger. Offen. (1972).
12. A.C. Larson, R.B. Von Dreele, "General Structure Analysis System (GSAS)," *Los Alamos National Laboratory Report LAUR*, 86-784 (2004); B.H. Toby, *J. Appl. Crystallogr.*, **34** (2001), 210.
13. P. Woodward, R.-D. Hoffmann, A.W. Sleight, *J. Mater. Res.*, **9** (1994), 2118.
14. H. Mizoguchi, A.W. Sleight, M.A. Subramanian, *Inorg. Chem.*, **50** (2011), 10.
15. J.-C. Bernier, P. Poix, *Comp. Rend. Serie C, Acad. Sci. Paris*, **265** (1967), 1247.
16. L. A. Klinkova, E. D. uSkrebkova, *Russ. J. Inorg. Chem.*, **23** (1978), 100.

## Chapter

### 9. General Conclusions and Future Work

In the current work, several systems of oxides containing tellurium were studied. Structure-property relationships were discussed in each system. In solid state chemistry, properties of the materials are strongly related to chemistry of compositional elements and interactions between them. By understanding the structure of a compound and the nature of its compositions, one can predict its properties or even synthetic methods. Novel materials with improved or novel properties can be designed based on the same principles.

As a member of heavy post transition metals, tellurium is unique because of its lone pair electrons and diffused *s* orbital. These two characteristics result in unique structures which give rise to interesting properties.

First observation of electronic conductivity in mixed valence oxides containing tellurium was discovered in series of novel pyrochlore oxides with the formula  $\text{Cs}(\text{M},\text{Te})_2\text{O}_6$  ( $\text{M} = \text{Al}, \text{Ga}, \text{Cr}, \text{Fe}, \text{Co}, \text{In}, \text{Ho}, \text{Lu}, \text{Yb}, \text{Er}, \text{Ge}, \text{Rh}, \text{Ti}, \text{Zn}, \text{Ni},$  and  $\text{Mg}$ ). Detailed structural and properties analysis indicated the mixed valency of  $\text{Te}^{4+}/\text{Te}^{6+}$  which resulted in the unusual color and electrical properties. Relatively high conductivities and, in some cases, degenerate semiconducting behavior were found and rationalized. This investigation provided in-depth information on the structure of defect pyrochlore oxides and the novel property of oxides containing tellurium.

Novel oxygen deficient phases in  $\text{CsTe}_2\text{O}_6$  have been reported. Systematic studies of series of composition  $\text{CsTe}_2\text{O}_{6-x}$  where  $x = 0, 0.15, 0.25, 1.5$  and  $\text{CsTe}_2$ .



$x\text{W}_x\text{O}_6$  where  $x=0.2-0.5$  led to more understanding in the ordering of cations and vacancies in pyrochlore framework. This is a clear example of how lone pair electrons in heavy post transition metals can greatly affect structures and properties of the compounds.

Novel cubic pyrochlores with the formula  $(\text{CdBi})(\text{MTe})\text{O}_7$ ,  $\text{M} = \text{Al}, \text{Cr}, \text{Ga}, \text{In}, \text{Fe}, \text{Mn},$  and  $\text{Sc}$  have been prepared. Magnetic and dielectric measurements were analyzed. This study possibly leads to many new pyrochlore oxides containing  $\text{Te}^{6+}$ .

Complete solid solutions of  $\text{Tl}_{2-x}\text{In}_x\text{TeO}_6$  were prepared and studied. When  $x$  is varied, electrical properties of the compounds varied from insulating ( $x=2$ ) to metallic ( $x=0$ ) which were clearly explained by percolation model. As electrical conductivity of materials could be easily controlled by their composition, future applications in industry might be potential.

We have investigated structures and properties of  $\text{Rh}_2\text{MO}_6$  where  $\text{M} = \text{Mo}, \text{W},$  and  $\text{Te}$ . Valence degeneracy between atomic orbitals of  $\text{Rh}$  and  $\text{M}$  cations resulted in interesting electrical and magnetic properties. Although more studies are needed to improve  $\text{ZT}$  of the compounds, this work actually provides another example of the effects of structures and compositional elements to the properties of materials.

Study is a never-ending process. The more we learn, the more we realize how much is left to be learned. All knowledge and discoveries only lead to more questions. This study is not an exception as it leads to more questions and future works. For example, we have shown that mixed valence tellurium oxides can be conducting; however, no metallic conduction or superconductivity was found. Variations from the

ideal formula might lead to more understanding in the conducting mechanism. Interesting variations include substitutions in A sites or anion sites of  $\text{Cs}(\text{M},\text{Te})_2\text{O}_6$ , for instance. As high ionic conductivity is commonly observed in pyrochlore, coexistence of ionic and electronic conductivity might be possible in this system, too. On the other hand, electrical properties of  $\text{In}_2\text{TeO}_6$  oxides might be improved by manipulating the composition of the compound. Oxygen deficiency is known to increase electronic conductivity in a transparent  $\text{In}_2\text{O}_3$ . Similar mechanism might also improve the conductivity of  $\text{In}_2\text{TeO}_6$  which probably lead to a new transparent conductive oxide. As some compositions of  $\text{Tl}_{2-x}\text{In}_x\text{TeO}_6$  have high conductivities and light color, thin film based on  $\text{Tl}_{2-x}\text{In}_x\text{TeO}_6$  solid solutions might be as well interesting.

## Bibliography

- M. Abbate, J.A. Guevara, S.L. Cuffini, Y.P. Mascarenhas, E. Morikawa, *Eur. Phys. J.*, **B 25** (2002), 203.
- S. Adams, softBV, Version 0.96, 2004. <http://kristall.uni-mki.gwdg.de/softbv/>
- E. Aleshin, R. Roy, *J. Am. Ceram. Soc.*, **45** (1962), 18.
- J. A. Alonso, C. Cascales, I. Rasines, *Z. Anorg. Allg. Chem.*, **537** (1986), 213.
- J. A. Alonso, A. Castro, I. Rasines, X. M. Turrillas, *J. Matter. Sci.*, **23** (1988), 4103.
- J. A. Alonso, X. Turrillas, *Dalton Trans.*, (2005), 865.
- M. Amarilla, M. L. Veiga, C. Pico, M. Gaitan, A. Jerez, *Inorg. Chem.*, **28** (1989), 1701.
- P. Atkins, T. Overton, J. Rourke, M. Weller, F. Armstrong, 'Inorganic Chemistry', 4<sup>th</sup> ed., Oxford University Press, (2006).
- J. P. Badaud, J. Omaly, *C. R. Acad. Sci. Paris*, **278** (1974), 521.
- D. R. Baker, G. Paul, S. Sreenivasan, H. E. Stanley, *Phys Rev.*, **E66** (2002), 046136.
- P. W. Barnes, P. M. Woodward, Y. Lee, T. Vogt, J. A. Hriljac, *J. Am. Chem. Soc.*, **125** (2003), 4573.
- N. Barrier, S. Malo, O. Hernandez, M. Hervieu, B. Raveau, *J. Solid State Chem.*, **179** (2006), 3484.
- N. Barrier, J. M. Rueff, M. B. Lepetit, J. Contreras-Garcia, S. Malo, B. Raveau, *Solid State Sci.*, **11** (2009), 289.
- G. Bayer, *Fortschr. Miner.*, **46** (1969), 41.
- I.N. Belyaev, D.S. Lesnykh and T.G. Lupeiko, *Zh. Neorg. Khim.*, **14** (1969), 648.
- F. Bernard, P. Rose, M. Daniele, *Mat. Res. Bull.*, **10** (1975), 1305.
- J.-C. Bernier, P. Poix, *Comp. Rend. Serie C, Acad. Sci. Paris*, **265** (1967), 1247.
- H. Beyer, *Z. Kristallogr.*, **124** (1967), 228.
- T. Birchall and A.W. Sleight, *J. Solid State Chem.*, **13** (1975), 118.
- I. L. Botto and E. J. Baran, *Z. Anorg. Allg. Chem.*, **468** (1980), 221.
- R. J. Bouchard, J. L. Gilson, *Mat. Res. Bull.*, **6** (1971), 669.
- D. D. Brown, 'Mixed-Valence Compounds; Theory and Applications in Chemistry, Physics, Geology, and Biology', Proceedings of the NATO Advanced Study Institute, (1979).
- I. D. Brown, *J. Solid State Chem.*, **11** (1974), 214.
- A. Castro, I. Rasines, X. M. Turrillas, *J. Solid State Chem.*, **80** (1989), 227.
- M. Catti, C. M. Mari, E. Cazzanelli, G. Mariotto, *Solid State Ionics*, **40** (1990), 900.
- R. J. Cava, R. S. Roth, T. Siegrist, B. Hessen, J. J. Krajewski, W. F. Peck Jr., *J. Solid State Chem.*, **103** (1993), 359.
- R. J. Cava, B. Batlogg, G. P. Ramirez, J. J. Krajewski, W. F. Peck Jr., L. W. Rupp Jr., A. S. Cooper. *Nature*, **339** (1989), 291.
- A. K. Cheetam, P. Day, 'Solid-State Chemistry: techniques', Oxford University Press, (1987).

- N. G. Chernorukov, N. P. Egorov, E. V. Suleimanov, *Zh. Neorg. Khim.*, **34** (1989), 2995.
- A. Coucou, M. Figlarz, *Solid state ionics*, **28-30** (1988), 1762.
- P. A. Cox, *The electronic Structure and Chemistry of Solids*, Oxford University Press, (1987).
- P. A. Cox, W. R. Flavell, and R. G. Egdell, *J. Solid State Chem.*, **68** (1987) 340.
- D. E. Cox, A.W. Sleight, *Solid State Commun.*, **19** (1976), 969.
- B. D. Cullity, S. R. Stock, *Elements of X-ray Diffraction*, 3<sup>rd</sup> ed., Prentice-Hall, Inc., (2001).
- W. I. F. David, K. Shankland, L. B. McCusker, Ch. Baerlocher, *Structure Determination from Powder Diffraction Data*, Oxford University Press, (2002).
- B. Darriet, M. Devalette, B. Latourrette, *Acta. Cryst.*, **B34** (1978), 3528.
- B. Darriet, M. Rat, J. Galy, P. Hagenmuller, *Mat. Res. Bull.*, **6** (1971), 1305.
- P. K. Davies, H. Wu, A. Y. Borisevich, I. E. Molodetsky, L. Farber, *Annu. Rev. Mater. Res.*, **38** (2008), 369.
- L. Degueldre, Y. Gobillon, L. Clerbols, L. Bourgeois, U.S. Patent #3,736,270, 1973.
- L. Degueldre, L. Clerbols, Y. Gobillon, L. Bourgeois, *Ger. Offen.* (1972).
- G. S. Deshmukh, V. D. Anand, A. K. Vishwanath, *Fresen. Z. Anal. Chem.*, **172** (1960), 260.
- A. Dityatiev, P. S. Berdonosov, V. A. Dolgikh, D. W. Aldous, P. Lightfoot, *Solid State Sci.*, **8** (2006), 830.
- O. A. Dityat'ev, S. Yu. Stefanovich, V. A. Prituzhalov, V. A. Dolgikh, *Inorg. Matter.*, **40** (2004), 740.
- R. G. Dosch, T. J. Headley, C. J. Northrup, P. F. Hlava, *Sandia National Laboratories Report*, **82-2980** (1982), 1.
- Y. Dou, R. G. Egdell, D. S. L. Law, N. M. Harrison, and B. G. Searle, *J. Phys.: Cond. Matter.*, **10** (1988), 8447.
- A. Driouiche, F. Abraham, M. Touboul, M. Figlarz, *Mat. Res. Bull.*, **26** (1991), 901.
- D. Dumora, P. Hagenmuller, *C. R. Acad. Sci. Paris, Ser. C*, **266** (1968), 276.
- M. Durand, B. Ayrault, Y. Marqueton, E. A. Decamps, *C. R. Acad. Sci.*, **B283** (1976), 377.
- M. Dutreilh, P. Thomas, J. C. Champarnaud-Mesjard, B. Frit, *Solid State Sci.*, **3** (2001), 423.
- P. P. Edwards, T. V. Ramakrishnan, C. N. R. Rao, *J. Phys. Chem.*, **99** (1995), 5228.
- N. P. Egorov, N. G. Chermorukov, I. A. Korshunov, *Zh. Neorg. Khim.*, **34** (1989), 827.
- T. S. Ercit, F. C. Hawthorne, P. Cerny, *Can. Mineral.*, **24** (1986), 655.
- M. Faucher, P. Caro, *J. Solid State Chem.*, **12** (1975), 1.
- X. B. Feng, N. M. Harrison, *Phys Rev. B*, **69** (2004), 35114.
- G. Ferey, M. Leblanc, R. de Pape., *J. Solid State Chem.*, **40** (1981), 1.
- F. Folger, *Z. Anorg. Allg. Chem.*, 411 (1975), 111.
- P. Forzatti, G. Tieghi, *J. Solid State Chem.*, **25** (1978), 387.
- P. Forzatti, P. Tittarelli, *J. Solid State Chem.*, **33** (1980), 421.

- H. Föll, "Electronic Materials", Accessed February 2011.  
[http://www.tf.unikiel.de/matwis/amat/elmat\\_en/index.html](http://www.tf.unikiel.de/matwis/amat/elmat_en/index.html)
- G. Frand, O. Bohnke, P. Lacorre, J. L. Fourquet, A. Carre, B. Eid, J. G. Theobald, A. Gire, *J. Solid State Chem.*, **120** (1995), 157.
- K. Friese, J.-Y. Gesland, A. Grzechnik, *Z. Kristallogr.*, **220** (2005) 614.
- B. Frit, M. Jaymes, *Bull. Soc. Chim. Fr.*, **1974** (1974), 402.
- P. Ganguly, N. Y. Vasanthacharya, C. N. R. Rao, *J. Solid State Chem.*, **54** (1984), 400.
- S. Garcia-Martin, M. L. Veiga, A. Jerez, C. Pico, *Mat. Res. Bull*, **26** (1991), 789.
- S. Garcia-Martin, M. L. Veiga, A. Jerez, M. Gaitan, C. Pico, *J. Chem. Soc., Dalton Trans.*, **8** (1988), 2141.
- J. S. Gardner, M. J. P. Gingras, J. E. Greedan, *Rev. Mod. Phys.*, **82** (2010), 53.
- G. Gattow, O. J. Lieder, *Naturwissenschaften*, **50** (1963), 662.
- P. Glans, T. Learmonth, K. E. Smith, J. Guo, A. Walsh, G. W. Watson, F. Terzi and R. G. Egdell, *Phys. Rev. B*, **71** (2005), 235109.
- J. B. Goodenough, *J. Solid State Chem.*, **3** (1971), 490.
- J. B. Goodenough, S. L. Cooper, *Struct. Bond.*, 'Localized to itinerant electronic transition in perovskite oxides', Springer, (1965).
- J. Goodey, J. Broussard, P. Shiv, Halasyamani, *Chem. Mater.*, **14** (2002), 3174.
- J. Goodey, K. M. Ok, J. Broussard, C. Hofmann, F. V. Escobedo, P. S. Halasyamani, *J. Solid State Chem.*, **175** (2003), 3.
- L. Gor'kov, V. Kresin, *J. Super.*, **13** (2000), 239.
- G. Gospodinov, L. Atanasova, *J. Therm. Anal. Calorim.*, **83** (2006), 273.
- H. Gould, J. Tobochnik, W. Christian, 'Handout for Physics 125/225: Chapter 13 percolation', 2001, 443.
- J. E. Greedan, A. O'Reilly, C. V. Stager, *Phys. Rev. B*, **35** (1987), 8770.
- N. N. Greenwood, A. Earnshaw, 'Chemistry of the Elements', Pergamon Press, (1984).
- D. Groult, J. Pannetier, B. Raveau, *J. Solid State Chem.*, **41** (1982), 277.
- A. Gualtieri, P. Norby, J. Hanson, J. Hriljac, *J. Appl. Cryst.* **29** (1996), 707.
- I. Hamberg, C. G. Granqvist, K. F. Berggren, B. E. Sernelius, and L. Engstrom, *Phys. Rev. B*, **30**, (1984), 3240.
- T. Hasegawa, N. Ogita, Y. Nagao, J.-I. Yamaura, Z. Hiroi, M. Udagawa, *Physica C*, in press.
- R. M. Hazen, C. T. Prewitt, *Am. Mineral.*, **62** (1977), 309.
- M. Heinemann, H. J. Terpstram, C. Haas, and R. A. deGroot, *Phys. Rev. B*, **52** (1995), 11740.
- T. J. B. Holland, S. A. T. Redfern, *Mineralogical Magazine*, **61** (1997), 65.
- C. Hormillosa, S. Healy, T. Stephen and I.D. Brown, Bond Valence Calculator, Version 2.0, 1993. <http://www.ccp14.ac.uk>
- H. S. Horowitz, J. M. Longo, J. T. Lewandowski, *ibid.*, **16** (1981), 489.
- Y.-S. Hong, M. Zakhour, M. A. Subramanian, J. Darriet, *J. Mater. Chem.*, **8** (1998), 1889.
- J. M. Honig, L. L. van Zandt, *Annu. Rev. Mater.Sci.*, **5** (1975), 225.

- P. Höss, A. Osvet, F. Meister, M. Batentschuk, A. Winnacker, T. Schleid, *J. Solid State Chem.*, **181** (2008), 2783.
- F. W. Hützler, H.-G. Burckhardt and M. Trömel., *Z. Kristallogr.*, **172** (1984), 116.
- M. Imada, A. Fujimori and Y. Tokura. *Rev. Mod. Phys.*, **70** (1998), 1039.
- J. Isasi, M. L. Lopez, M. L. Veiga, C. Pico, *Solid State Ionics*, **89** (1996), 321
- J. Isasi, M. L. Lopez, M. L. Veiga, E. Ruiz-Hitzky, C. Pico, *J. Solid State Chem.*, **116** (1995), 290.
- Ismunandar, I. Haryanto, S. Dewi, *Jurnal Matematika dan Sains*, **8** (2003), 27.
- F. Izumi, T. Ikeda, *Mater. Sci. Forum*, **321-324** (2000), 198.
- K. T. Jacob, R. Subramanian, *J Phase Equil. Diff.*, **29** (2008), 136.
- J. E. Jaffe, R. Pandey, and A. B. Kunz, *Phys. Rev. B*, **43** (1991), 4030.
- B. Jeansannetas, P. Thomas, J. C. Champarnard-Mesjard, B. Frit, *Mat. Res. Bull.*, **32** (1997), 51.
- T. Kar, R. N. P. Choudhary, *Mater. Sci. Eng. B*, **90** (2002), 224.
- S. O. Kasap, 'Thermoelectric Effects in Metals: Thermocouples', An e-booklet (1997-2001).
- V. V. Kharton, E. V. Tsipis, A. A. Yarenchenko, N. P. Vyshatko, A. L. Shaula, E. N. Naumovich, J. R. Frade, *J. Solid State Electrochem.*, **7** (2003), 468.
- J.-H. Kim, P. Shiv Halasyamani, *J. Solid State Chem.*, **181** (2008), 2108.
- W. D. Kingery, H. K. Bowen, D. R. Uhlmann, 'Introduction to Ceramics', 2<sup>nd</sup> ed., John Wiley & Sons: New York, (1976).
- W. Klein, J. Curda, E.-M. Peters, M. Z. Jansen, *Anorg. Allg. Chem.*, **631** (2005), 2893.
- L. A. Klinkova, E.D.Skrebkova, *Russ. J. Inorg. Chem.*, **23** (1978), 100.
- H. Kobayash R. Kanno, Y. Kawamoto, T. Kamiyama, R Izumi and A.W. Sleight, *J. Solid State Chem.*, **114** (1995), 15.
- W. Kobayashi, S. Hebert, D. Pelloquin, O. Perez, A. Maignan, *Phys. Rev. B*, **76** (2007), 245102.
- K. Kohn, S. Akimoto, Y. Uesu, K. Asai, *J. Phys. Soc. Jpn.*, **37** (1974), 1169.
- K. Kohn, K. Inoue, O. Horie, S.-I. Akimoto, *J. Solid State Chem.*, **18** (1976), 27.
- R. Kozłowski, J. Słoczyński, *J. Solid State Chem.*, **18** (1976), 51.
- D. Kolar, V. Urbanc, L. Golic, V. Ravnik, B. Volavsek, *J. Inorg. Nucl. Chem.*, **33** (1971), 3693.
- I. P. Kondratyuk, L. A. Muradyan, Yu. V. Pisarevskii, B. I. Simonov, *Kristallogr.*, **21** (1987), 609.
- R. Kykyneshi. M.S. Thesis, Oregon State University, Corvallis, OR, 2004
- T. S. Lakshmi Narasimhan, M. S. Baba, R. Viswanathan, *J. Phys. Chem. A*, **110** (2006), 13705.
- A.C. Larson and R.B. Von Dreele, "General Structure Analysis System (GSAS)," Los Alamos National Laboratory Report LAUR, 2004, 86-784; B.H. Toby, EXPGUI, a graphical user interface for GSAS, *J. Appl. Cryst.*, **34** (2001), 210.
- G. Lawes, T. Kimura, C. M. Varma, M. A. Subramanian, N. Rogado, R. J. Cava, A. P. Ramirez, *Prog. Solid State Chem.*, **37** (2009), 40.
- V. B. Lazarev, I.I. Prosychev, I.S. Shaplygin, *Zh. Neorg. Khim.*, **24** (1979) 313.
- H. Leiva, R. Kershaw, K. Dwight, A. Wold, *J. Solid State Chem.*, **47** (1983), 293.

- J. Li, T. Siritanon, J. K. Stalick, A. W. Sleight, M. A. Subramanian, *Inorg. Chem.*, **50** (2011), 5747.
- J. Li, A. E. Smith, K.-S. Kwong, C. Powell, A. W. Sleight, M. A. Subramanian, *J. Solid State Chem.*, **183** (2010), 1388.
- D. R. Lide, 'Handbook of Chemistry and Physics CRC', 84<sup>th</sup> ed., CRC press, (2003)
- I. Lidqvist, *Acta Chem. Scand.*, **14** (1960), 960.
- O. Lindqvist, W. Mark, *Acta Cryst.*, **B31** (1975), 1255.
- O. Lindqvist, J. Moret, *Acta Cryst. Sect. B*, **29** (1973), 643.
- J. M. Longo, P. M. Racciah, J. B. Goodenough, *Mat. Res. Bull.*, **4** (1969), 191.
- J. M. Longo, P.M. Racciah, J. A. Kafalas, J. W. Pierce, *Mater. Res. Bull.*, **7** (1971), 137.
- B. O. Loopstra, K. Goubitz, *Acta Cryst. C*, **42** (1986), 520.
- J. Loub, *Collect. Czech. Chem. Commun.*, **58** (1993), 1717.
- J. Loub, *Z. Anorg. Allg. Chem.*, **362** (1968), 98.
- J. Loub, J. Rosicky, *Z. Anorg. Allg. Chem.*, **365** (1969), 308.
- R. A. Macculey, F. A. Hummel, *J. Solid State Chem.*, **33** (1980), 99.
- S. A. Magarill, R. F. Klevtsova, *Sov. Phys. Crystallogr.*, **16** (1972), 645.
- G. D. Mahan, J. O. Sofo, *Proc. Natl. Acad. Sci.*, **19** (1996), 7436.
- C. Malika, O. M. Sreedharan, *Thermochim. Acta*, **190** (1991), 217.
- J. A. Malone, J. F. Dorrian, O. Muller, R. E. Newnham, *J. Am. Ceram. Soc.*, **52** (1969), 570.
- M. Marezio, D. B. McWhan, J. P. Remeika, P. D. Dernier, *Phys. Rev. B*, **5** (1972), 2541.
- S. Margadonna, T. Muranaka, K. Prassides., I. Maurin, K. Brigatti, R. M. Ibberson, M. Arai, M. Takana, J. Akimitsu, *J. Phys.: Condens. Matter.*, **13** (2001), L795.
- V. R. R. Medicherla, T. Shripathi, N. P. Lalla, *J. Condens. Matter*, **20** (2008), 035219.
- C. Michel, D. Groult, B. Raveau, *J. Inorg. Nucl. Chem.*, **37** (1975), 247.
- K. Min Ok, P. Shiv, Halasyamani, *Solid State Sci.*, **4** (2002), 793.
- A. Mineshige, M. Kobune, S. Fujii, Z. Ogumi, M. Inaba, T. Yao, K. Kikuchi, *J. Solid State Chem.*, **142** (1999), 374.
- A. Mineshige, M. Inaba, T. Yao, Z. Ogumi, K. Kikuchi, M. Kawase, *J. Solid State Chem.*, **121** (1996), 423.
- M. P. Minimol, K. Vidyasagar, *Inorg. Chem.*, **44** (2005), 9369.
- H. Mizoguchi, A. P. Ramirez, T. Siegrist, L. N. Zakharov, A. W. Sleight, M. A. Subramanian, *Chem. Mater.*, **21** (2009), 2300.
- H. Mizoguchi, A.W. Sleight, M.A. Subramanian, *Inorg. Chem.*, **50** (2011), 10.
- H. Mizoguchi, L.N. Zakharov, W.J. Marshall, A.W. Sleight, M.A. Subramanian, *Chem. Mater.*, **21** (2009), 994.
- B. G. Müller, *J. Fluorine Chem.*, **17** (1981), 317.
- D. W. Murphy, J. L. Dye, S. M. Zahurak., *Inorg. Chem.*, **22** (1983), 3679.
- Y. Nakamura, K. Oguro, I. Uehara, E. Akiba, *J. Alloys Compd.*, **298** (2000), 138.
- T. S. Narasimhan, M. S. Baba, S. Nalini, R. Viswanathan, *Thermochim. Acta*, **410** (2004), 149.
- S. Nathanson, *J. Inorg. Nucl. Chem.*, **30** (1968), 741.

- Ocean Optics, Inc. "We Make A Fiber For That!" Ocean Optics, Inc. <http://www.oceanoptics.com/Products/opticalfibers.asp>. Accessed May 2010.
- K. Okada, H. Morikawa, F. Marumo, S. Iwai, *Acta Cryst.*, **B31** (1975), 1200.
- H. Ohta, K. Sugiura, K. Koumoto, *Inorg. Chem.*, **47** (2008), 8429.
- M. Oliver, J. O. Dimmock, A. L. Mcwhorter, T. B. Reed, *Phys. Rev. B*, **5** (1972), 1078.
- L. Ortega-San Martin, J. P. Chapman, G. Cuello, J. Gonzalez-Calbet, M. I. Arriortua, T. Rojo, *Z. Anorg. Allog. Chem.*, **631** (2005), 2127.
- J. Pannetier, *J. Phys. Chem. Solids*, **34** (1973), 583.
- J. Pannetier, J. Lucas, *Mat. Res. Bull.*, **5** (1970), 797.
- D. J. Payne, R.G. Egdell, D.S.L. Law, P-A. Glans, T. Learmouth, K.E. Smith, J. Guo, A. Walsh, G.W. Watson, *J. Mater. Chem.*, **17** (2007), 267.
- M. V. Pentegova, Y. Y. Tomashpol'skii, *Neorg. Mater.*, **12** (1976), 362.
- E. Philippot, M. Maurin, *Revue de Chimie Minerale*, 1976, 13, 162.
- E. D. Politova, Y. N. Venevtsev, *Mat. Res. Bull.*, **10** (1975), 319.
- Y. Porter, N. S. P. Bhuvanesh, P. Shiv Halasyamani, *Inorg. Chem.*, **40** (2001), 1172.
- J. P. Pouget, C. Noguera, A. H. Moudden, R. Moret, *J. Physique*, **46** (1985), 1731.
- K. Prassides, P. Day, A.K. Cheetham, *Inorg. Chem*, **24** (1985), 545.
- I. I. Prosychev, V.B. Lazarev, I.S. Shaplygin, *Zh. Neorg. Khim*, **25** (1980) 1159.
- I.I. Prosychev, V.B. Lazarev, I.S. Shaplygin, *Zh. Neorg. Khim.*, **26** (1981) 3154.
- Quantum Design. 'Physical Property Measurement System Hardware and Operations Manual', 2<sup>nd</sup> Ed., Quantum Design, (1999).
- M. Rh. Rabadanov, A. A. Loshmanov, Yu. V. Shaldin, *Crystal. Rep.*, **42** (1997), 592.
- R. Rai, S. Sharma, R. N. P. Choudhary, *J. Mater. Sci. Lett.*, **21** (2001), 297.
- R. S. Rai, S. Sharma, R. N. P. Choudhary, *Ferroelectr.*, **275** (2002), 11.
- K. Ramesha, L. Sebastian, B. Eichhorn, J. Gopalakrishnan, *J. Mater. Chem.*, **13** (2003), 2011.
- A.P. Ramirez, G. Lawes, D. Li, M.A. Subramanian, *Solid State Commun.*, **131** (2004), 251.
- K. J. Range, W. Hegenbart, A. M. Heyns, F. Rau, K. Klement, *Z. Naturforsch.*, **B45** (1990), 107.
- K. J. Range, U. Klement, F. Rau, U. Schiessl, A. M. Heyns, *Z. Kristallogr.*, **203** (1993), 318.
- C. N. R. Rao, M. Motin Seikh, C. Narayana, *Top. Curr. Chem.*, **234** (2004), 786.
- M. J. Redman, W. P. Binnie, W. J. Mallio, *J. Less Common Metals.*, **23** (1971), 313.
- B. Rehak, K. Horcic, M. Frumar, L. Koudelka, *J. Cryst. Growth*, **68** (1984), 647.
- H. M. Rietveld, *Acta Crystallogr.*, **22** (1967), 151
- H. M. Rietveld, *J. Appl. Crystallogr.*, **2** (1969), 65.
- Rigaku Corporation, 'X-Ray Diffractometer MiniFlex II Instruction Manual', 2<sup>nd</sup> ed., Rigaku Corporation, (2006).
- M. B. Robin, P. Day, *Adv. Inorg. Chem. Radiochem.*, **10** (1967), 247.
- J. Rodriguez-Carvajal, *Physica B*, **192** (1993), 55.
- J. Rosicky, J. Loub, J. Pavel, *Z. Anorg. Allg. Chem.*, **334** (1965), 312.
- P. Rozier, L. Vendier, J. Galy, *Acta. Cryst.*, **C58** (2002), i111.



- K. K. Samplavskaya, M. Kh. Karapet'yants, *Zh. Neorg. Khim.*, **22** (1977), 2333.
- H. R. Shanks, P.H. Sidles, G.C. Danielson, *Adv. Chem. Ser.*, **39** (1963), 237.
- R. D. Shannon, *Acta Crystallogr., Sect. A*, **32** (1976), 751.
- R. D. Shannon, J. L. Gillson, R. J. Bouchard, *J. Phys. Chem. Solids.*, **38** (1977), 877.
- G.M. Sheldrick, SHELEXTL, Version 6.14, Bruker Analytical X-ray Instruments, Inc., Madison, WI, 2003.
- B. Shemirani, F. P. Koffyberg, *Mat. Res. Bull.*, **27** (1992), 693.
- Y. Shimizu, K. Maeda, *Sensor Actuat. B-Chem.*, **52** (1998), 84.
- A. Simon, J. Ravez, P. Hagenmuller, B. Frit, *Solid State. Commun.*, **29** (1979), 815.
- T. Siritanon, G. Laurita, R. T. Macaluso, J. N. Millican, A.W. Sleight, M.A. Subramanian, *Chem. Mater.*, **21** (2009), 5572.
- A.W. Sleight, *Mater. Res. Bull.*, **9** (1974), 1437.
- A. W. Sleight, *Inorg. Chem.*, **7** (1968), 1704.
- A. W. Sleight, *Mat. Res. Bull.*, **6** (1971), 775.
- A.W. Sleight, J. L. Gilson, P.E. Bierstedt, *Solid State Commun.*, **17** (1975) 27.
- A. W. Sleight, J. L. Gillson, B. L. Chamberland, *Mater. Res. Bull.*, **5** (1970), 807.
- A. W. Sleight, J. E. Gulley, T. Berzins, *Adv. Chem.*, **183** (1977), 195..
- J. Sloczynski, *Z. Anorg. Allg. Chem.*, **438** (1978), 287.
- Z. A. Solodovnikova, S. F. Solodovnikov, *Acta Cryst.*, **C62** (2006), i53.
- B. Stöger, W. Matthias, E. Zobetz, G. Giester, *Acta Cryst.*, **B65** (2009), 167.
- M. A. Subramanian, G. Aravamudan, G. V. Subba Rao, *Mat. Res. Bull.*, **14** (1979), 1457.
- M. A. Subramanian, G. Aravamudan, G. V. Subba Rao, *Prog. Solid State Chem.*, **15** (1983), 55.
- M. A. Subramanian, R. L. Harlow, A. P. Ramirez, *Inter. J. Inorg. Mater.*, **2** (2000), 131.
- M. A. Subramanian, D. Li, N. Duan, B. A. Reisner, A. W. Sleight, *Solid State Chem.* **151** (2000), 323.
- M. A. Subramanian, W. J. Marshall, R. L. Harlow, *Mat. Res. Bull.*, **31** (1996), 585.
- M. A. Subramanian, A. P. Ramirez, *Mat. Res. Soc. Symp. Proc. (Solid-State Chemistry of Inorganic Materials II)*, **547** (1999), 169.
- M. A. Subramanian, A. P. Ramirez, W. J. Marshall, *Phys. Rev. Lett.*, **82** (1999), 1558.
- M. A. Subramanian, A. W. Sleight, *Mat. Res. Bull.*, **21** (1986), 727.
- M.A. Subramanian, R. Subramanian, A. Clearfield, *Solid State Ionics*, **15** (1985), 15.
- M. A. Subramanian, C. C. Torardi, J. C. Calabrese, J. Gopalakrishnan, K. J. Morrisry, T. R. Askw, R. B. Flippen, U. Chowdhry, A. W. Sleight, *Science*, **239** (1988), 1015.
- I. Terasaki, N. Murayama, eds., *Oxide Thermoelectrics (Research Signpost, Trivandrum, India, 2002)*.
- P. A. Thomas, *J. Phys. C*, **21** (1988), 4611.
- G.J. Thorogood, P.J. Saines, B.J. Kennedy, R.L. Withers, M.M. Elcombe, *Mat. Res. Bull.*, **43** (2008), 787.
- G. Tieghi, P. Forzatti, *J. Appl. Crystallogr.*, **11** (1978), 291.
- B. C. Tofield, W. R. Scott, *J. Solid State Chem.*, **10** (1974), 183.

- A. Tressaud, R. De Pape, J. Portier, P. Hagenmuller, *Bull. Soc. Chim. Fr.*, **10** (1970) 3411.
- T. M. Tritt, M. A. Subramanian, *MRS Bull.*, **31** (2006), 188.
- M. Troemel, F.W. Huetzler, H.G. Burckhardt, C. Platte, E. Muench, *Z. Anorg. Allg. Chem.*, **551** (1987), 95.
- A. R. West, '*Solid State Chemistry and Its Applications*', John Wiley & Sons: New York, (1984).
- M. Trömer, D. Schmid, *Z. Anorg. Allg. Chem.*, **387** (1972), 230.
- X. Turrillas, G. Delabouglise, J. C. Joubert, *Solid State Ionics*, **21** (1986), 195.
- S. Uma, S. Kodialam, A. Yokochi, N. Khosrovani, M. A. Subramanian, A. W. Sleight, *J. Solid State Chem.*, **155** (2000), 225.
- E. J. W. Verwey, *Nature*, **144** (1939), 327.
- F. A. Weber, S. F. Meier, T. Schleid, *Z. Kristallogr. Suppl.*, **180** (2001), 149.
- F. A. Weber, T. Schleid, *Z. Anorg. Allg. Chem.*, **626** (2000), 1285.
- R. L. Weiher and R. P. Ley, *J. Appl. Phys.*, **37**, (1966), 299.
- M. Weil, *Solid State Sci.*, **6** (2004), 29.
- M. Weil, B. Stöger, *Acta Cryst.*, **C64** (2008), i79.
- M. T. Weller, M. J. Pack, N. B. Binsted, S. E. Dann, *J. Alloys Compd.*, **282** (1999), 76.
- A. R. West, '*Basic Solid State Chemistry*', John Wiley & Sons: New York, (1988).
- A. R. West, '*Solid State Chemistry and Its Applications*', John Wiley & Sons: New York, (1984).
- K. R. Whittle, G. R. Lumpkin, S. E. Ashbrook, *J. Solid State Chem.*, **179** (2006), 512.
- K. Wiegardt, H. Siebert, *J. Mol. Structure*, **7** (1971), 305.
- R. M. Wilson, J. C. Elliott, S. E. P. Dowker, R. I. Smith, *Biomater.*, **25**(2004), 2205.
- Th. Wisser, R. Hoppe, *Z. Anorg. Allg. Chem.*, **584** (1990), 105.
- F. Wöhler, *Ann. Phys. Chem. Pogg.*, **7** (1826), 417.
- P. Woodward, R.-D. Hoffmann, A.W. Sleight, *J. Mater. Res.*, **9** (1994), 2118.
- P. M. Woodward, A. W. Sleight, L.-S. Du, C. P. Grey, *J. Solid State Chem.*, **147** (1999), 99.
- T. G. Worlton, R. A. Beyerlein, *Phys. Rev. B.*, **12** (1975), 1899.
- T. Yamada, H. Iwasaki, *Appl. Phys. Lett.*, **21** (1972), 89.
- T. Yamada and H. Iwasaki. *J. Appl. Phys.* **44** (1973), p. 3934.
- Y. Yamamoto, R. Kanno, Y. Takeda, O. Yamamoto, Y. Kawamoto, M. Takano, *J. Solid State Chem.*, **109** (1994), 372.
- J.-I. Yamaura, S. Yonezawa, Y. Muraoka, Z. Hiroi, *J. Solid State Chem.*, **179** (2006), 336.
- R. A. Young, '*The Reitveld Method*', Oxford University Press, (1993).
- S. Yu. Stefanovich, V. A. Zhurov, S. A. Ivanov, L. A. Sadovskaya, K. V. Domoratsky, V. A. Dolgikh, *Ferroelectr.*, **241** (2000), 303.
- V. E. Zavodnik, *Acta Crystallogr. Sect. E: Struct. Rep. Online*, **E63** (2007), i75.
- V. E. Zavodnil, S. A. Ivanov, A. I. Stash, *Acta Crystallogr. Sect. E: Struct. Rep. Online*, **E64** (2008), i52.
- V. E. Zavodnil, S. A. Ivanov, A. I. Stash, *Acta Crystallogr. Sect. E: Struct. Rep. Online*, **E63** (2007), i151.

- V. E. Zavodnil, S. A. Ivanov, A. I. Stash, *Acta Crystallogr. Sect. E: Struct. Rep. Online*, **E63** (2007), i111
- V. E. Zavodnil, S. A. Ivanov, A. I. Stash, *Acta Crystallogr. Sect. E: Struct. Rep. Online*, **E63** (2007), i75.
- H. Zu, Y. Wang, P. Zhao, W. L. Bourcier, R. V. Konynenburg, H. F. Shaw, *Environ. Sci. Technol.*, **38** (2004), 1480.
- [http://www.khyberminerals.com/tucson09\\_1.htm](http://www.khyberminerals.com/tucson09_1.htm), Accessed February 2011.